博士論文

Rock physics study on the frequency dependence of seismic attenuation in methane hydrate-bearing sediments

（メタンハイドレート賦存層における地震波減衰の周波数依存性に関する岩石物理学的研究）

詹 林森

ROCK PHYSICS STUDY ON THE FREQUENCY DEPENDENCE OF SEISMIC ATTENUATION IN METHANE HYDRATE-BEARING SEDIMENTS

メタンハイドレート賦存層における地震波減衰の周波数依存性に関する岩石物理学的研究

By

Linsen Zhan

Supervisor: Dr. Jun Matsushima
Associate Professor of Department of
Technology Management for Innovation

TABLE OF CONTENTS

LIST OF TABLES

LIST OF FIGURES

LIST OF SYMBOLS AND ABBREVIATIONS

Symbols

a_{si} Tortuosity for sand flowing through ice

a_{fi} Tortuosity for water flowing through ice

a_{is} Tortuosity for ice flowing through sand

b_{si0} Friction coefficient between solid grain and ice

b_{sh0} Friction coefficient between solid grain and hydrate

b_{ss} Friction coefficient between sand grains

b_{ii} Friction coefficient between ices

b_{hh} Friction coefficient between hydrates

c_{pf} Fraction of pore-filling hydrate

c_i Fluid inclusion concentration

c_s Consolidation coefficient for sand grains

c_{ice} Consolidation coefficient for ice

c_h Consolidation coefficient for hydrate

F_s Fraction of sand when containing clay

$F(\zeta)$ Viscodynamic operator

f Source frequency

g_s Consolidation coefficient for sand grains

g_i Consolidation coefficient for ice

g_h Consolidation coefficient for hydrate

h Average thickness of the water layer

K_s Solid bulk modulus

K_i Ice bulk modulus

K_f Fluid bulk modulus

K_h Hydrate bulk modulus

K_{sm} Bulk modulus of the matrix formed by sand grains

K_{im} Bulk modulus of the matrix formed by ice

K_{hm} Bulk modulus of the matrix formed by hydrate

$K_{\max}$ Kuster-Toksoz bulk modulus for the ice matrix

K_{av} Average bulk modulus

K'_{dryc} Bulk modulus of the dry frame for contact cementing hydrate

K'_{drypf} Bulk modulus of the frame for pore-filling hydrate

K'_{dry} Effective bulk modulus of the dry frame

K'_{fp} Effective bulk modulus of fluid phase

K'_{solid} Effective solid bulk modulus

n Sand grain coordination number

n_{kc} Intrinsic permeability exponent for contact cementing hydrate

n_{kp} Intrinsic permeability exponent for pore-filling hydrate

Δr Standard deviation of sand grain radius

r_{av} Average pore radius

P Effective pressure

R_{ss} Rigidity coefficient between sand grains

R_{si} Rigidity coefficient between sand grain and ice

R_{sh} Rigidity coefficient between sand grain and hydrate

R_{ii} Rigidity coefficient between ices

R_{hh} Rigidity coefficient between hydrates

R_{ff} Rigidity coefficient between fluid

R_{sf} Rigidity coefficient between fluid and sand grain

R_{fi} Rigidity coefficient between fluid and ice

R_{fh} Rigidity coefficient between fluid and hydrate

r_{sf} Geometrical aspect of the boundary separating fluid and sand

r_{si} Geometrical aspect of the boundary separating sand and ice

r_{sh} Geometrical aspect of the boundary separating sand and hydrate

r_{is} Geometrical aspect of the boundary separating ice and sand

r_{hs} Geometrical aspect of the boundary separating hydrate and sand

r_{fi} Geometrical aspect of the boundary separating fluid and ice

r_{fh} Geometrical aspect of the boundary separating fluid and hydrate

r_s Average radius of sand grains

S_i Ice saturation

S_h Hydrate saturation

t Tortuosity

α_i Fluid inclusion aspect ratio

ε Ratio of the volume of inclusion to pore

ϕ_0 Initial porosity

ϕ_c Critical porosity

ϕ_s Fraction of sand grains

ϕ_f Fraction of fluid and it also means real porosity

ϕ_i Fraction of ice

ϕ_h Fraction of hydrate

γ Relaxation time

η_0 Initial viscosity at freezing point

η_D Dynamical viscosity of interstitial water

k_0 Intrinsic permeability without hydrate

k Intrinsic permeability

k_{s0} Solid matrix permeability

k_{i0} Ice matrix permeability

k_{h0} Hydrate matrix permeability

k_s Effective permeability of sands

k_i Effective permeability of ices

k_h Effective permeability of hydrates

μ_{si0} Coupling shear modulus between solid grain and ice

μ_{sh0} Coupling shear modulus between solid grain and hydrate

μ_s Solid shear modulus,

μ_i Ice shear modulus

μ_h Hydrate shear modulus

μ_{sm} Shear modulus of the matrix formed by sand grains

$\mu_{\max}$ Kuster-Toksoz shear modulus for the ice matrix

μ_{im} Shear modulus of the matrix formed by ice

μ_{hm} Shear modulus of the matrix formed by hydrate

μ_{av} Average shear modulus

μ_{ss} Shear modulus in solid grain phase

μ_{si} Cementation between ice and sand grains

μ_{sh} Cementation between hydrate and sand grains

μ_{ii} Shear modulus in ice phase

μ'_{dry} Effective shear modulus of the dry frame

μ'_{dryc} Shear modulus of the dry frame for contact cementing hydrate

μ'_{drypf} Shear modulus of the frame for pore-filling hydrate

μ'_{solid} Effective solid shear modulus

ν Sand grain Poisson's ratio

ν_h Hydrate Poisson's ratio

ρ_e Effective density of sediment

ρ_s Sand grain density

ρ_i Ice density

ρ_h Hydrate density

ρ_f Fluid density

ρ_{ss} Mass density due to the oscillation of sand grans

ρ_{sf} Mass density due to the oscillation of sand grans into fluid

ρ_{si} Mass density due to the oscillation of sand grans into ice

ρ_{sh}	Mass density due to the oscillation of sand grans into hydrate
ρ_{ii}	Mass density due to the oscillation of ice
ρ_{hh}	Mass density due to the oscillation of hydrate
ρ_{ff}	Mass density due to the oscillation of fluid
ρ_{fi}	Mass density due to the oscillation of fluid into ice
ρ_{fh}	Mass density due to the oscillation of fluid into hydrate
ω	Angular frequency

Abbreviations

BISQ	Biot and squirt flow
BSR	Bottom simulating reflector
HEG	Hydrate effective grain model
MH	Methane hydrate
MITI	Japanese Ministry of International Trade and Industry
NMR	Nuclear Magnetic resonance
OBS	Ocean bottom seismometer
P-wave	Compressional (primary) wave
PSW	Post survey well
SCA	Self-consistent model
S-wave	Shear (secondary) wave
THF	Tetrahydrofuran
USGS	U.S. Geological Survey
VSP	Vertical seismic profile
w-VSP	Walkaway vertical seismic profile

SUMMARY

Methane hydrates (MH) are well known to have an influential effect on the physical properties of MH-bearing sediments such as velocity and attenuation. Geophysical techniques such as VSP (Vertical Seismic Profiling) and well logging have been widely used for mapping and quantifying hydrate for MH-bearing sediments. Ultrasonic measurements for synthetic or core MH samples can provide insight on the exploration of MH-bearing sediments, and partially frozen system is considered to be an effective substitution for synthetic or core MH samples.

Most sonic logging data acquired in MH-bearing zones have shown an increasing velocity of compressional (P-) and shear (S-) waves accompanied by high attenuation of P- and S-waves. In addition to field data, ultrasonic experimental investigations also showed simultaneous high velocity and high attenuation of ultrasonic P- and S- waves near the freezing point of brine in partially frozen systems. More controversially, no significant or significant attenuation was observed at seismic frequencies in MH-bearing sediments of various geological environments. Intuitively, one would expect that the higher velocity would be corresponding to the lower attenuation. Unexpectedly, significantly large attenuation was observed at sonic frequencies in MH-bearing sediments and at ultrasonic frequencies for partially frozen systems. Due to the lack of understanding on how MH affects the physical properties of MH-bearing sediments, using geophysical methods to accurately identify and quantify the extent of MH-bearing sediments is remain challenging and unreliable.

The combined use of various measurement methods at different frequencies such as sonic, VSP, and ultrasonic transmission measurements provides an opportunity to examine the frequency-dependent attenuation in MH-bearing sediments. For a more detailed understanding of the rock physical mechanisms responsible for the attenuation at different frequencies (VSP, sonic, and ultrasonic frequencies), different rock physics models are adopted to predict the P- and S-wave velocities and attenuations at MH-bearing sediments and partially frozen systems, and then the predicted values by rock physics modeling are compared with those derived from field sonic logging, VSP, and ultrasonic measurement data. In this study, two different rock physics models that have recently been developed to consider the squirt flow in porous/microporous hydrate and the interaction between sand and hydrate grains in MH-bearing sediments are applied. Also, an effective medium model is applied to partially frozen brine and a three-phase extension of Biot model is applied to partially frozen unconsolidated sands.

By matching the predicted and measured values, the input parameters of the rock physics models are adjusted, (1) such as hydrate morphologies, water inclusion concentration, water inclusion aspect ratio, and initial sand sediment and hydrate permeability for MH-bearing sediments, (2) such as average pore radius of porous ice, viscosity and density of brine, and freezing point for partially frozen systems. I find influential input parameters for different rock physics models, and carefully make a definition for these parameters, and then provide a good agreement between measured and predicted values. Finally, for field data, I infer that this frequency-dependent P-wave attenuation may be due to the squirt flow caused by the combined effect of the degree of hydrate saturation and two permeable systems (one is between sand grains and the other is between hydrate grains), or due to the squirt flow caused by fluid inclusions with different aspect ratios in a microporous hydrate. Furthermore, the similar frequency-dependent S-wave attenuation is predicted by rock physical modeling, and I infer that both the Biot flow and friction between hydrate and sand grains dominate S-wave attenuation at seismic frequencies, whereas friction alone is dominant at sonic logging frequencies.

In ultrasonic transmission measurements, for partially frozen brine, my rock physical study indicates that squirt flow caused by unfrozen brine inclusions in porous ice could be responsible for high P-wave attenuation around the freezing point. Decreasing P-wave attenuation below the freezing point can be explained by the gradual decrease of squirt flow due to the gradual depletion of unfrozen brine. For partially frozen unconsolidated sands, based on the rock physical study I infer that squirt flow between ice grains is a dominant factor for P-wave attenuation around the freezing point. With decreasing temperature below the freezing point, the friction between ice and sand grains becomes more dominant for P-wave attenuation. The increasing friction between ice and sand grains caused by ice formation is possibly responsible for increasing S-wave attenuation at decreasing temperatures. Then, further generation of ice with further cooling reduces the elastic contrast between ice and sand grains, hindering their relative motion and thus reducing the P- and S-wave attenuations.

The laboratory measurement results at ultrasonic frequencies and field data at seismic and well logging frequencies for MH-bearing sediments are separately discussed due to different performances of physical properties at different frequencies. This study tries to elucidate the underlying attenuation mechanisms responsible for P- and S-wave attenuations at various frequencies. This study also provides a geophysical basis for identifying the occurrence of MH and characterizing the amount of MH using P- and S-wave attenuations at various frequencies, and then the physical properties of MH-bearing sediments inferred from rock physics modeling are beneficial for field production monitoring of MH-bearing sediments.

CHAPTER 1. INTRODUCTION

This thesis ultimately focuses on the frequency dependent velocity and attenuation of both P- and S-waves for methane hydrate (MH)-bearing sediments. To do this, the different responses of physical properties at different frequency domains must be investigated and the effect of the presence of hydrate on physical properties of MH-bearing sediments should be fully clarified. In this chapter, an overview of this study will be provided firstly. The basic crystal structure, the global distribution, impacts on economy and environment, and naturally occurring morphologies of MH will be introduced. Then the current geophysical exploration methods for MH-bearing sediments, including vertical seismic profile (VSP) method, surface seismic method, and well logging method will be described. The previous studies on velocity and attenuation of MH-bearing sediments at frequencies from VSP to sonic logging will be reviewed. In addition to geophysical techniques, laboratory measurements of in situ or synthetic MH samples are also a complementary method to study the rock properties of MH-bearing sediments. The measurements usually are conducted from seismic to ultrasonic frequency domain, and these measurements will be introduced in this section. Next, theoretical rock physics modeling also can be used for describing the rock properties of MH-bearing sediments, and a comprehensive review and comparison of previous rock physics models will be provided here. Finally, the aims and outlines of this thesis will be given.

1.1 Gas hydrates

1.1.1 What are gas hydrates

Gas hydrate is a crystalline compound consisting of water and guest molecules that forms under high pressure and low temperature (Sloan & Koh, 2006). When the guest molecule is methane and the crystal lattice is made up of water molecules, this compound is used in terms of methane hydrate (MH). For uniformity, the term “methane hydrate (MH)” will be used instead of “gas hydrate” in the following section of this thesis. The most commonly encountered MH in nature comes in dodecahedral structure (see Fig. 1.1). The structure and physical properties of MH are very similar to that of ice in many ways, although unlike ice, their rigidity is slightly different and hydrate can forms under a temperature higher than 0 °C at high pressure but ice cannot (Buffett, 2000).

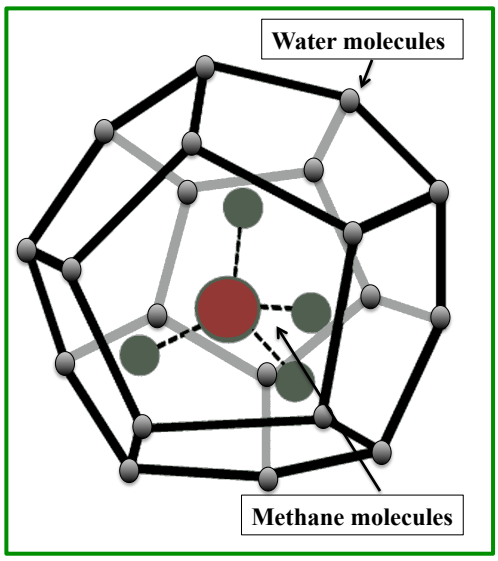

Figure 1. 1 Crystal structure of methane hydrate (MH) (adapted from Sloan & Koh, 2006).

1.1.2 Impacts of gas hydrates

A great amount of efforts have been focused on several impacts of MH: the potential of MH as a main alternative energy resource, and important effects on global climate change and sub-marine geohazards (Haq, 1999).

The discovery of MH accumulations in terrestrial permafrost and beneath the ocean along the continental margins worldwide have triggered our interest on MH as a potential and unconventional energy resource for the next few decades (Kelland, 1994). Although there still is disagreement over the concentration of MH within MH-bearing sediments and the total amount of methane stored in MH accumulations, the estimated amount of methane in MH accumulations worldwide is considered to contain more potential energy than conventional oil, gas and coal deposits (Dawe & Thomas, 2007; Demirbas, 2010; Demirbas et al., 2016; Singh, 2015). There are two factors to make MH as a potential energy resource: the enormous amount of methane within MH accumulations and widespread distribution of MH-bearing sediments (Kvenvolden, 1993). Previous estimates of the available amount of methane in MH are highly varied over a wide range because direct sampling and analysis of MH in the natural state are an almost impossible task (Haq, 1999) . Kvenvolden (1993) roughly estimated that the available amount of methane worldwide in MH will be up to $2\times10^{16}\ \ m^3$. Demirbas (2010) estimated that the amount of methane within MH was about $2.1\times10^{16}\ \ m^3$, which is more than all conventional fossil fuel. Kelland (1994) concluded that the in situ MH estimate is within the range of $1.4\times10^{13}-3.4\times10^{16}m^3$ for the onshore continental margins, and $3.1\times10^{15}-7.6\times10^{18}m^3$ for the ocean offshore. Based on an exhaustive review of other assessments and existing drilling programs,

Boswell and Collett (2011) indicated that the amount of MH accumulations appears most likely to be $3\times10^{15}m^3$. Collett (2002) indicated that whether an estimation is precisely accurate or not is dependent on following five primary reservoir parameters: (1) coverage of the MH occurrence, (2) reservoir thickness, (3) sediment porosity, (4) MH saturation, and (5) the methane yield volumetric parameter, which defines how much free gas (at standard temperature and pressure) is stored within an MH. The five reservoir parameters can be estimated by field measurements such as remote seismic and down-hole methods (Kvenvolden, 1993).

Besides being potential energy resource, MH also leads to global climate change and submarine geohazards (Boswell & Collett, 2011; Dawe & Thomas, 2007). The principal component of greenhouse gas is CO_2, and its concentration is presently increasing at a rate of about 0.35% per year. In contrast, methane is also one important component in the atmosphere and its concentration increase at a fast rate of about 1 to 2% per year. Previous studies tended to speculate that the MH dissociation was a potential threat associated with global warming due to the following two factors: (1) because methane is radioactively active, it is a greenhouse gas that has a global warming potential 20 times more than an equivalent weight of CO_2, (2) if the enormous amount of methane trapped in MH accumulations releases out of control, this massive release might have a significant impact on atmospheric composition and thus on the global climate change (Harvey & Huang, 1995; Kvenvolden, 1988, 1993). In fact, large-scale MH dissociation is not only as a potential driver for enhanced warming if released methane from MH reaches the atmosphere, but also is a consequence of warming because the global warming might change the sea level (pressure) and ocean temperature, thus affect the stabilization condition of intermediate-pressure and low temperature (Ruppel & Kessler, 2017). Kvenvolden (1988) indicated that the contribution of methane released from destabilized MH to greenhouse warming is probably small, and then this atmospheric methane on global climates will likely be minimal. Ruppel (2011) and Ruppel and Kessler (2017) indicated that some factors might mitigate the impact of MH dissociation on atmosphere greenhouse gas concentration: (1) the depth of MH-bearing sediments, (2) because the sediments and ocean column strongly sink, released methane at sea floor cannot reach to sea-air interface or atmosphere. Therefore, they concluded that there is no convincing proof that methane associated with MH is reaching the atmosphere now.

In addition to the potential effect on global climate change, the dissociation of MH accumulation also might trigger submarine slope failure or sediment slump (Paull, 2001; Kvenvolden, 1993; Maslin et al., 2010; McIver, 1977; Paull et al., 2002; Paull et al., 2007). The lowering of sea level or an increase of ocean bottom will destroy the stability conditions of MH (high pressure and relatively low temperature), and then cause MH dissociation. Accompanied by this releasing of methane, submarine sediment slumps and slides can occur. The first submarine slope failure and slump possibly caused by

dissociation of MH is recognized by McIver (1977). Kvenvolden (1993) provided several possible examples related to the sediment slides and slumps on the continental slope including: the South West Africa (Summerhayes et al., 1979), the U.S. Atlantic continental slope (Carpenter, 1981), Norwegian continental margin (Bugge et al., 1987), the British Columbia (Bornhold & Prior, 1989), and the Alaskan Beaufort Sea continental margin (Kayen & Lee, 1991). Although it is complicated to verify the interaction between geological slope failure and MH activity, Maslin et al. (2010) provided some recent and famous evidence of geologic slope failure which are believed to relate to MH decomposition including: U.S. Atlantic margin (Hornbach et al., 2007) and Storegga slide off Norway (Haflidason et al., 2004, 2005). If submarine slope failures occur, seismic mapping of the seafloor has shown that seismic evidence of gas and fluid pathways in the sediment is often recognized near slide (Maslin et al., 2010).

1.1.3 Global distribution of gas hydrates

The presence of MH is a finely balanced system in equilibrium, and the reduction of pressure and increase of temperature will cause the decomposition of MH (Chong et al., 2016; Zatsepina & Buffett, 1997). The occurrences of MH-bearing sediments are restricted to two types of geologic locations: (1) under permafrost in polar continental shelves, (2) sediments beneath the ocean floor. As shown in Fig. 1.2, the section outlined by blue, red and green curves illustrates the stability zones of MH in permafrost (Fig. 1.2a) and oceanic sediments (Fig. 1.2b) where the pressure and temperature conditions and the concentration of methane are within the stability regions. The purple zones correspond to MH zones with dissolve methane, while yellow regions possibly coexist dissolved methane and free gas. The phase boundary curve (red curve) defines the stability of hydrate, and the geothermal curve (blue curve) along with ocean water temperature curve (green curve) defines the change of temperature with depth which are originated from Paull (2001) and Sloan & Koh (2006). Note that MH stability calculations usually use hydrostatic pressure in shallow sub-seafloor sediments owing to their high porosity (Dawe & Thomas, 2007; Ruppel & Kessler, 2017). As shown in Fig. 1.2, temperature decreases and then increases from sea level to the sea floor in marine sediments (Fig. 1.2b), while monotonically increases from ground surface to sediments in permafrost (Fig. 1.2a). MH can exist when the pressure/temperature conditions are in the left side of the phase boundary (red curve) in Figs 1.2a and 1.2b (Merey, 2016; Ruppel & Kessler, 2017).

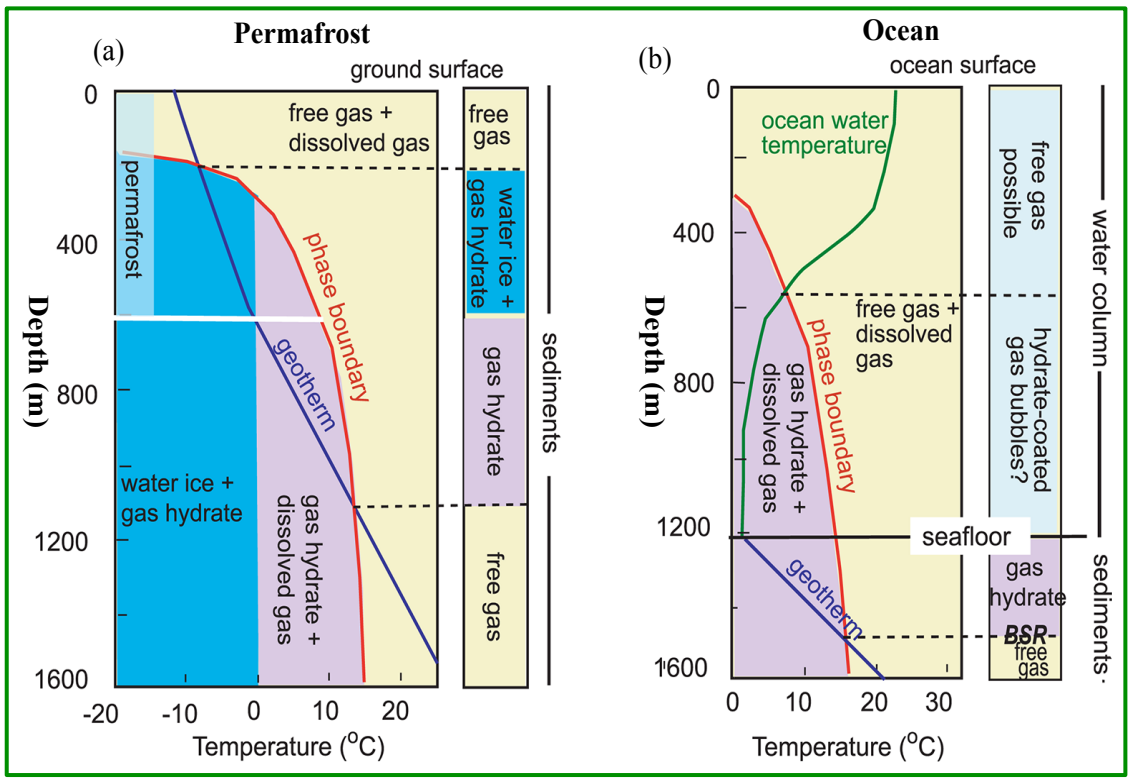

Figure 1. 2 Methane hydrate stability zones for (a) permafrost and (b) marine sediment (modified from Ruppel & Kessler, 2017). BSR in Fig. 1.2(b) refers to bottom simulating reflector that marks the boundary between free gas and overlying hydrate-bearing sediment in the marine reservoir.

A series of recent field expeditions have provided new insights into the nature of MH occurrence. The confirmed MH-bearing sediments occur in a wide variety of geologic settings, and the field data have indicated that MH-bearing coarse and fine sands are superior reservoirs due to their higher permeability (Boswell & Collett, 2011). The MH-filled fractures in clay-dominated reservoirs also became potential energy production targets (Boswell & Collett, 2011; Demirbas, 2010). As shown in Fig. 1.3, MH-bearing sediments have been identified in marine environments near almost every continental margin, and also have been found in permafrost regions below the continental surface because these zones are organic-rich and temperature/pressure conditions are suitable for formation of MH accumulations (Merey, 2016). However, only a limited number of MH accumulations have been investigated in detail. Chong et al. (2016) and Collett (2002) reviewed and described some best-known marine and permafrost MH-bearing sediments. They are located at: (1) the Blake Ridge along the southeastern continental margin of the U.S. (Borowski, 2004; Coren et al., 2001; Ghosh et al., 2010b; Holbrook et al., 1996; Hornbach et al., 2003; Wood et al., 2000), (2) the Cascadia continental margin off the Pacific coast of Canada (Dash & Spence, 2011; Dillon et al., 1993; Riedel et al., 2006; Westbrook et al., 2008; Yuan et al., 1996, 1999), (3) the Nankai Trough off the eastern coast of Japan

(Ashi et al., 2002; Baba & Yamada, 2004; Konno et al., 2010, 2017; Nouzé et al., 2004; Tsuji et al., 2004; Uchida et al., 2004), (4) the North Slope of Alaska (Collett et al., 2011; Lee et al., 2009; Winters et al., 2010), (5) the Malik site in the Mackenzie Delta, Canada (Bellefleur et al., 2006; Carcione & Gei, 2004; Riedel et al., 2009), and (6) the Krishna-Godavari basin of India (Collett et al., 2014; Cook & Goldberg, 2008; Kumar et al., 2014; Lee & Collett, 2009; Priest et al., 2014). So far these field tests are conducted by using thermal stimulation method, inhibitor injection method, and depressurization method (considered to be the most economical and efficient) (Singh, 2015). USGS (U.S. Geological Survey) provided the possible and challenging research prospects about MH from 2015 to 2030 including the characterization of MH system, development of in situ sampling technologies, and development of production technology. In this thesis, my primary interest in MH-bearing sediments is located at the Nankai Trough of Japan, which is subjected to extensive studies including various geophysical methods, core sampling, and rock physical modeling. The other best-known MH reservoirs will be used as a reference in this thesis.

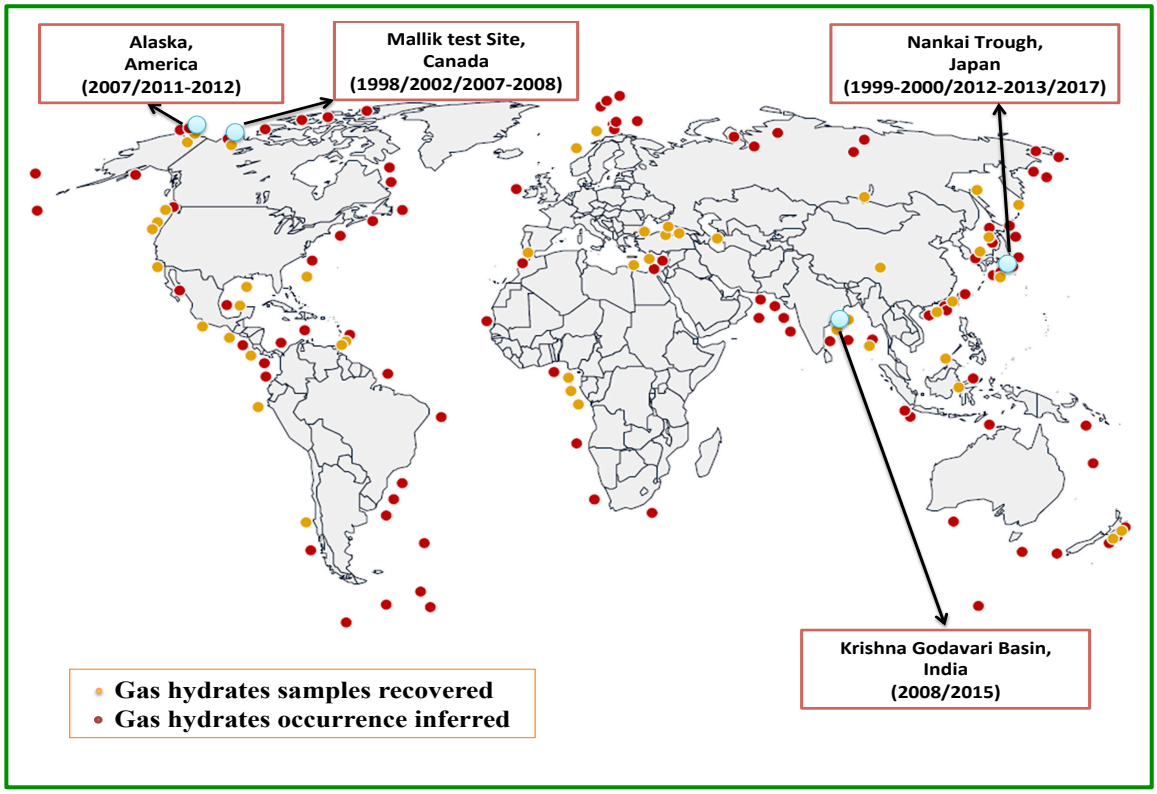

Figure 1. 3 Global distribution of known MH-bearing occurrence in oceanic sediments of outer continental margins and permafrost regions (modified from Collett, 2002) (orange dot indicates gas hydrate samples recovered and red dot indicate inferred gas hydrate occurrence). Red boxes show the field names of MH-bearing sediments, which will be discussed in this thesis.

1.1.4 Gas hydrate morphology

Natural methane hydrate (MH) usually occurs in sediments with following morphologies: enveloping of grains (envelope cementing hydrate) (Fig. 1.4a), cementing of grain contacts (contact cementing hydrate) (Fig. 1.4b), connecting neighboring grains as a sediment frame (load-bearing hydrate) (Fig. 1.4c), and growth away from grains in pore spaces (pore-filling hydrate) (Fig. 1.4d) (Yun et al. 2005). It has been recognized that the MH morphologies significantly affect the overall rock physical properties of MH-bearing sediments, and the MH morphology is dependent on the sediment lithology, pore structure, and MH saturation (Waite et al., 2009). Unfortunately, MH in cores are almost impossibly survivor during the coring process due to the changing of temperature and pressure; therefore MH morphology is complicated to identify from field samples in situ.

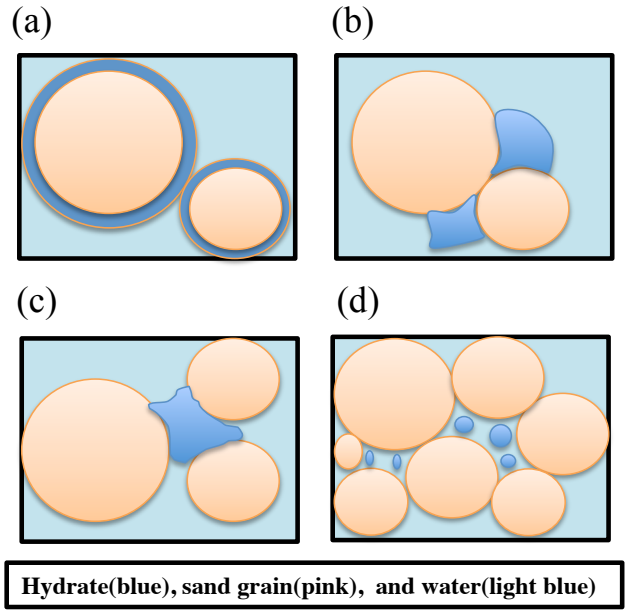

Figure 1. 4 Hydrate morphologies in sediment: (a) envelope cementing hydrate, (b) contact cementing hydrate, (c) load-bearing hydrate, and (d) pore-filling hydrate. The blue indicates hydrate, pink indicates sand grain, and light blue indicates ocean water.

There are few studies to investigate how natural MH grows in sediments. Hydrate morphology at the Blake Ridge site is inferred as load-being hydrate with a maximum hydrate saturation below 18% (Ecker et al., 1998, 2000; Helgerud et al., 1999). Hydrate morphology in the Mallik site is inferred as load-bearing or pore-filling hydrate with a maximum hydrate saturation between 80% and 90% (Chand et al., 2004; Lee & Waite, 2008). There are also few researches on the hydrate morphology at Nankai Trough. Jin et al. (2016) indicated that the hydrate morphology of MH-bearing sediments in the Nankai Trough demonstrated a load-bearing morphology type, and Jia et al. (2017) demonstrated that hydrate is attached to the grain surfaces of rock matrix rather than floating in pore space. Furthermore, patchy hydrate (100% hydrate saturated pore are embedded into hydrate-free sands) also

seems to be a reasonable hydrate morphology (Dai et al., 2012). The load-bearing and pore-filling hydrate morphologies are generally interpreted as natural hydrate morphologies from field data, especially for high hydrate saturation. In laboratory measurements for synthetic MH-bearing rock samples, hydrate could be designed to grow as cementing morphology by using "excess gas method" and as pore-filling morphology by using "excess water method", or changing hydrate morphology with the growing hydrate saturation: initially cements at grain contacts, then fills the pore space, finally grows as load frame (Bu et al., 2017; Choi et al., 2014; Priest et al., 2005, 2009; Yun et al., 2005).

Although hydrate morphology should be dependent on different geological environments, there seems to be no consensus even for the same location. Many rock physical models were proposed to predict the rock physical properties (velocity, attenuation, hydrate saturation) of MH-bearing sediment, and it should be noted that hydrate morphology is required information in these predictions (Ecker et al., 1998, 2000; Helgerud et al., 1999; Jakobsen et al., 2000). However, the prediction for physical properties of MH-bearing sediments seems to be still problematic because of unknown prior information on hydrate morphology. In this thesis, I try to provide insights into the natural MH morphology at the Nankai Trough by using rock physics modelling.

1.2 Geophysical exploration for MH-bearing sediments

The presence of MH essentially affects the properties of MH-bearing sediments as following: (1) physical properties, such as shear strength, porosity, permeability, (2) geophysical properties, such as resistivity, velocity and attenuation, (3) geochemical properties, such as fluid composition and movement (Kvenvolden, 1993; Waite et al., 2009). The presence of hydrate can significantly affect the properties of the hosted sediments. This results in geophysical anomalies allowing us to employ a corresponding geophysical method to characterize MH-bearing sediments. Among these geophysical anomalies, the velocity and attenuation of P- and S-waves have been extensively used to characterize the occurrence and distribution of hydrate and assess the hydrate saturation of hydrate-bearing sediments (Waite et al. 2009). This thesis mainly focuses on how the presence of MH affects the P- and S-wave velocities and attenuations.

1.2.1 Wave propagation in MH-bearing sediments

1.2.1.1 Wave velocity

Seismic velocity of MH-bearing sediments is known to increase compared to sediments without hydrate. The presence of MH makes the sediments stiffer, and it might cement the grains together, and then cause the bulk and shear moduli significantly increase, thus increase both P- and S-wave velocity.

However, the degree of increase of velocity is dependent on hydrate saturation and hydrate morphology (Yun et al., 2005, 2007).

To relate P-wave velocity (V_p) and S-wave velocity (V_s) to hydrate saturation, bulk and shear moduli of MH-bearing sediments should be expressed as functions of mineral, sediment, pore fluid, and hydrate properties. MH-bearing sediments have been considered as an effective medium model (Helgerud et al., 1999; Jakobsen et al., 2000) or as a three-phase frameworks: sediments framework, hydrate framework, and pore fluid (free gas and water) (Carcione & Seriani, 1998; Carcione & Tinivella, 2000; Davide & Carcione., 2003; Lee & Waite, 2008). Previous rock physics modeling has taken into account the effect of hydrate morphology on velocity. The disseminated hydrate tends to form pore-filling hydrate at low hydrate saturation, while it tends to become load-bearing sediments as hydrate saturation exceeds 25%-40% (Yun et al., 2005, 2007). The velocities of P- and S- wave for cementing hydrate-bearing sediment sharply increase even at a low hydrate saturation (<3%), conversely those are insensitive to hydrate saturation until hydrate saturation exceeds 40% for load-bearing and pore-filling hydrate (Lee et al., 2010; Priest et al., 2005, 2009). By using rock physics modeling, this thesis tries to provide physical insight into the relationship among hydrate morphology, hydrate saturation and P- and S-wave velocities of MH-bearing sediments.

1.2.1.2 Wave attenuation

Since the attenuation is the main focus of this thesis, general attenuation of non-hydrate sediments will be provided firstly. Attenuation is a measure of energy loss when the elastic wave travels through a rock (Barton, 2007). It can be divided into apparent attenuation and intrinsic attenuation. Intrinsic attenuation refers to the seismic energy loss by conversion to heat such as inertial friction and attenuation related to fluid flow, while apparent attenuation refers to the redistribution of unobserved part of wave field such as scattering caused by random heterogeneities and geometric spreading caused by a non-planar wavefront (Lerche & Menke, 1986; Menke & Dubendorff, 1985). The intrinsic attenuation is more important because it can reflect rock and fluid properties. Several important intrinsic attenuation mechanisms are dependent on sediment lithology, fluid saturation, frequency, and strain amplitude, etc. as following (Barton, 2007; Johnston et al., 1979):

1. Matrix anelasticity.
2. Friction dissipation due to relative motions between grains and crack surfaces (Walsh, 1966), and this friction dissipation increases with increasing strain amplitude (Winkler & Nur, 1982a), Winkler and Nur (1982) concluded that since sliding friction only could be observed at large strain and small confining pressure and this required condition

generally didn't occur in seismic wave propagation in the earth, then suggested that friction was not a significant attenuation mechanism in situ.

3. Squeezing gas pockets for the case of partial saturation (Tisato et al., 2015; White, 1975).
4. Global Biot flow. Relative motion of matrix frame with respect to fluid in fully saturated rock. For water-saturated rock, the transition frequency of the Biot flow is proportional to viscosity and inversely proportional to the permeability (Biot, 1956a; Leclaire et al., 1994).
5. Local squirt flow. The local variations of pore pressure due to contraction and expansion of the pore space may trigger the pore fluid flow in partially or fully saturated rocks. The attenuation caused by local squirt flow maybe pronounced at the characteristic frequency, and the transition frequency is inversely proportional to the viscosity (Jones, 1986; Mavko & Jizba, 1991; Mavko & Nur, 1979; Murphy et al., 1986; Murphy, 1983).
6. Wave-induced flow due to mesoscopic scale patches. The wave-induced fluid flow occurring at mesoscopic scale is capable of explaining the measured attenuation within the seismic frequencies (1 to 10^4 Hz) (Ba et al., 2008; Müller & Gurevich, 2005; Pride et al., 2004; Tisato & Quintal, 2013).

As referred above, it is believed that intrinsic attenuation for fluid-saturated rocks is frequency dependent over a broadband frequency range through a series of experiment data (Batzle et al., 2006; Best et al., 2001; Jones, 1986; Murphy, 1983; Sams et al., 1997),

The presence of MH makes the attenuation mechanism more complicated. The attenuation is affected by hydrate saturation and interaction between hydrate and sand grains (Best et al., 2013; Guerin & Goldberg, 2005; Marín-Moreno et al., 2017). The proposed attenuation mechanisms associated with MH-bearing sediments include global Biot flow and local squirt flow (Guerin & Goldberg 2005; Best et al. 2013; Marín-Moreno et al. 2017), cementation and frictional loss between hydrate and solid grain (Guerin & Goldberg 2005), mesoscale wave-induced fluid flow (Tisato & Quintal 2013; Mikhaltsevitch et al. 2014), the effect of hydrate morphology on attenuation (Priest et al. 2006; Best et al. 2013; Marín-Moreno et al. 2017), and gas bubble damping (Marín-Moreno et al. 2017) (Fig. 1.5).

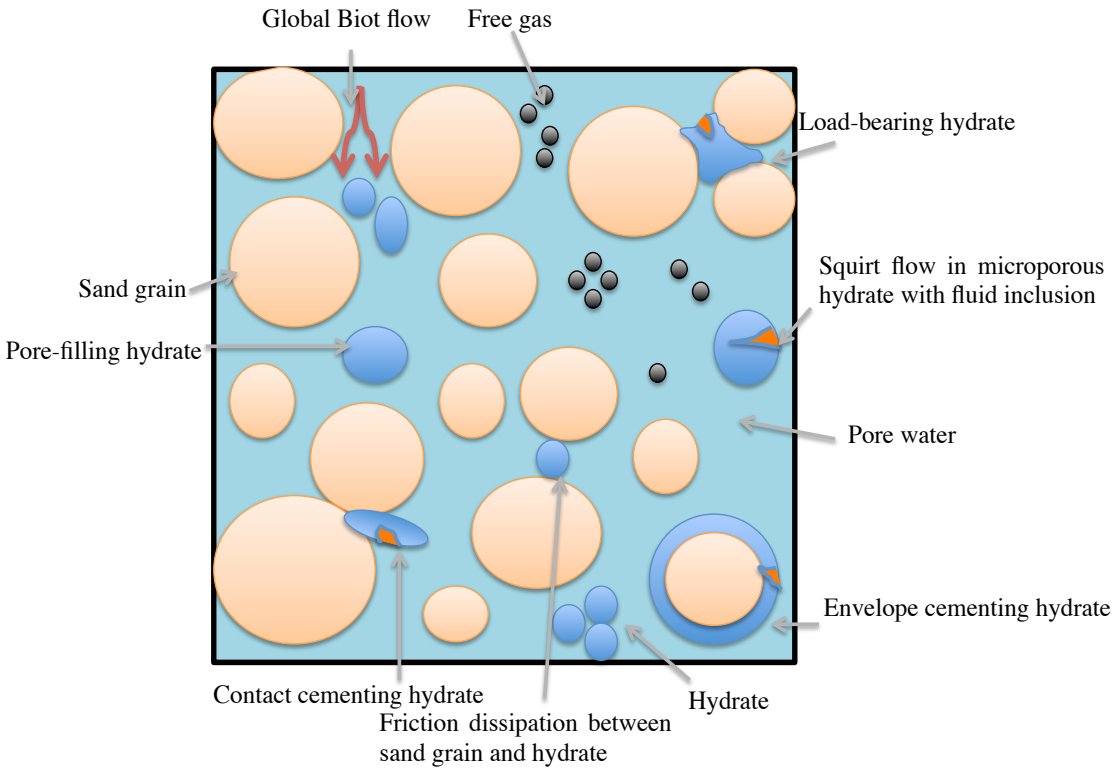

Figure 1. 5 Proposed attenuation mechanisms associated with MH-bearing sediments. The blue indicates hydrate, pink indicates sand grain, orange indicates fluid inclusion, light blue indicates ocean water, and black indicates gas.

Unfortunately, estimation of intrinsic attenuation of MH-bearing sediments is easily disturbed by the effects of geometric spreading and spatially impedance heterogeneity (Huang et al., 2009; Lee & Waite, 2007). Moreover, the attenuation mechanisms for different frequency domain have not yet been clarified. These challenges have limited the reliability of attenuation as an effective tool for evaluation of MH-bearing sediments. By using rock physical modeling, this thesis tries to elucidate the attenuation mechanisms responsible for different frequency domains.

1.2.2 Detection and quantification for MH-bearing sediments

Over the past few decades, several national MH programs exist in countries such as Japan (Uchida et al., 2004), the United States (Boswell & Collett, 2011), Canada (Guerin & Goldberg, 2002), China (Wang et al., 2011, 2012), India (Kumar et al., 2016), and Korea (Ryu & Riedel, 2017). A tremendous number of geophysical exploration expeditions and deep-drilling expeditions were conducted to understand the occurrence of MH-bearing sediments. Geophysical exploration is one of the important approaches to identify and characterize MH-bearing sediments such as hydrate

saturation, lithology, permeability, porosity, and extent and thickness of MH-bearing sediments (Boswell & Collett, 2011).

The physical property of MH is similar to that of ice (Sloan & Koh, 2006). MH behaves a higher seismic P-wave velocity (3300 m/s), a lower density than water (0.9 g/cm^3), and a comparable elastic moduli with ice (Riedel et al., 2010). The formation of hydrate in pore space will reduce the porosity and increase the resistivity of sediment, which is commonly described by Archie's empirical relation (Archie, 1942). The presence of free gas, even a small amount, will drastically reduce P-wave velocity (almost has no effect on S-wave velocity). All these changes in the physical properties of sediments caused by the presence of MH or free gas will result in geophysical anomalies, and then the associated geophysical methods can be applied in the characterization of MH-bearing sediments such as seismic bright spot, high resistivity, and bottom-simulating reflector (BSR) in seismic profile, etc.

1.2.2.1 Seismic technique

The most commonly used geophysical technique for detecting MH is the seismic method. The BSR in seismic reflection profile is often used to identify the base of MH stability zone in the marine environment (Holbrook et al., 1996). The MH-bearing sediments are buried so deeply that temperatures at the base of MH stability zones are no longer stable. Thus the base of MH-bearing sediment becomes unstable, and this instability will lead to a weak zone with low shear strength. The contrast of shear strength between free gas and MH layer would result in a sharp decrease in seismic velocity along the interface between overlying MH-bearing sediment (high seismic velocity) and the underlying free gas layer (low seismic velocity) (Paull et al., 2002). This contrast would trigger a seismic anomaly, which is called the bottom-simulating reflector (BSR) (Sloan & Koh, 2006). However, it is incapable to use the BSR alone to infer hydrate saturation. Moreover, it should be noted that hydrate can also be present in areas without BSR (Ashi et al., 2002; Ecker et al., 2000; Pecher, 2003), and the BSR is considered to be only related to the top of free gas, and not necessarily the base of MH stability zones (Chand & Minshull, 2003).

Locating the seismic receivers at the ocean floor (ocean bottom seismometers, OBS) allows the accurate velocity and geologic structure analysis. This technique has been applied in several MH-bearing locations (Hobro et al., 2005; Petersen et al., 2007; Riedel et al., 2010). Using rock physics modeling, seismic velocity estimated from seismic data can be related to hydrate saturation. Thus, the evaluation of MH-bearing reservoirs (structure, thickness, lateral extent) can be complemented (Dai et al., 2012). It should be noted that determination of hydrate saturation from the measuring P- and S-wave velocities of MH-bearing sediments is still difficult because velocity is also strongly dependent on sediment composition, porosity and hydrate morphology.

1.2.2.2 VSP technique

The vertical seismic profiling (VSP) method can also be employed to help identify hydrate in the subsurface. VSP is a kind of measurement conducted inside wellhole, and can obtain higher resolution than seismic method but lower resolution than well logging method. This technique uses a source near or offsetting the well and the geophones are located inside the wellhole with a specific interval. It allows us to measure the in situ velocity and amplitude at seismic frequencies (Holbrook et al., 1996; Matsushima, 2006). Combined use of the surface seismic technique and VSP, it enables us to identify the lateral and vertical seismic velocity and amplitude. In addition to vertical resolution and source frequencies, VSP method is very similar to well logging method.

1.2.2.3 Well logging technique

Logging techniques are beneficial for characterization of MH-bearing sediments. The physical properties of MH-bearing sediments can be measured in situ by well logging techniques including: caliper, gamma ray, resistivity, amplitude of the waveform, sonic velocity, and density and neutron porosity, etc. Sonic velocity logs of P- and S-waves have been used to identify MH-bearing sediments (Riedel et al., 2010). The resistivity of MH-bearing sediments is larger than that of non-hydrate bearing sediments, and resistivity logs are commonly used to estimate hydrate saturation by using Archie's equation (Archie, 1942). Other parameters (gamma-ray, porosity, and density) are also very important for the evaluation of MH-bearing sediments. In the recent decade, the sonic amplitude of P- and S-waves becomes critical information to assess MH by using acoustic attenuation analysis (Guerin & Goldberg, 2002; Guerin & Goldberg, 2005; Matsushima, 2005).

1.2.3 Geophysical exploration at the Nankai Trough

In the present study, the sonic and VSP data were acquired in the Nankai Trough, which is located beneath the Pacific Ocean off the southeast coast of Japan. The Japanese Ministry of International Trade and Industry (MITI) drilled six wells including the main well, two pilot wells, and three post survey wells with the narrow well spacing of 10-100 m at the position as shown in Fig. 1.6. The drilling program and geologic setting of this area are described in greater detail by Tsuji et al. (2004) and Uchida et al. (2004). The wireline logging and VSP data from two post survey wells (PSW1 and PSW3) are analyzed in the present study due to their high data quality (Matsushima 2005, 2006).

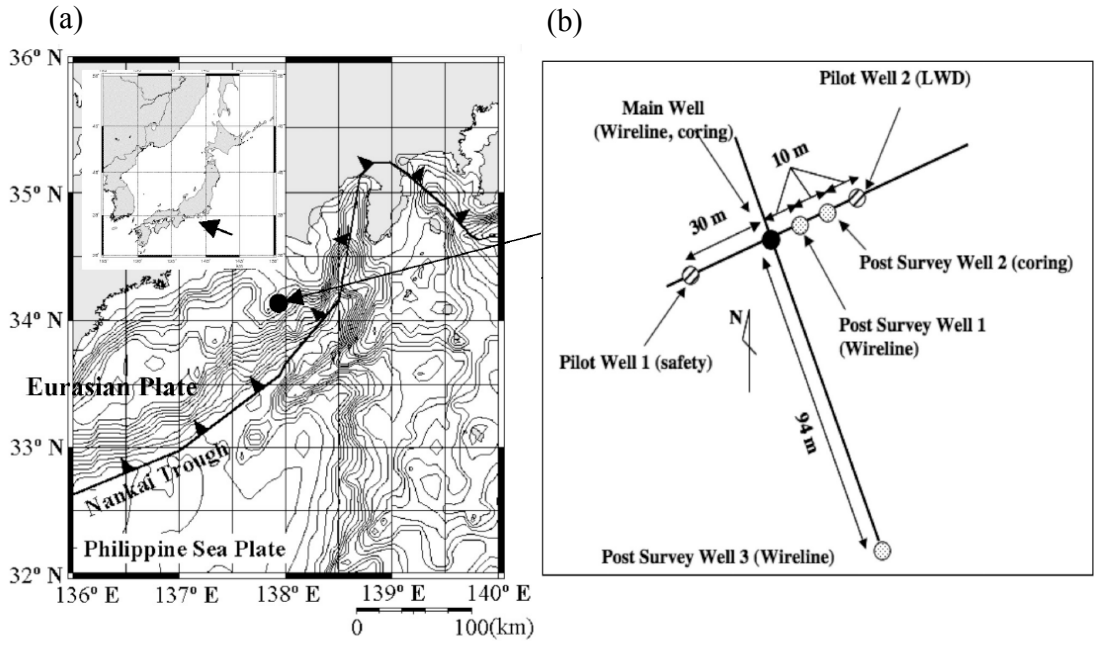

Figure 1. 6 (a): bathymetry and physiographic features of the eastern Nankai Trough and the location of MITI Nankai Trough wells; (b): enlargement shows the configuration of the MITI Nankai Trough drilling campaign site. In this drilling campaign, a total of six wells were drilled within 100 m of the main well. Post survey well 1 (PSW1) was drilled 10 m ENE of the main well, while post survey well 3 (PSW3) was drilled 94 m SSE of the main well (Matsushima, 2005).

Fig. 1.7 shows 2D seismic section across the MITI well. Well-logging curves of caliper, natural gamma ray, neutron, density, resistivity, and VSP survey (zero-offset VSP, offset VSP, walk away VSP) were carried out in Nankai Trough. Wireline logging for PSW1 was conducted at depths of 998-1296 m, while for PSW3 are 999-1293 m. VSP surveys were carried out at both PSW1 and PSW3 over a depths of 1005-1350 m with recording interval of 5 m, while the walkaway VSP survey was carried out in the main well at depth of 1130-1210 m with recording interval of 10 m (the bottom of the ocean is 945 m) (Matsushima, 2006). As shown in Fig. 1.7, the existence of BSR can be clearly confirmed.

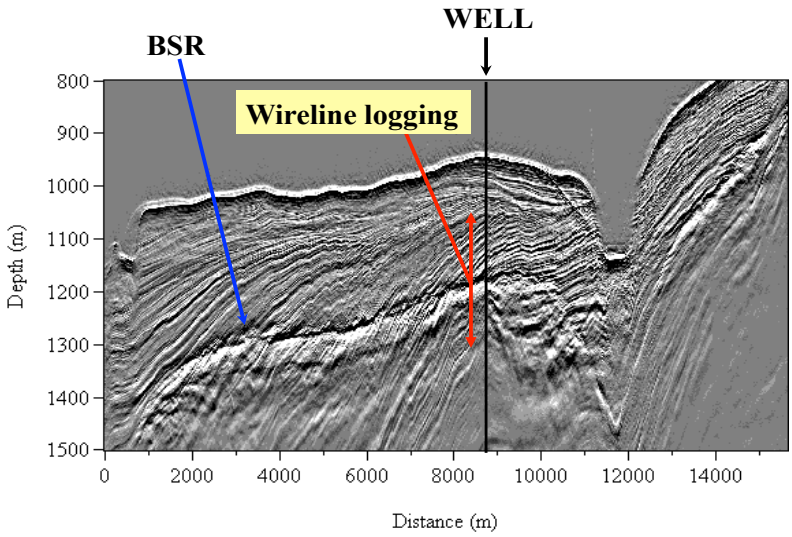

Figure 1. 7 Depth converted seismic section across the MITI well. The strong reflector around 1200 m is the BSR with opposite polarity relative to the seafloor (Matsushima, 2005).

In the present study, the results for PSW1 and PSW3 are shown. The presence of methane hydrate was confirmed by coring, and hydrate saturation was calculated by resistivity logging data. During the processing of sonic log data, the frequency band of the band-pass filter is 10 to 20 kHz for the P-wave and 500 to 1,000 Hz for the S-wave, and is 30 to 110 Hz for VSP survey (Matsushima 2005, 2006). Suzuki and Matsushima (2013) calculated the stable attenuation values of P- and S-waves for the primary hydrate-bearing zones of interest from sonic data using a modified median frequency shift method (Figs 1.8d and 1.8e). Matsushima et al. (2016) provided a stable P-wave attenuation profile for hydrate-bearing zones by combining seismic interferometry and the modified median frequency shift method from VSP data (Fig. 1.8f).

Four primary hydrate zones at PSW1 were identified: zone A at 1,139 to 1,145 m, zone B at 1,150 to 1,155 m, zone C at 1,182 to 1,190 m, and zone D at 1,203 to 1,212. Among these zones, the principal hydrate-bearing layers with high hydrate saturation occur are zones C and D (Fig. 1.8a). The velocities of the P- (Fig. 1.8b) and S-waves (Fig. 1.8c) are enhanced accompanied by a significant increase in the attenuations of the P- (Fig. 1.8d) and S-waves (Fig. 1.8e) corresponding to hydrate-bearing layers. However, the highest attenuation for VSP data (Fig. 1.8f) corresponds to the principle free gas zone. To compare the sonic attenuation with the calculated VSP attenuation, the measured hydrate saturation at the sonic scale is up-scaled from the sonic scale to the VSP wavelength scale by arithmetically averaging the sonic hydrate saturation in VSP wavelength. After up-scaling, hydrate saturation of 1.7% and 13.7% at the VSP scale are chosen to compare with sonic data as shown in Fig. 8f (see samples 1 and 2) for PSW1. Similar to Fig. 1.8, Fig. 1.9 shows sonic logging and VSP results

for PSW3, and the primary MH-bearing zones are identified as zone E at 1195-1202 m and zone F at 1206 and 1213 m (Fig. 1.9a). The velocities of the P- (Fig. 1.9b) and S-waves (Fig. 1.9c) and the attenuations of the P- (Fig. 1.9d) and S-waves (Fig. 1.9e) corresponding to hydrate-bearing layers increase at the same time. Hydrate saturations of 15.8% and 17.0% at the VSP scale are chosen to compare with sonic data as shown in Fig. 1.9f (see samples 1 and 2) for PSW3. It should be noted that the P-wave velocity was significantly low within the intervals of 1215-1221m and 1237-1244 m for PSW1 (Fig. 1.8b), and 1218-1225 m and 1235-1260 m for PSW3 (Fig. 1.9b). In these intervals, sonic data could not yield effective P-wave velocity, and thus the constant velocity of 1600 m/s derived from VSP data are used in these zones (Takayama et al., 2004).

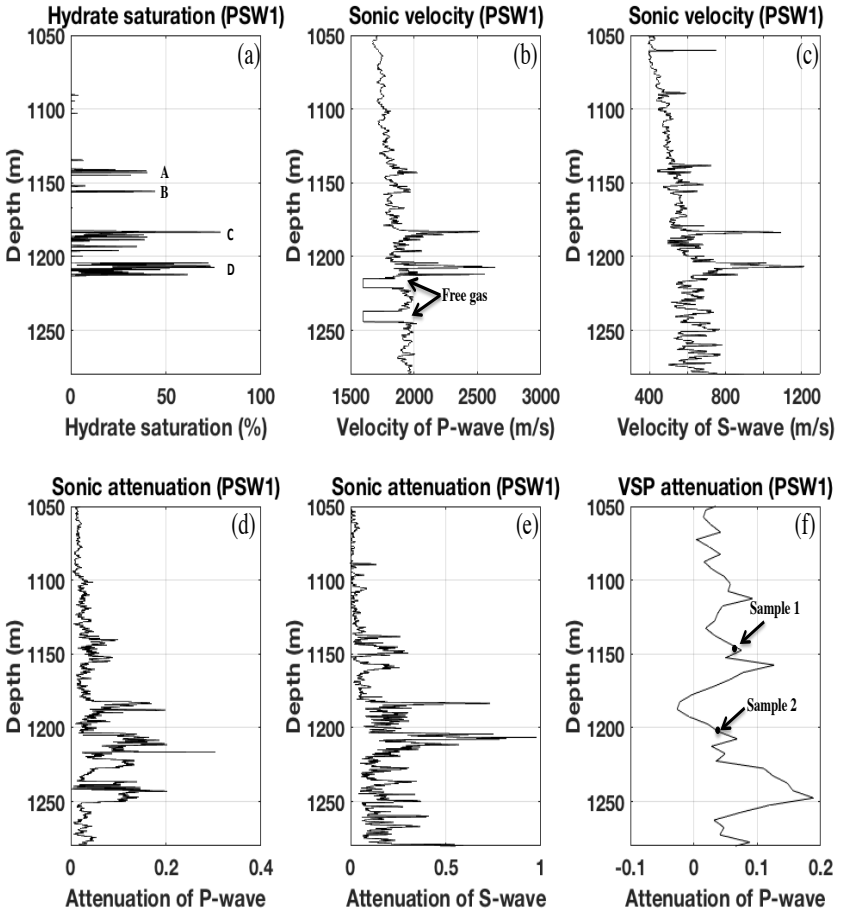

Figure 1. 8 Logging data (PSW1): (a) hydrate saturation derived from the log of resistivity using Archie's equation (A, B, C, and D indicate hydrate-bearing layers); (b) velocity of the P-wave (arrows denote free gas corresponding to significant attenuation of the P-wave); (c) velocity of the S-wave; (d) attenuation of the P-wave (free gas corresponding to significant attenuation of the P-wave); (e) attenuation of the S-wave; and (f) VSP attenuation, and samples 1 and 2 are chosen for comparison with sonic attenuation in the following section (adapted from Matsushima, 2006).

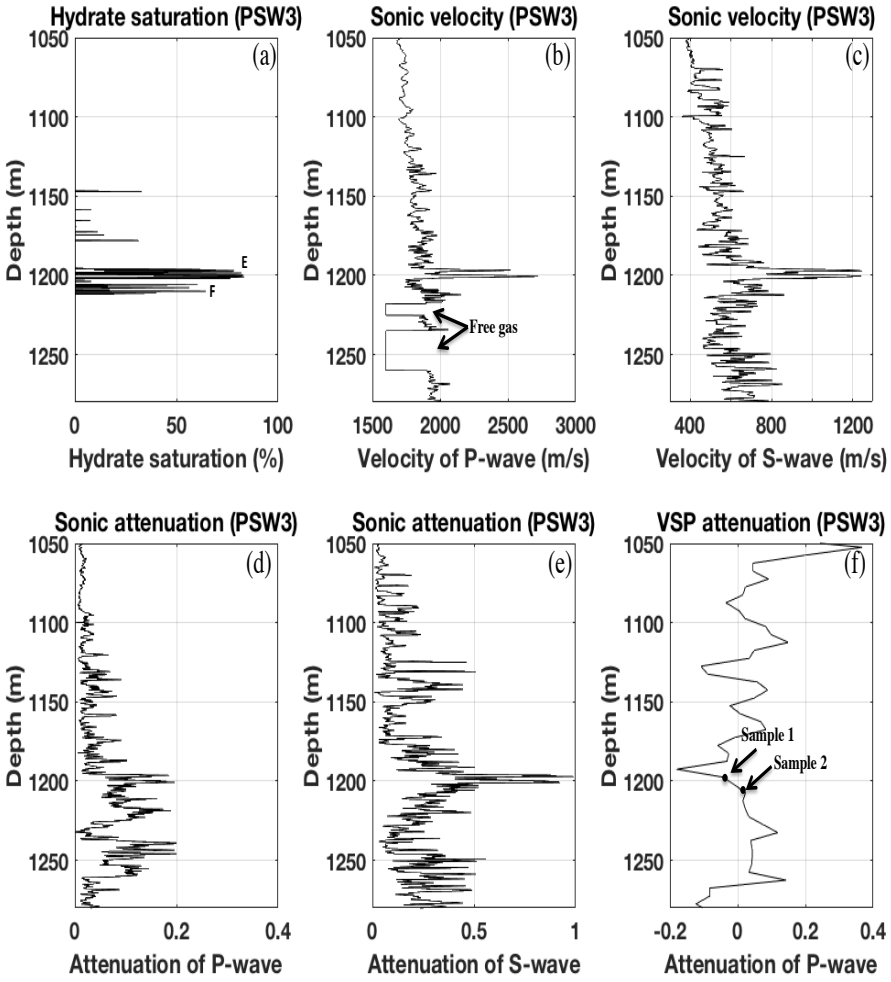

Figure 1. 9 Logging data (PSW3): (a) hydrate saturation derived from the log of resistivity using Archie's equation (E and F indicate hydrate-bearing layers); (b) velocity of the P-wave (arrows denote free gas corresponding to significant attenuation of the P-wave); (c) velocity of the S-wave; (d) attenuation of the P-wave (free gas corresponding to significant attenuation of the P-wave); (e) attenuation of the S-wave; and (f) VSP attenuation, and samples 1 and 2 are chosen for comparison with sonic attenuation in the following section (adapted from Matsushima, 2006).

1.3 Laboratory measurements

1.3.1 Laboratory studies for synthetic hydrate-bearing samples

It is challenging to retrieve intact MH samples during the coring process because the unstable temperature and pressure condition, therefore, laboratory analysis of artificial MH becomes an important part for the understanding of MH occurrence. There are several autoclave systems for laboratory measurements, which are developed to measure physical properties (P- and S-wave velocity, porosity, permeability, and electrical resistivity) of samples (Winters et al., 2009). Priest et al. (2005, 2006) and Best et al. (2013) proposed a method based on a resonant column technique, and

measured the acoustic properties (P- and S-wave velocities and attenuations) over a much lower frequency domain (< 550 Hz), while the common laboratory measurements are conducted in the ultrasonic frequencies (several hundred kHz). The tetrahydrofuran (THF) hydrate system is proposed over the past few years to be an alternate methodology (Santamarina & Ruppel, 2010). Although there are some differences between THF hydrate and MH, quite similar mechanical properties between them have been observed at a hydrate saturation lower than 40% (Lee et al., 2007).

There are two main challenges for laboratory measurements of natural or artifical MH samples. The way of formation of MH samples affects the hydrate morphology, thus in turn affects the physical properties of MH-bearing sediments samples. The previous studies about the in situ MH exhibit a specific pore-filling or load-bearing hydrate morphology, while laboratory synthetic samples formed from free gas generally result in cementing hydrate morphology at lower hydrate saturation (Priest et al., 2005, 2006; Sloan & Koh, 2006; Waite et al., 2009). However, Best et al. (2013) also indicated that using "excess water" method tends to result in pore-filling hydrate morphology. These discrepancies allow us to investigate the effects of hydrate morphology on physical properties of MH sediment samples in laboratory measurements. In addition, when the measured physcial properties of small hydrate samples in laboratory is applied to data obtained from logging or seismic method, there will be a problem of scale difference (Riedel et al., 2010; Waite et al., 2009).

1.3.2 Laboratory studies for partially frozen systems

In addition to tetrahydrofuran (THF) hydrate, partially frozen system is also a possible candidate because of the similarity of mechanical properties between MH and ice (Riedel et al., 2010; Sloan & Koh, 2006). In addition to the great insight into the rock physical properties of MH-bearing sediments (Guerin and Goldberg, 2005), the knowledge of partially frozen systems is also critical to the permafrost regions (Dou et al., 2016) and glaciers (Peters et al., 2012). There are several ultrasonic transmission measurements for the rock physical properties of partially frozen systems in the past several decades (Timur, 1968; Spetzler and Anderson, 1968; Prasad and Dvorkin, 2004; Matsushima et al., 2008; Lee et al., 2004; Nakano et al., 1972; Nakano and Arnold, 1973; Zimmerman and King, 1986; Sondergeld and Rai, 2007; Dou et al., 2017). Matsushima et al. (2016) conducted ultrasonic measurements on partially frozen unconsolidated sands and measured ultrasonic P- and S-wave attenuations as a function decreasing temperature. In this study, the comparison between measured ultrasonic attenuations and predicted values by rock physics modeling might provide an insight into the attenuation mechanisms at ultrasonic frequencies for MH-bearing sediments.

1.4 Rock physics modeling

Theoretical rock physics modeling can improve the understanding of physical properties of MH-bearing sediments. Rock physics modeling provides a method to link hydrate saturation in MH-bearing sediments with the measurable physical properties (P- and S-wave velocities and attenuations, resistivity) (Guerin & Goldberg, 2005; Yuan et al., 1996). The commonly used rock physical modeling method for MH-bearing sediments includes: the weighted equation method (Carcione & Seriani, 1998; Chand et al., 2004; Lee et al., 1996), three phase effective medium model (Best et al., 2013; Ecker et al., 1998, 2000; Helgerud et al., 1999; Marín-Moreno et al., 2017), differential effective medium model (Chand et al., 2004; Jakobsen et al., 2000), and three-phase Biot extent theory (Carcione & Gei, 2004; Carcione & Tinivella, 2000; Davide & M., 2003; Guerin & Goldberg, 2002; Guerin et al., 1999; Leclaire et al., 1994).

When using rock physics modeling to investigate MH-bearing sediments, the selection of input parameters is most important. More in situ information (such as coring information) makes the input parameters closer to rock properties of given MH-bearing sediments, thus allowing us to obtain more accurate prediction for physical properties of MH-bearing sediments.

1.5 Aims and outlines of the thesis

1.5.1 Definitions of problems of this thesis

The presence of MH is known to affect the physical properties of MH-bearing sediments. Seismic velocity increases with the increasing hydrate saturation. However, apart from hydrate saturation, the degree of increase is strongly dependent on hydrate morphology, and this dependency will become more complicated for the complex MH-bearing reservoir. At Nankai Trough, the previous studies basing on the assumption of sole hydrate morphology indicated that hydrate morphology tends to pore-filling or load-bearing morphology (Jia et al., 2017; Konno et al., 2015). By using rock physical modeling, the measured velocity was used to predict hydrate saturation of MH-bearing sediments. The information of hydrate morphology is required information for estimation of hydrate saturation, but the hydrate morphology at Nankai Trough needs further investigation.

It is generally accepted that both the P- and S-wave velocities increase with increasing hydrate saturation. However，significantly high attenuation has been widely observed along with the increase in velocity for both P- and S-waves in MH-bearing sediments in the sonic logging frequency range (Guerin & Goldberg, 2002; Guerin et al., 1999; Guerin & Goldberg, 2005; Matsushima, 2005; Nittala et al., 2017; Suzuki & Matsushima, 2013). However, the attenuation mechanisms responsible for this counterintuitive P- and S-wave attenuation at sonic frequency domain at Nankai Trough are not fully clarified.

In contrast to high attenuation at sonic frequencies in MH-bearing sediments, attenuation at seismic frequencies (typically 10 to 150 Hz) is more contentious in existing studies (Bauer et al., 2008; Bellefleur et al., 2007; Best et al., 2013; Davide & M., 2003; Dvorkin & Uden, 2004; Madrussani et al., 2010; Matsushima, 2006; Matsushima et al., 2016; Nittala et al., 2017; Priest et al., 2006; Rossi et al., 2007). The attenuation mechanisms in the frequency range from VSP to sonic data have not yet been fully clarified.

Contrary to our intuition that higher velocity corresponds to lower attenuation, the increasing velocity accompanied by an increasing attenuation in partially frozen systems is a widely observed phenomenon (Bellanger et al., 1996; Dou et al., 2016; Matsushima et al., 2015; Prasad & Dvorkin, 2004; Spetzler & Anderson, 1968; Wu et al., 2017). The attenuation mechanisms responsible for the ultrasonic wave propagation in partially frozen systems have not yet been clarified. Meanwhile, there are extremely limited numbers of rock physical modeling focusing on elucidating the ultrasonic attenuation of the partially unfrozen system during the freezing process.

1.5.2 Aims of thesis

The aims of this thesis are summarized as the following:

1. To investigate how hydrate morphology affects the P- and S-wave velocities and attenuations, and to infer possible hydrate morphology at Nankai Trough.
2. To clarify the attenuation mechanisms responsible for the frequency-dependent P-wave attenuation between sonic logging data (Suzuki & Matsushima, 2013) and VSP data (Matsushima et al., 2016), and the frequency-dependent S-wave attenuation between sonic logging data (Suzuki & Matsushima, 2013) and w-VSP data (Matsushima, 2015) in the MH-bearing sediments at the Nankai Trough.
3. To elucidate the velocity and attenuation observed in the ultrasonic measurements on partially frozen brine (Matsushima et al., 2008) and unconsolidated sands (Matsushima et al., 2016) and to clarify the attenuation mechanisms responsible for both partially frozen systems.

The goal of this thesis is to investigate how hydrate affects the physical properties (P- and S-wave velocities and attenuations) of MH-bearing sediments at seismic, sonic, and ultrasonic frequency domains by using various rock physics modeling. The final result would provide insights into the hydrate morphologies at Nankai Trough, the attenuation mechanisms at different frequency domains, and mechanisms responsible for frequency dependent P- and S- attenuations of MH-bearing sediments (Fig. 1.10).

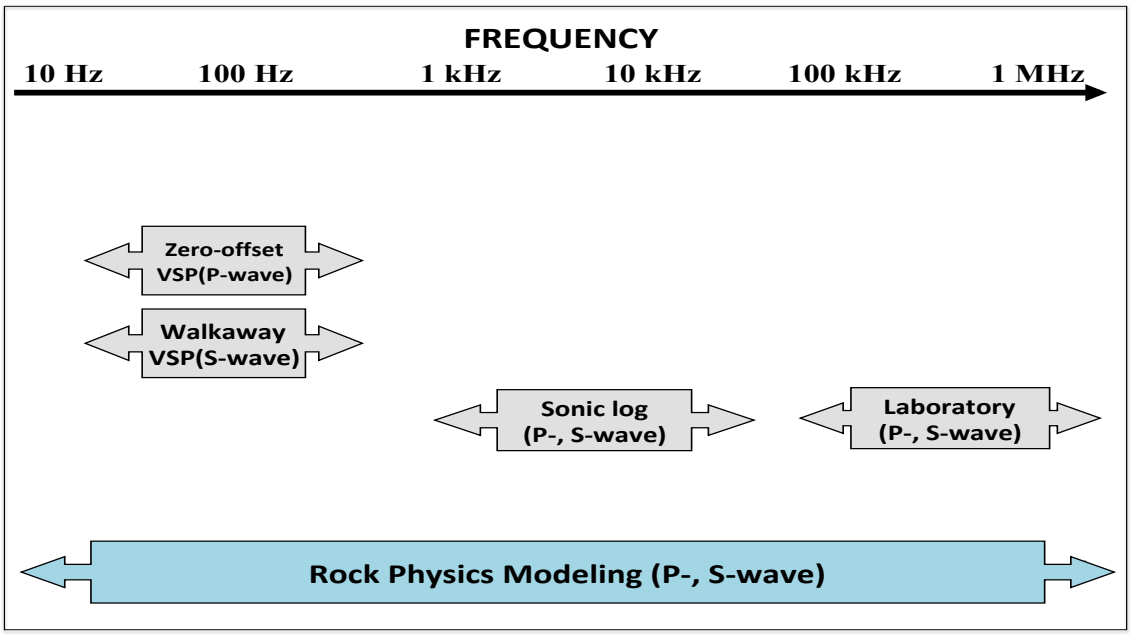

Figure 1. 10 Broadband frequency attenuation (P- and S-waves) (Matsushima, 2005).

1.5.3 Outlines of thesis

The schematic diagram of rock physics modeling in this study is shown as Fig. 1.11. By using VSP (w-VSP) and sonic data, the attenuation mechanisms at frequencies from VSP to sonic frequencies can be investigated. Although lacking of knowledge of natural hydrate samples, the attenuation mechanisms for partially frozen systems can be used to infer attenuation mechanisms for MH-bearing sediments. This thesis consists of the following chapters:

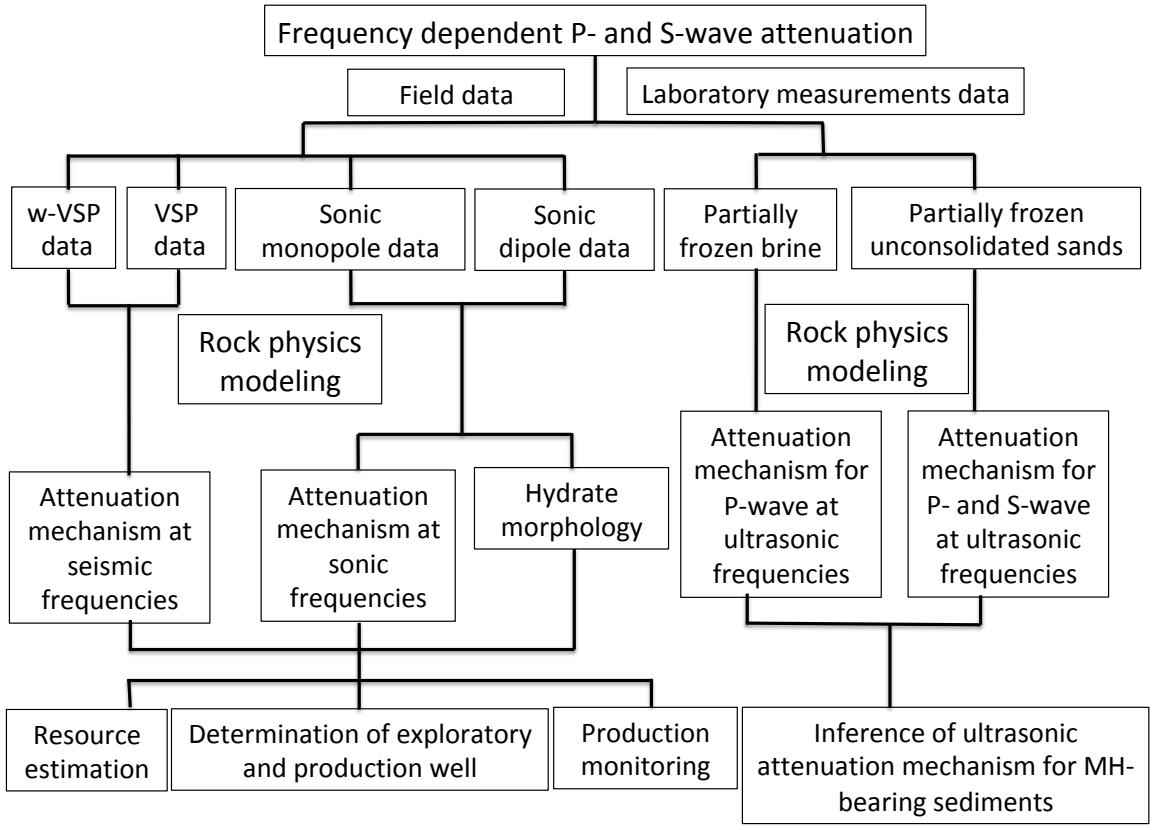

Figure 1. 11 Schematic diagram of rock physics modeling by using VSP (w-VSP), sonic, and ultrasonic data.

Chapter 2 begins with a review of the current rock physics models on methane hydrate (or ice), followed by the calculation workflows, main characteristics, assumptions, and attenuation mechanisms of the rock physics models applied in this thesis.

Chapter 3 discusses the possible attenuation mechanisms of P- and S-waves at sonic frequency domain by using an effective medium model (the Marin-Moreno model) and three-phase Biot extension models (the Leclaire model, the Carcione model, the Guerin model). The velocity and attenuation of P- and S-waves are predicted as a function of hydrate saturation by using these rock physics models, and then the predicted velocity and attenuation are compared with those derived from field sonic logging data at Nankai Trough. In this chapter, in addition to possible attenuation mechanisms, the sensitivity analysis of input parameters of these rock physics models, the selection of input parameters, and the effect of hydrate morphology on velocity and attenuation are also investigated.

Chapter 4 discusses the attenuation mechanisms responsible for frequency dependent attenuation for P- and S-waves at sonic and VSP frequency domains by using an effective medium model (the Marin-Moreno model) and three-phase Biot extension models (the Leclaire model, the Carcione model, the Guerin model). The velocity and attenuation of P- and S-waves in the broadband frequency range are predicted, and then the predicted velocity and attenuation are compared with those derived from field sonic logging and VSP data. In this section, comprehensive investigations of the effects of hydrate saturation, frequency domain, and physical properties (permeability and pore structure) on velocity and attenuation of P- and S-waves are conducted.

Chapter 5 discusses the possible attenuation mechanisms of P- and S-waves for partially frozen brine and partially frozen unconsolidated sands during the freezing process. An effective medium model (the Leurer model) and a two-phase Biot extension model [the Carcione (2007) model] are adopted for partially frozen brine, while three-phase extension of Biot models (the Leclaire model, the Carcione model, the Guerin model) are adopted for partially frozen unconsolidated sands to predict the velocity and attenuation of P- and S-wave as a function of temperature. Then the predicted velocity and attenuation are compared with those derived from ultrasonic measurements. The effects of some key parameters such as viscosity, average pore radius, and freezing point on P- and S- wave velocity and attenuation during the freezing process are also investigated.

Chapter 6 addresses the conclusion of this thesis. Some limitations of this thesis and recommendations for future study are also provided in this chapter.

CHAPTER 2. ROCK PHYSICS MODELING

In this chapter, I provide the main characteristics, assumptions, workflows, attenuation mechanisms, and input parameters for the effective medium models (the Marin-Moreno model) and the three-phase Biot extension models (the Leclaire model, the Carcione model, and the Guerin model) applied to MH-bearing field data. I also present the main characteristics, assumptions, workflows, attenuation mechanisms, and input parameters for the effective medium model (the Leurer model) and a two-phase Biot extension model [the Carcione (2007) model] applied to partially frozen brine, and the three-phase extension of Biot models (the Leclaire model, the Carcione model, and the Guerin model) applied to partially frozen unconsolidated sands. Using different rock physical modeling in a joint study allows different but complementary attenuation mechanisms to be taken into consideration. The combined study on VSP (w-VSP) data and sonic data from MH-bearing sediments and ultrasonic measurements from partially frozen unconsolidated sands provides more robust inference on attenuation mechanisms responsible for frequency dependent attenuation of MH-bearing sediments.

2.1 Review of rock physics models

Rock physics modeling is an effective method to investigate the effects of hydrate on velocity and attenuation for MH-bearing sediments, and is categorized into two approaches: effective medium model (Leurer 1997; Leurer & Brown 2008; Best et al. 2013; Marin-Moreno et al. 2017) and three-phase Biot extension model (Leclaire et al. 1994; Guerin & Goldberg 2002, 2005). Best et al. (2013) adopted inclusion theory based on self-consistent model (SCA) (Wu 1966; Walsh 1969; Berryman 1995), and considered the effect of pore-filling hydrate morphology (Dvorkin & Nur 1996; Ecker et al. 1998, 2000; Dvorkin et al. 1999; Helgerud et al. 1999; Jakobsen et al. 2000; Chand et al. 2004; Lee & Waite 2008), then proposed hydrate effective grain (HEG) model including the attenuation mechanisms caused by squirt flow in microporous hydrate, viscoelasticity of hydrate frame and global Biot flow. Marin-Moreno et al. (2017) further extended HEG model to introduce the local viscous squirt flow between connected pores due to the formation of hydrate and gas bubble damping. On the other hand, Leclaire et al. (1994) extended Biot theory to a three-phase model (sand, ice, water), then incorporated Biot flow in sand grains and ice grains respectively, but they made an important assumption that there is no contact between ice and sand grain. Carcione & Tinivella (2000) modified the Leclaire model to introduce the interaction between sand grains and hydrate, and the cementation effect between sand grains and hydrate. Furthermore, Guerin & Goldberg (2005) reformulated a BISQ (Biot-squirt) attenuation mechanism proposed by Diallo & Appel (2000) to introduce squirt flow in sand grain and hydrate based on Carcione model, and introduced a viscous friction loss between sand

grain and hydrate. Each of above mentioned rock physical models has a particular focus on different attenuation mechanisms. Therefore, the application of different rock physical models possibly allows us to investigate different effects of different attenuation mechanisms in MH-bearing sediments.

Rock physical modeling of the velocity and attenuation for partially frozen systems under various physical conditions is also an effective method to interpret laboratory observations quantitatively. Carcione et al. (2007) proposed a poroelastic model based on the Biot theory to calculate ultrasonic velocity and attenuation in partially frozen orange juice. Matsushima et al. (2011) employed this poroelastic model to describe the propagation of ultrasonic P-wave through the partially frozen brine. They concluded that Biot flow could not completely predict the measured attenuation. Leurer (1997) and Leurer and Brown (2008) assumed an effective medium made up of homogeneous elastic mineral phase that is isotropically interspersed with penny-shaped inclusion of low aspect ratio representing intracrystalline water layer, and then proposed "effective grain model" to calculate the velocity and attenuation of unconsolidated fine-grained and coarse-grained saturated marine sediments. The Leurer model and the Carcione (2007) model are applied to describe the wave propagation in partially frozen brine. Similar to the rock physical modeling for MH-bearing sediments, the hydrate is substituted with ice, and then the Leclaire model, the Carcione model, and the Guerin model are applied to partially frozen unconsolidated sands to describe the wave propagation in the partially frozen system. A review of attenuation mechanisms in different rock physical models applied in this study is shown as Table 2.1. The Marin-Moreno model, the Leclaire model, the Guerin model, and the Carcione model are applied to VSP (w-VSP) data and sonic data from MH-bearing sediments. The attenuation mechanisms associated with these models include global Biot flow and squirt flow in pores between hydrate and sands, friction between hydrate and sands, hydrate frame viscoelasticity, cementation between hydrate and sands, and inertial coupling among sands, hydrate and water. The Leurer model, the Carcione (2007) model, the Leclaire model, the Guerin model, and the Carcione model are applied to partially frozen systems. The attenuation mechanisms associated with these models include global Biot flow and squirt flow in partially frozen ice and sands, friction between ice and sands, cementation between ice and sands, and inertial coupling among sands, ice and brine.

Table 2. 1 Comparison of attenuation mechanisms between different rock physics models

Mechanisms / Model	Biot flow	Squirt flow	Friction between sand grains and hydrate	Frame Viscoelasticity	Cementation between sand grains and hydrate	Inertial coupling among ice/hydrate, sand, and water
Leurer model	×	○ (Ice)	×	×	×	×
Carcione (2007) model	○ (Ice)	×	×	×	×	×
Leclaire model	○ (Ice/hydrate, sand)	×	×	×	×	○
Carcione model	○ (Ice/hydrate, sand)	×	×	×	○	○
Guerin model	○ (Ice/hydrate, sand)	○ (Ice/hydrate, sand)	○	×	○	○
Marin-Moreno model	○ (Sand)	○ (Sand)	×	○	○	×

Footnote: "○"means consideration, "×" means no consideration.

2.2 Effective medium models

2.2.1 The Leurer model

The Leurer model is applied to calculate P- and S-wave velocities and attenuations of partially frozen brine as a function of decreasing temperature based on a combination of the effective medium model (Leurer, 1997; Leurer and Brown, 2008) and Leclaire model. A detailed description of the calculation formulas in the Leurer model is given in Appendix A, and the input parameters and symbols of the Leurer model are described in Tables 2.2 and 2.5. Fig. 2.1 provides the calculation workflow of the Leurer model.

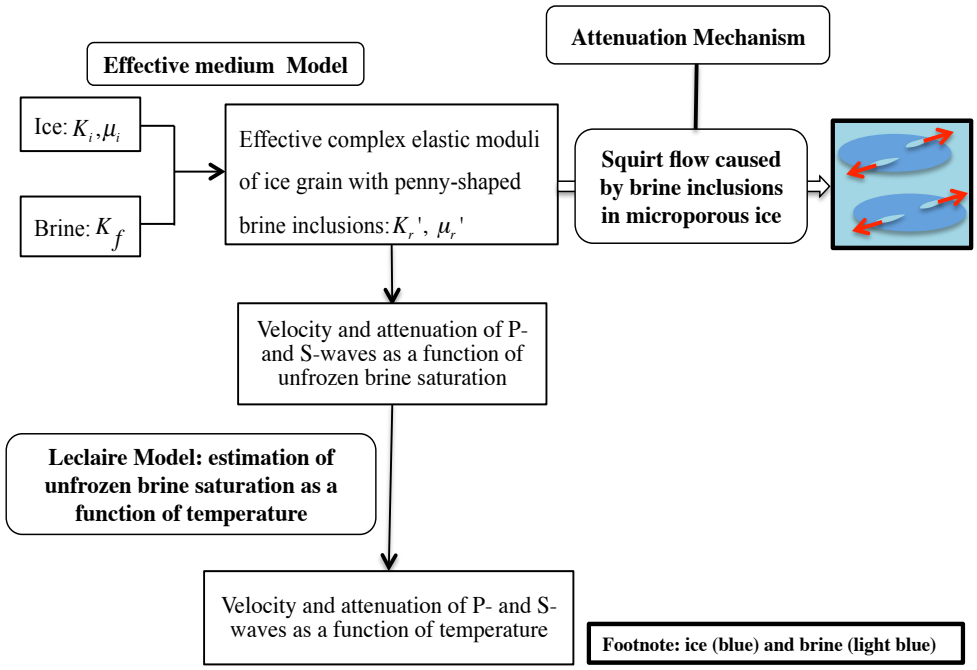

Figure 2. 1 Workflow of the Leurer model. Attenuation mechanism in the Leurer model is squirt flow caused by brine inclusions in porous ice.

Table 2. 2 List of symbols of the Leurer model (Leurer, 1997)

Parameters	Value
$K_f^{'}$	Effective bulk modulus of fluid inclusion
$K_r^{'}$	Effective bulk modulus of ice with fluid inclusion
ε	$\phi_0 S_i c_i / \phi$, ratio of the volume of inclusion to pore
γ	$3\eta K_i / [2\alpha^2 K_f (1+\varepsilon)]$, relaxation time

η	Effective viscosity as a function of reducing temperature
$\mu_f^{'}$	Effective shear modulus of fluid inclusion
$\mu_r^{'}$	Effective shear modulus of ice with fluid inclusion
ρ_e	$\rho_f(1-S_i)+\rho_i S_i$, effective density of partially frozen brine

Introducing fluid inclusions into ice grains is an effective method for relating the geometrical shape of micropores and the physical properties of inclusions to the velocity and attenuation of the effective grain (Berryman, 1995). The elastic grain is finally replaced by an effective medium composed of homogeneous, isotropic elastic mineral and interspersed ellipsoidal inclusions. The squirt flow due to brine inclusions in porous ice is incorporated by applying the correspondence principle to the bulk and shear moduli of fluid inclusion (Johnston et al. 1979). In this way, the effective bulk and shear moduli of ice with fluid inclusions become complex numbers (Fig. 2.1). The final P- and S-wave velocities and attenuations can be calculated by the effective and complex moduli of effective medium as a function of unfrozen brine saturation (Appendix A). Using the Leclaire model, the unfrozen brine saturation can be estimated as a function of decreasing temperature, and then the P- and S-wave velocities and attenuations are transformed as a function of temperature.

Due to the two-phase nature of the effective grain model, I can match it to a two-phase binary ice-brine system and then evaluate the effect of squirt flow caused by brine inclusions in porous ice on the attenuation of P- and S-waves in partially frozen brine. Application of the Leurer model to the ice-brine system has two advantages. First, by applying the distribution of aspect ratio α_m, ranging from 0.0005 to 0.05, I can avoid a negative value for the shear modulus of effective hydrate grains when applying the effective medium model due to the violation of the non-interaction assumption for higher inclusion concentrations (Kuster and Toksoz, 1974). Moreover, it can dynamically describe the decreasing concentration of brine inclusions with decreasing temperature and formation of ice. Leurer (1997) assumed that total water inclusion concentration c_i corresponds to the volume fraction of 50% of the water in a montmorillonite-water system. In this study, I assumed that c_i corresponds to 50% brine saturation in the ice-brine system. As a result, c_i decreases with decreasing brine saturation as temperature decreases.

2.2.2 The Marin-Moreno model

The Marin-Moreno model is applied to calculate frequency dependent P- and S-wave velocities and attenuations of MH-bearing sediments based on the combination of effective medium model

(Leurer 1997; Leurer & Brown 2008), hydrate contact model (Ecker et al. 1998, 2000), and Biot-Stoll model (Stoll & Bryan 1970). Fig. 2.2 provides the calculation workflow of the Marin-Moreno model. The detailed description of calculation formulas of the Marin-Moreno model is given in Appendix B, the symbols of the Marin-Moreno model are listed as in Table 2.3, and the description of input parameters are shown as in Table 2.6.

Table 2. 3 List of symbols of the Marin-Moreno model (Best et al., 2013; Marín-Moreno et al., 2017).

Parameter	Description
a	$C1^2 - MH$
$A1$	$K_{solid}^{'}[1+\phi(K_{solid}^{'}/K_{fp}^{'}-1)]$
b	$Hq + M\rho_e - 2C1\rho_f$
c	$\rho_f^2 - 2\rho_e q$
$C1$	$[(K_{solid}^{'}-K_{dry}^{'})K_{solid}^{'}]/(A1-K_{dry}^{'})$
$F(\xi)$	the viscodynamic operator (Marín-Moreno et al. 2017)
F_s	$F_s=(1-\phi_0)/\{1-[1-S_h(1-c_{pf})]\phi_0\}$, fraction of sand
H	$K_{dry}^{'}+4\mu_{dry}^{'}/3+(K_{solid}^{'}-K_{dry}^{'})^2/(A1-K_{dry}^{'})$
k	$\{c_{pf}/[k_0(1-S_h)^{n_{kp}}]+(1-c_{pf})/[k_0(1-S_h)^{n_{kc}}]\}^{-1}$, intrinsic permeability
$K_{dryc}^{'}$	bulk modulus of the dry frame for contact cementing hydrate (Ecker et al. 1998)
$K_{drypf}^{'}$	bulk modulus of the frame for pore-filling hydrate (Ecker et al. 2000)
$K_{dry}^{'}$	$[c_{pf}/K_{drypf}^{'}+(1-c_{pf})/K_{dryc}^{'}]^{-1}$, effective bulk modulus of the dry frame
$K_{fp}^{'}$	$[\phi_0(1-S_h)/K_f+S_h c_{pf}/K_h^{'}]^{-1}$, effective bulk modulus of fluid phase
$K_f^{'}$	effective bulk modulus of fluid inclusion
$K_h^{'}$	effective bulk modulus of hydrate with fluid inclusion
$K_{solid}^{'}$	$K_{solid}^{'}=\{F_s K_{sand}+(1-F_s)K_h^{'}+[F_s/K_{sand}+(1-F_s)/K_h^{'}]^{-1}\}/2$, effective solid bulk modulus
M	$K_{solid}^{'\,2}/(A1-K_{dry}^{'})$
n_{kc}	3, intrinsic permeability exponent for contact cementing hydrate
n_{kp}	2, intrinsic permeability exponent for pore-filling hydrate
q	$t\rho_f/\phi - j\eta F(\xi)/(2\pi f k)$
ε	$\phi_0 S_h c_i/\phi$, ratio of the volume of inclusion to pore
ϕ , ϕ_f	$\phi_0(1-S_h)$, real porosity
ϕ_h	$\phi_0 S_h$
ϕ_s	$1-\phi_0$
γ	$8\eta K_h/[\alpha K_f(1+\varepsilon)]$, relaxation time

$\mu_f^{'}$	effective shear modulus of fluid inclusion
$\mu_h^{'}$	effective shear modulus of hydrate with fluid inclusion
$\mu_{dry}^{'}$	$[c_{pf} / \mu_{drypf}^{'} + (1 - c_{pf}) / \mu_{dryc}^{'}]^{-1}$
$\mu_{dryc}^{'}$	shear modulus of the dry frame for contact cementing hydrate (Ecker et al. 1998)
$\mu_{drypf}^{'}$	shear modulus of the frame for pore-filling hydrate (Ecker et al. 2000)
$\mu_{solid}^{'}$	$\mu_{solid}^{'} = \{F_s \mu_{sand} + (1 - F_s)\mu_h^{'} + [F_s / \mu_{sand} + (1 - F_s) / \mu_h^{'}]^{-1}\} / 2$, effective solid shear modulus
ρ_e	$\rho_{sand}\phi_s + \rho_f \phi_f + \rho_h \phi_h$

In order to investigate the effects of inclusion concentration (c_i) and inclusion aspect ratio (α) on the physical properties of MH-bearing sediments, single inclusion aspect ratio (α) value rather than distribution in a specific range is adopted, and an inclusion concentration (c_i) that is not related to water saturation is applied. In addition to these differences in the implication of effective model between the Leurer model and the Marin-Moreno model, the calculation of effective medium model in the application of the Marin-Moreno model is similar to that in the Leurer model. By incorporating the squirt flow due to fluid inclusion in a microporous hydrate through the application of correspondence principle to the bulk and shear moduli of fluid inclusion (Johnston et al., 1979), the effective bulk and shear moduli of the hydrate with fluid inclusion become complex number and frequency dependent (Leurer, 1997; Best et al., 2013; Marín-Moreno et al., 2017) (see Fig. 2.2). Then the real bulk and shear moduli of hydrate in the hydrate contact model proposed by Ecker et al. (1998, 2000) can be replaced with the abovementioned complex bulk and shear moduli of the effective hydrate (see Fig. 2.2). The dry effective bulk and shear moduli of MH-bearing sediment with four modes of hydrate morphologies (contact cementing, envelope cementing, load-bearing, and pore-filling) can be obtained. In the present study, multiple hydrate morphologies (contact cementing and pore-filling) are assumed. Note that in this formulation the assumption that contact cementing hydrate forms part of the solid frame and pore-filling hydrate is part of the fluid is considered. Therefore, the effective elastic moduli for solid phase (sand grains and contact cementing hydrate), and fluid phase (water and pore-filling hydrate) also become complex number (Marín-Moreno et al., 2017). Finally, The abovementioned effective and complex moduli of solid and fluid phases are then introduced into Biot-Stoll model (Stoll & Bryan, 1970), and then the final frequency dependent P- and S-wave velocities and attenuations can be calculated (see Appendix B).

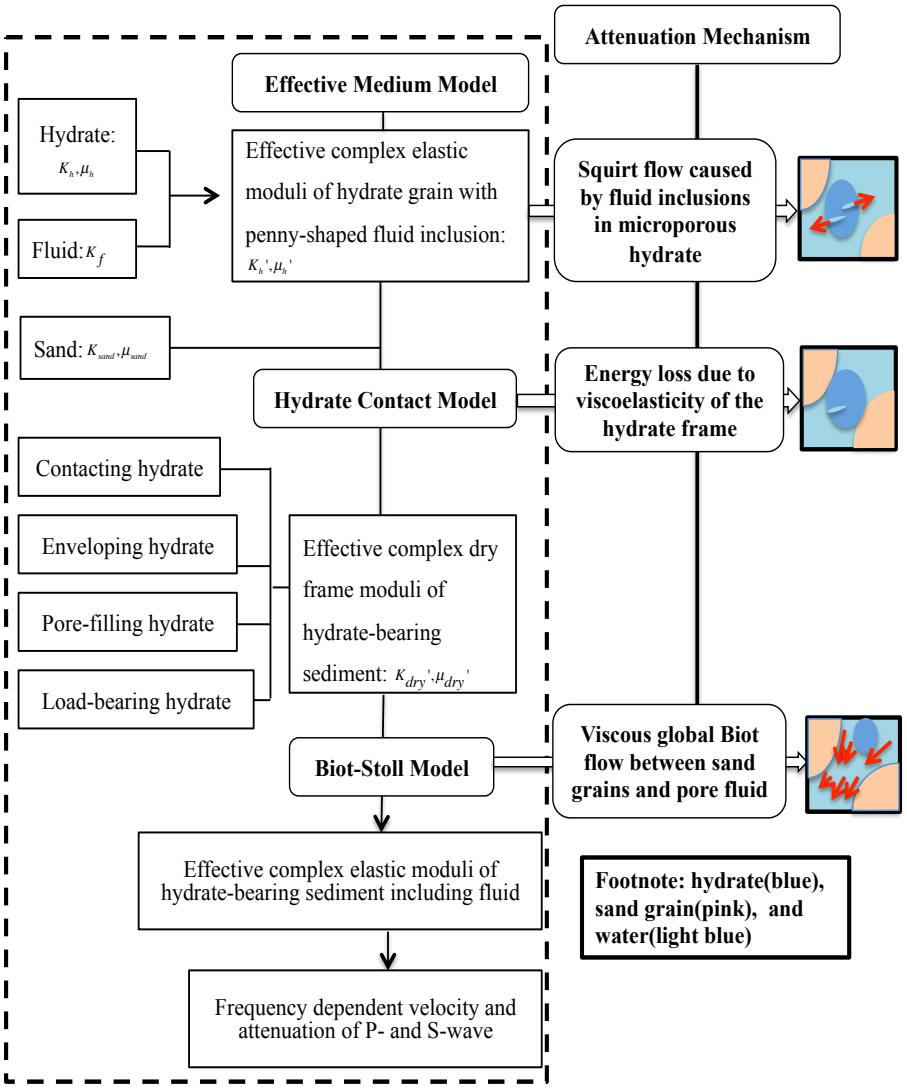

Figure 2. 2 Workflow of the implication of the Marin-Moreno model. The text boxes on the right indicate the corresponding attenuation mechanisms. The total attenuation in our application is attributed to the squirt flow in microporous hydrate, and the energy loss due to the viscoelasticity of the hydrate frame, as well as the global Biot flow. I neglect the attenuation mechanisms caused by gas bubble damping and local squirt flow between connected pores with different aspect ratios that are included in the original Marin-Moreno model.

The original Marin-Moreno model considers the attenuation caused by two types of squirt flow: flow of fluid inclusions between micropores in hydrate and pore, and connected pores with different aspect ratios formed during the growth of hydrates. In addition, it also introduces attenuation caused by Biot flow and gas bubble damping. The Marin-Moreno model allows us to consider the effect of different hydrate morphologies on P- and S- wave velocities and attenuations (Marín-Moreno et al.,

2017). Here, we need to consider that, although the evidence of existence of free gas in hydrate-bearing sediments has been provided by several authors (Matsushima, 2005, 2006), and the presence of free gas, even a small amount, will significantly increase the attenuation of the P-wave. In addition, the effect of viscous local squirt flow between pores with different aspect ratios appears to be mainly active in the ultrasonic frequency range (Marín-Moreno et al., 2017). With these considerations in mind, since our primary interest is the attenuation occurred in the pure hydrate-bearing layer in the sonic and VSP frequency bands, the attenuations caused by gas bubble damping and local squirt flow between connected pores with different aspect ratios are neglected in our application of the Marin-Moreno model.

2.3 Three-phase Biot extension models

The common three-phase Biot extension models are based on the Leclaire model. The Carcione model and the Guerin model extended it to include attenuation caused by the cementation and friction between hydrate and sand grains, squirt flow in pores between sand grains and pores between hydrate. In this thesis, the Leclaire model, the Carcione model, and the Guerin model are applied to predict the frequency dependent velocity and attenuation of P- and S-waves for MH-bearing sediments at Nankai Trough. The detailed description of calculation formulas of these three models is given in Appendix C, and symbols of these three models are listed as in Table 2.4, and the description of input parameters are shown as in Table 2.6.

2.3.1 The Leclaire model

Fig. 2.3 provides the calculation workflow of the Leclaire model. By using of percolation theory, the Leclaire model incorporates the Biot flow (Biot, 1956a, 1956b) in sand grains and ice, and described the transition from a continuous to a discontinuous state during the freezing process. However, the Leclaire model made an important assumption that there was no contact between ice and solid grains (Leclaire et al., 1994). Therefore, as shown in Fig. 2.3, the rigidity coefficient (R_{sh}), mass density coefficient (ρ_{sh}), friction coefficient (b_{sh}), and shear modulus (μ_{sh}) between sand grains and hydrate equal to 0. The Leclaire model includes the attenuation mechanisms due to energy dissipation caused by inertial coupling among three different phases, and global Biot flow (Fig. 2.3).

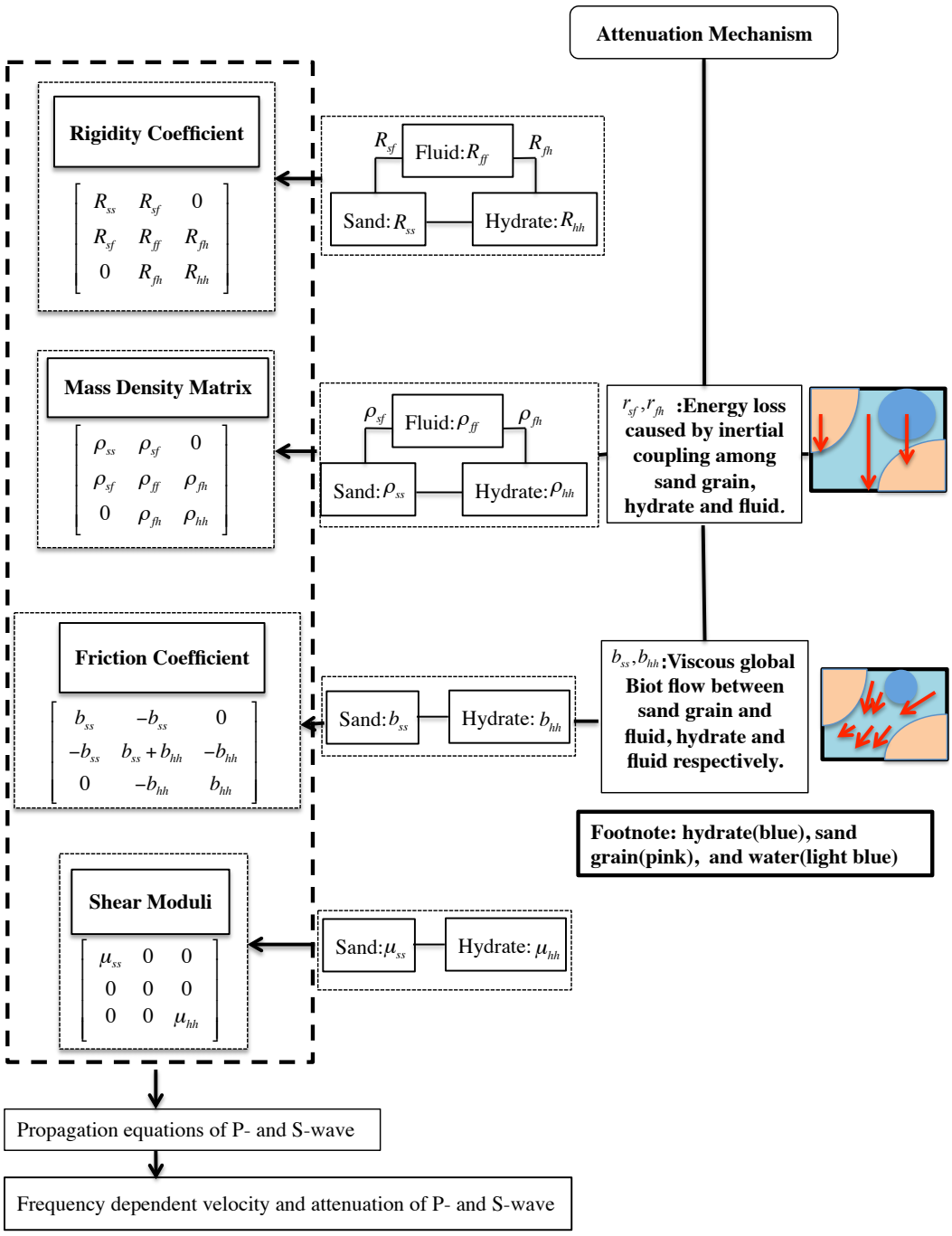

Figure 2. 3 Workflow of the Leclaire model. The text boxes on the right indicate the expressions including attenuation and corresponding attenuation mechanisms. Attenuation mechanisms in the Leclaire model include energy dissipation caused by inertial coupling among different phases, and global Biot flow.

2.3.2 *The Carcione model*

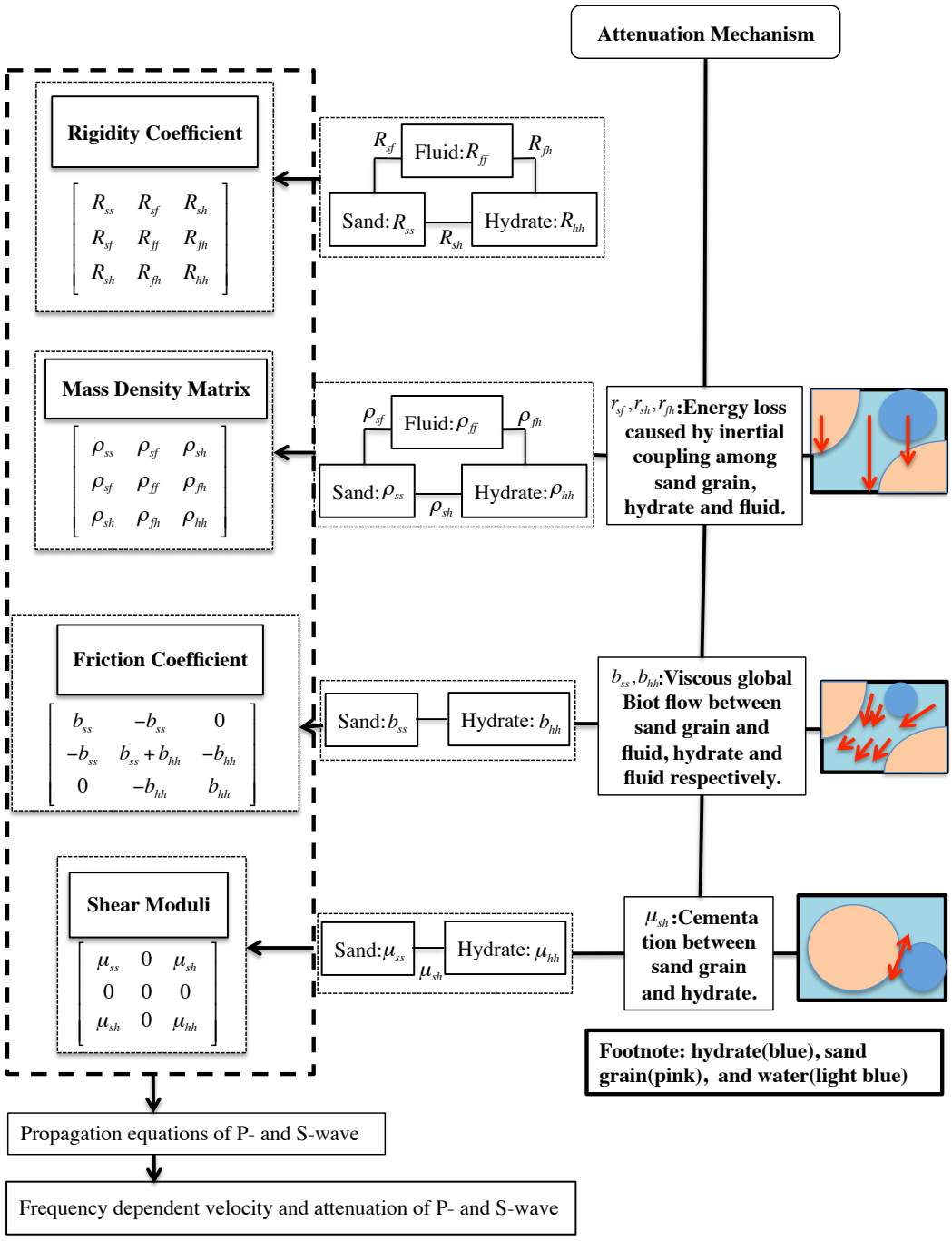

Figure 2. 4 Workflow of the Carcione model. The text boxes on the right indicate the expressions including attenuation and corresponding attenuation mechanisms. Attenuation mechanisms in the Carcione model include energy dissipation caused by inertial coupling among different phases, cementation between sand grains and hydrate, and global Biot flow.

The Leclaire model assumes no contact between ice and sand grains, but Carcione and Tinivella (2000) took this contact (R_{sh}) into consideration (see Fig. 2.4). In addition, Carcione and Tinivella (2000) added the apparent mass density between sand and hydrate grains (ρ_{sh}) (see Fig. 2.4), which was neglected in the Leclaire model. Carcione and Tinivella (2000) also introduced the viscous Biot dissipation of shear waves between a solid (sand and hydrate) and a fluid, which was neglected by Leclaire et al. (1994). Although extremely small, this effect is included in my simulation. Carcione et al. (2000) showed that some shear energy is transmitted between solid grain and ice (Carcione & Tinivella, 2000). However, the Carcione model is failed to predict obvious attenuation for hydrate-bearing sediments. The Carcione model includes the attenuation mechanisms due to energy dissipation caused by inertial coupling among three different phases, cementation between sand grains and hydrate, and global Biot flow (Fig. 2.4)**.**

2.3.3 The Guerin model

With regard to the inertial coupling coefficients among sand grains, hydrate, and fluid, Carcione and Tinivella (2000) set the coupling coefficients of r_{sh} and r_{hs} to 0, and Guerin and Goldberg (2005) showed that the coupling coefficients of r_{fh} as 0 (which indicates the absence of inertial coupling between hydrate and fluid) significantly increase attenuation. In the present study, I follow this definition. Moreover, Guerin and Goldberg (2005) suggested that the cementation between hydrate and sand grains (μ_{sh}) would sharply increase the velocity of the S-wave at higher hydrate saturation. Furthermore, Guerin and Goldberg (2005) introduced squirt flow in sand grains and hydrate grains (R_{sf} , R_{ff} , and R_{fh}) and the friction between sand grains and the hydrate (b_{sh}) (see Fig. 2.5). The initial friction coefficient (b_{sh0}) and shear coefficient (μ_{sh0}) are the few free parameters when applying the Guerin model. Table 2.4 provides the required symbols in the Guerin model, and the required input parameters are given in Table 2.6.

The resulted Guerin model considers the BISQ attenuation mechanisms in sand grains and hydrate respectively. It also employs cementation between hydrate and solid grain, and friction between hydrate and solid grain. In addition, the effect of inertial coupling among hydrate, sand grains, and fluid has been taken into account in the Guerin model. In the implication of the Guerin model, I fully follow the original Guerin model to consider the associated attenuation mechanisms.

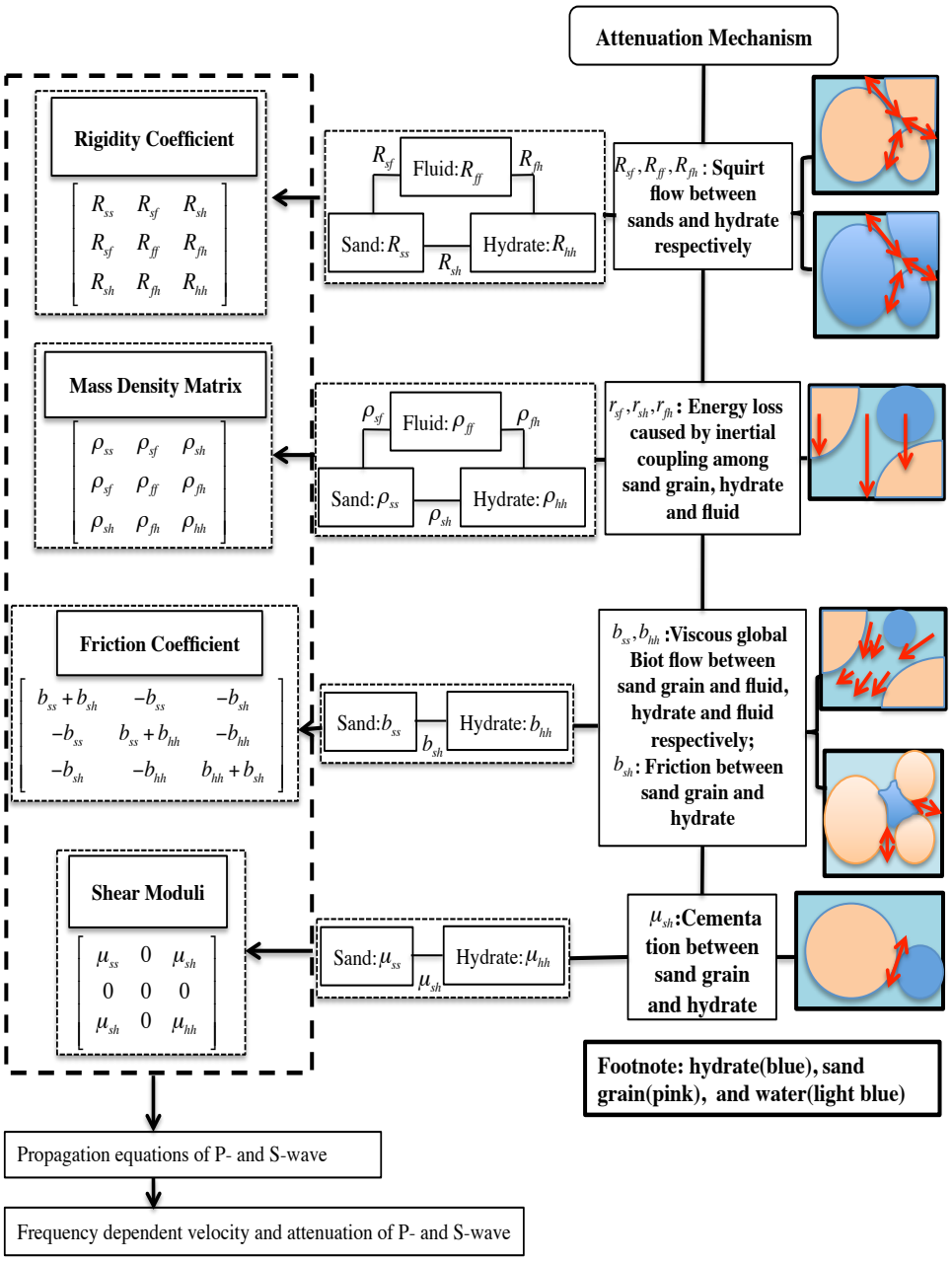

Figure 2. 5 Workflow of the Guerin model. The text boxes on the right indicate the expressions including attenuation and corresponding attenuation mechanisms. Attenuation mechanisms in the Guerin model include squirt flow between hydrate and sand grains, energy dissipation caused by inertial coupling among different phases, friction between sand grains and hydrate, and global Biot flow. In the implication of the Guerin model, I fully follow the original Guerin model to consider the associated attenuation mechanisms.

Table 2. 4 List of symbols of the Guerin model (Carcione & Tinivella, 2000; Guerin & Goldberg, 2005)

Parameter	Description
a_{sh}	$1+r_{sh}\phi_h(\phi_s\rho_s+\phi_h\rho_h)/[\phi_s\rho_s(\phi_s+\phi_h)]$, tortuosity for solid flowing through hydrate
a_{fh}	$1+r_{fh}\phi_h(\phi_f\rho_f+\phi_s\rho_s)/[\phi_f\rho_f(\phi_f+\phi_s)]$, tortuosity for water flowing through hydrate
a_{hs}	$1+r_{hs}\phi_s(\phi_s\rho_s+\phi_h\rho_h)/[\phi_h\rho_h(\phi_s+\phi_h)]$, tortuosity for hydrate flowing through solid
b_{ss}	$\eta_D\phi_f^2/k_s$
b_{hh}	$\eta_D\phi_f^2/k_h$
c_s	$K_{sm}/\phi_s K_s$, consolidation coefficient for the solid
c_h	$K_{hm}/\phi_h K_h$, consolidation coefficient for hydrate
$Re[F(\xi)]$	$1+(1/0.7178)e^{[0.7178(\xi-3.2)]}/12, \xi \le 3.2$
$Re[F(\xi)]$	$0.5+[2\xi+e^{-0.7178(\xi-3.2)}]/12, \xi \ge 3.2$
$Im[F(\xi)]$	$\xi/6$
g_s	$\mu_{sm}/(\phi_s\mu_s)$, consolidation coefficient for the solid
g_h	$\mu_{hm}/(\phi_h\mu_h)$, consolidation coefficient for the hydrate
h	$r_s[(1+\phi_f/\phi_s)^{1/3}-1]$, average thickness of the water layer
K_s	$\frac{1}{2}[\gamma_c K_{clay}+(1-\gamma_c)K_{sand}+\frac{K_{sand}K_{clay}}{K_{sand}\gamma_c+K_{clay}(1-\gamma_c)}]$, solid bulk modulus
K_{sm}	Bulk modulus of the matrix formed by solid given by Dvorkin et al. (1999)
K_{hm}	$K_{\max}[\phi_h/(1-\phi_s)]^{3.8}$, bulk modulus of the matrix formed by hydrate
$K_{\max}$	Kuster-Toksoz's bulk modulus for the hydrate matrix(Zimmerman and Kingt 1986)
K_{av}	$[(1-c_s)\phi_s/K_s+\phi_f/K_f+(1-c_h)\phi_h/K_h]^{-1}$
r_{sf}	Geometrical aspect of the boundary separating fluid from sand (0.5 in our study)
r_{sh}	Geometrical aspect of the boundary separating solid from hydrate (0 in our study)
r_{hs}	Geometrical aspect of the boundary separating hydrate from sand (0 in our study)
r_{fh}	Geometrical aspect of the boundary separating fluid from hydrate (0 in our study)
r_s	50 μm, average radius of sand grain
R_{ss}	$[(1-c_s)\phi_s]^2 K_{av}+K_{sm}+4\mu_{ss}/3$
R_{sh}	$(1-c_s)(1-c_h)\phi_s\phi_h K_{av}+2\mu_{sh}/3$
R_{hh}	$[(1-c_h)\phi_h]^2 K_{av}+K_{hm}+4\mu_{hh}/3$
R_{ff}	$R_{ff}=f_1\phi_1+f_3\phi_3$, $\phi_1=\phi_f/(1-\phi_h)$, $Q_1=K_s/(1-\phi_1-K_{sm}/K_s)$, $\phi_3=\phi_f/\phi$, $f_1=1/[1/K_f+1/(\phi_1 Q_1)]$, $Q_3=K_h/(1-\phi_3-K_{hm}/K_h)$, $f_3=[1/K_f+1/(\phi_3 Q_3)]^{-1}$
R_{sf}	$R_{sf}=f_1(\alpha_1-\phi_1)$, $\alpha_1=(1-K_{sm}/K_s+2\phi_1)/3$
R_{fh}	$R_{fh}=f_3(\alpha_3-\phi_3)$, $\alpha_3=(1-K_{hm}/K_s+2\phi_3)/3$
ϕ_f	$\phi_0(1-S_h)$, real porosity, ϕ
ϕ_h	$\phi_0 S_h$
ϕ_s	$1-\phi_0$

γ_c	$0.8-0.6S_h$, fraction of clay content (Guerin & Goldberg 2005)
η_D	$\eta F(\xi)$, dynamical viscosity of interstitial water
k_{s0c}	$k_{s0}(1-\gamma_c)^3$
k_s	$k_{s0c}[\phi_f/(1-\phi_s)]^3$
k_h	$k_{h0}[(1-\phi_s)/\phi_h]^2[\phi_f/\phi_s]^3$
μ_s	$\frac{1}{2}[\gamma_c\mu_{clay}+(1-\gamma_c)\mu_{sand}+\frac{\mu_{sand}\mu_{clay}}{\mu_{sand}\gamma_c+\mu_{clay}(1-\gamma_c)}]$, solid shear modulus
μ_{sm}	Shear modulus of the matrix formed by solid given by Dvorkin et al. (1999)
$\mu_{\max}$	Kuster-Toksoz's shear modulus for the hydrate matrix(Zimmerman and Kingt 1986)
μ_{hm}	$\mu_{\max}[\phi_h/(1-\phi_s)]^{3.8}$, shear modulus of the matrix formed by hydrate
μ_{av}	$1/[(1-g_s)\phi_s/\mu_s+\phi_f/j\omega\eta+(1-g_h)\phi_h/\mu_h]$
μ_{ss}	$[(1-g_s)\phi_s]^2\mu_{av}+\mu_{sm}$
μ_{sh}	$(1-g_s)(1-g_h)\phi_s\phi_h\mu_{av}+\mu_{sh0}$
μ_{hh}	$[(1-g_h)\phi_h]^2\mu_{av}+\mu_{hm}$
ρ_{ss}	$\phi_s\rho_s a_{sh}+\phi_f\rho_f(a_{sf}-1)+\phi_h\rho_h(a_{hs}-1)-j(b_{ss}+b_{sh})/\omega$
ρ_{sf}	$-\phi_f\rho_f(a_{sf}-1)+jb_{ss}/\omega$
ρ_{sh}	$-\phi_s\rho_s(a_{sh}-1)-\phi_h\rho_h(a_{hs}-1)+jb_{sh}/\omega$
ρ_{hh}	$\phi_h\rho_h a_{hs}+\phi_f\rho_f(a_{fh}-1)+\phi_s\rho_s(a_{sh}-1)-j(b_{hh}+b_{sh})/\omega$
ρ_{ff}	$\phi_f\rho_f(a_{sf}+a_{fh}-1)-j(b_{ss}+b_{hh})/\omega$
ρ_{fh}	$-\phi_f\rho_f(a_{fh}-1)+jb_{hh}/\omega$
ρ_s	$\gamma_c\rho_{clay}+(1-\gamma_c)\rho_{sand}$, solid phase density
ξ	$\xi=(h/2)(\omega\rho_f/\eta)^{0.5}$

It should be noted that the Leclaire model, the Carcione model, the Guerin model are applied to partially frozen unconsolidated sands and MH-bearing sediments in this thesis. In the original Guerin model, the effect of clay on permeability of MH-bearing sediments has taken into account (Guerin & Goldberg, 2005). Because the presence of clay at Nankai Trough has been testified, I follow this definition when applying the Guerin model to MH-bearing sediment at Nankai Trough. Obviously, there is no clay in partially frozen unconsolidated sands, therefore, in the application of the Guerin model to partially frozen unconsolidated sands, this effect of clay is neglected, thus the input parameters of the Guerin model for partially frozen unconsolidated sands (Table 2.5) and MH-bearing sediments (Table 2.6) are slightly different. Moreover, whether there is clay also makes initial permeability in sand grains (k_{so}) and hydrate (k_{ho}) or ice (k_{io}) of the Guerin model for partially frozen unconsolidated sands (Table 2.5) and MH-bearing sediment (Table 2.6) different. Only the calculation

workflow of the Guerin model for the partially frozen unconsolidated sands is listed as Appendix C, and it is similar for MH-bearing sediments. However, the input parameters of the Guerin model for the partially frozen unconsolidated sands (Table 2.5) and MH-bearing sediments (Table 2.6) are listed respectively.

2.4 Description of input parameters

2.4.1 Input parameters of rock physics modelling for partially frozen systems

The input parameters of rock physics models applied to the partially frozen systems are listed in Table 2.5. The initial salinity of brine in the measurements was 2% (Matsushima et al., 2016). I speculated somewhat for the initial freezing point T_0 for the two partially frozen systems but finally set it at –2 °C, similar to the freezing point of ocean water (Adkins, 2002), if not otherwise specified. The initial porosity ϕ_0 of brine-saturated Toyoura sand was given as 41% (Matsushima et al., 2016). The critical porosity was set to 38% (Ecker et al., 1998, 2000). As in previous studies, the initial viscosity of brine was 1.798 mPa·s (Carcione and Seriani, 1998). The effective pressure was assumed to be the atmospheric pressure of 0.1 MPa because the ultrasonic measurements by Matsushima et al. (2008, 2016) were conducted under atmospheric conditions. Since the sand grain coordination number n is usually assumed to be 8–9 for grain packs, a value of 8.5 was used in this study based on previous studies (Ecker et al., 2000; Marín-Moreno et al., 2017). In the estimation of ice saturation with decreasing temperature, the average pore radius r_{av}, standard deviation of capillary pore radius Δr, and free parameter r_0 need to be specified. I assumed r_0 as 0.228 μm and Δr as 10 μm, following the definition proposed by Carcione et al. (2007). I found that r_{av} significantly affected the estimation of the unfrozen brine saturation and then disturbed the predicted attenuation versus temperature curve. Therefore, the results section (Chapter 5) includes a discussion of the effect of r_{av} on velocity and attenuation.

The key free parameters for the Leurer model are the brine inclusion aspect ratio α_m and the total brine inclusion concentration c_i. I assumed that α_m had a distribution from 0.05 to 0.0005 (Leurer, 1997) and c_i corresponded to 50% brine saturation in the ice-brine system, following the definitions of Leurer (1997) and Leurer and Brown (2008). The Guerin model introduced double permeability k_{s0} and k_{i0} to consider the BISQ mechanism in sand and ice, respectively. k_{s0} is set as 5×10^{-13} m^2 and k_{i0} as 1×10^{-12} m^2 in the application of the Guerin model to unconsolidated sand. The

two key free parameters for the Guerin model are the friction coefficient b_{si0} and the shear coefficient μ_{si0}. I applied the values used by Guerin and Goldberg (2005).

Table 2. 5 Input parameters for the Leurer model and the Guerin model

Parameters and units	Value
K_s : solid bulk modulus, Pa	38×10^9 (Guerin and Goldberg,2005)
K_i : ice bulk modulus, Pa	7.9×10^9 (Guerin and Goldberg,2005)
K_f : fluid bulk modulus, Pa	2.67×10^9 (King and Marsden, 2002)
μ_s : solid shear modulus, Pa	44×10^9 (Guerin and Goldberg,2005)
μ_i : ice shear modulus, Pa	3.3×10^9 (Guerin and Goldberg,2005)
ρ_s : sand grain density, kg/m^3	2700 (Guerin and Goldberg,2005)
ρ_i : ice density, kg/m^3	900 (Guerin and Goldberg,2005)
ρ_f : brine density, kg/m^3	1040(King and Marsden, 2002)
ϕ_0 : porosity, %	41 (Matsushima et al., 2015)
ϕ_c : critical porosity, %	38 (Ecker et al. 2000)
η_0 : viscosity of water at freezing point, mPa s	1.798 (Carcione and Seriani, 1998)
Δr : standard deviation, μm	10 (Carcione et al., 2007)
r_0 : free parameter, μm	0.228 (Carcione et al., 2007)
r_{av} : average pore radius, μm	
f : source frequency ($\omega = 2\pi f$,angular frequency)	
S_i : ice saturation	
Case dependent parameters (the Leurer model)	
c_i : brine inclusion concentration	
α_i : brine inclusion aspect ratio	
Case dependent parameters (the Guerin model)	
k_{s0} : solid matrix permeability, m^2	5×10^{-13}
k_{i0} : ice matrix permeability, m^2	1×10^{-12}
μ_{si0} : coupling shear modulus between solid grain and ice, Pa	4.4×10^{10}(Guerin and Goldberg,2005)
b_{si0} : friction coefficient between solid grain and ice, kg/(m^3 s)	2.2×10^8(Guerin and Goldberg,2005)

2.4.2 Input parameters of rock physics modelling for MH-bearing sediments

The input parameters of rock physics models for MH-bearing sediments are listed in Table 2.6. Two considerations are crucial to the successful prediction of velocity and attenuation: (1) avoiding an

excessive number of free parameters and (2) approximating the input parameters to the real rock properties of the Nankai Trough. The porosity estimated from the core samples of hydrate-bearing sediment in the Nankai Trough appears to vary approximately in the range of 35% to 43% (average porosity: 40%) (Jin et al., 2016). Therefore, when using the hydrate contact model, the actual porosity is set to 40%, and critical porosity is set to 38% (Ecker et al., 1998, 2000). Although we have no knowledge of the change of strata pressure with depth at Nankai Trough, we can roughly estimate the effective pressure according to the ocean depth (about 945 m) and the depth of hydrate-bearing sediments (about 1200 m) (Matsushima, 2006). Moreover, because the limited thickness of the primary hydrate-bearing layer of interest is less than 100 m, the variation of effective pressure with depth is ignored in the theoretical calculation. I also evaluate the effective pressure (P) on the P- and S-wave velocities and attenuations, and then compare the predicted values calculated from various effective pressure (P) with the sonic data, finally assume the effective pressure as 0.5 MPa. As in previous studies, the viscosity of water is chosen as 0.0018 Pa·s (Guerin & Goldberg, 2005). For a random system of pores with all orientations, the tortuosity (t) in the Biot-Stoll model is usually used set to 3 (Stoll & Bryan, 1970). Since the sand grain coordination number (n) is usually assumed to be 8 to 9 for grain packs, a value of 8.5 is used in the present study based on previous studies (Ecker et al., 2000; Marin-Moreno et al., 2017). The frequencies of P- and S-waves for sonic data in my simulation are chosen as 14,000 Hz and 1,000 Hz, respectively, and 100 Hz is used for VSP data.

In addition, the key free parameters for the Marin-Moreno model are the inclusion aspect ratio (α), the inclusion concentration (c_i), and the fraction of pore-filling hydrate (c_{pf}). Best et al. (2013) indicated that for a given frequency, c_i controls the position of attenuation peaks with respect to hydrate saturation (S_h), whereas α controls the magnitude of the attenuation peak. Marin-Moreno et al. (2017) suggested that for a given frequency, the maximum P-wave attenuation occurs at a particular inclusion aspect ratio (α), and the magnitude of attenuation depends on inclusion concentration (c_i). Best et al. (2013) and Marin-Moreno et al. (2017) compared their simulation results with experiment data at 200 Hz (Priest et al., 2006; Best et al., 2013). The fraction of pore-filling hydrate (c_{pf}) is considered to be dependent on the hydrate saturation (S_h). The fraction of pore-filling hydrate (c_{pf}) of 0 means that there is no pore-filling hydrate and 100% contact cementing hydrate is present. The effects of the inclusion concentration (c_i), the inclusion aspect ratio (α), and the fraction of pore-filling hydrate (c_{pf}) on P- and S-wave velocities and attenuations are evaluated firstly. Then the sonic data is used to compare with the predicted values with various parameter combinations, and finally I found that the inclusion concentration (c_i) of 0.3, and the inclusion aspect ratio (α) of 0.0004 seem to fit the sonic P- and S-wave velocities and attenuations at the whole hydrate saturation best.

On the other hand, two key free parameters for the Guerin model are the friction coefficient (b_{sh0}) and the shear coefficient (μ_{sh0}). Since the hydrate-bearing zone in the Nankai Trough is composed of a sandy reservoir, which is similar to the Mallik field, the values used by Guerin and Goldberg (2005) is applied here. With respect to permeability, although the effect of changing permeability caused by the formation of hydrate on attenuation was considered by the Guerin model and the Marin-Moreno model (Guerin & Goldberg, 2005; Marín-Moreno et al., 2017), the influence on the attenuation mechanism is completely different. In fact, the permeability affects the relaxation frequency of the Biot flow, but does not affect the characteristic frequency of squirt flow in microporous hydrate for the Marin-Moreno model (Best et al., 2013; Marín-Moreno et al., 2017). In other words, the attenuation in the sonic and VSP frequency bands for the Marin-Moreno model is insensitive to the permeability, and the initial sand permeability (k_0) without hydrate was set to be 5×10^{-11} m^2 as the initial sand permeability (k_{s0}) by Guerin and Goldberg (2005). Unlike the Marin-Moreno model, the Guerin model introduced double permeability to consider the BISQ mechanisms in sand and hydrate, respectively (k_{s0} and k_{h0}). I follow the definition of k_{s0} and k_{h0} as in Guerin and Goldberg (2005).

Table 2. 6 Input parameters for the Marin-Moreno model and the Guerin model

Parameters and units	Value
K_{sand} : sand bulk modulus, Pa	38×10^9 (Guerin & Goldberg, 2005)
K_h : hydrate bulk modulus, Pa	7.9×10^9 (Best et al., 2013)
K_f :water bulk modulus, Pa	2.67×10^9 (Guerin & Goldberg, 2005)
μ_{sand} : sand shear modulus, Pa	44×10^9 (Guerin & Goldberg, 2005)
μ_h : hydrate shear modulus, Pa	3.3×10^9 (Guerin & Goldberg, 2005)
ρ_{sand} : sand grain density, kg/m^3	2700 (Guerin & Goldberg, 2005)
ρ_h : hydrate density, kg/m^3	900 (Guerin & Goldberg, 2005)
ρ_f : water density, kg/m^3	1000 (Guerin & Goldberg, 2005)
ϕ_0 : porosity, %	40 (Jin et al., 2016)
ϕ_c : critical porosity, %	38 (Ecker et al., 2000)
η : viscosity of water, kg/(m·s)	0.0018 (Guerin & Goldberg, 2005)
P : effective pressure, MPa	0.5 (Priest et al., 2006)
f : monopole source frequency, Hz	14000
f : dipole source frequency, Hz	1000
f : VSP source frequency, Hz	100
S_h : hydrate saturation	
ω : angular frequency($\omega = 2\pi f$)	
Case dependent parameters (Marin-Moreno model)	
k_0 : intrinsic permeability without hydrate	5×10^{-11} (Guerin & Goldberg, 2005)

α : aspect ratio of inclusion	0.0004 (Marín-Moreno et al., 2017)
c_i : concentration of inclusion	0.3 (Best et al., 2013)
c_{pf} : fraction of pore-filling hydrate	
t : tortuosity	3 (Stoll & Bryan, 1970)
n : sand grain coordination number	8.5 (Ecker et al., 2000)
ν : sand grain Poission's ratio	0.062 (Marín-Moreno et al., 2017)
ν_h : hydrate Poission's ratio	0.32 (Marín-Moreno et al., 2017)
Case dependent parameters (Guerin model)	
K_{clay} : clay bulk modulus, Pa	21.2×10^{9} (Guerin & Goldberg, 2005)
μ_{clay} : clay shear modulus, Pa	6.67×10^{9} (Guerin & Goldberg, 2005)
ρ_{clay} : clay grain density, kg/m^3	2580 (Chand et al., 2006)
k_{s0} : initial sand matrix permeability, m^2	5×10^{-11} (Guerin & Goldberg, 2005)
k_{h0} : initial hydrate matrix permeability, m^2	1×10^{-7} (Guerin & Goldberg, 2005)
μ_{sh0} : coupling shear modulus between sand grain and hydrate, Pa	4.4×10^{10} (Guerin & Goldberg, 2005)
b_{sh0} : friction coefficient between sand grain and hydrate, kg/(m^3 s)	2.2×10^{8} (Guerin & Goldberg, 2005)

CHAPTER 3. APPLICATION OF ROCK PHYSICS MODELLING TO WELL-LOGGING DATA AT NANKAI TROUGH

In this Chapter, the sensitivity of input parameters of the Marin-Moreno model and the Guerin model to sonic data at the Nankai Trough is tested firstly, and then the best parameters setting is confirmed, thereby possible mechanisms for P- and S-wave attenuations of MH-bearing sediments at sonic frequency domain are discussed. The possible hydrate morphology at Nankai Trough will be inferred based on the application of the Marin-Moreno model.

3.1 Introduction

It is generally accepted that both the P- and S-wave velocities increase with increasing hydrate saturation because the presence of hydrate stiffens the bulk and shear moduli of MH-bearing sediments. Therefore, sonic velocities have been widely used to estimate hydrate saturation (Lee & Collett, 2009; Lee & Waite, 2008). In addition to hydrate saturation, hydrate morphology and distribution also have a profound influence on the velocity of MH-bearing sediments (Ecker et al., 1998, 2000; Konno et al., 2015; Priest et al., 2009). Hydrate saturation was estimated using sonic P- and S-wave velocities obtained from well logging profiles based on different effective medium models and hydrate morphologies (Carcione & Gei, 2004; Chand et al., 2004; Collett & Ladd, 2000; Helgerud et al., 1999; Kim et al., 2011; Lee & Waite, 2008; Shankar & Riedel, 2011). Obviously, uncertainties in the estimation of hydrate saturation stem from the choice of effective medium model and hydrate morphology. Some studies showed that hydrate saturation obtained from sonic velocity were different from those calculated from sonic resistivity logs by Archie's equation (Kim et al., 2011), while some studies indicated good agreement between them (Carcione & Gei, 2004; Lee & Waite, 2008). Carcione and Gei (2004) indicated that the estimation based on the P-wave velocity was more reliable than those based on the S-wave velocity. In addition, existing rock physics models are mostly based on the isotopic assumption, and are easy to yield misleading hydrate saturation for anisotropic clay-rich or fractured sediments (Ghosh et al., 2010a; Lee & Collett, 2009).

Seismic attenuation is generally considered to be more sensitive to changes in sediments properties than velocity (Winkler & Nur, 1982). This high sensitivity may facilitate characterization of the rock properties of MH-bearing sediments using sonic logging attenuation. Significantly high attenuation has been widely observed to accompany the increase in velocity for both P- and S-waves in MH-bearing sediments in the sonic logging frequency range (typically 10 to 30 kHz for monopole data and 300 Hz to 8 kHz for dipole data) in several geologic environments: Blake Ridge site (Guerin

et al., 1999), Nankai Trough (Matsushima, 2005; Suzuki & Matsushima, 2013), Mallik field (Guerin & Goldberg, 2002; Guerin & Goldberg, 2005), and Krishna-Godavari Basin (Nittala et al., 2017) (no obvious S-wave attenuation).

Guerin & Goldberg (2005) have made an exhaustive investigation on the attenuation mechanisms responsible for P- and S-wave attenuations at sonic frequency domain. However, because of the nature of percolation theory in the Guerin model, the attenuation mechanism related to microporous hydrate and hydrate morphology cannot be included and it is necessary to be further investigated. There are extremely few studies on the effect of hydrate morphology on P- and S-wave attenuation (Best et al., 2013). Using the sonic P-and S-wave attenuations at Nankai Trough, the effect of hydrate morphology on attenuations is systematically investigated, thereby the possible morphology at Nankai Trough is also inferred.

3.2 Sonic data description at Nankai Trough

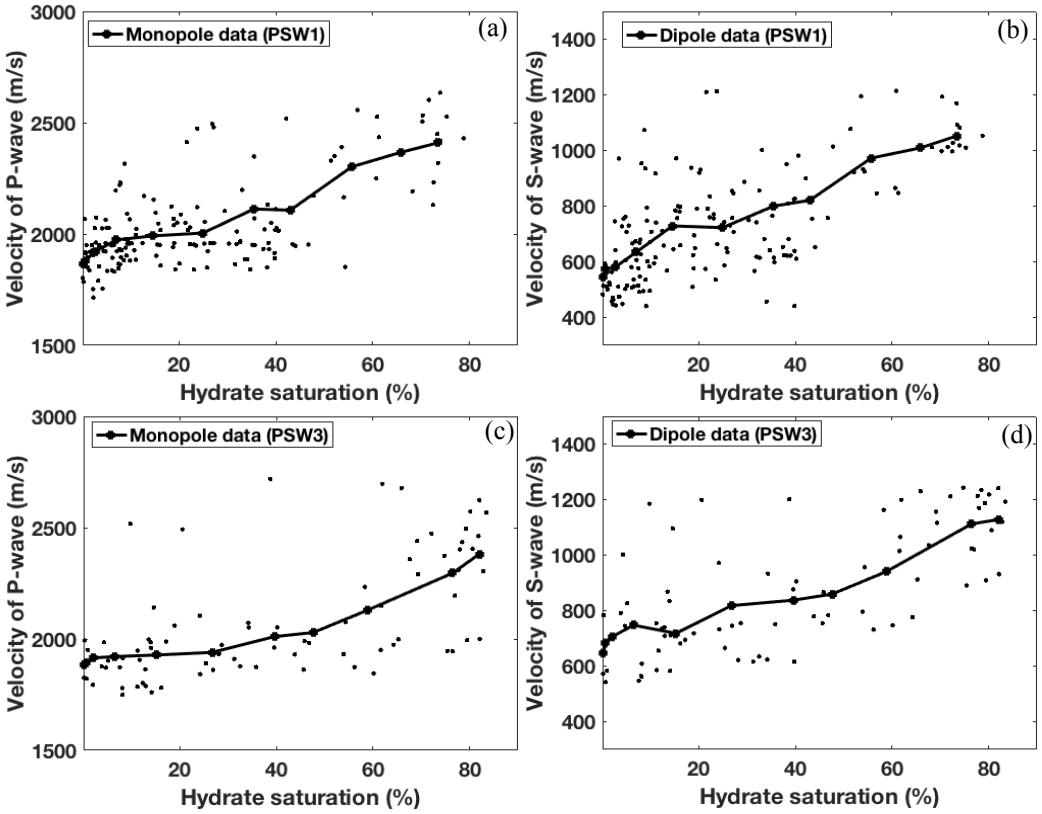

Figure 3. 1 Averaged sonic velocities of P- and S-wave. (a) Averaged P-wave velocity at PSW1. (b) Averaged S-wave velocity at PSW1. (c) Averaged P-wave velocity at PSW3. (d) Averaged S-wave velocity at PSW3.

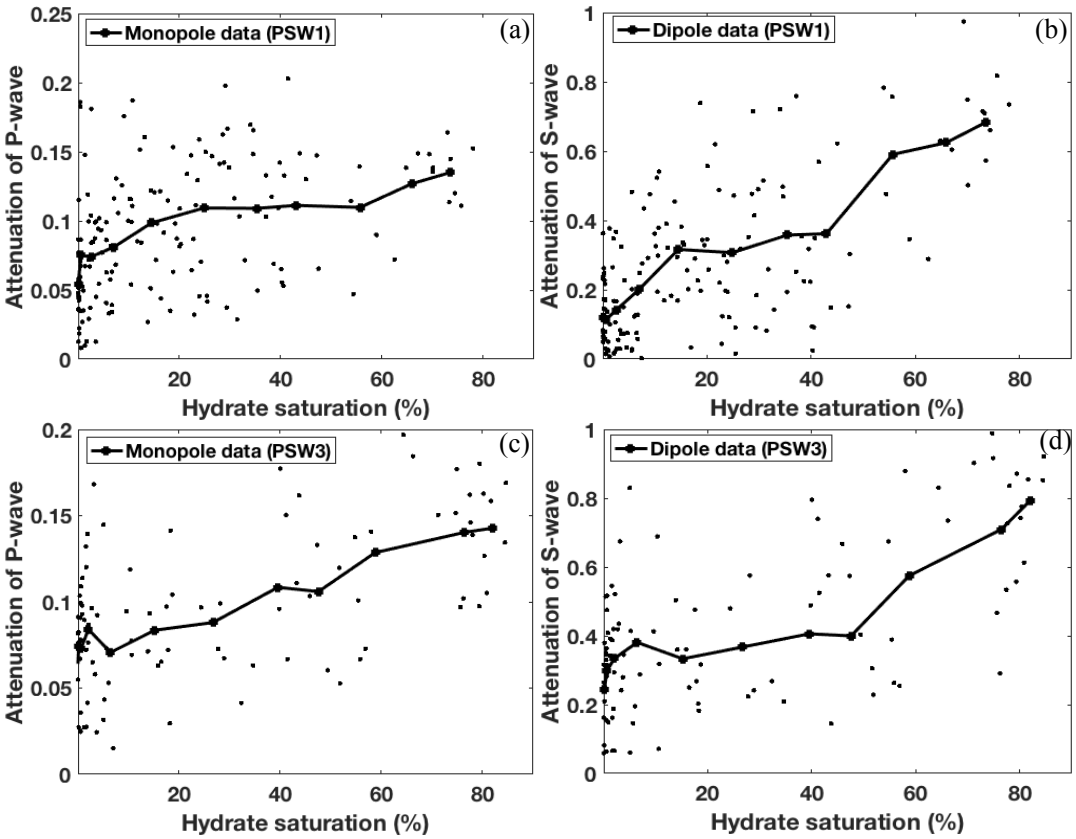

Figure 3. 2 Averaged sonic attenuations of P- and S-wave. (a) Averaged P-wave attenuation at PSW1. (b) Averaged S-wave attenuation at PSW1. (c) Averaged P-wave attenuation at PSW3. (d) Averaged S-wave attenuation at PSW3.

Suzuki and Matsushima (2013) calculated the stable attenuation of P- and S-waves for the primary hydrate-bearing zones of interest from sonic data using a modified median frequency shift method. In order to compare predicted P- and S-wave velocities and attenuations curves from rock physical modeling with sonic data, scattered sonic velocities and attenuations at specific hydrate saturation ranges are averaged. The measured sonic velocities of the P- and S-waves (Fig. 3.1) and measured sonic attenuations of P- and S-waves (Fig. 3.2) are averaged for hydrate saturation ranges of 0 to 0.5%, 0.5 to 1%, 1 to 5%, 5 to 10%, 10 to 20%, 20 to 30%, 30 to 40%, 40 to 47%, 47 to 58%, 58 to 69%, and 69 to 78% for PSW1, while 0 to 0.1%, 0.1 to 0.5%, 0.5 to 1%, 1 to 5%, 5 to 10%, 10 to 18%, 18 to 28%, 28 to 43%, 43 to 51%, 51 to 66%, 66 to 79%, and 79 to 84 % for PSW3. These velocities and attenuations are shown as black fitting curves in Figs 3.1 and 3.2. In the low hydrate saturation interval below 5%, we can see that initial significant increasing for velocity (Fig 3.1) and attenuation (Fig 3.2), which may be caused by cementing hydrate as indicated by Priest et al. (2005) and Priest et al. (2006). After the significant increasing below a hydrate saturation of 5%, the velocity

and attenuation of P- and S-waves increase gently until the hydrate saturation below 50-55%, then increases dramatically again until hydrate saturation up to the maximum around 75-80%.

With regarding to the averaged method, taking the hydrate saturation range of 0 to 0.5% as an example, I arithmetically average the sonic hydrate saturation ranging from 0 to 0.5% estimated from resistivity data, and then the averaged hydrate saturation is considered as representative of the hydrate saturation ranging from 0 to 0.5%. At the same time, the sonic P- and S-wave velocities and attenuations at the hydrate saturation ranging from 0 to 0.5% are also averaged by the same method, and are considered as representative of velocities and attenuations ranging from 0 to 0.5%.

3.3 Sensitivity of input parameters of rock physics modeling

3.3.1 The Marin-Moreno model

3.3.1.1 The effect of inclusion aspect ratio on velocity and attenuation

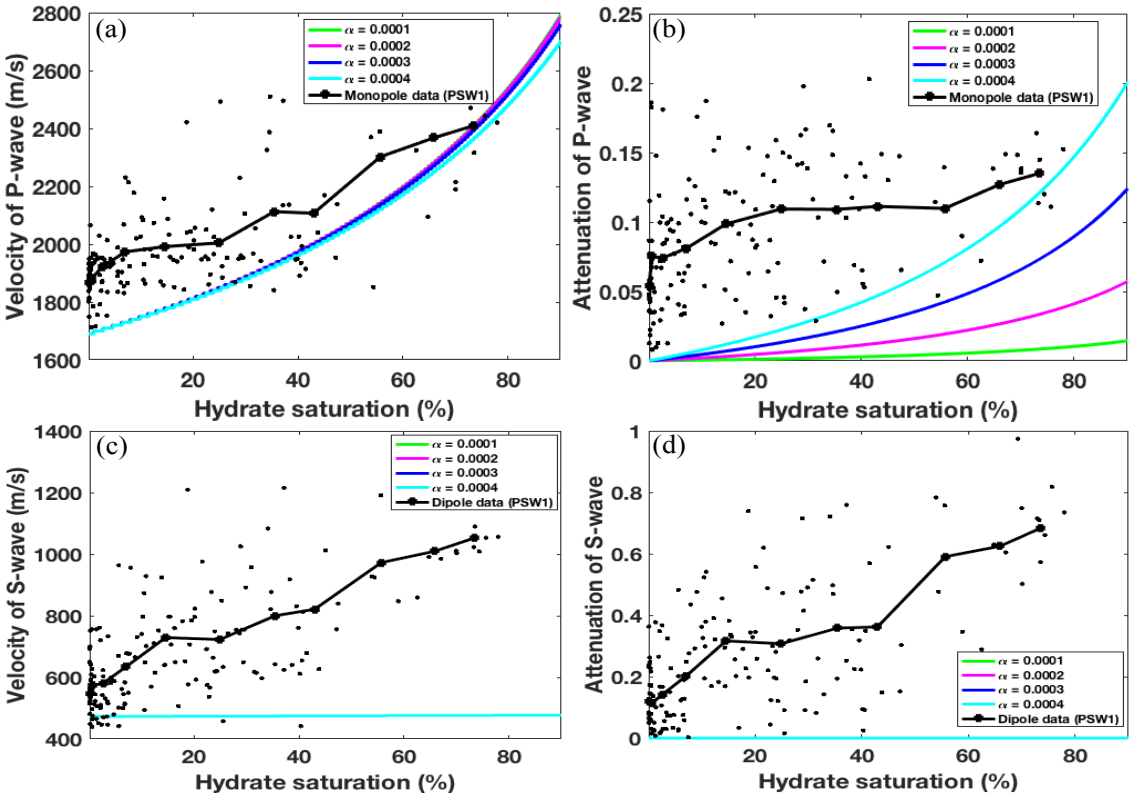

Figure 3. 3 Measured velocities and attenuations at PSW1 and those predicted by the Marin-Moreno model for P- and S-waves with various inclusion aspect ratios (α) changing from 0.0001 to 0.0004. The inclusion concentration (c_i) is assumed as a value of 0.3 and hydrate is assumed as pore-filling morphology. (a) P-wave velocity. (b) P-wave attenuation. (c) S-wave velocity. (d) S-wave attenuation.

It should be noted that the frequencies of the monopole and dipole sources are assumed as 14,000 and 1,000 Hz respectively in this study. About the input parameters for the Marin-Moreno model, the input parameters are shown as Table 2.6 in Chapter 2. We can find that inclusion concentration (c_i) and inclusion aspect ratio (α) have an extremely small impact on the P- and S-wave velocities, while the P-wave attenuation strongly depends on inclusion concentration (c_i) and inclusion aspect ratio (α). Before application of the Marin-Moreno model to the Nankai Trough, many tests for input parameters are made. For Fig. 3.3, c_i is assumed as 0.3 and c_{pf} is assumed as 1 (totally pore-filling hydrate). For S-wave velocity (Fig. 3.3c) and attenuation (Fig. 3.3d), because pore-filling hydrate is seemed as a part of fluid, and has no effect on the calculation of shear modulus, and thus aspect ratio (α) of inclusion in hydrate has no effect on S-wave velocity (Fig. 3.3c) and S-wave attenuation (Fig. 3.3d). The S-wave velocity (Fig. 3.3c) remains constant at a low value, and S-wave attenuation (Fig. 3.3d) also performs an extremely low value and keeps constant. The P-wave velocity (Fig. 3.3a) and attenuation (Fig. 3.3b) increase with increasing hydrate saturation. We also can find that the inclusion aspect ratio (α) has slight effect on P-wave velocity (Fig. 3.3a), while the P-wave attenuation (Fig. 3.3b) increases with increasing inclusion aspect ratio (α).

Different from the assumption of pore-filling hydrate morphology for Fig. 3.3, assuming contact cementing and pore-filling hydrate, and the fraction of pore-filling hydrate (c_{pf}) is set as 0.2. The inclusion concentration (c_i) is assumed as 0.3 and the other input parameters are shown as Table 2.6 in Chapter 2. When assuming the fraction of pore-filling hydrate (c_{pf}) as 0.2, the predicted P-wave (Fig. 3.4a) and S-wave (Fig. 3.4c) velocities agree better with the averaged sonic ones (black fitting curves) than the situation of pore-filling hydrate (Figs. 3.3a and 3.3c). Both of them increase with increasing hydrate saturation. The inclusion aspect ratio (α) almost has no effect on P-wave velocity (Fig. 3.4a), while has a small effect on S-wave velocity (Fig. 3.4c). P-wave attenuation (Fig. 3.4b) increases with increasing hydrate saturation, while S-wave attenuation (Fig. 3.4d) almost remains constant (Fig. 3.4d) at a small value. This is because the shear modulus of the effective hydrate grains is negative when applying the effective medium model owing to the non-interaction assumption is violated for higher inclusion concentration (Kuster & Toksoz, 1974). In such a situation, the complex shear modulus of effective hydrate with fluid inclusion is substituted by the real shear modulus of hydrate. Therefore, the final attenuation for the S-wave reflects the effect of the complex bulk modulus of the effective grain (Dr. Hector Marin-Moreno, private communication, 2017). This solution challenges the application of the Marin-Moreno model to the S-wave attenuation. The P-wave attenuation (Fig. 3.4b) increases with increasing aspect ratio (α). We can find that when assuming

the fraction of pore-filling hydrate (c_{pf}) as 0.2 and inclusion concentration (c_i) as a value of 0.3, the P-wave attenuation (Fig. 3.4b) at the aspect ratio (α) of 0.0004 agrees the averaged sonic value best at sonic frequency domain.

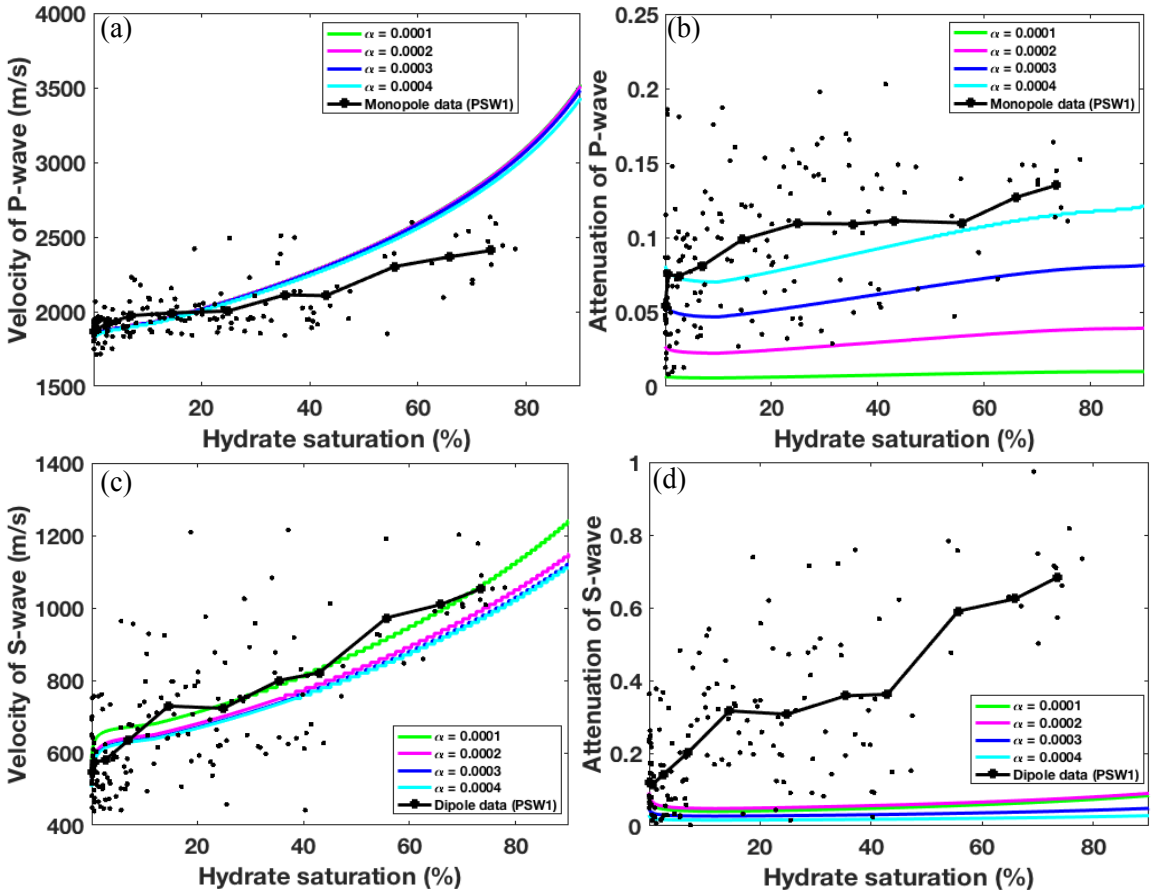

Figure 3. 4 Measured velocities and attenuations at PSW1 and those predicted by the Marin-Moreno model for P- and S-waves with various inclusion aspect ratios (α) changing from 0.0001 to 0.0004. The inclusion concentration (c_i) is assumed as a value of 0.3 and hydrate is assumed as contact cementing and pore-filling morphology (c_{pf} = 0.2). (a) P-wave velocity. (b) P-wave attenuation. (c) S-wave velocity. (d) S-wave attenuation.

3.3.1.2 The effect of inclusion concentration on velocity and attenuation

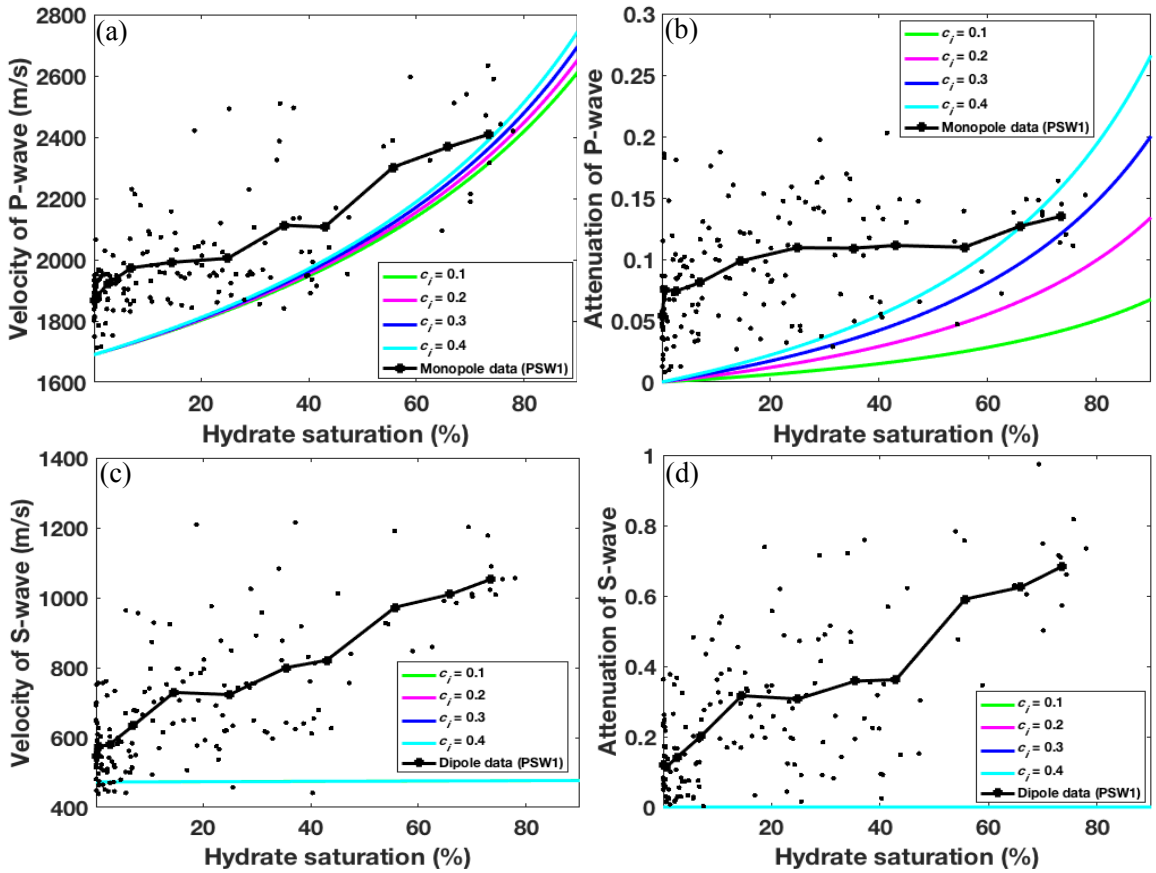

Figure 3. 5 Measured velocities and attenuations at PSW1 and those predicted by the Marin-Moreno model for P- and S-waves with various inclusion concentrations (c_i) changing from 0.1 to 0.4. The inclusion aspect ratio (α) is assumed as a value of 0.0004 and hydrate is assumed as pore-filling morphology. (a) P-wave velocity. (b) P-wave attenuation. (c) S-wave velocity. (d) S-wave attenuation.

It is the same as Fig. 3.3, because pore-filling hydrate seems to be a part of fluid, concentrations (c_i) of inclusion in hydrate has no effect on S-wave velocity (Fig. 3.5c) and S-wave attenuation (Fig. 3.5d). The S-wave velocity (Fig. 3.5c) and S-wave attenuation (Fig. 3.5d) remain constant at an extremely low value. We also can find that the inclusion concentration (c_i) has a slight effect on P-wave velocity (Fig. 3.5a), while the P-wave attenuation (Fig. 3.5b) increases with increasing inclusion concentration (c_i).

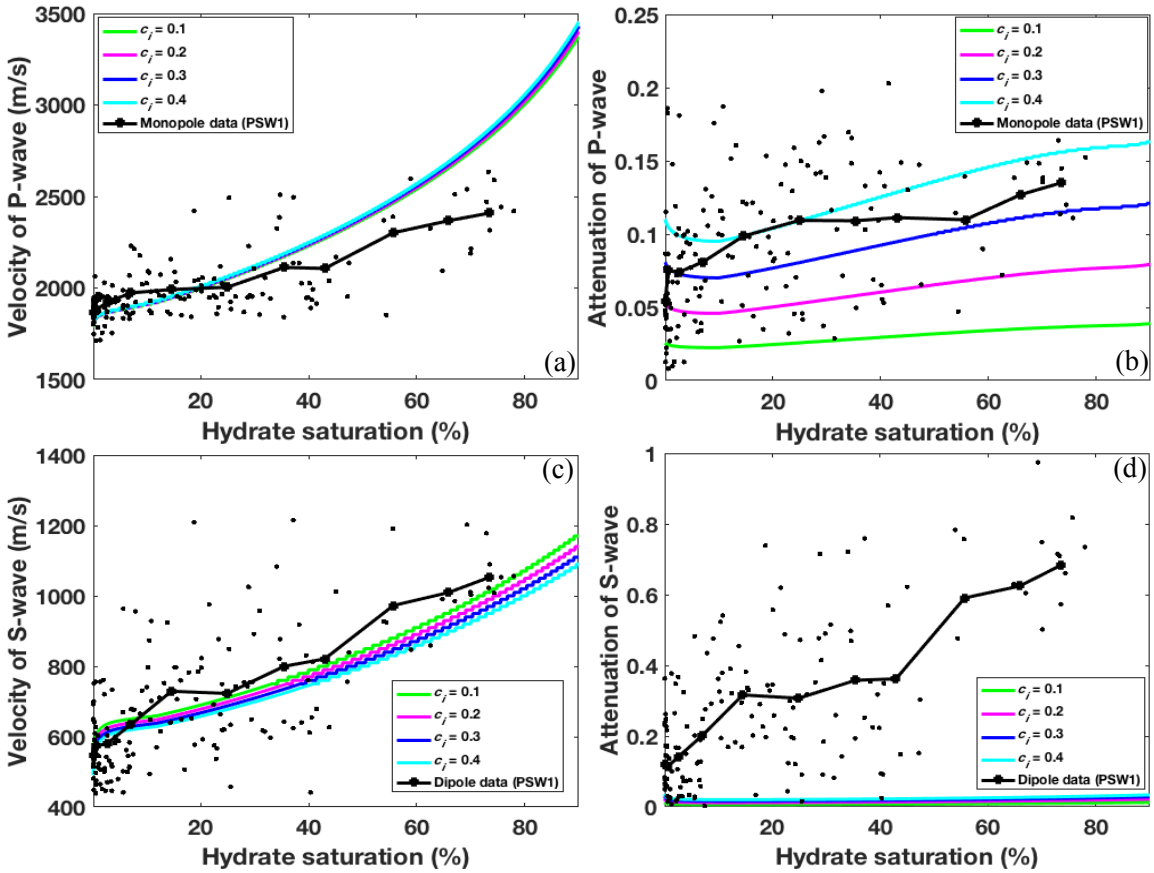

Figure 3. 6 Measured velocities and attenuations at PSW1 and those predicted by the Marin-Moreno model for P- and S-waves with various inclusion concentrations (c_i) changing from 0.1 to 0.4. The inclusion aspect ratio (α) is assumed as a value of 0.0004 and hydrate is assumed as contact cementing and pore-filling morphology (c_{pf} = 0.2). (a) P-wave velocity. (b) P-wave attenuation. (c) S-wave velocity. (d) S-wave attenuation.

P-wave (Fig. 3.6a) and S-wave velocity (Fig. 3.6c) predicted by the Marin-Moreno model when assuming the fraction of pore filling hydrate (c_{pf}) as 0.2 agree well with the averaged sonic ones (black fitting curves). Both of them increase with increasing hydrate saturation. The inclusion concentration (c_i) almost has no effect on P-wave velocity (Fig. 3.6a), while has a small effect on S-wave velocity (Fig. 3.6c). Similar to S-wave attenuation at various inclusion aspect ratios (Fig. 3.4d), S-wave attenuation (Fig. 3.6d) almost remains constant at a small value. The P-wave attenuation (Fig. 3.6b) increases with increasing inclusion concentration (c_i). We can find that when assuming the fraction of pore-filling hydrate (c_{pf}) as 0.2 and aspect ratio (α) of 0.0004, the P-wave attenuation (Fig. 3.6b) at the inclusion concentration (c_i) of 0.3 agrees the averaged sonic value best at sonic frequency domain.

3.3.1.3 The effect of initial permeability in MH-bearing sediments on velocity and attenuation

Furthermore, it is essential that the intrinsic permeability should be altered due to the formation of hydrate. The inclusion concentration (c_i) is assumed as 0.3, the fraction of pore-filling hydrate (c_{pf}) is assumed as 0.2, aspect ratio (α) is assumed as 0.0004, and the other input parameters are shown as Table 2.6 in Chapter 2. As shown in Fig. 3.7, the effect of initial sediment permeability on the velocities (Fig. 3.7a) and attenuations (Fig. 3.7b) of P-wave, and the velocities (Fig. 3.7c) and attenuations (Fig. 3.7d) of S-wave at sonic frequency band are investigated by applying the Marin-Moreno model. The permeability affects the fluid flow, and has no effects on P- (Fig. 3.7a) and S-wave (Fig. 3.7c) velocities. In Figs 3.7b and 3.7d, the red, blue, and green curves are also approximately the same. This indicates that the attenuation of P- and S-waves at the sonic frequency band is insensitive to the initial sand permeability in the sonic frequency band in the application of the Marin-Moreno model.

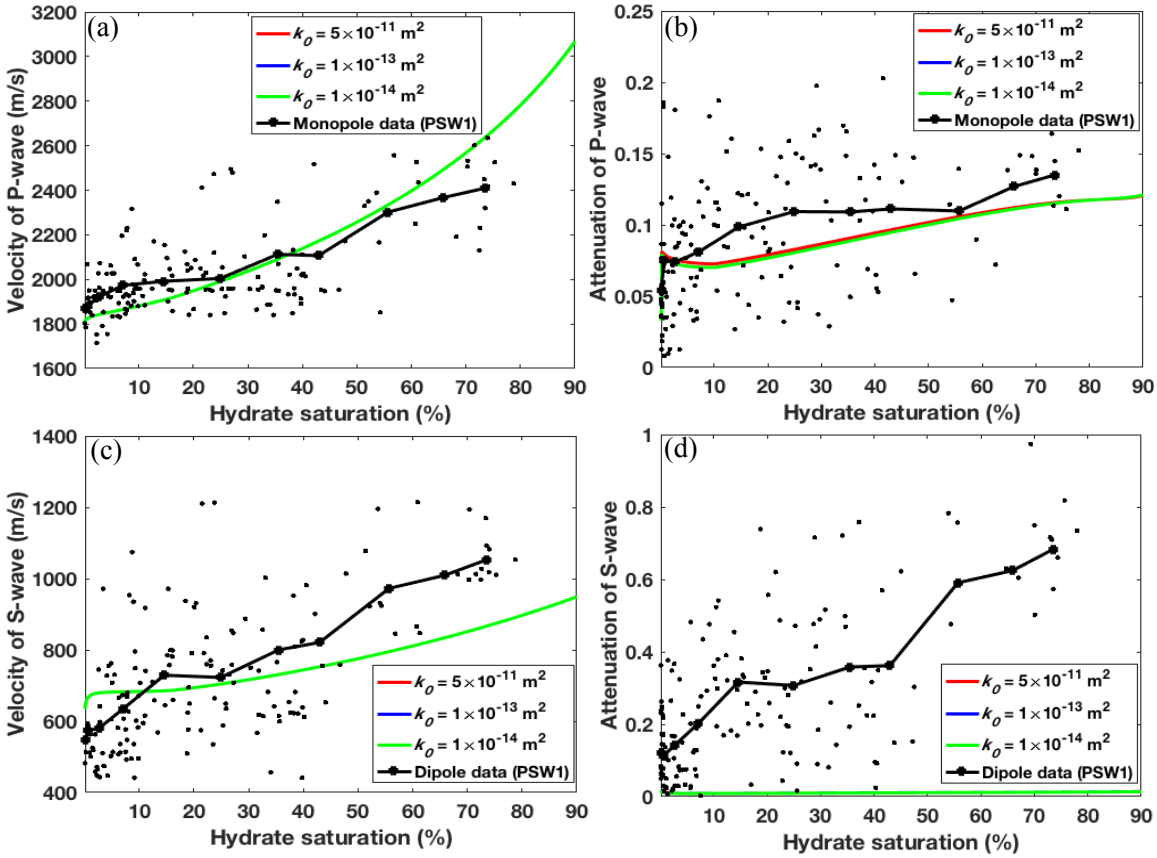

Figure 3. 7 Measured velocity and attenuation and those predicted by the Marin-Moreno model for P- and S-waves at various initial sediment permeabilities. (a) P-wave velocity. (b) P-wave attenuation. (c) S-wave velocity. (d) S-wave attenuation.

3.3.2 The Guerin model

3.3.2.1 The effect of permeability on P- and S-wave attenuation

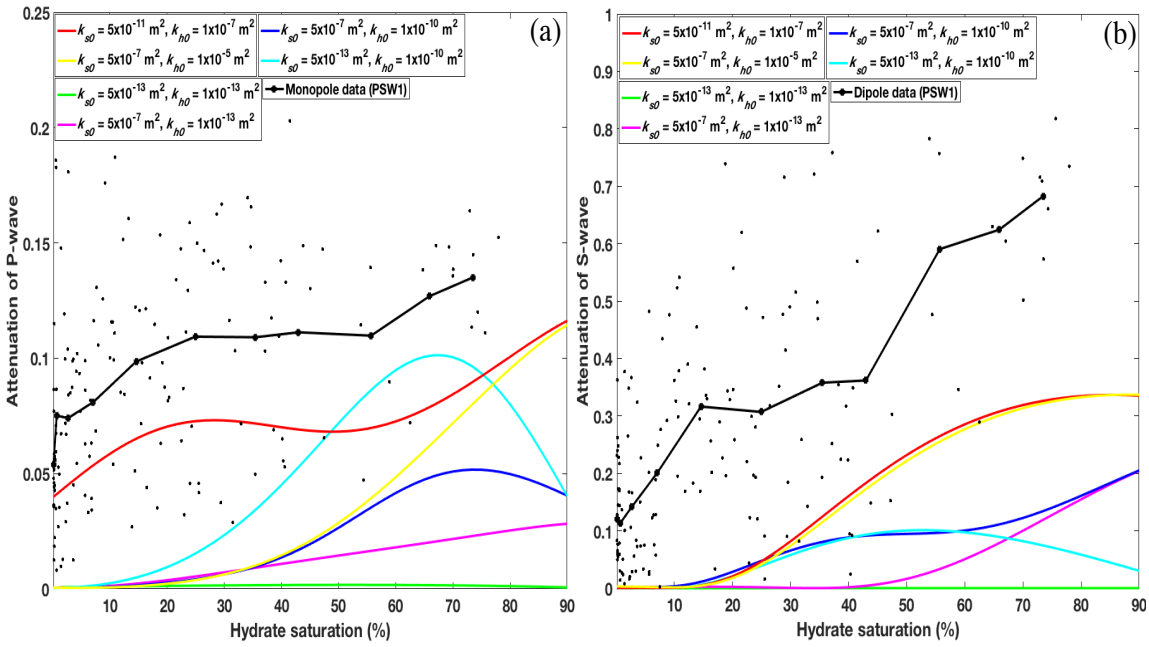

Figure 3. 8 Measured attenuations at PSW1 and attenuations predicted by the Guerin model for P- and S-waves at various initial sediment and hydrate permeabilities. (a) P-wave attenuation. (b) S-wave attenuation.

In the rock physics modeling, by applying the Guerin model and controlling the permeability in the hydrate and sand grains, the attenuations of the P- and S-waves are calculated as a function of hydrate saturation and are compared with field sonic data (Fig. 3.8). The attenuations of the P-wave (Fig. 3.8a) and the S-wave (Fig. 3.8b) exhibit a complex dependence on initial sand permeability (k_{s0}) and initial hydrate permeability (k_{h0}). When the initial sand permeability (k_{s0}) is fixed as 5×10^{-7} m^2, as indicated by the yellow, blue, and pink curves in Figs 3.8a and 3.8b, the P-wave attenuation represented by the yellow curve ($k_{h0}=1\times10^{-5}$ m^2) is the highest, and that represented by the pink curve ($k_{h0}=1\times10^{-13}$ m^2) is the lowest. The S-wave attenuation in Fig. 3.8b exhibits the same trend. In addition, when the initial hydrate permeability (k_{h0}) is fixed as 1×10^{-13} m^2, as indicated by the green and pink curves in Figs 3.8a and 3.8b, the attenuation represented by the pink curve ($k_{s0}=5\times10^{-7}$ m^2) is higher than that represented by the green curve ($k_{s0}=5\times10^{-13}$ m^2). The S-wave attenuation in Fig.

3.8b exhibits the same trend. These results indicate that P- and S- wave attenuations increase with increasing initial sand (k_{s0}) or hydrate permeability (k_{h0}) due to enhanced fluid flow when either of two permeabilities is fixed. In fact, the effective permeability of sand does not change monotonically with increasing hydrate saturation (Guerin & Goldberg 2005). In Fig. 3.9, the comparison between predicted P- and S-wave attenuation and measured ones at PSW3 shows the similar trend. Moreover, the permeability pair of $k_{s0} = 5 \times 10^{-11}$ m^2 and $k_{h0} = 1 \times 10^{-7}$ m^2 appears to capture the attenuation of the P- and S-wave better than other permeability pairs. Therefore, this pair is applied to the calculations in the application of the Guerin model, unless otherwise specified.

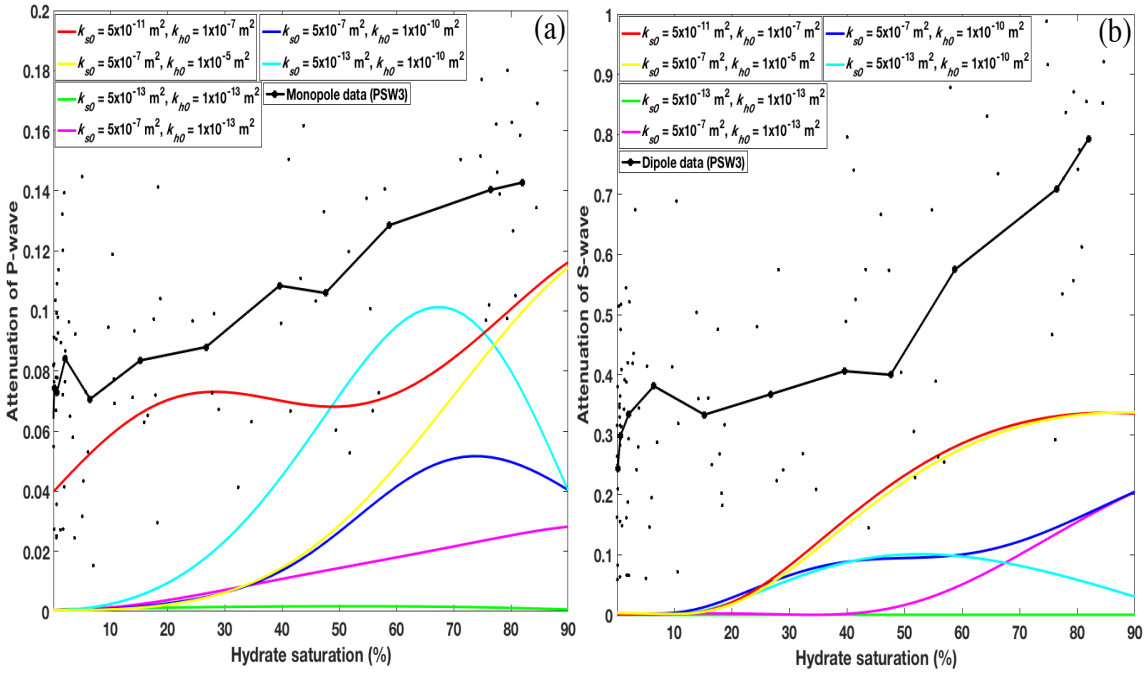

Figure 3. 9 Measured attenuations at PSW3 and attenuations predicted by the Guerin model for P- and S-waves at various initial sediment and hydrate permeabilities. (a) P-wave attenuation. (b) S-wave attenuation.

3.3.2.2 The effect of viscosity on P- and S-wave attenuation

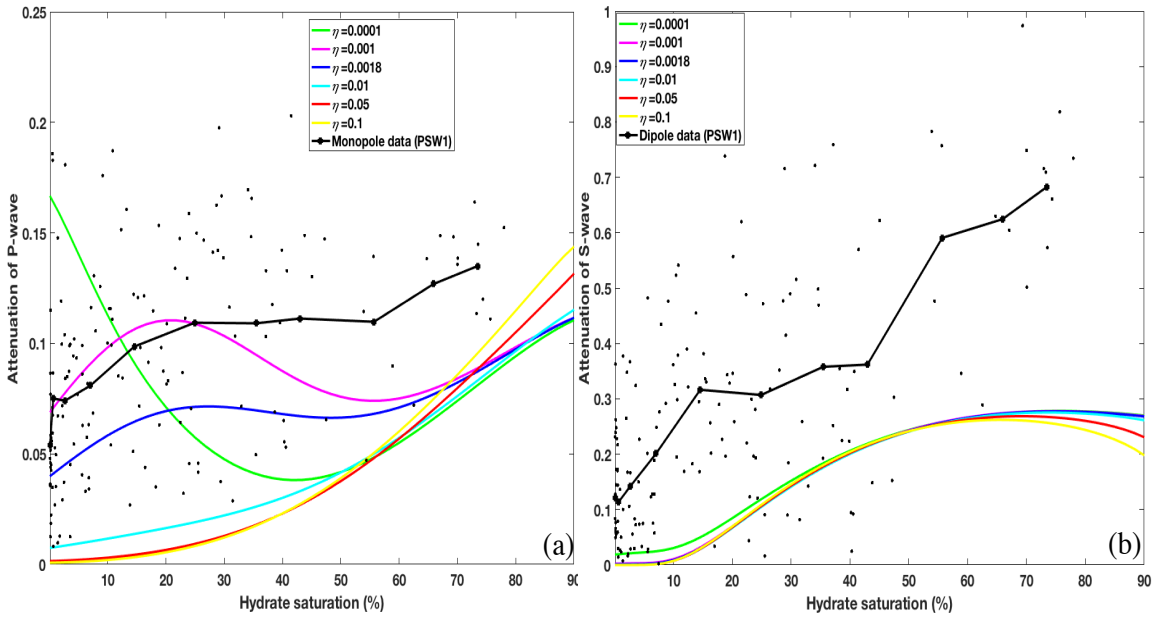

Figure 3. 10 Measured attenuation at PSW1 and attenuation predicted by the Guerin model for P- and S-waves at various viscosities. (a) P-wave attenuation. (b) S-wave attenuation.

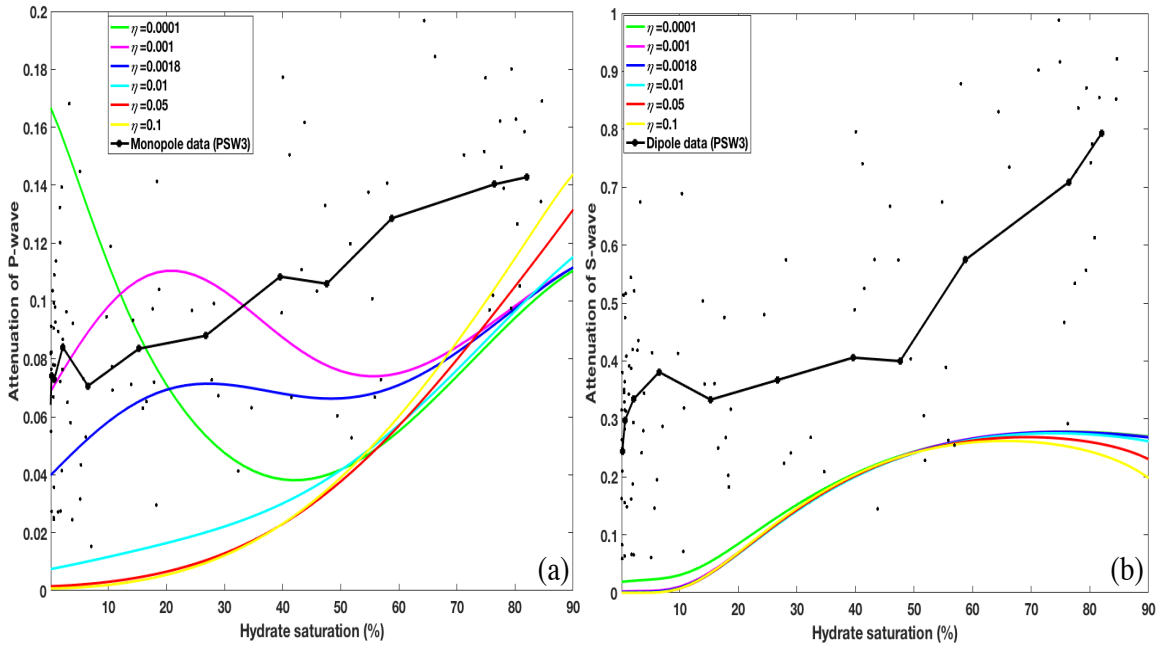

Figure 3. 11 Measured attenuation at PSW3 and attenuation predicted by the Guerin model for P- and S-waves at various viscosities. (a) P-wave attenuation. (b) S-wave attenuation.

The fluid viscosity is also an important parameter controlling attenuation (Jones, 1986). The viscosity is always regarded as a constant with the magnitude of 0.001 Pa s due to the limited change of the temperature in geophysical survey. Because it is often associated with fluid-related attenuation,

the effect of viscosity on attenuation can provide insight into the effect of fluid flow on attenuation. Attenuations of P- and S-waves are calculated to compare with sonic data at PSW1 using different viscosity (Fig. 3.10). As you can see from Fig. 3.10a and 3.10b, predicted results show that at larger hydrate saturation than 70% for P-wave (Fig. 3.10a) and whole hydrate saturation for S-wave (Fig. 3.10b), viscosity has extremely low effect on attenuation. I inferred that fluid-related attenuation mechanism (local squirt flow in sand grain and hydrate) in the Guerin model has extremely low effect on P- and S-wave attenuation in these cases. In addition, attenuation of P-wave increase with decreasing viscosity at low hydrate saturation, then I speculated that fluid-related attenuation mechanisms were responsible for P-wave attenuation at low hydrate saturation. Furthermore, using a viscosity of 0.001-0.0018 Pa s the Guerin model captures the trend of field attenuation best. The same study is also conducted for PSW3 and similar trends are observed (Fig. 3.11).

3.3.2.3 The effect of effective pressure on P- and S-wave attenuation

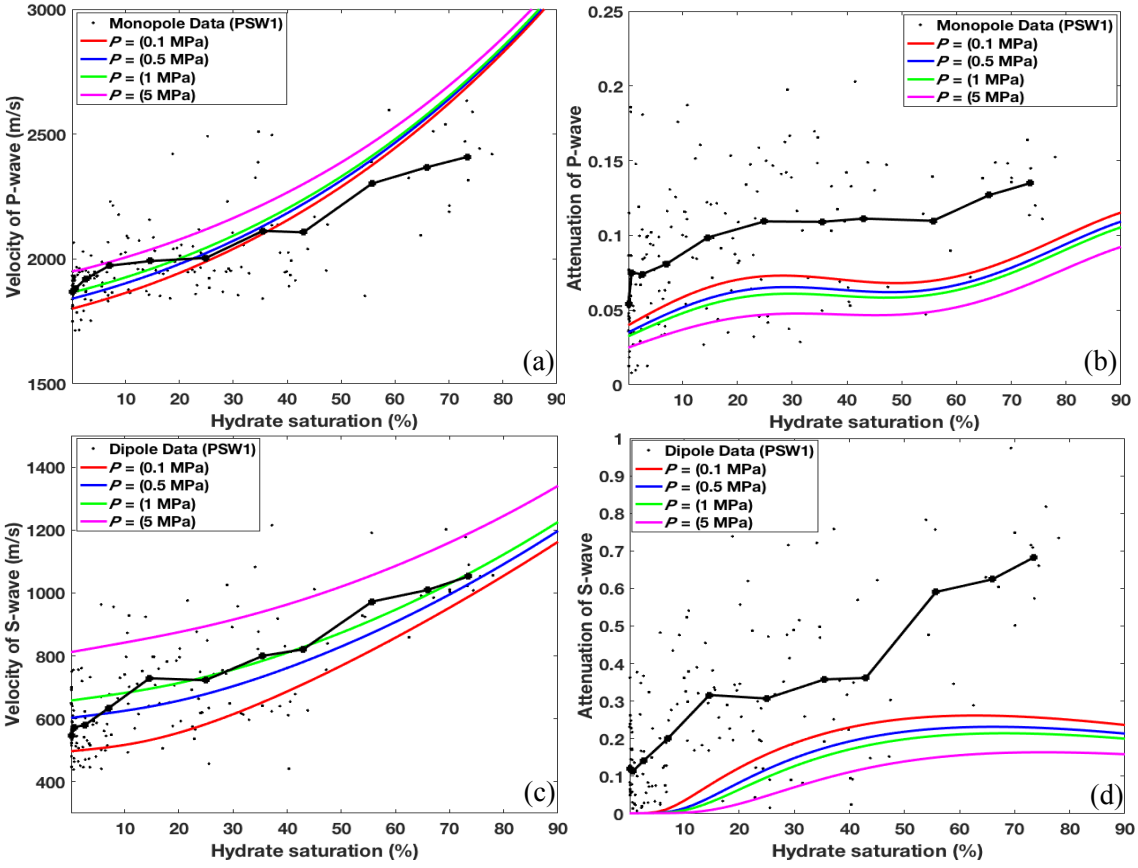

Figure 3. 12 Measured velocity and attenuation at PSW1 and those predicted by the Guerin model for P- and S-waves with different P (effective pressure). (a) P-wave velocity. (b) P-wave attenuation. (c) S-wave velocity. (d) S-wave attenuation.

The hydrate zones at Nankai Trough are located about 1,200 m below sea level. Nearly all of the natural gas hydrate accumulations identified in the Nankai Trough region occur at a depth less than 300 meters below the seafloor (1,240 meters below sea level and the ocean depth is about 945 m) (Matsushima 2006). Therefore, the effective pressure of 0.5 MPa is assumed and the detail information about the selection of effective pressure is shown as description of input parameters in Chapter 2. Before the implication of the Marin-Moreno model and the Guerin model to Nankai Trough, the effect of effective pressure (P) on velocity and attenuation is tested. As shown in Fig. 3.12, the P- (Fig. 3.12a) and S-wave (Fig. 3.12c) velocity increase with increasing effective pressure (P), while the P- (Fig. 3.12b) and S-wave (Fig. 3.12d) attenuations decrease with increasing effective pressure (P) (P from 0.1 to 5 MPa). Moreover, the changes of the attenuation due to changes of the effective pressure (from 0.1 to 5 MPa) are small compared with the absolute value of P- and S-wave attenuations. The same study for PSW3 is also conducted and the similar trends are observed (Fig. 3.13).

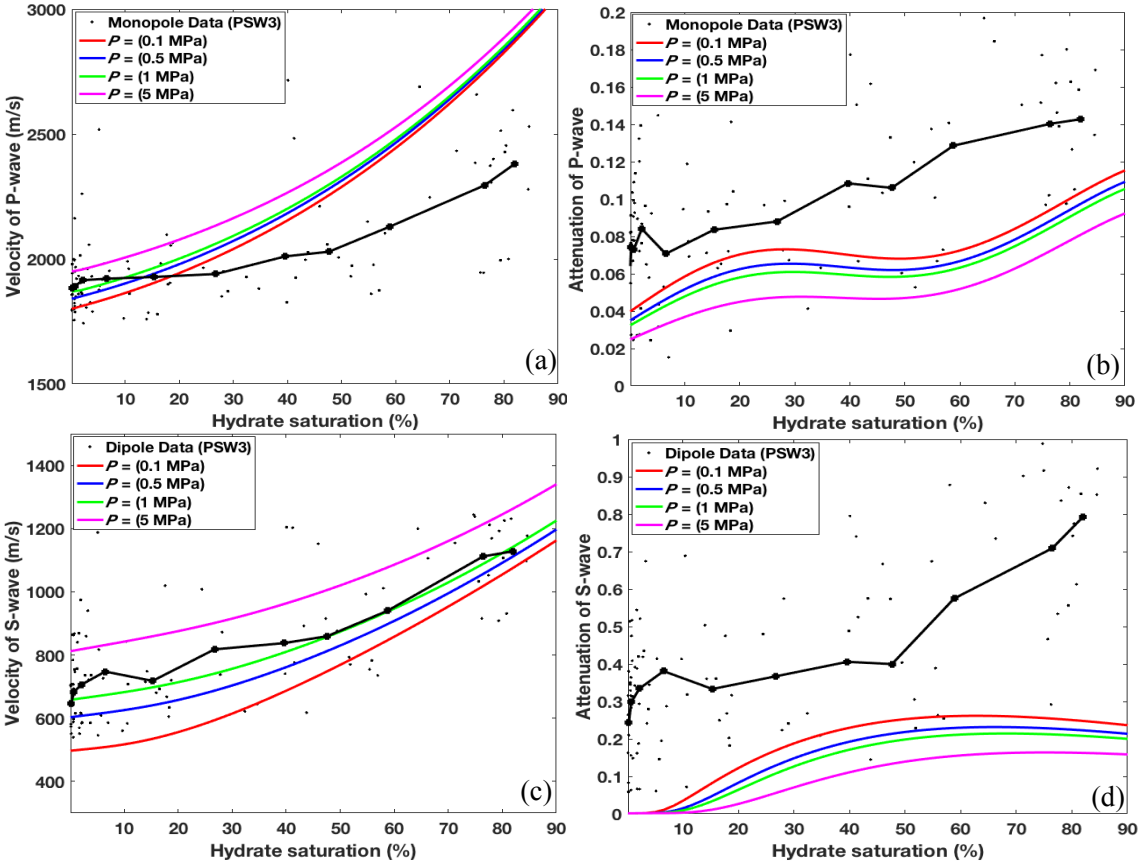

Figure 3. 13 Measured velocity and attenuation at PSW3 and those predicted by the Guerin model for P- and S-waves with different P (effective pressure). (a) P-wave velocity. (b) P-wave attenuation. (c) S-wave velocity. (d) S-wave attenuation.

3.4 Application of the Guerin model to sonic data

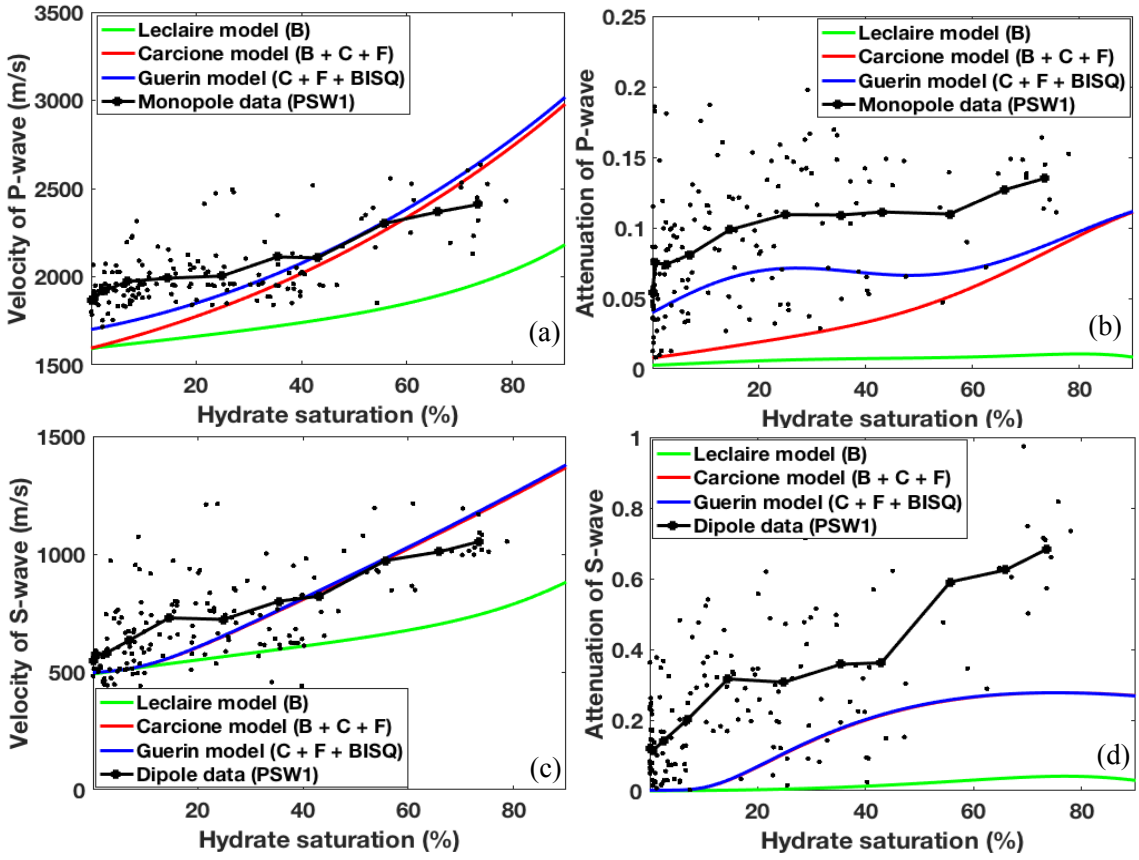

Figure 3. 14 Measured velocity and attenuation at PSW1 and those predicted by the Guerin model for P- and S-waves with different rock physics models. (a) P-wave velocity. (b) P-wave attenuation. (c) S-wave velocity. (d) S-wave attenuation.

For the Guerin model, "C" indicates cementation between hydrate and sand grains, "B" indicates the Biot flow, and "F" indicates the friction between the hydrate and sand grains, which was neglected in Carcione and Tinivella (2000) but is added in the calculation using the Carcione model. The "BISQ" indicates the Biot flow and the squirt flow. In Figs 3.14 and 3.15, the blue curve represents the predicted P-wave attenuation from the Guerin model, while the red curve represents attenuation from the Carcione model and the green curve represents attenuation from the Leclaire model.

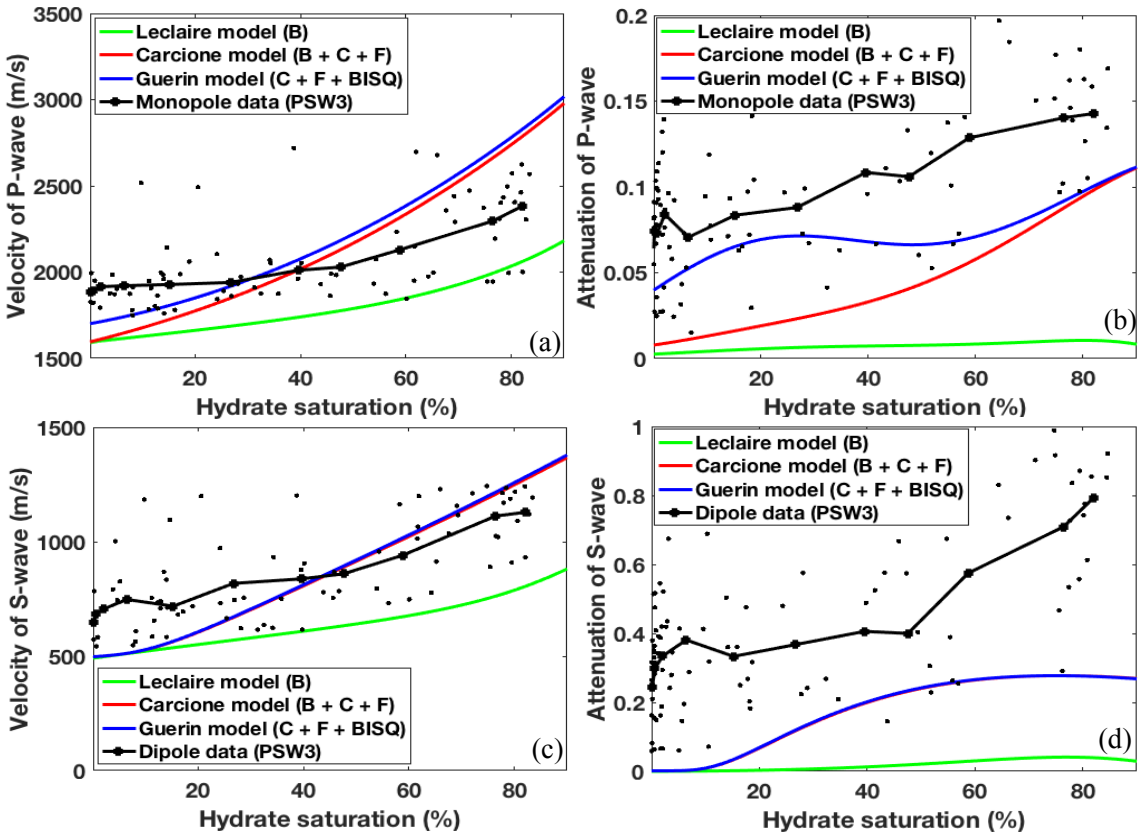

Figure 3. 15 Measured velocity and attenuation at PSW3 and those predicted by the Guerin model for P- and S-waves with different rock physics models. (a) P-wave velocity. (b) P-wave attenuation. (c) S-wave velocity. (d) S-wave attenuation.

The calculated theoretical results of S-wave using the Carcione model (red curves in Figs 3.14c and 3.14d) and the Guerin model (blue curves in Figs 3.14c and 3.14d) are the same because squirt flow has no effect on S-wave. In order to clarify the effect of the BISQ attenuation mechanism and friction between sand grains and hydrate, I modified the model proposed by Carcione & Tinivella (2000) to include the friction in the Carcione model. The P- (Fig. 3.14a) and S- (Fig. 3.14c) wave velocities calculated by the Carcione model (red curve) are significantly larger than that predicted by the Leclaire model (green curve), especially for higher hydrate saturation due to the cementation between sand grains and hydrate included in the Caricone model. The velocity predicted by the Guerin model (blue curve) and the Carcione model (red curve) agree with the averaged values (black fitting curve) better than that predicted by the Leclaire model (green curve). The P- (Fig. 3.14b) and S- (Fig. 3.14d) wave attenuation calculated by the Leclaire model (green curve) is obviously lower than averaged values (black fitting curve), implying the Biot flow cannot predict the P- and S-wave attenuations of MH-bearing sediments. In Fig. 3.14d, although the predicted S-wave attenuation by the Guerin model is still lower than measured sonic values, it is significantly larger than those predicted

by the Leclaire model (green curve). In Fig. 3.14b, the P-wave attenuation predicted by the Carcione model (red curve) is similar to the averaged values (black fitting curve) at larger hydrate saturation, while it is apparently lower than the averaged values (black fitting curve) at lower hydrate saturation than 50%. However, the P-wave attenuation predicted by the Guerin model (blue curve) significantly increases at lower hydrate saturation than 50%, and fits to the averaged values (black fitting curve) best. The same study for PSW3 is also conducted and the similar trends are also observed (Fig. 3.15).

3.5 Application of the Marin-Moreno model to sonic data

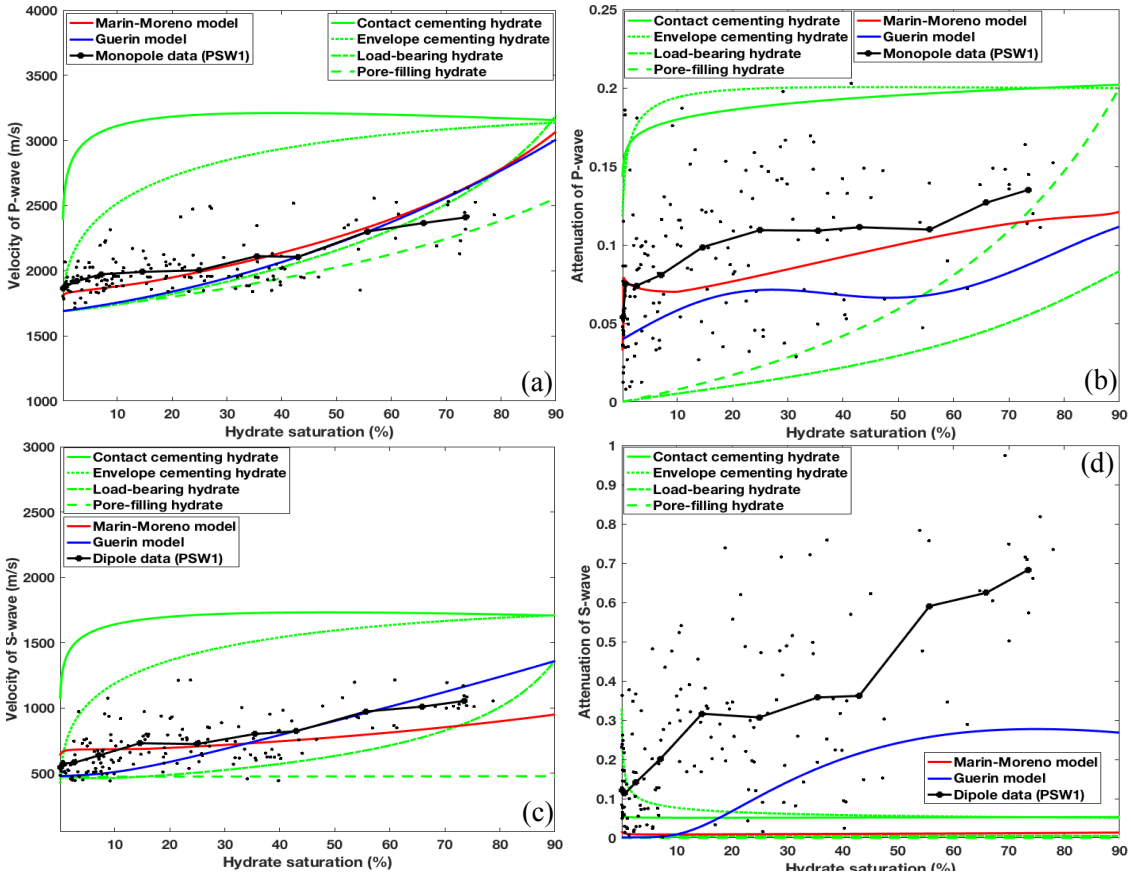

Figure 3. 16 Measured and predicted velocities and attenuations of P- and S-waves using the Marin-Moreno model and the Guerin model at PSW1: (a) P-wave velocity, (b) P-wave attenuation, (c) S-wave velocity, and (d) S-wave attenuation.

The velocity (Figs 3.16a and 3.16c) and attenuation (Figs 3.16b and 3.16d) of the P- and S-waves for MH-bearing sediments are predicted as a function of hydrate saturation. The red curve indicates the velocity predicted by the Marin-Moreno model, and the blue curve indicates the velocity predicted by the Guerin model. The predicted velocities of P- and S-waves include velocities based only on the presence of hydrate morphology (four types), indicated by green lines, the Marin-Moreno model

(contact cementing and pore-filling hydrate), and the Guerin model. In order to investigate the effects of hydrate morphology on velocity and attenuation, c_{pf} is assumed as 20% (pore-filling hydrate: 20%, contact cementing hydrate: 80%) when applying the Marin-Moreno model in this section.

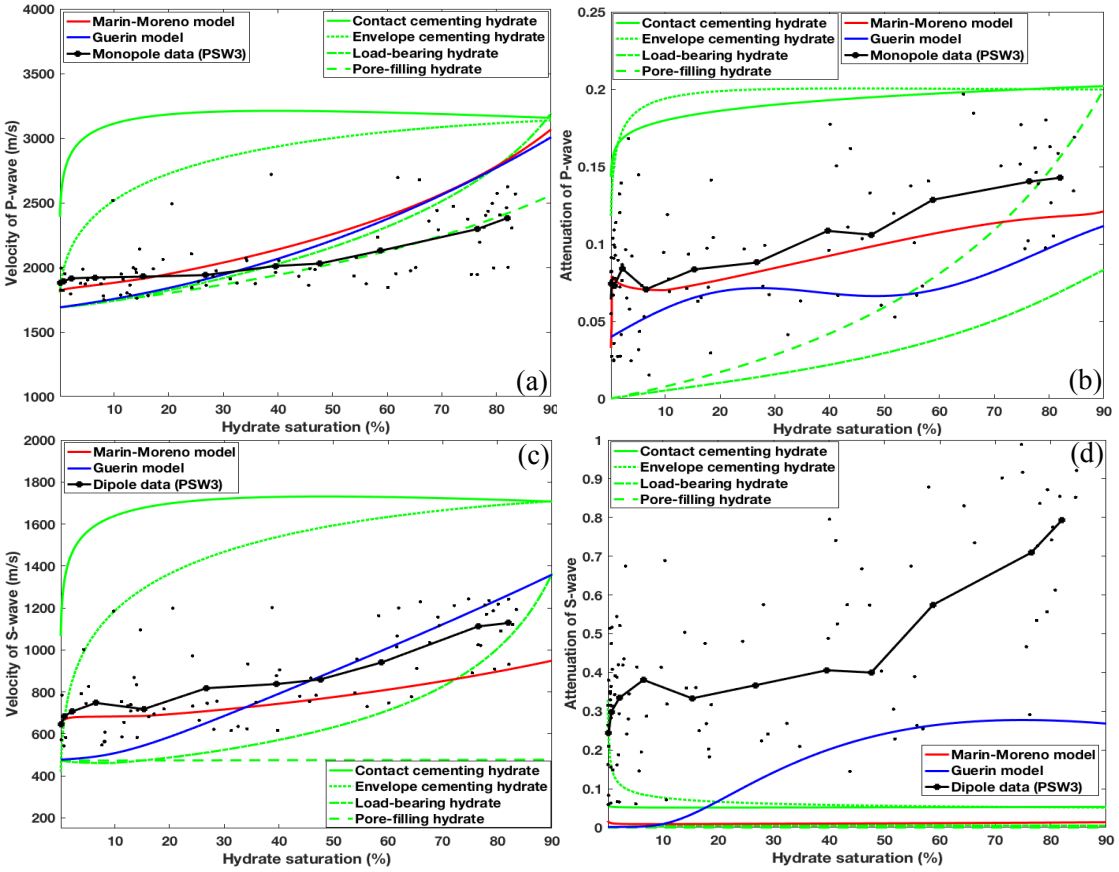

Figure 3. 17 Measured and predicted velocities and attenuations of P- and S-waves using the Marin-Moreno model and the Guerin model at PSW3: (a) P-wave velocity, (b) P-wave attenuation, (c) S-wave velocity, and (d) S-wave attenuation.

Then, the predicted curve is compared with the sonic velocity and attenuation of P- and S-waves. In Figs 3.16a and 3.16c, the velocity-versus-hydrate saturation curves calculated from the Marin-Moreno model based on different hydrate morphologies (green curves) indicate that the velocities of the P- and S-waves are strongly dependent on hydrate morphology. Contact cementing hydrate and envelope cementing hydrate increase the velocities of P- and S-waves dramatically at very low hydrate saturation, whereas load-bearing and pore-filling hydrate will increase the velocities at larger hydrate saturation. We can see that the predicted P- (Fig. 3.16a) and S-wave (Fig. 3.16c) velocities for sole presence of hydrate morphology as either higher (contact cementing and envelope cementing hydrate) or lower (load-bearing and pore-filling hydrate) than the average velocity of hydrate-bearing sediment for most levels of hydrate saturation. However, the predicted curve (red curves) for the

presence of multiple hydrate morphologies (Marin-Moreno model) successfully captures the trend of increasing average velocity (black curves) with increasing hydrate saturation for P- (Fig. 3.16a) and S-waves (Fig. 3.16c). The velocity values predicted by the Guerin model (blue curves) for the P- (Fig. Fig. 3.16a) and S-waves (Fig. Fig. 3.16c) are also plotted as a function of hydrate saturation. We can see that the P- and S-wave velocities calculated using the Guerin model are lower at lower hydrate saturation, and are higher at higher (than average) hydrate saturation (black curve). Moreover, the velocities predicted by the Guerin model (blue curves) are similar to those predicted by load-bearing hydrate morphology in the Marin-Moreno model (green dash-dotted lines). The reason for this similarity is possibly due to the assumption of suspended hydrate and the percolation model in the Guerin model.

In Figs 3.16b and 3.16d, the attenuation-versus-hydrate saturation curves calculated from the Marin-Moreno model based on different hydrate morphologies (green curves) also indicate that attenuation of the P-wave (Fig. 3.16b) is strongly dependent on hydrate morphology. The trend of P-wave attenuation curves (green lines) calculated from different hydrate morphologies is similar to the trends of velocity curves. In case of P-wave attenuation (Fig. 3.16b), the predicted attenuation for the presence of multiple hydrate morphologies by the Marin-Moreno model (red curve) appears to successfully capture the trend of increasing average attenuation (black curve) with increasing hydrate saturation. The predicted attenuation of the S-wave (Fig. 3.16d) at the sonic frequency (1,000 Hz) is extremely low, which is similar to the results predicted by Marín-Moreno et al. (2017) at the seismic frequency (200 Hz). The reason for this extremely low attenuation of the S-wave may be due to the friction loss between sand grains and the hydrate not being considered in the Marin-Moreno model. In Fig. 3.16b, the attenuations predicted by the Guerin model (blue curve) are lower than the average P-wave attenuation curve (black curve), and, as shown in Fig. 3.16d, the attenuations predicted by the Guerin model (blue curve) are also lower than the average S-wave attenuation curve (black curve). In Fig. 3.16d, comparing the S-wave attenuation predicted by the Marin-Moreno model (red curve) and the Guerin model (blue curve), the red curve is much lower than the average curve (black curve), whereas, to a certain extent, the blue curve captures the trend of the average S-wave attenuation. This can be explained by the following two considerations. First, the sonic attenuation for the S-wave at the Nankai Trough may have been overestimated, as discussed later herein. Second, Guerin and Goldberg (2005) attributed the S-wave attenuation at sonic frequency primarily to friction between sand and hydrate grains. The S-wave attenuation calculated using the Guerin model (blue curve), including this viscous friction, shows an obviously increasing S-wave attenuation with increasing hydrate saturation, whereas the Marin-Moreno model does not consider the friction between sand and hydrate grains. The same study is also conducted for PSW3 and similar trends can be observed (Fig. 3.17)

3.6 Discussion

Comparing the sonic attenuation estimates at the Nankai Trough with those at the Mallik field (Guerin & Goldberg, 2005), the S-wave attenuation at the Nankai Trough (maximum: 0.8) is significantly larger than that (maximum: 0.25) at the Mallik field. Suzuki and Matsushima (2013) indicated that the near-field effects in sonic attenuation estimates caused the possible overestimation of the S-wave attenuation. Moreover, they suggested that the scattering effects due to the thin hydrate-bearing layer and source-coupling effect between the source and the formation might contribute to the larger attenuation estimates, especially for the S-wave at the Nankai Trough. The larger average S-wave attenuation at sonic frequency band compared with the predicted values by the Marin-Moreno model (Figs 3.16d and 3.17d) and the Guerin model (Figs 3.14d and 3.15d) may be due to the overestimation of S-wave attenuation by Suzuki and Matsushima (2013). In addition, we should note the uncertainty of the comparison between the average and predicted attenuation because the average velocity and attenuation curves (Figs 3.1 through 3.17) are obtained from the scattered distribution of velocity and attenuation values calculated by Suzuki and Matsushima (2013). Furthermore, for sonic attenuation of P- and S-waves (Figs 3.1 and 3.2), when the hydrate saturation is zero, the attenuation is obviously nonzero. Even at the same hydrate saturation, the attenuation exhibits scattered values. In the Nankai Trough, MH-bearing sandy layers are very thin (< 1 m) and consist of light gray-to-olive gray unconsolidated fine-to-coarse-grained sand (Uchida et al., 2004). Therefore, I inferred that attenuation at zero hydrate saturation may be caused by squirt flow in clay or between sand and clay grains (Leurer, 1997; Marketos & Best, 2010). Although the Guerin model has taken into account the effect of the fraction of clay on effective sand permeability (also included in the implication of the Guerin model), this effect of permeability on attenuation should be different from the attenuation caused by squirt flow in clay or between sand and clay grains. In the future, the rock physical model will need to consider the attenuation caused by clay grains. The scattered distribution of measured velocity and attenuation (Figs 3.1 and 3.2) may be due to the diversity of the micro-distribution of hydrate, as discussed later.

3.6.1 Evidence of hydrate morphology at Nankai Trough

There are few researches on the hydrate morphology at Nankai Trough by using P- and S-wave velocities. Jin et al. (2016) indicated that the hydrate morphology of MH-bearing sediments in the Nankai Trough might be load-bearing morphology, and Jia et al. (2017) demonstrated that hydrate is attached to the grain surfaces of rock matrix rather than floating in pore space. Both Jin et al. (2016) and Jia et al. (2017) used P- and S-wave velocities to infer the hydrate morphology. Konno et al. (2015) measured P-wave velocities of pressure cores near in situ pressure, and their measurements prevent MH from dissociating. They indicated that the measured P-wave velocities agree well with

predicted velocities for load-bearing hydrate morphology. As shown in Figs 3.16a and 3.16c, we also can find that the average P- and S-wave velocities from sonic data are similar to values predicted from the load-bearing hydrate morphology based on the Marin-Moreno model. However, we can also find that P- and S-wave velocities and attenuations estimated from sonic data perform an extremely scattered distribution (Figs 3.1 and 3.2). Moreover, the upper limit (contact or envelope cementing hydrate) and lower limit (pore-filling hydrate) restrict the scattered distribution of the field P-wave velocity (Fig. 3.16a), the S-wave velocity (Fig. 3.16c) and the P-wave attenuation (Fig. 3.16b). This implies the diversity of hydrate morphology of the MH-bearing sediment in the Nankai Trough. So I carefully infer that the natural hydrate morphology behaves diversity rather than make a clear definition on hydrate morphology at Nankai Trough, and thus different from previous studies I make an assumption of the multiple hydrate morphologies (contact cementing and pore-filling hydrate).

In addition to the velocity of P- and S-waves, P-wave attenuation is firstly applied to infer hydrate morphology. In Fig. 3.16b, the P-wave attenuation (red curve) predicted by the Marin-Moreno model assuming the presence of multiple hydrate morphologies appears to agree with the measured data (black curve) better than any individual hydrate morphology. Figure 3.16b also provides evidence of the effect of hydrate morphology on P-wave attenuation. Assuming the pore-filling hydrate component is 20% (the majority of hydrate is contact cementing hydrate) may reflect the nature of hydrate morphology at lower hydrate saturation (Priest et al., 2006; Bu et al., 2017). Yun et al. (2005) also indicated that the hydrate formation mechanism followed neither a pure cementation model nor a pure pore-filling model at the microscale and hydrate began to interact with the granular skeleton only at hydrate concentration higher than 40%.

3.6.2 P-wave attenuation mechanisms at sonic frequency domain

The Marin-Moreno model assumes a squirt flow caused by fluid inclusion in a microporous hydrate (see Fig. 2.2), whereas the Guerin model assumes a squirt flow due to the fluid flow in pore spaces between hydrate grains and pore spaces between sand grains (see Fig. 2.5). Fig. 3.16b indicates that the attenuation curve predicted by the Marin-Moreno model (red curve) appears to best match the average P-wave attenuation obtained from sonic data. This means that the squirt flow due to fluid inclusion in a microporous hydrate may be a reasonable attenuation mechanism for the P-wave attenuation in the sonic frequency band in the Nankai Trough. On the other hand, as shown in Figs 3.15b and 3.16b, for the Guerin model, the BISQ mechanism in the pore space between hydrate grains and pore spaces between solid grains dominates the P-wave attenuation at lower hydrate saturation and maybe another attenuation mechanism for the P-wave at sonic frequency band. More evidence is required in order to determine whether the mechanism responsible for P-wave attenuation is squirt flow in microporous hydrate or the BISQ mechanism in pore spaces between hydrate grains and pore

spaces between solid grains. The presence of microporous hydrate has been observed by scanning electron microscopy (Kuhs et al., 2004). However, there is still a lack of evidence for hydrate-bearing sediments in the Nankai Trough. Anyhow, in consideration of the performance of the application of the Marin-Moreno model and the Guerin model to sonic data, I infer that squirt flow due to the formation of hydrate may be the dominant mechanism of P-wave attenuation in the sonic frequency range.

3.6.3 S-wave attenuation mechanisms at sonic frequency domain

Attenuation caused by friction remains a subject of debate. Johnston et al. (1979) indicated that friction on thin cracks and grain boundaries is the dominant attenuation mechanism for consolidated rocks under most conditions in their ultrasonic frequency range. Winkler et al. (1982) reported that frictional sliding is not a significant source of seismic attenuation in situ because the strain caused by seismic wave propagation is extremely low. Murphy et al. (1982) also reported similar results. However, Guerin & Goldberg (2005) suggested that the friction loss between solid grains and hydrate is the dominant component of energy loss because the interaction between hydrate and solid grains is similar to the viscous friction of fluid, which is fundamentally different from the intergranular interaction. Fig 3.15d indicates that the BISQ mechanism (the difference between the Carcione model and the Guerin model) is negligible for attenuation of S-wave, and the dominant attenuation mechanism is friction between sand grains and hydrate (the difference between the Carcione model and the Leclaire model). In addition, the Marin-Moreno model, which does not consider the friction between solid grains and hydrate, provides extremely low attenuation of S-wave, as shown in Figs 3.16d and 3.17d, whereas the Guerin model including this attenuation mechanism provides attenuation comparable to the sonic attenuation of S-wave. Therefore, I believe that the responsible attenuation mechanism for S-wave at sonic frequency domain is viscous friction between solid grains and hydrate in the Guerin model.

3.7 Conclusion of this chapter

In the application of two different rock physics models (the Marin-Moreno and Guerin models), the sensitivity analysis of input parameters shows best parameters setting for the application of rock physics models at sonic frequency domain: c_i of 0.3, α of 0.0004, P of 0.5MPa, and η of 0.001-0.0018 Pa s. This parameters setting might provide insight into the selection of input parameters when transplanting these rock physics models to other geologic environments.

Unlike previous inference on hydrate morphology at Nankai Trough based on sole hydrate morphology, two factors are considered firstly: (1) multiple hydrate morphology (contact cementing

and pore-filling hydrate morphology) and (2) effect of hydrate morphology on P-wave attenuation, then demonstrated the diversity of distribution of hydrate morphology at Nankai Trough. The rock physics modeling of P- and S-wave velocity and P-wave attenuation indicate that multiple hydrate morphologies (contact cementing and pore-filling hydrate morphology) might be the possible hydrate morphology at Nankai Trough.

In terms of P-wave attenuation in the sonic frequency range, two types of squirt flow may be dominant attenuation mechanisms: 1) squirt flow due to fluid inclusion in a microporous hydrate and 2) the Biot-squirt (BISQ) mechanism in pore spaces between hydrate grains and pore spaces between solid grains.

In terms of S-wave attenuation in the sonic frequency range, the friction between hydrate and solid grains is possible the dominant attenuation mechanism for S-wave.

CHAPTER 4. FREQUENCY DEPENDENT P- AND S-WAVE ATTENUATION AT NANKAI TROUGH: FROM VSP AND SONIC LOG DATA

Based on the application of the Marin-Moreno model and the Guerin model to sonic and VSP data at the Nankai Trough, the possibly dominated attenuation mechanisms for P- and S-wave attenuations in MH-bearing sediments at seismic frequency domain are discussed. The possible explanation for the frequency-dependent attenuation in the VSP to sonic frequency range is also discussed.

4.1 Introduction

In contrast to high attenuation at sonic frequencies in MH-bearing sediments, attenuation at seismic frequencies (typically 10 to 150 Hz) is more contentious in existing studies (Matsushima, 2006; Bellefleur et al., 2007; Rossi et al., 2007). No significant increased attenuation of P-waves has been observed in crosswell seismic data (20 to 150 Hz) (Wood et al. 2000), at the VSP frequency (30 to 110 Hz) (Matsushima, 2006; Matsushima et al., 2016), or at the seismic frequency (10 to 45 Hz) (Nittala et al., 2017), and no attenuation of P-waves has been observed in ocean bottom seismographs (OBSs) data (20 to 200 Hz) (Rossi et al., 2007; Madrussani et al., 2010) or from predicted values at about 30 Hz (Gei & Carcione, 2003). In contrast, significantly increased attenuation of P-waves is observed in resonant column laboratory measurements (< 550 Hz) (Priest et al., 2006; Best et al., 2013), VSP data (10 to 200 Hz) (Dvorkin & Uden, 2004; Bellefleur et al., 2007), and crosshole seismic data (100 to 1,000 Hz) (Bauer et al., 2008). In order to solve the controversy associated with attenuation at seismic frequencies, it is necessary to elucidate the attenuation mechanisms responsible for the broadband frequency response in MH-bearing sediments.

Previous studies have shown that the existence of MH results in high S-wave velocity and attenuation in MH-bearing sediments at sonic frequencies domain (Guerin & Goldberg, 2005; Suzuki & Matsushima, 2013). In the eastern Nankai Trough, the S-wave attenuation also shows a significant increase in MH-bearing sediments at sonic frequency domain (0.5 to 1 kHz) (Suzuki & Matsushima, 2013). Although S-wave attenuation at MH-bearing sediments is estimated in the past studies, there are few examples to estimate S-wave attenuation at seismic frequencies so far. In order to develop a reasonable attenuation mechanism for S-wave in MH-bearing sediments, it is important to obtain S-wave attenuation at various frequencies. Matsushima (2015) used walkaway vertical seismic profile (w-VSP) from the Nankai Trough to derive the S-wave attenuation in MH-bearing sediments at seismic frequencies (30 to 100 Hz) by using centroid frequency shift method.

The proposed attenuation mechanisms associated with MH-bearing sediments include global Biot and local squirt flow in MH-bearing sediments (Guerin & Goldberg, 2005; Best et al., 2013; Marín-Moreno et al., 2017), cementation and frictional loss between hydrate and solid grain (Guerin & Goldberg, 2005), mesoscale wave-induced fluid flow (Tisato & Quintal, 2013; Mikhaltsevitch et al., 2014), the effect of hydrate morphology on attenuation (Priest et al., 2006; Best et al., 2013; Marín-Moreno et al., 2017), and gas bubble damping (Marín-Moreno et al., 2017). In addition, other factors may cause frequency-dependent attenuation for MH-bearing sediments, including differences in source coupling efficiency to the surrounding medium inside fluid-filled boreholes between VSP and sonic logging measurement (Lee & Waite, 2007), the thickness of the hydrate zone, the uncertainty caused by windowing effects or choosing reference when applying attenuation estimation methods, differences in geologic environments (Jaiswal et al., 2012), and scattering attenuation from large- and small-scale heterogeneities (Huang et al., 2009). In the Nankai Trough, attenuation of MH-bearing sediments are observed through a stable estimation method for sonic data (Suzuki & Matsushima, 2013) and zero-offset VSP data (Matsushima et al., 2016). However, the attenuation mechanisms responsible for the attenuation values in the frequency range from VSP to sonic data have not yet been fully clarified.

4.2 Description of field VSP and walkaway VSP data

Matsushima et al. (2016) provided a stable P-wave attenuation profile at PSW1 for MH-bearing zones by combining seismic interferometry and the modified median frequency shift method at VSP frequency domain (Fig. 1.8f). The P-wave attenuation profile at PSW3 (Fig. 1.9f) based on the same method proposed by Matsushima et al. (2016) is also shown in this study. About the up-scaling process, in order to compare the sonic data with VSP data, I have to up-scale the sonic data at sonic wavelength into VSP wavelength. The sonic hydrate saturation is arithmetically averaged with a sliding window (the length of window is about VSP wavelength), and then sample 1 and 2 (PSW1 and PSW3) are chosen to compare with average sonic data. The averaged hydrate saturations of sample 1 and 2 at PSW1 (Fig. 1.8) are 1.7% and 13.7% with corresponding P-wave attenuation of 0.05 and 0.07, while at PSW3 (Fig. 1.9) are 15.8% and 17.0% with corresponding P-wave attenuation of – 0.043 and 0.02. The same up-scaling process is conducted for w-VSP data, and then the averaged hydrate saturations of 3.4% and 3.1% with corresponding S-wave attenuations of 0.04 and 0.05 are obtained.

To make a summary, the P-wave attenuation (VSP data) and S-wave attenuation (w-VSP data) obtained from the Nankai Trough are shown as in Table 4.1.

Table 4. 1 P- and S- wave attenuations at seismic frequency (30 – 110 Hz) at Nankai Trough

	Hydrate saturation	Attenuation
PSW1 (VSP)	1.7%	0.05
	13.7%	0.07
PSW3 (VSP)	15.8%	–0.043
	17.0%	0.02
Main well (w-VSP)	3.4%	0.04
	3.1%	0.05

4.3 Application of rock physics models to sonic and VSP data

4.3.1 Application of the Marin-Moreno model to sonic and VSP data

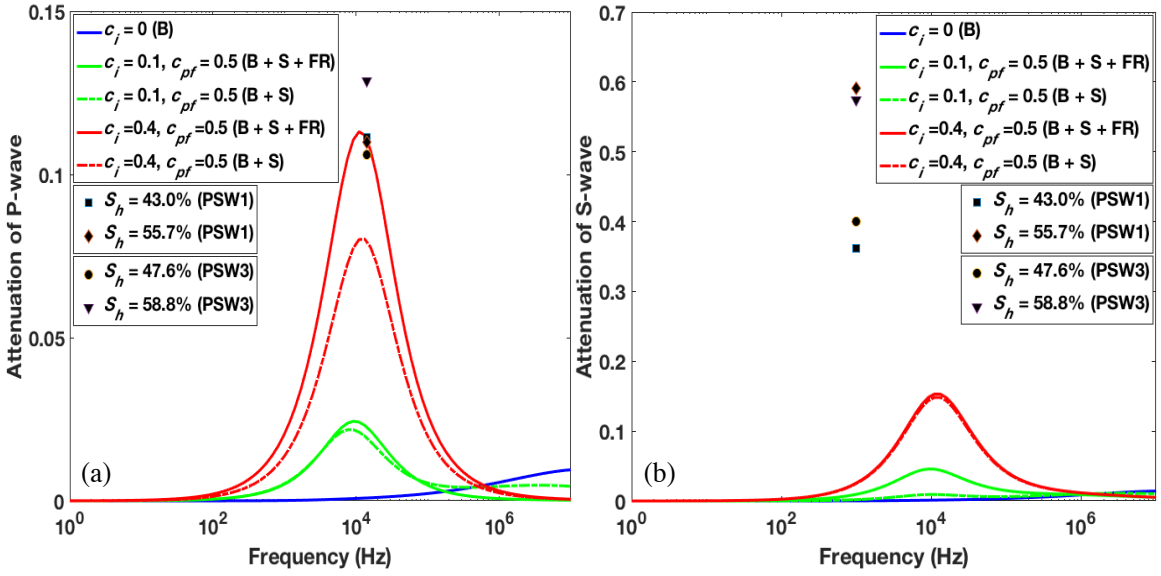

Figure 4. 1 Measured attenuation and attenuation predicted by the Marin-Moreno model for P- and S-waves as a function of frequency (S_h = 50%): (a) P-wave attenuation, (b) S-wave attenuation.

In order to investigate the frequency-dependent attenuation, the Marin-Moreno model is used to predict attenuation in a broadband frequency. For possible attenuation mechanisms, the implication of the Marin-Moreno model considers the effect of the frame viscoelasticity of the hydrate, squirt flow in a microporous hydrate, and the global Biot flow. Assuming $c_i = 0$ in the Marin-Moreno model indicates that only the Biot flow is considered, that is indicated by "B" (see the blue curves in Figs

4.1a and 4.1b). In Fig 4.1a, we can see that Biot flow ($c_i = 0$) is dominant, especially for P-waves in the ultrasonic frequency band (> 10^6 Hz). Then, we can make the complex bulk and shear moduli of the contact cementing hydrate real and substitute these moduli into the hydrate contact model. The attenuation predicted in this case has no effect on the frame viscoelasticity of the hydrate, and is plotted as red and green dotted curves in Figs 4.1a and 4.1b. The red and green solid curves represent the final attenuation, including the global Biot flow ("B"), the effect of the frame viscoelasticity of the hydrate (abbreviated as "FR"), and the squirt flow in a microporous hydrate (abbreviated as "S") at various inclusion concentrations (c_i) (0.1 and 0.4). In Fig. 4.1a, comparison of the red (green) solid curve and red (green) dotted curve reveals that the squirt flow in a microporous hydrate ("S") is dominant for P-wave attenuation from 10^2 to 10^6 Hz. The effect of the frame viscoelasticity of the hydrate ("FR") on P-wave attenuation from 10^2 to 10^6 Hz is significantly smaller than the effect of squirt flow in a microporous hydrate. In Fig. 4.1b, the S-wave attenuation (red and green curves) has a similar frequency response to the P-wave attenuation. This is because the shear modulus of the effective hydrate grains is negative when applying the effective medium model because the non-interaction assumption for higher inclusion concentration is violated (Kuster & Toksoz, 1974). In such a situation, the complex shear modulus of effective hydrate with fluid inclusion is substituted by the real shear modulus of hydrate. Therefore, the final attenuation for the S-wave reflects the effect of the complex bulk modulus of the effective grain. As a result, P- and S-wave attenuations show similar frequency responses.

In Fig. 4.1, four samples with hydrate saturations of 43.0% and 55.7% for PSW1 and 47.6% and 58.8% for PSW3 are compared with the predicted attenuation at hydrate saturation of 50% based on the Marin-Moreno model (red curve). The average sonic attenuation values at hydrate saturations of 43.0% and 55.7% (PSW1), and 47.6% and 58.8% (PSW3) are plotted at corresponding frequencies: 14,000 Hz for the P-wave and 1,000 Hz for the S-wave. In Fig. 4.1a, the predicted P-wave attenuation (red curve) agrees well with the average attenuation, whereas in Fig. 4.1b the predicted S-wave attenuation is lower (red curve) than the average S-wave attenuation.

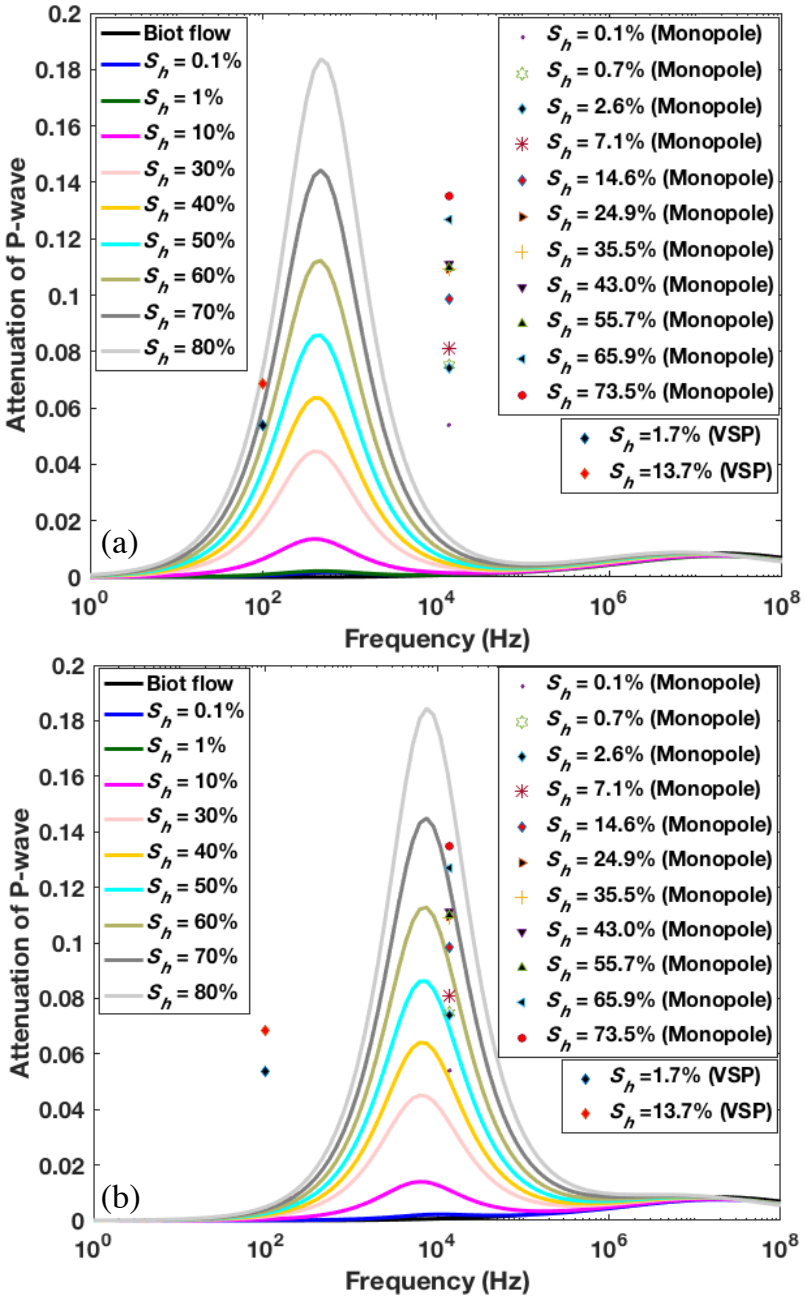

Figure 4. 2 Measured attenuation at PSW1 and attenuation predicted by the Marin-Moreno model for the P-wave as a function of frequency (c_{pf} =80%): (a) P-wave attenuation (α = 0.0001) and (b) P-wave attenuation (α = 0.0004). Except for α, the parameters are the same between (a) and (b). The curves represented by various colors (from black to grey) are the predicted P-wave attenuations by the Marin-Moreno model, while the various color dots at a frequency of 1, 4000 Hz represent the measured P-wave attenuations calculated from monopole sonic data, and the orange and blue diamonds at a frequency of 100 Hz represent the measured P-wave attenuations calculated from VSP data.

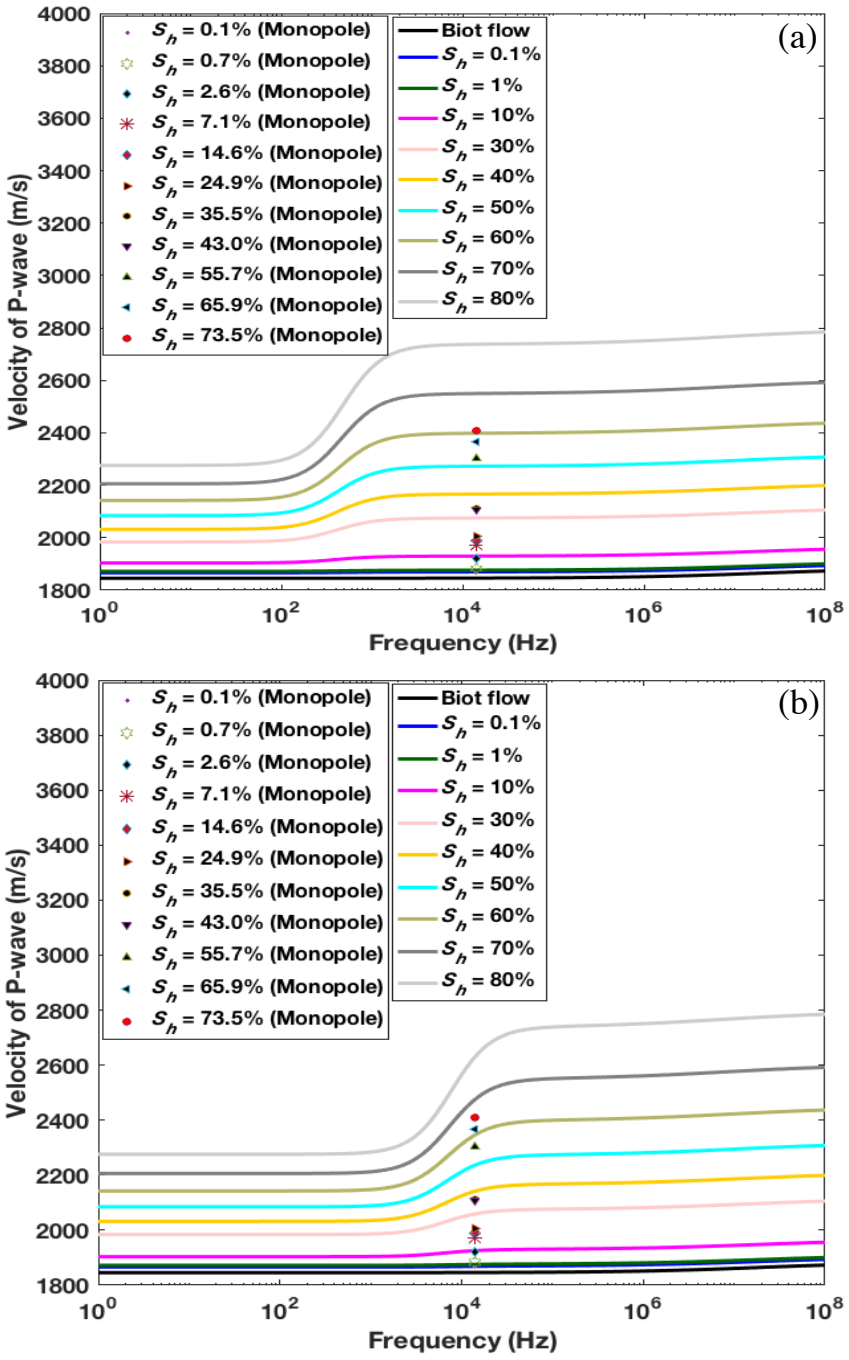

Figure 4. 3 Measured velocity at PSW1 and velocity predicted by the Marin-Moreno model for the P-wave as a function of frequency (c_{pf} =80%): (a) P-wave velocity (α = 0.0001) and (b) P-wave velocity (α = 0.0004). Except for α, the parameters are the same between (a) and (b). The curves represented by various colors (from black to grey) are the predicted P-wave velocities by the Marin-Moreno model, while the various color dots at a frequency of 1, 4000 Hz represent the measured P-wave velocities calculated from monopole sonic data.

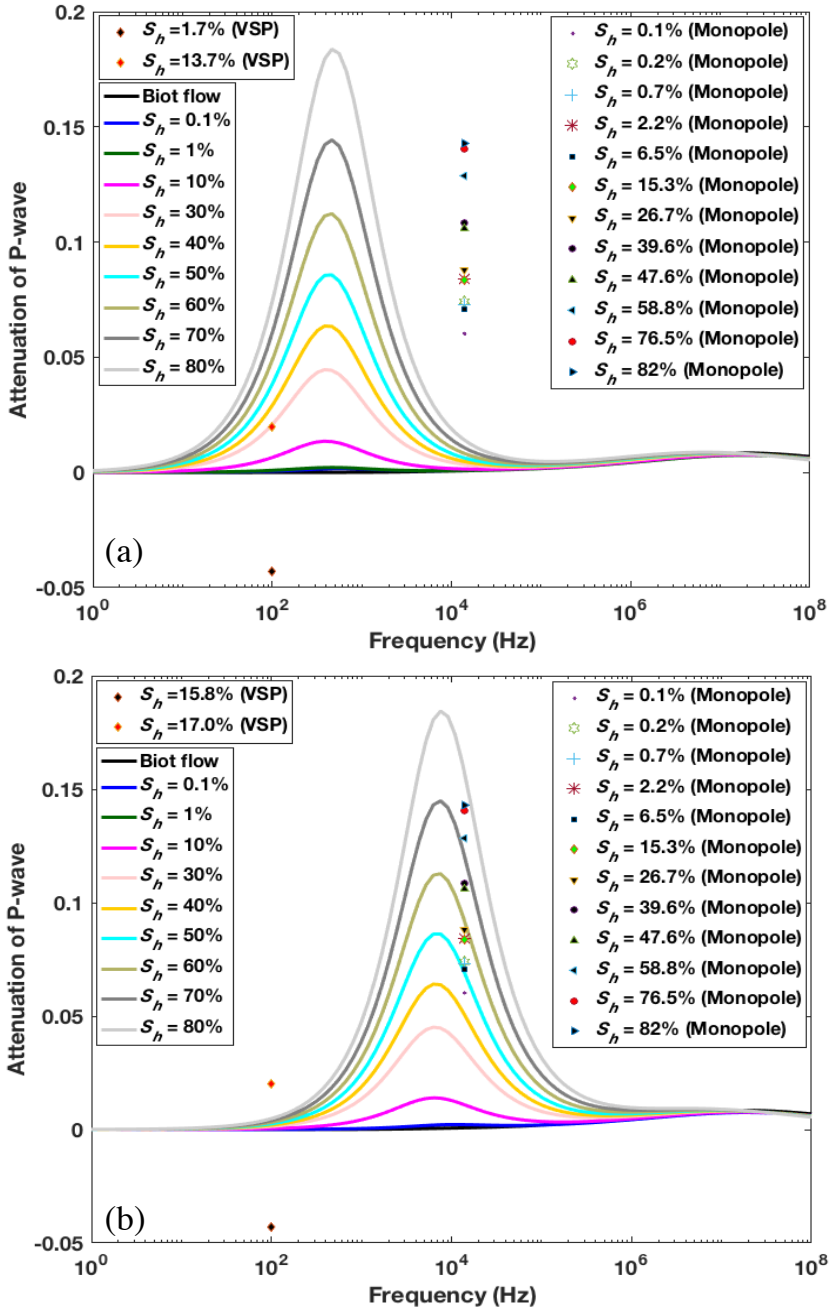

Figure 4. 4 Measured attenuation at PSW3 and attenuation predicted by the Marin-Moreno model for the P-wave as a function of frequency (c_{pf} =80%): (a) P-wave attenuation (α = 0.0001) and (b) P-wave attenuation (α = 0.0004). Except for α, the parameters are the same between (a) and (b). The curves represented by various colors (from black to grey) are the predicted P-wave attenuations by the Marin-Moreno model, while the various color dots at a frequency of 1, 4000 Hz represent the measured P-wave attenuations calculated from monopole sonic data, and the orange and blue diamonds at a frequency of 100 Hz represent the measured P-wave attenuations calculated from VSP data.

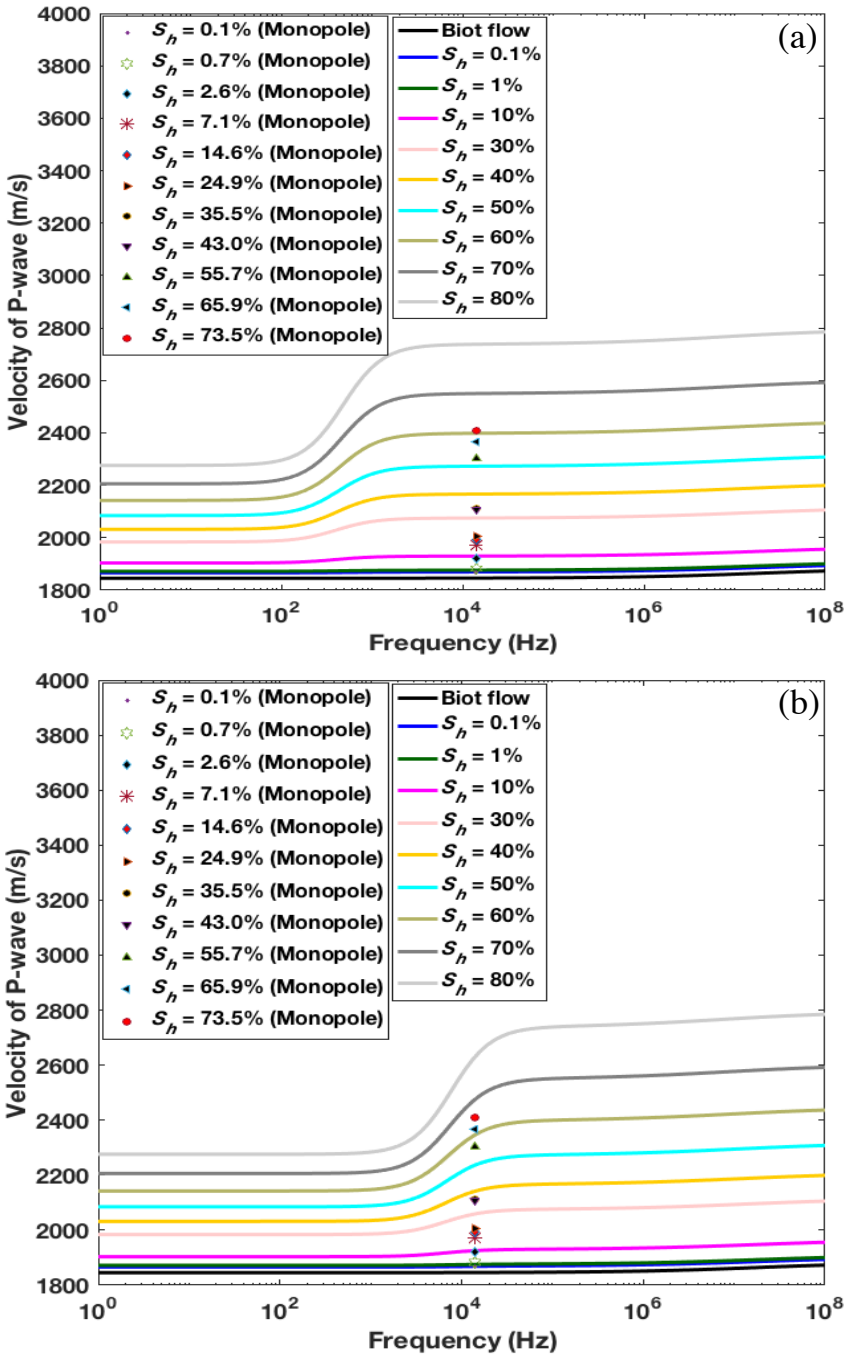

Figure 4. 5 Measured velocity at PSW3 and velocity predicted by the Marin-Moreno model for the P-wave as a function of frequency (c_{pf} =80%): (a) P-wave velocity (α = 0.0001) and (b) P-wave velocity (α = 0.0004). Except for α, the parameters are the same between (a) and (b). The curves represented by various colors (from black to grey) are the predicted P-wave velocities by the Marin-Moreno model, while the various color dots at a frequency of 1, 4000 Hz represent the measured P-wave velocities calculated from monopole sonic data.

Applying the Marin-Moreno model, the attenuation responses at various hydrate saturations are calculated as a function of frequency for comparison with the sonic and VSP attenuations (Fig. 4.2). In addition to sonic attenuation, two samples of VSP attenuation from Zones C and D are plotted in Figs 4.2a and 4.2b. In Fig. 4.2b, the squirt flow in a microporous hydrate results in significant P-wave attenuation from 10^2 to 10^6 Hz, and the predicted attenuation caused by squirt flow increases with increasing hydrate saturation. If c_{pf} is assumed as 80% (i.e., the majority of hydrate is pore-filling hydrate) (Fig. 4.2), the predicted P-wave attenuation exhibits better agreement with the average sonic attenuation when the hydrate saturation exceeds 60%, whereas the predicted P-wave attenuation obviously lower than the average sonic attenuation when the hydrate saturation smaller than 60%. Fig. 4.3b shows an obvious velocity dispersion zone corresponding to the attenuation peak in Fig. 4.2b. The attenuation peak caused by squirt flow is associated with greater velocity dispersion, whereas the lower attenuation due to Biot flow is related to smaller velocity dispersion. As shown in Fig. 4.3b, the predicted velocity at most hydrate saturations appears to agree with the average sonic P-wave velocity.

In order to investigate possible attenuation mechanisms responsible for VSP attenuation, the VSP attenuations at hydrate saturations of 1.7% and 13.7% (Fig. 1.8f) are compared with the predicted attenuation based on the Marin-Moreno model. In Fig. 4.2a, the VSP attenuation is 0.05 at a hydrate saturation of 1.7% and is 0.07 at a hydrate saturation of 13.7%. Parameters other than the aspect ratio of inclusion (α) remain unchanged between Figs 4.2a and 4.2b. The aspect ratio of fluid inclusion (α) is set to be 0.0001 in Fig. 4.2a and 0.0004 in Fig. 4.2b. Comparing Figs 4.2a and 4.2b reveals that the attenuation peak due primarily to squirt flow in a microporous hydrate moves to a higher frequency (from 10 to 10^5 Hz) with increasing α. Fig. 4.2a shows that, although two samples of VSP attenuation are larger than the predicted values at the corresponding hydrate saturations (green and pink curves), the VSP attenuation is comparable to that predicted at a frequency near 100 Hz. Fig. 4.3a also shows the velocity dispersion zone corresponding to the attenuation peak at a frequency near 100 Hz, and the predicted velocity is greater than the average sonic velocity. Comparing Figs 4.2a and 4.2b reveals that attenuation primarily due to squirt flow in a microporous hydrate is dominant at different frequency bands and depends significantly on the aspect ratio of inclusion (α), whereas the global Biot flow is dominant at frequencies greater than 10^6 Hz. When α is 0.0001, the predicted attenuation appears to agree with the VSP attenuation near 100 Hz, and, when α is 0.0004, the predicted attenuation appears to agree with the sonic attenuation near 14,000 Hz.

Similar to PSW1, the same study is conducted for PSW3, and then the P-wave attenuation (Fig. 4.4) and velocity (Fig. 4.5) are predicted by the Marin-Moreno model as a function of frequency. The VSP attenuations at hydrate saturations of 15.8% and 17.0% (Fig. 1.9f) are compared with the predicted attenuation based on the Marin-Moreno model. In Fig. 4.4, the VSP attenuation is – 0.043 at

a hydrate saturation of 15.8% and is 0.02 at a hydrate saturation of 17.0%. The similar results to those for PSW1 are obtained. However, we should note that there is a negative VSP value (– 0.043), which is counterintuitive but usually presents in the attenuation estimation at seismic frequency domain. These negative values maybe interpreted as a very small attenuation (Winkler & Nur, 1982b), or the scattering effect caused by the elastic heterogeneities (Yang et al., 2007).

4.3.2 Application of the Guerin model to sonic and VSP data

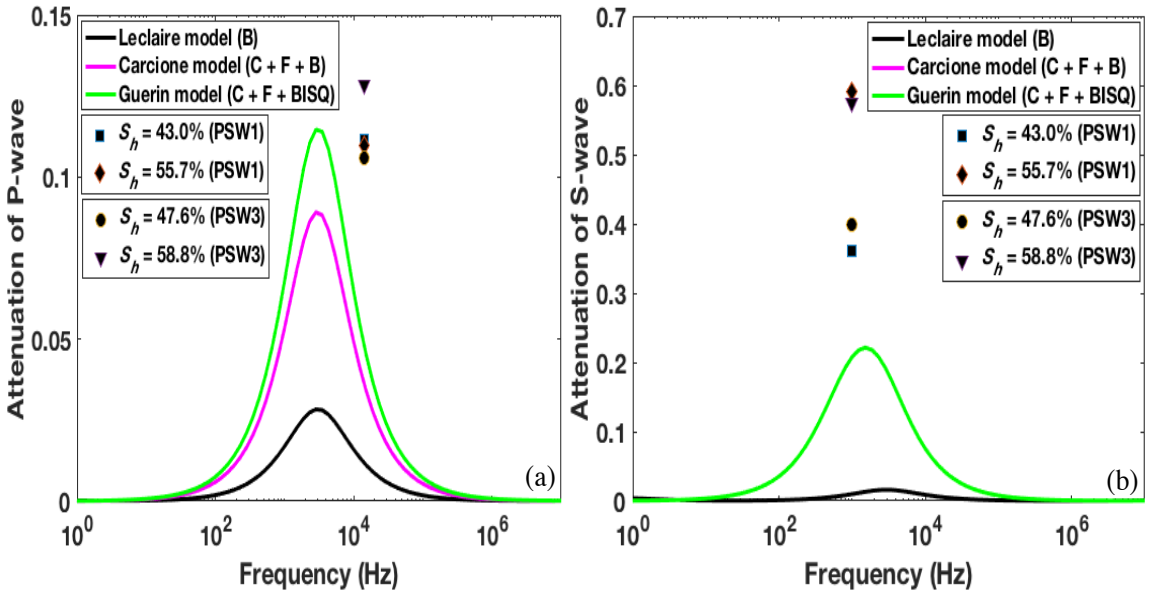

Figure 4. 6 Measured attenuation and attenuation predicted by the Guerin model for P- and S-waves as a function of frequency (S_h = 50%): (a) P-wave attenuation, and (b) S-wave attenuation. The theoretical results calculated using the Carcione model and the Guerin model are the same because squirt flow has no effect on the attenuation of S-waves.

For the Guerin model, "C" indicates cementation, "B" indicates Biot flow, and "F" indicates the friction between the hydrate and sand grains, which was neglected in Carcione and Tinivella (2000) but is added in my calculation using the Carcione model. In Fig. 4.6a, the green curve represents the predicted P-wave attenuation from the Guerin model, while the pink curve represents that from the Carcione model and the black curve represents that from the Leclaire model. The square and diamond at a frequency of 1, 4000 Hz represent the measured P-wave attenuations calculated from monopole sonic data at hydrate saturations of 43.0% and 55.7% for PSW1, and 47.6% and 58.8% for PSW3 respectively. It is the same for S-wave (Fig. 4.6b), but the measured S-wave attenuations from dipole sonic data are plotted at a frequency of 1, 000 Hz. By comparing the attenuation calculated using the Leclaire model and the Carcione model (Figs 4.6a and 4.6b), the friction between the hydrate and solid grains is found to dominate at frequencies between 10^2 and 10^5 Hz for both P- and S-waves at a

hydrate saturation of 50%. Figs 4.6a and 4.6b also indicate that the BISQ attenuation in hydrate and sand grains has a significant effect on P-wave attenuation from 10^2 to 10^5 Hz. As shown in Fig. 4.6b, the squirt flow has no effect on S-wave attenuation because the S-wave attenuation calculated using the Carcione model (red curve) completely corresponds to that calculated using the Guerin model (green curve). Comparing the attenuation predicted by the Guerin model (red curve) at a hydrate saturation of 50% with the average sonic attenuation at a hydrate saturation of approximately 50% for P- (Fig. 4.6a) and S-waves (Fig. 4.6b), the predicted attenuation is lower than the average sonic attenuation.

Applying the Guerin model, the attenuation responses at various hydrate saturations for two initial sand/hydrate permeability pairs are calculated as a function of frequency for comparison with the sonic and VSP attenuations (Fig. 4.7). Essentially, the attenuation curve predicted by the Guerin model is attributed to two separate BISQ attenuations: the attenuation in sand grains and the attenuation in hydrate grains. These two BISQ attenuation mechanisms may act individually (Fig. 4.7a) or together (Fig. 4.7b) by specifically selecting different initial permeabilities of sand and hydrate grains. The initial sand permeability (k_{s0}) in Fig. 4.7a is larger than that in Fig. 4.7b, while the other parameters remain unchanged. Comparing Figs 4.7a and 4.7b reveals that a larger permeability generates an attenuation peak in a lower frequency range of from 1 to 10^2 Hz. As shown in Fig. 4.7a, the VSP attenuations at hydrate saturations of 1.7% and 13.7% are close to the predicted attenuation at a hydrate saturation of 10% (black curve). We can also see that the VSP attenuation can be partly explained by the BISQ mechanism in sand grains when applying this parameter setting, as shown in Fig. 4.7a. Fig. 4.8 shows the P-wave velocity dispersion corresponding to the attenuation in Fig. 4.7. Fig. 4.8 shows that the attenuation peaks correspond to the largest velocity dispersion in the same frequency zones. The larger attenuation peak corresponds to larger velocity dispersion, and no attenuation change corresponds to no velocity dispersion. At hydrate saturations of less than 20%, the predicted velocity is lower than the measured velocity, and at a hydrate saturation of greater than 60% the predicted velocity is larger than the measured velocity. Similar to PSW1, the same study is conducted for PSW3, and then the P-wave velocity (Fig. 4.9) and attenuation (Fig. 4.10) are predicted by the Guerin model as a function of frequency. We can get the similar results to those for PSW1.

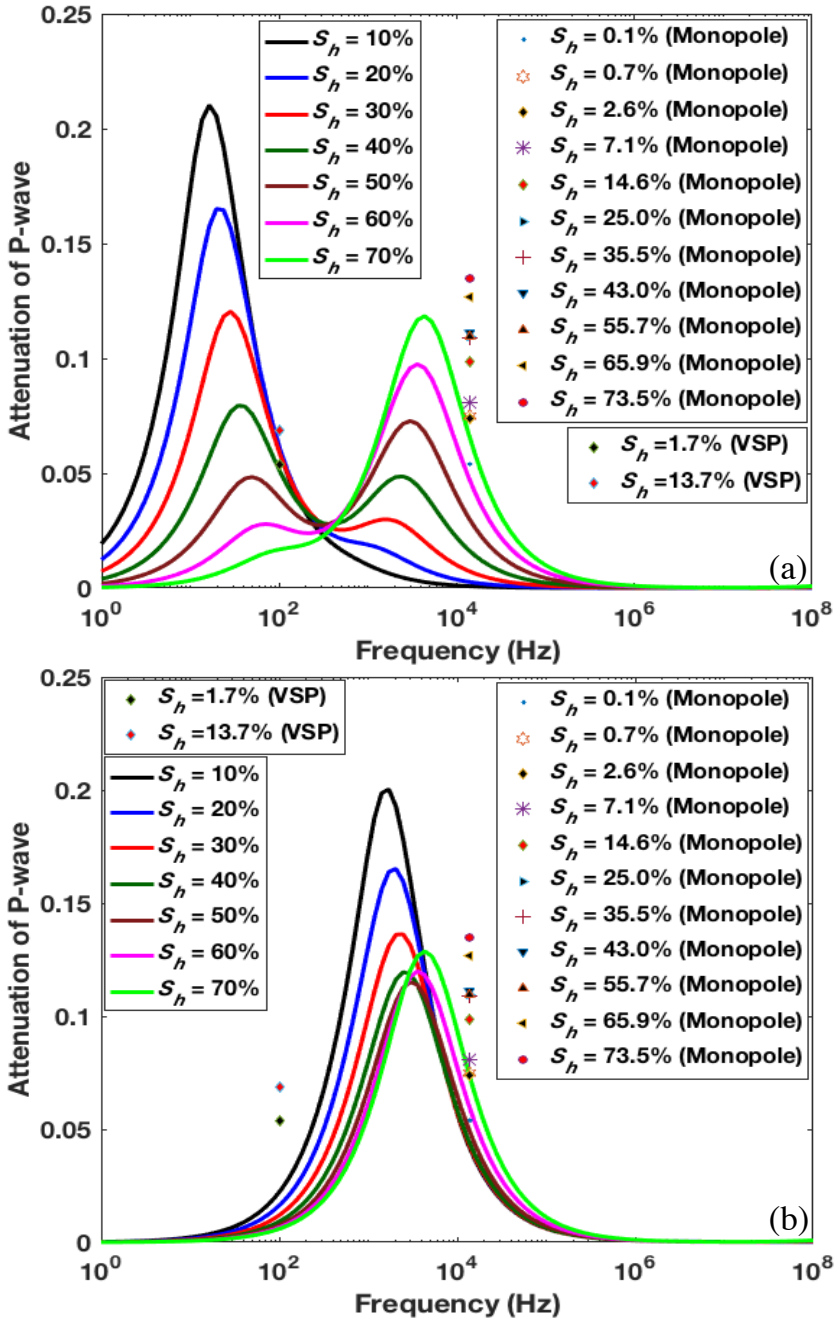

Figure 4. 7 Measured attenuation at PSW1 and attenuation predicted by the Guerin model at various initial hydrate and sand grain permeabilities as a function of frequency: (a) $k_{s0} = 5\times10^{-9}$, $k_{h0} = 1\times10^{-7}$; and (b) $k_{s0} = 5\times10^{-11}$, $k_{h0} = 1\times10^{-7}$. Except for k_{s0}, the parameters are the same between (a) and (b). The curves represented by various colors (from black to green) are the predicted P-wave attenuations by the Guerin model, while the various color dots at a frequency of 1, 4000 Hz represent the measured P-wave attenuations calculated from monopole sonic data, and the orange and blue diamonds at a frequency of 100 Hz represent the measured P-wave attenuations calculated from VSP data.

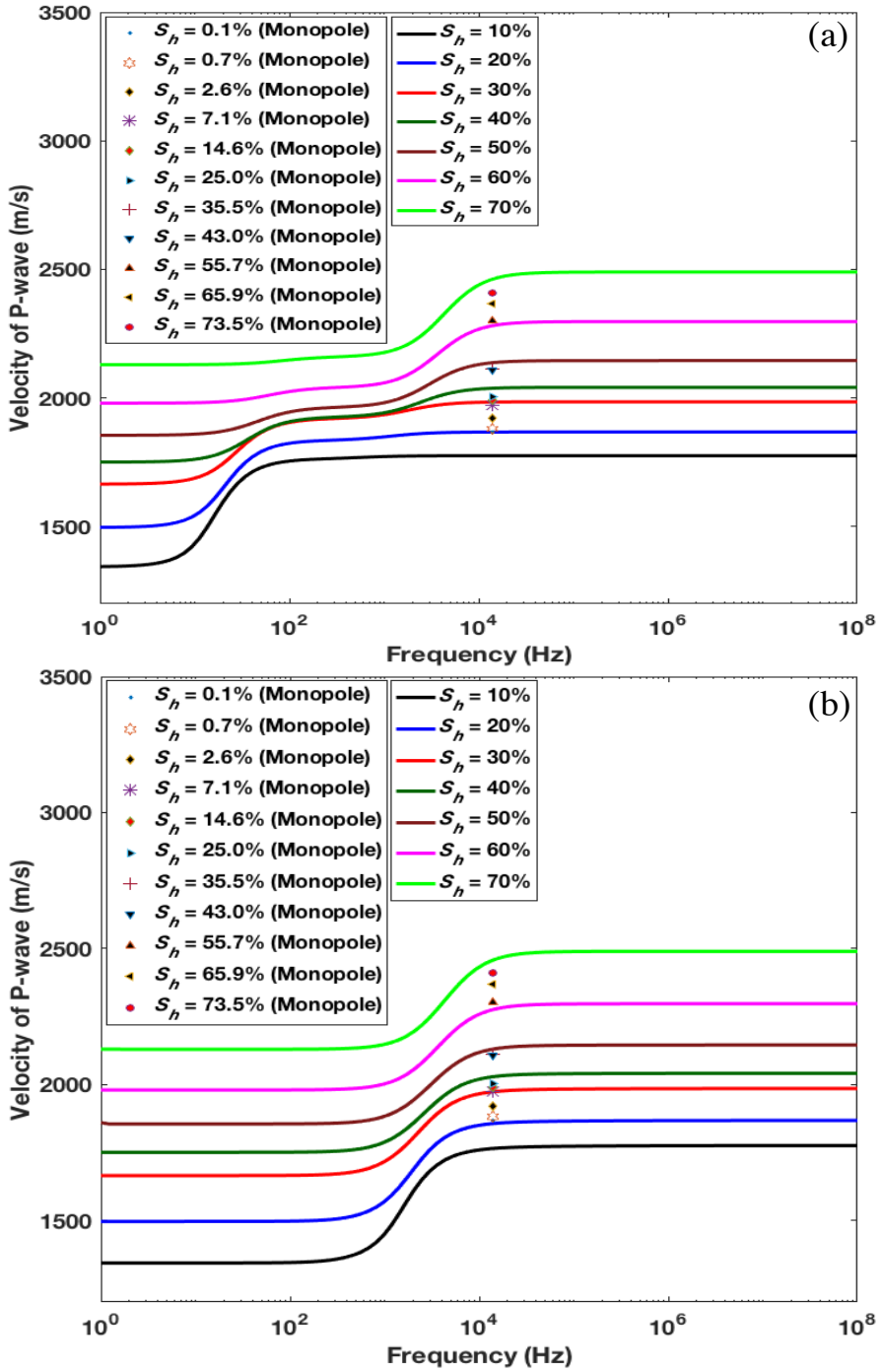

Figure 4. 8 Measured velocity at PSW1 and velocity predicted by the Guerin model at various initial hydrate and sand grain permeabilities as a function of frequency: (a) k_{s0} = 5×10^{-9}, k_{h0} = 1×10^{-7}; and (b) k_{s0} = 5×10^{-11}, k_{h0} = 1×10^{-7}. Except for k_{s0}, the parameters are the same between (a) and (b). The curves represented by various colors (from black to green) are the predicted P-wave velocities by the Guerin model, while the various color dots at a frequency of 1, 4000 Hz represent the measured P-wave velocities calculated from monopole sonic data.

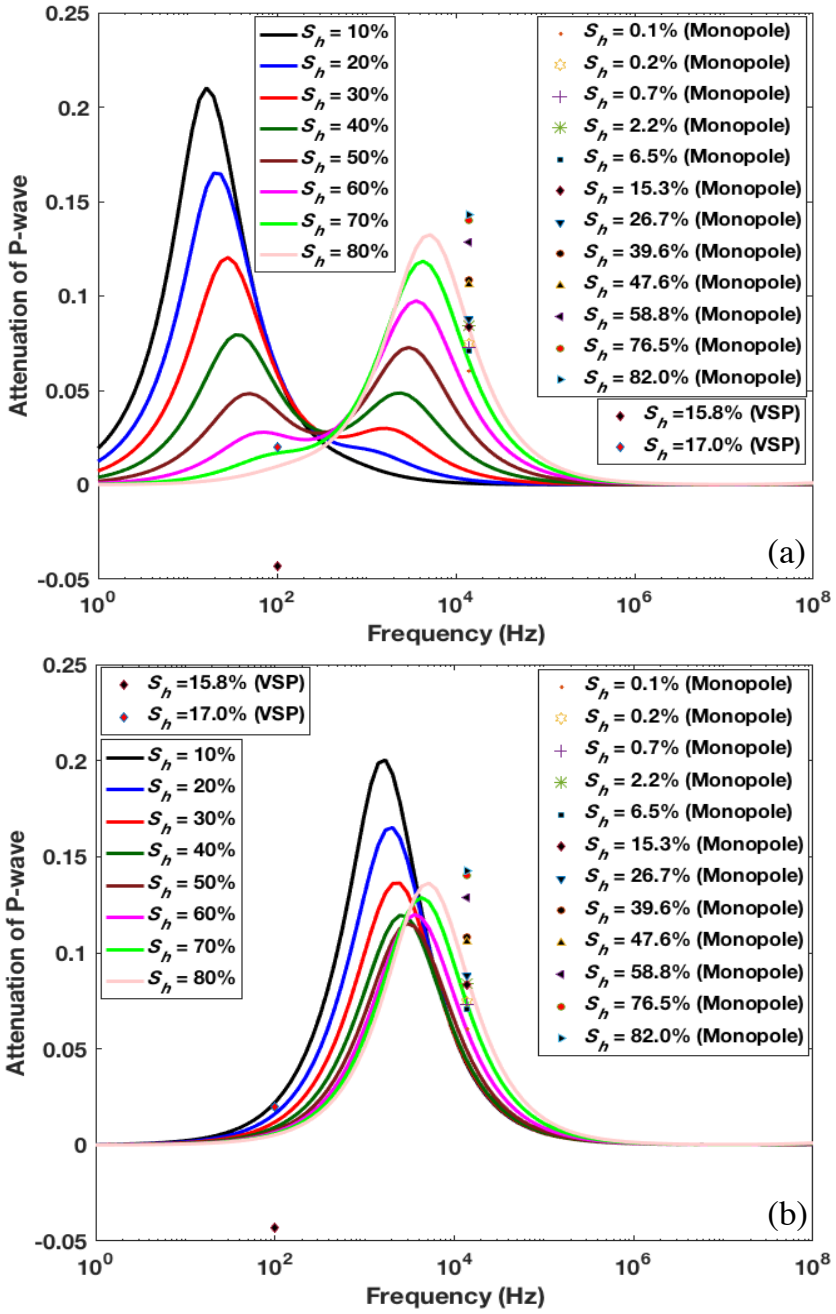

Figure 4. 9 Measured attenuation at PSW3 and attenuation predicted by the Guerin model at various initial hydrate and sand grain permeabilities as a function of frequency: (a) $k_{s0} = 5\times10^{-9}$, $k_{h0} = 1\times10^{-7}$; and (b) $k_{s0} = 5\times10^{-11}$, $k_{h0} = 1\times10^{-7}$. Except for k_{s0}, the parameters are the same between (a) and (b). The curves represented by various colors (from black to green) are the predicted P-wave attenuations by the Guerin model, while the various color dots at a frequency of 1, 4000 Hz represent the measured P-wave attenuations calculated from monopole sonic data, and the orange and blue diamonds at a frequency of 100 Hz represent the measured P-wave attenuations calculated from VSP data.

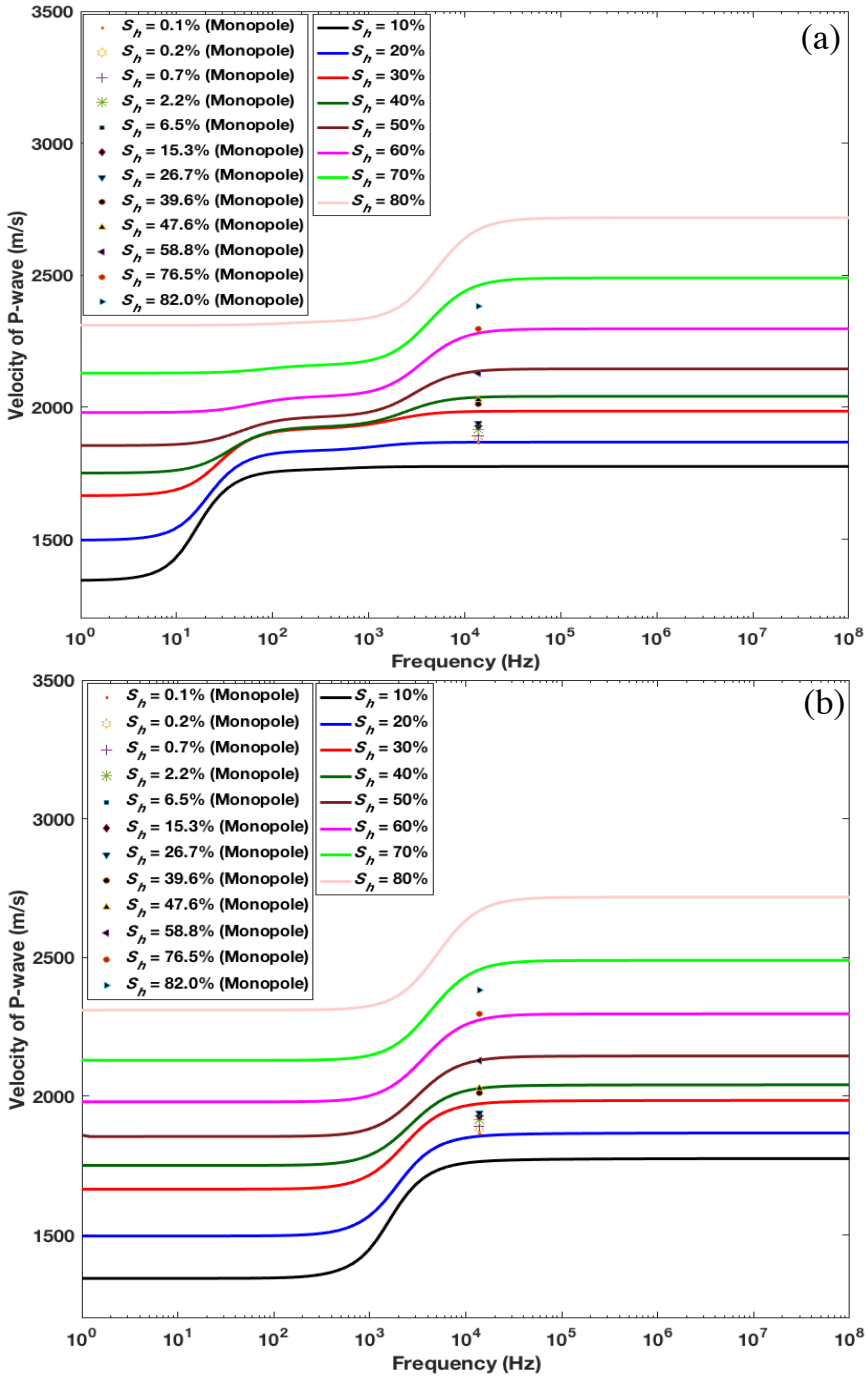

Figure 4. 10 Measured velocity at PSW3 and velocity predicted by the Guerin model at various initial hydrate and sand grain permeabilities as a function of frequency: (a) $k_{s0} = 5\times10^{-9}$, $k_{h0} = 1\times10^{-7}$; and (b) $k_{s0} = 5\times10^{-11}$, $k_{h0} = 1\times10^{-7}$. Except for k_{s0}, the parameters are the same between (a) and (b). The curves represented by various colors (from black to green) are the predicted P-wave velocities by the Guerin model, while the various color dots at a frequency of 1, 4000 Hz represent the measured P-wave velocities calculated from monopole sonic data.

Moreover, the measured hydrate saturation from resistivity curves at sonic frequencies is up-scaled into w-VSP frequency scale by using average method over the S-wave wavelength, then hydrate saturation at the two receiver depth intervals (1, 150-1, 190 m and 1, 150-1, 200 m) are converted into 3.1% and 3.4% at w-VSP frequency scale. The averaged S-wave attenuation values are 0.04 (1, 150-1, 190 m) and 0.05 (1, 150-1, 200 m) as shown in Matsushima (2015). The S-wave attenuations from w-VSP data are plotted at frequency of 100 Hz, while S-wave attenuation from sonic dipole data is plotted at frequency 1, 000 Hz. The estimated S-wave attenuation for w-VSP data (100 Hz) and the average S-wave attenuation at the sonic frequencies (1, 000 Hz) exhibit an obvious frequency dependence in the w-VSP to sonic frequency range (Fig.4.11). The broadband frequency response of S-wave attenuation calculated by the Guerin model also indicates frequency-dependent attenuation for MH-bearing sediment in the w-VSP to sonic frequency range, as shown in Fig. 4.11. Between Figs 4.11a and 4.11b, the initial sand permeability (k_{s0}) in Fig. 4.11a is larger than that in Fig. 4.11b, while the other parameters remain unchanged. The higher initial sand permeability (Fig. 4.11a) causes another S-wave attenuation peak at seismic frequencies (< 100 Hz) compared with extremely small values for lower initial sand permeability (Fig. 4.11b). Fig. 4.12 shows the S-wave velocity dispersion corresponding to the attenuation in Fig. 4.11. In Fig. 4.12, the S-wave velocity predicted by the Guerin model is lower than sonic S-wave velocity at lower hydrate saturation, while the predicted S-wave velocity is larger than measured ones at higher hydrate saturation possibly due to the overestimation of cementation between hydrate and sand grains.

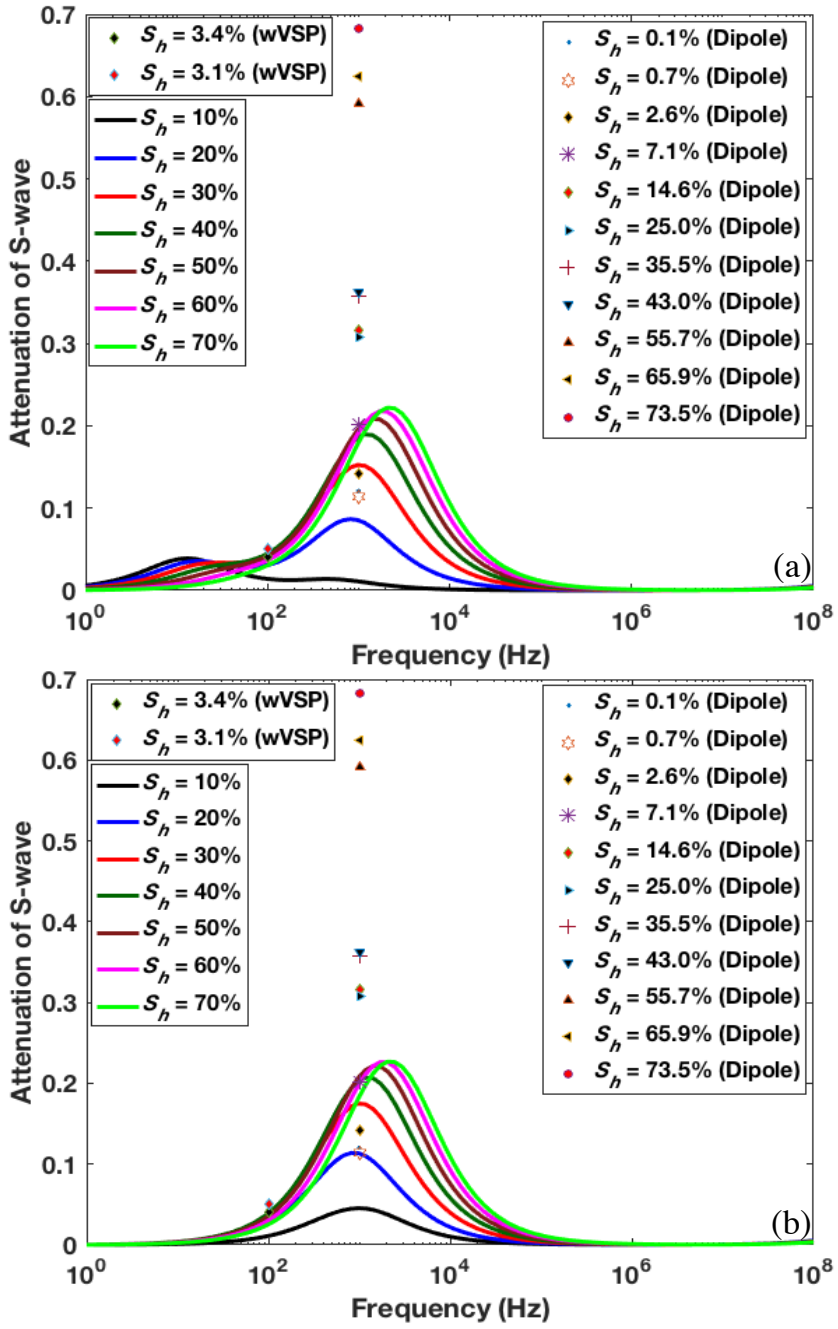

Figure 4. 11 Measured S-wave attenuation and attenuation predicted by the Guerin model at various initial hydrate and sand grain permeabilities as a function of frequency: (a) $k_{s0} = 5\times10^{-9}$, $k_{h0} = 1\times10^{-7}$; and (b) $k_{s0} = 5\times10^{-11}$, $k_{h0} = 1\times10^{-7}$. Except for k_{s0}, the parameters are the same between (a) and (b). The curves represented by various colors (from black to green) are the predicted S-wave attenuations by the Guerin model, while the various color dots at a frequency of 1, 000 Hz represent the measured S-wave attenuations calculated from dipole sonic data, and the orange and blue diamonds at a frequency of 100 Hz represent the measured S-wave attenuations calculated from w-VSP data.

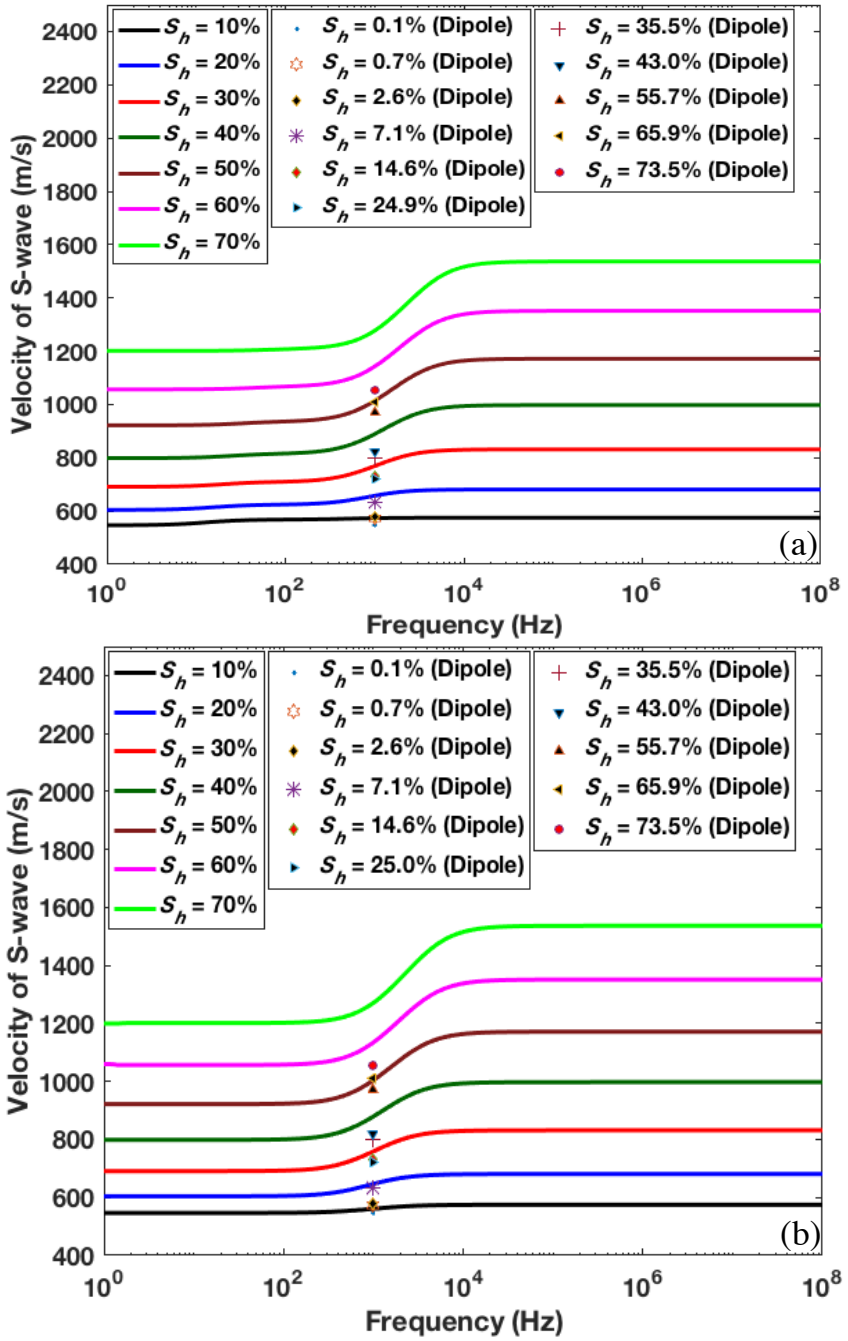

Figure 4. 12 Measured S-wave velocity and velocity predicted by the Guerin model at various initial hydrate and sand grain permeabilities as a function of frequency: (a) $k_{s0} = 5\times10^{-9}$, $k_{h0} = 1\times10^{-7}$; and (b) $k_{s0} = 5\times10^{-11}$, $k_{h0} = 1\times10^{-7}$. Except for k_{s0}, the parameters are the same between (a) and (b). The curves represented by various colors (from black to green) are the predicted S-wave velocities by the Guerin model, while the various color dots at a frequency of 1, 000 Hz represent the measured S-wave velocities calculated from dipole sonic data.

4.4 Discussion

4.4.1 Mechanisms for frequency dependent P-wave attenuation

Table 4. 2 Published seismic attenuation for MH-bearing sediment or synthetic hydrate-bearing sample

Location	Frequency	Attenuation
Nankai Trough	30-110 Hz	VSP data: 0.02-0.07 (Matsushima et al., 2016)
Blake Ridge	20-150 Hz	Single channel seismic data: 0.002-0.01 (Wood et al., 2000)
Mallik field	100-1000 Hz	Crosshole seismic data: 0.15-0.2 (Bauer et al., 2008)
	10-200 Hz	0.12 (maximum) (Dvorkin & Uden, 2004)
	10-200 Hz	VSP data: 0.07-0.14 (Bellefleur et al., 2007)
Krishna-Godavari(KG) basin	10-45 Hz	Seismic CDP gathers: 0.0029 (Nittala et al., 2017)
Offshore Svalbard (Arctic)	20-200 Hz	OBSs data: 0.004-0.014 for P-wave (Rossi et al., 2007; Madrussani et al., 2010)
Laboratory measurement	<400 Hz	0.034 (maximum) for P-wave; 0.026 (maximum) for S-wave (Priest et al., 2006)
	50-550 Hz	0.11 (maximum) for P-wave; 0.05 (maximum) for S-wave (Best et al., 2013)

Essentially, the estimation of seismic attenuation of MH-bearing sediments remains challenging. Seismic attenuation may not be directly associated with the intrinsic attenuation of MH-bearing sediments, and instead, should be largely attributed to scattering from small-scale heterogeneity and leaky mode propagation caused by large-scale heterogeneity (Huang et al., 2009). As shown in Table 4.2, several attenuation values are estimated from seismic data for existing MH-bearing sediments. The VSP attenuation values for the Nankai Trough were estimated by Matsushima et al. (2016) and were lower than those at the Mallik field, which were estimated by Dvorkin et al. (2004), Bellefleur et al. (2007), and Bauer et al. (2008). In addition, the VSP attenuation values in this study were larger than the seismic attenuation calculated for the Krishna-Godavari (KG) basin by Nittala et al. (2017) and for the offshore Svalbard (Arctic) by Rossi et al. (2007) and Madrussani et al. (2010). The VSP attenuation values in this study were comparable to laboratory measurement data reported by Best et al. (2013). It is not clear which seismic attenuation is more reasonable for MH-bearing sediments due to the different geology environments. In the Mallik field, the significant seismic attenuation is

explained by macroscopic squirt flow due to elastic heterogeneity in the rock frame elastic moduli, which are more relevant to the seismic frequency range (Dvorkin & Uden, 2004). This appears to be reasonable for the Mallik field because of the large thickness of the hydrate intervals (individual gas hydrate intervals are up to 40 m thick) (Bellefleur et al., 2007; Bauer et al., 2008). Nittala et al. (2017) suggested that the MH-bearing layers for the KG basin, which is dominated by shale associated with incensing faults, could be represented by the horizontal transverse isotropy (HTI) model, and alternating thin layers could represent the MH-bearing layer in the Nankai Trough. In addition, Priest et al. (2006) suggested that the absorbed thin water film remaining between grain contacts and cementing hydrate resulted in a significant squirt flow and subsequent significant seismic attenuation. In a recent study, such water films between solid grains and newly formed hydrate were observed by X-ray micro-tomography, and the squirt flow caused by these water films was shown to cause significant seismic attenuation (Sell et al., 2017). The squirt flow due to water films between solid grains and hydrate is not included in our simulations using the Guerin model. In a 3D sense these water films are connected with the macro pores, and then the resulting squirt flow might be very similar to the micro squirt flow proposed by Marin-Moreno et al. (2017). However, Marin-Moreno et al. (2017) also indicated this type of squirt flow mainly occurred at ultrasonic frequency band.

P-wave attenuation in the seismic frequency band is partly explained by the comparison between VSP attenuation and values predicted by the Marin-Moreno model and the Guerin model. Between Figs 4.2a and 4.2b, except aspect ratio (α), I kept all the parameters the same. As shown in Fig. 4.2a, the VSP (100 Hz) attenuation appears to be captured by squirt flow in a microporous hydrate with a lower aspect ratio ($\alpha = 0.0001$). In Fig. 4.2b, the sonic P-wave (14,000 Hz) attenuation appears to be due to squirt flow in microporous hydrate with a higher aspect ratio ($\alpha = 0.0004$). Best et al. (2013) simply summed two attenuations with different inclusion aspect ratios to fit their modeling curve to the laboratory attenuation measured at 200 Hz. Since attenuations with different fluid aspect ratios act in different frequency bands (Marín-Moreno et al., 2017), the predicted curves with aspect ratios of 0.0001 and 0.0004 can be simply added to accumulate the attenuation contribution for the sonic and VSP frequency bands. The natural aspect ratio can be assumed as a distribution of the aspect ratio. However, the limited information concerning the inclusion aspect ratio limits the application of the Marin-Moreno model to sonic and VSP attenuation prediction.

Unlike the Marin-Moreno model, the double permeability system (k_{s0} and k_{h0}) in the Guerin model enables us to investigate the effect of relative magnitude of double permeability on attenuation. In a single permeability system, Dvorkin et al. (1993, 1995) proposed the BISQ model to investigate the frequency (ω: angular frequency) response of permeability (k) on attenuation. The attenuation peak shifts to a higher frequency with increasing permeability in the BISQ model, whereas the

attenuation peak shifts to a lower frequency with increasing permeability in the Biot model. This can be explained by the fact that, in the Biot model, the attenuation depends on the product ωk, whereas, in the BISQ model, the attenuation depends on the ratio ω/k. Note that the BISQ flow theory in the Guerin model was proposed by Diallo and Appel (2000) and their reformulated BISQ model showed the same trend, whereby the attenuation peak shifts towards a lower frequency with increasing permeability, as the Biot model (Diallo & Appel, 2000). This is because, in the reformatted BISQ model, the attenuation depends on the product ωk, similar to the Biot model. Guerin and Goldberg (2005) introduced the reformulated BISQ model to his double permeability system (k_{s0} and k_{h0}) in sand grains and hydrate. Thus, the higher permeability component would result in significant attenuation in a lower frequency band. Between Figs 4.7a and 4.7b, except the initial permeability of solid matrix (k_{s0}), I kept all the parameters the same. The initial permeability of the solid matrix (k_{s0}) in Fig. 4.7a was made to be larger than that in Fig. 4.7b. As shown in Fig. 4.7a, the larger permeability in sand grains gives rise to an attenuation peak in the seismic frequency band. Moreover, the peak of attenuation increases with decreasing hydrate saturation. The attenuation in this frequency range is comparable to VSP attenuation samples (see Fig. 4.7a). Therefore, I infer that the higher permeability component in hydrate/solid grains, combined with the effect of hydrate saturation, could explain VSP attenuation. Furthermore, the presence of high permeability in sand grains in our parameter setting may facilitate local squirt flow, thereby enhancing the attenuation of P-wave at seismic frequencies (10 to 100 Hz).

The predicted attenuation for VSP data (100 Hz) and the average P-wave attenuation in the sonic frequency band (14,000 Hz) are plotted in Figs 4.2 and 4.7. The field attenuation exhibits an obvious frequency dependency in the VSP to sonic frequency range. The broadband frequency response of P-wave attenuation calculated by the Marin-Moreno model and the Guerin model indicates frequency-dependent attenuation of P-waves for hydrate-bearing sediment in the VSP to sonic frequency range, as shown in Figs 4.2 and 4.7. Nittala et al. (2017) compared the sonic attenuation with the seismic attenuation in the KG basin and concluded that viscous fluid flow acts in the sonic frequency range but not in the seismic frequency range. They attributed this difference in attenuation between the sonic and VSP frequency bands to the thickness of hydrate layers. On the other hand, I believe that the different responses of attenuation between the sonic and VSP frequencies at the Nankai Trough are explained by frequency-dependent attenuation in MH-bearing sediments. Furthermore, this frequency-dependent P-wave attenuation may be due to the squirt flow caused by the combined effect of the degree of hydrate saturation and two permeable systems (between sand grains and between hydrate) (Fig. 4.7), or due to the squirt flow caused by fluid inclusions with different aspect ratios in a microporous hydrate (Fig. 4.2).

4.4.2 Mechanisms for frequency dependent S-wave attenuation

The study has attempted to investigate the frequency-dependent S-wave attenuation from w-VSP to sonic frequencies and elucidate its mechanisms. There are extremely limited examples for S-wave attenuation at seismic frequencies because of the low SNR of S-wave events. Matsushima (2015) improved the SNR by horizontally stacking traces after linear moveout over the offset range and by selecting better-quality S-wave events observed in MHBS (possibly due to better coupling between the geophones and MHBS), and obtained S-wave attenuation of 0.04 and 0.05 at seismic frequencies. The S-wave attenuation from OBS data in MH-bearing sediments at Offshore Svalbard was estimated to be 0.062 to 0.33 (Madrussani et al., 2010; Dr. Giuliana Rossi, private communication, 2018), which is larger than the estimates from w-VSP data at the Nankai Trough by Matsushima (2015). Tsuji et al. (2004) mentioned that the MHBS at the Nankai Trough is less than 1 m in thickness. This is much smaller than the wavelength of w-VSP, which may lead to an underestimation of the attenuation. Comparing the w-VSP S-wave attenuation with the sonic S-wave attenuation obtained by Suzuki & Matsushima (2013), the latter is significantly larger. Suzuki & Matsushima (2013) pointed out the near-field effects, which cause a possible overestimation of the S-wave attenuation from sonic log data. Although frequency-dependent S-wave attenuation is observed between w-VSP and sonic frequencies, uncertainties arose from various factors.

In Fig. 4.11a, for obvious S-wave attenuation at seismic frequencies (< 100 Hz), since squirt flow does not influence S-wave attenuation (Guerin & Goldberg, 2005), I infer that global Biot flow and the friction between sand grains and hydrate are possible attenuation mechanisms. In Figs 3.14d and 3.15d, the S-wave attenuation predicted by the Leclaire model is significantly lower than that measured from sonic data. This implies that the Biot flow is negligible as a mechanism for S-wave attenuation at sonic frequencies. However, the S-wave attenuation predicted by the Carcione and Guerin models is lower than but similar to the measured value at sonic frequencies. I infer that the friction between sand and hydrate grains dominates S-wave attenuation at sonic frequencies. Furthermore, the S-wave attenuation at the MH-bearing sediments from the w-VSP data is obviously smaller than that from the sonic data (Fig. 4.11a). This implies frequency-dependent S-wave attenuation at the MH-bearing sediments. The broadband frequency response of S-wave attenuation calculated by the Guerin model also indicates frequency dependence at the MH-bearing sediments, as shown in Fig. 4.11. I infer that the larger k_{s0} might enhance the Biot flow and then increase the clear S-wave attenuation at seismic frequencies. In Fig. 4.11, the S-wave attenuation at sonic frequencies increases with increasing hydrate saturation, which might be because of the increasing friction between hydrate and sand grains caused by increasing hydrate saturation.

4.5 Conclusion of this chapter

In terms of P-wave attenuation in the seismic frequency range, squirt flow is also a dominant attenuation mechanism, and two key parameters cause large variations in attenuation in the seismic frequency range: 1) the inclusion aspect ratio in hydrate grains and 2) the combined effect of the degree of hydrate saturation and two permeable systems in pore spaces between hydrate grains and pore spaces between sand grains.

The microporous hydrates with smaller inclusion aspect ratios resulted in significant P-wave attenuation at seismic frequency domain, while the larger inclusion aspect ratios led to significant P-wave attenuation at sonic frequency domain.

In the two permeable systems (sand grains and hydrate), the higher permeability component caused the significant P-wave attenuation at seismic frequency domain, while smaller permeability component resulted in significant P-wave attenuation at sonic frequency domain.

The present study demonstrated the frequency-dependent S-wave attenuation between w-VSP and sonic frequencies and clarified this dependence by the application of the Guerin model. Friction between hydrate and sand grains dominates the S-wave attenuation at sonic frequencies, whereas the Biot flow and friction between hydrate and sand grains are possible attenuation mechanisms at seismic frequencies.

CHAPTER 5. ROCK PHYSICS MODELING OF PROPAGATION OF ULTRASONIC P- AND S-WAVE IN PARTIALLY FROZEN BRINE AND UNCONSOLIDATED SANDS

In this Chapter, the ultrasonic measurement result for partially frozen systems is used to infer the attenuation mechanisms responsible for MH-bearing sediments at ultrasonic frequencies. To do this, combined with the attenuation mechanisms at VSP (w-VSP) and sonic frequencies in Chapter 3 and Chapter 4, the broadband frequency dependent attenuation for MH-bearing sediments can be investigated.

5.1 Introduction

The understanding of wave propagation in partially frozen systems is very important for seismic exploration in permafrost regions (Dou et al., 2016), glaciers (Peters et al., 2012), and MH-bearing sediments (Guerin and Goldberg, 2005). The coexistence of unfrozen water and ice complicates the description and characterization of partially frozen systems and significantly affects wave propagation in them (Matsushima et al., 2016). Ultrasonic pulse transmission is an effective method for investigating the physical properties of a partially frozen system under various physical conditions in the laboratory. Many experimental studies focusing on velocity measurements have shown that the onset of freezing results in a large increase of P- and S-wave velocities in consolidated porous media (Timur, 1968), systems in which ice and brine coexist (Spetzler and Anderson, 1968; Prasad and Dvorkin, 2004; Matsushima et al., 2008), partially frozen orange juice (Lee et al., 2004), and partially frozen unconsolidated saline soil or sand (Nakano et al., 1972; Nakano and Arnold, 1973; Zimmerman and King, 1986; Sondergeld and Rai, 2007; Dou et al., 2017). The measured P- and S-wave velocities of partially frozen systems have been predicted by several rock physics approaches: three-phase time-averaged model (Timur, 1968), three-phase Biot extension model (Leclaire et al., 1994; Carcione and Seriani, 1998, 2001), effective medium model (Zimmerman and King, 1986; Dou et al., 2017), and intergranular cementation theory (Jacoby et al., 1996). These previous theoretical studies provided good agreement with experimental data for partially frozen systems. Two major factors are believed to affect the P- and S-wave velocities of partially frozen systems: fraction of ice and pore-scale distribution in the ice (Schindler et al., 2016; Dou et al., 2017; Wu et al., 2017).

Several authors have measured wave attenuation in partially frozen systems. Spetzler and Anderson (1968) measured ultrasonic P- and S-wave attenuation in a two-phase system (ice and unfrozen brine). Prasad and Dvorkin (2004) and Matsushima et al. (2008) measured ultrasonic P-wave

attenuation in such a two-phase system. These authors observed markedly increasing velocities and attenuation at the onset of freezing. Bellanger et al. (1996) measured ultrasonic P-wave velocity and attenuation in limestone under freezing and thawing cycles. They observed increased velocity and attenuation and suggested that they were due to the creation of pseudo-cracks between the ice being formed and the solid walls characterizing the transition of water to ice. Matsushima et al. (2016) measured ultrasonic wave transmission with changing temperatures from 0 to −15 °C in unconsolidated sands to estimate the velocity and attenuation of P- and S-waves. They suggested that the existence of partially frozen liquid in unconsolidated sand increases the velocity and attenuation at temperatures of 0 °C to around the freezing point. Dou et al. (2016) measured ultrasonic P-wave transmission in a fine-grained permafrost core for a range of salinities and temperatures. They also observed that although velocity increased monotonically with increasing ice saturation, P-wave attenuation reached a maximum at intermediate ice saturation. Wu et al. (2017) measured the elastic moduli and attenuation in saline permafrost soils. They found a maximum attenuation at the temperature immediately below the freezing point. Pohl et al. (2017) measured ultrasonic P-wave velocity and attenuation in pure tetrahydrofuran (THF) hydrate at temperatures decreasing from 25 °C to 1 °C. Although they found that velocity increased, P-wave attenuation also increased after the formation of hydrates. From these studies, contrary to our intuition that higher velocity corresponds to lower attenuation, the increasing velocity accompanied by an increasing attenuation in partially frozen systems is a widely observed phenomenon.

Rock physics modeling of the velocity and attenuation in partially frozen systems under various physical conditions is an effective method for quantitatively interpreting laboratory observations and deepening our understanding of this interesting phenomenon. However, only a limited number of theoretical approaches can focus on the ultrasonic attenuation of partially frozen systems during the freezing process. Carcione et al. (2007) proposed a poroelastic model based on the Biot theory [hereafter referred as the Carcione (2007) model] to calculate ultrasonic velocity and attenuation in partially frozen orange juice. Matsushima et al. (2011) employed this poroelastic model to describe the propagation of ultrasonic P-waves through partially frozen brine. They concluded that Biot flow couldn't completely predict the measured attenuation. Leurer (1997) and Leurer and Brown (2008) assumed an effective medium made up of a homogeneous elastic mineral phase that is isotropically interspersed with ellipsoidal inclusions of low aspect ratio representing an intracrystalline water layer. Based on this, they proposed an effective grain model to calculate the velocity and attenuation of unconsolidated fine- and coarse-grained saturated marine sediment (hereafter referred to as the Leurer model).

In a three-phase model (sand, ice, and unfrozen liquid), the interaction between ice and sand grains further complicates the elastic response of partially frozen unconsolidated media. Leclaire et al. (1994) extended the Biot theory to a three-phase model and then incorporated Biot flow in two porous systems, sand grains and ice grains. They also provided a method (hereafter referred to as the Leclaire model) to estimate water saturation at reduced temperature during the freezing process. It should be noted that they assumed no contact between ice and sand grains. Carcione and Tinivella (2000) modified the Leclaire model to introduce interaction between sand and hydrate grains, as well as the cementation effect between sand and hydrate grains (hereafter referred to as the Carcione model with no date). Furthermore, based on the Carcione model, Guerin and Goldberg (2005) introduced viscous friction loss between sand and hydrate grains and squirt flow in two porous systems, sand grains and hydrate grains (hereafter referred to as the Guerin model). In another approach, Best et al. (2013) applied the effective medium model to include the attenuation mechanisms caused by squirt flow in microporous hydrate, viscoelasticity of the hydrate frame, and global Biot flow. Marín-Moreno et al. (2017) further included the attenuation mechanisms caused by gas bubble damping and the local viscous squirt flow between connected pores due to the formation of hydrates in their rock physics model. Due to the similar properties of hydrates and ice (Sloan and Koh, 2006), it seems reasonable to use models developed for characterizing MH to describe elastic response of partially frozen unconsolidated sand.

In this study, to elucidate the velocity and attenuation observed in the ultrasonic measurements of partially frozen brine (Matsushima et al., 2008) and unconsolidated sand (Matsushima et al., 2016), and further clarify the mechanisms responsible for attenuation in both partially frozen systems, two different rock physics models are adopted: an effective medium model (Leurer model) for partially frozen brine and a three-phase extension of the Biot model (Guerin model) for partially frozen unconsolidated sands. By matching the predicted and measured values, the input parameters of the rock physics models are carefully adjusted and the influential parameters are identified.

5.2 Laboratory measurements

Here, the ultrasonic laboratory measurements of two different partially frozen systems are briefly described: partially frozen brine (two-phase composed of ice and unfrozen brine) and unconsolidated sands (three-phase composed of ice, unfrozen brine, and sand).

5.2.1 Partially frozen brine

Matsushima et al. (2008) measured ultrasonic pulse transmission in an ice-brine binary system and observed the velocity and attenuation of P-waves with changing temperature from 0 °C to –15 °C.

When brine begins to freeze, salt is not incorporated into the ice crystals. Thus, the salinity of unfrozen brine increases in the brine-filled pores, decreasing the freezing point of the unfrozen brine (Matsushima et al., 2011). The total volume of unfrozen brine is controlled by the temperature and salinity. A one-cycle sinusoidal wave at 1 MHz was used as the ultrasound source. They calculated P-wave attenuation values based on a frequency-independent Q model at frequencies of 350–600 kHz. However, they could not obtain reliable S-wave data because of the poor consolidation of the partially frozen brine, which does not have enough shear stiffness to easily propagate S-waves. A detailed description of the laboratory and attenuation estimation methods is provided in Matsushima et al. (2008). In partially frozen brine with an initial salinity of 2%, varying the temperature could control the amount of unfrozen brine. Their results indicated that the ultrasonic P-wave attenuation peaked at –3 °C, where the fraction of the liquid phase was maximum and attributed it to the existence of unfrozen brine in the pore microstructure (Matsushima et al., 2008). Their obtained P-wave velocity and attenuation curves as a function of temperature were used in this study.

5.2.2 Partially frozen unconsolidated sands

Similar to the case of partially frozen brine, Matsushima et al. (2016) measured ultrasonic pulse transmission through partially frozen unconsolidated sand. Toyoura standard sand was saturated with the brine at an initial salinity of 2%, and then the temperature was reduced from 0 °C to –15 °C. The ultrasound source was a one-cycle sinusoidal wave at 1 MHz. They calculated attenuation values based on a frequency-independent Q model at frequencies of 350–600 kHz for P-waves and 100–200 kHz for S-waves. During the freezing process, two solid phases (sand and ice) and one fluid phase (brine) coexisted in the partially frozen unconsolidated medium. The details of the experiment setup and estimation of velocity and attenuation for P- and S-waves are given in Matsushima et al. (2016). Their results showed that P-wave attenuation reached its peak at the freezing point (i.e., around −2 to −3 °C) and decreased with decreasing temperature from –3 °C to –15 °C, but at a slower rate from –7 °C to –15 °C. In contrast, the maximum S-wave attenuation at –5 °C largely decreased at an almost constant rate of change with decreasing temperature. Their obtained P- and S-wave velocity and attenuation curves as a function of temperature were used in this study.

5.3 Prediction of brine viscosity

As described above, as ice is formed from brine, salt cannot be incorporated into the ice crystals. As the fluid freezes, the salt is rejected and concentrates in the brine; thus, as the salinity and density increase in the brine filling the pores, the freezing point of the remaining fluid is continuously reduced. After freezing begins, however, it is not easy to measure the salinity and viscosity in a system with coexisting ice and brine at lower temperatures (Matsushima et al., 2013). The solubility of NaCl is

around 35 g per 100 g of water at a temperature of 0 °C (corresponding to the salinity of around 25%), and it slightly decreases with decreasing temperature. Matsushima et al. (2013) validated the measurement of brine viscosity with decreasing temperature and an initial salinity of 25% to understand the influence of high viscosity fluid on ultrasonic wave propagation.

The viscosity of water is generally a function of temperature (Gilpin, 1980). Leclaire et al. (1994) provided an exponential regression formula to describe the changing viscosity of water with decreasing temperature even lower than –10 °C based on experiment data:

$$\eta = [\frac{\eta_0 (450 + h)}{h}] e^{-0.003753T} \qquad (1)$$

where η_0 is the viscosity of water at its freezing point, h is the average thickness of the unfrozen liquid layer calculated with the radius of sand grains, and T is the temperature. Moreover, η_0 at an initial salinity of 25% can be obtained from the measurements conducted by Matsushima et al. (2013), and then the viscosity at the initial salinity of 25% can be predicted using equation 1 and compared with values obtained at lower temperatures to validate equation 1. Note that I could not consider the effect of increasing salinity on viscosity during the freezing process using equation 1, and the equation basically only evaluates the effect of temperature on viscosity at different values for η_0.

5.4 Estimation of unfrozen brine saturation

Leclaire et al. (1994), Carcione et al. (2001), and Carcione et al. (2007) provided a thermodynamic relationship between unfrozen water saturation ϕ_w and temperature T given in kelvins as follows:

$$\phi_w = \frac{\phi_0}{\Delta r \sqrt{2\pi}} \int_{-\infty}^{\frac{r_0}{\ln(T_0/T)}} e[\frac{-(r - r_{av})^2}{2\Delta r^2}] dr \qquad (2)$$

where ϕ_0 is the initial porosity, r_{av} is the average pore radius, r is the capillary pore radius, Δr is the standard deviation, T_0 is the freezing point, and r_0 is fitted by experiment data. Note that this study used two types of pore spaces: pores in porous ice for partially frozen brine and pores between sand grains for partially frozen unconsolidated sand. Carcione et al. (2001) and Carcione et al. (2007) set the lower limit of the integral in equation 2 as 0. However, I found that this integral is very sensitive to the lower limit. I applied the definition of $-\infty$ from Leclaire et al. (1994) to the rock physics models (hereafter referred to as the Leclaire model). Dou et al. (2016, 2017) also provided an estimation

method for predicting brine saturation for a given initial salinity and freezing point (hereafter referred to as the Dou model). The unfrozen brine saturation predicted by the Leclaire and Dou models are compared with values measured by the nuclear magnetic resonance (NMR) technique for partially frozen brine and unconsolidated sand.

5.5 Results

5.5.1 Estimation of viscosity and unfrozen brine saturation

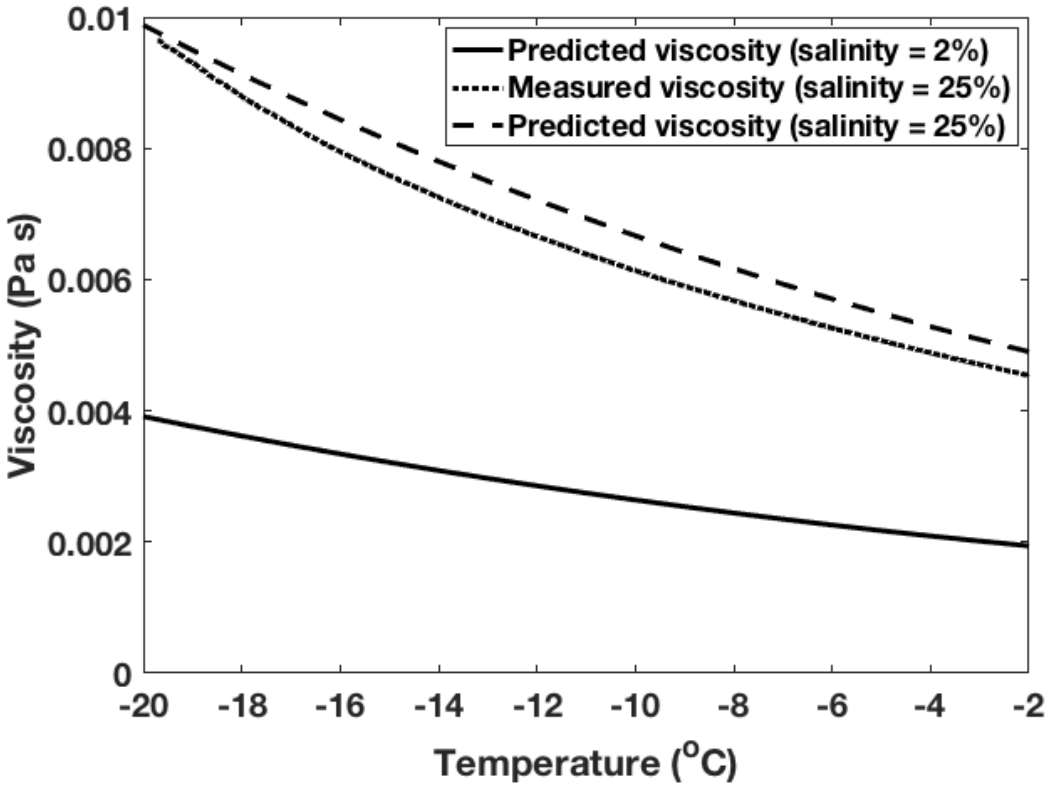

Figure 5. 1 Predicted and measured viscosity of unfrozen brine as a function of temperature. The viscosity of brine was measured at a salinity of 25% (dotted curve) and predicted at salinities of 2% (solid curve) and 25% (broken curve).

As Fig. 5.1 shows, the predicted viscosities at salinities of 25% (broken curve) and 2% (solid curve) indicated that the viscosity of partially frozen brine increases with decreasing temperature. The predicted (broken curve) and measured (dotted curve) viscosities at a salinity of 25% had a very small difference between them. Although equation 1 cannot reflect the effect of changing salinity with decreasing temperature, the measured viscosity at different temperatures seems to be successfully predicted by equation 1 at salinity of 25%. Therefore, I infer that it is reasonable to use equation 1 to

predict the changing viscosity with temperature at an initial salinity of 2% in the rock physics models (solid curve).

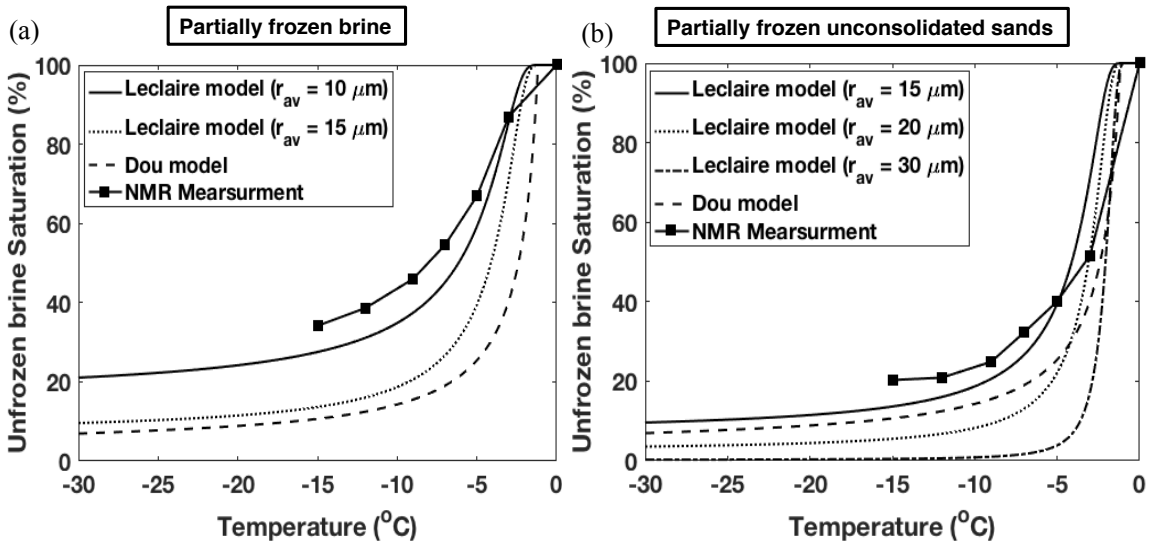

Figure 5. 2 Predicted and measured unfrozen brine saturation as a function of temperature: (a) partially frozen brine and (b) partially frozen unconsolidated sands. The brine saturation was measured by NMR at 0 to –15 °C (solid curve with solid squares). The brine saturation was also predicted by the Dou (broken curve) and Leclaire (solid and dotted curves) models at different average pore radii r_{av} .

Matsushima et al. (2008) estimated the total unfrozen brine saturation at each temperature using the solid-echo NMR technique for partially frozen brine, indicated by a solid curve with solid squares in Fig. 5.2a. Similarly, Matsushima et al. (2016) estimated the total unfrozen brine saturation at each temperature using the same NMR technique for partially frozen unconsolidated sand, as shown by a solid curve with solid squares in Fig. 5.2b. As we can see, even at temperatures lower than –15 °C, a large amount of brine remains unfrozen, 34% for partially frozen brine and 20% for partially frozen unconsolidated sand, because salt rejection lowers the freezing point of the remaining brine (Banin and Anderson, 1974; Foldvik and Kvinge, 1974). The Leclaire and Dou models can predict the unfrozen brine saturation. As Fig. 5.2 shows, unfrozen brine saturation versus temperature curves predicted by both the Dou and Leclaire models successfully captured the trend of the NMR data. At temperatures higher than –5 °C, the sharply decreasing brine saturation represents initial freezing, while at temperatures lower than –5 °C, the freezing rate decreases. The reason for this is described later. In order to accurately depict the drastic change of unfrozen brine saturation within temperature at –3 to –5 °C, the temperature in the rock physics modeling is controlled to a precision of 0.001 °C. In Fig. 5.2, by comparing the unfrozen brine saturation predicted by the Dou model at a salinity of 2% with the values measured by NMR, we can see that the unfrozen brine saturation predicted by the Dou

model (broken curve) was lower than the measured saturation (solid curve with solid squares). When the unfrozen brine saturation predicted by the Leclaire model was compared with measured saturation for partially frozen brine (Fig. 5.2a) and partially frozen unconsolidated sand (Fig. 5.2b), I found that the predicted values at an average pore radius r_{av} of 10 μm (solid curve in Fig. 5.2a) were most similar to measured values for partially frozen brine. Meanwhile, r_{av} of 15 μm (solid curve in Fig. 5.2b) produced the most similar predicted and measured values for unconsolidated sand. In fact, the unfrozen brine saturation as a function of temperature is a key problem for the comparison between experimental and predicted results by the rock physics model.

5.5.2 Application of Leurer model to partially frozen brine

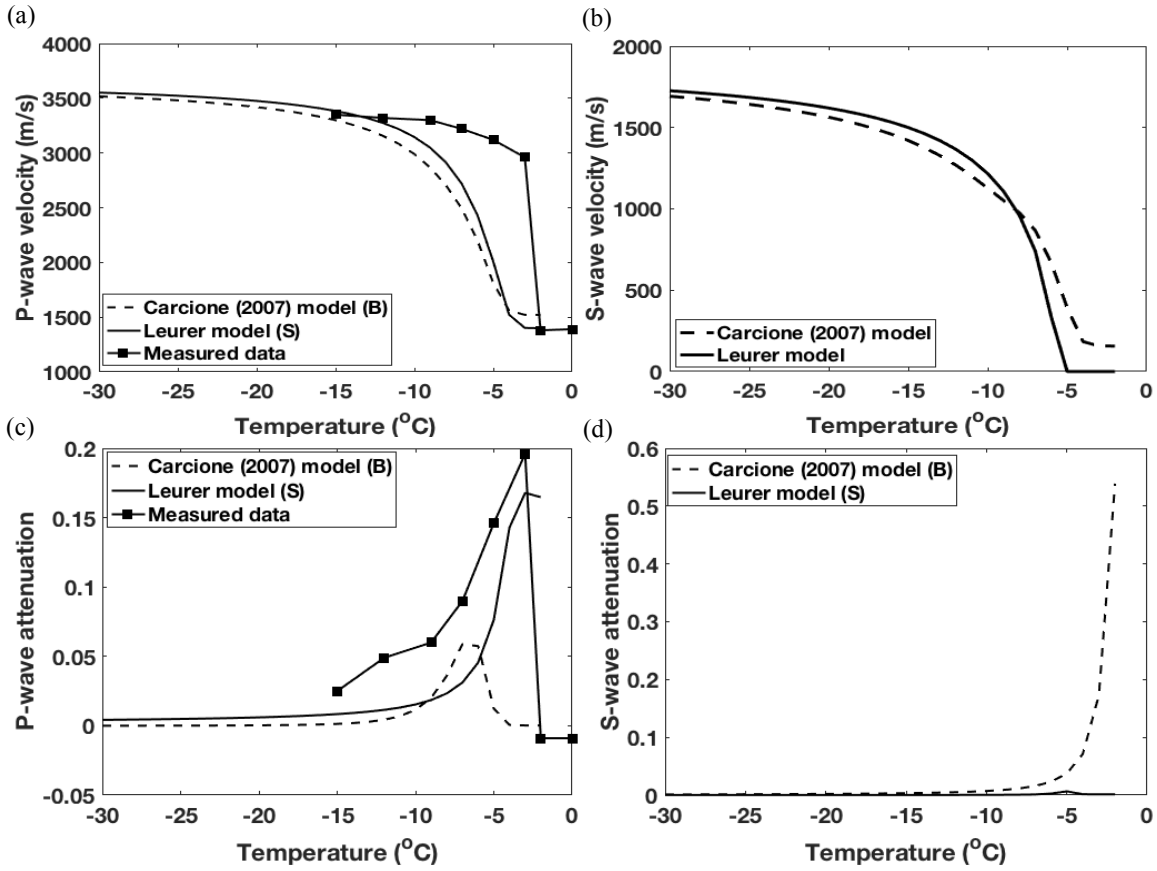

Figure 5. 3 Predicted and measured velocity and attenuation as a function of temperature in partially frozen brine: (a) P-wave velocity, (b) S-wave velocity, (c) P-wave attenuation, and (d) S-wave attenuation. The P-wave velocity and attenuation were measured at 0 to –15 °C (solid curve with solid squares). The velocity and attenuation were predicted by the Carcione (2007) (broken curve) and Leurer (solid curve) models, respectively. For the Carcione (2007) model, "B" indicates Biot flow, and for the Leurer model, "S" indicates squirt flow in porous ice.

To compare predictions with ultrasonic measurements for partially frozen brine, the P-wave frequency as 500 kHz, freezing point T_0 as –2 °C, and average pore radius r_{av} as 15 μm are assumed. The P-wave velocity (Fig. 5.3a) and attenuation (Fig. 5.3c) were predicted by the Carcione (2007) (broken curve) and Leurer (solid curve) models, respectively. In Fig. 5.3a, the measured (solid curve with solid squares) and predicted (solid and broken curves) P-wave velocities are plotted as a function of temperature. We can see that their closest approach to each other was at lower temperatures (–10 °C), while the predicted values were lower than the measured values at temperatures higher than –10 °C. This may be due to the underestimation of ice saturation at lower temperatures in the rock physics model. In Fig. 5.3c, we can see that the P-wave attenuation predicted by the Leurer model (solid curve) was larger than that predicted by the Carcione (2007) model (broken curve), and it was closer to the measured attenuation at temperatures higher than –5 °C.

Similarly, an S-wave frequency as 150 kHz, freezing point T_0 as –2 °C, and average pore radius r_{av} as 15 μm are assumed. The S-wave velocity (Fig. 5.3b) and attenuation (Fig. 5.3d) were predicted by the Carcione (2007) (broken curve) and Leurer (solid curve) models, respectively. In Fig. 5.3b, we can see that the S-wave velocity predicted by the Carcione (2007) (broken curve) and Leurer (solid curve) models were almost the same. However, in contrast to P-wave attenuation, the S-wave attenuation predicted by the Carcione (2007) model (broken curve) was significantly higher than that predicted by the Leurer model (solid curve), and also significantly higher than the P-wave attenuation. The higher S-wave attenuation predicted by the Carcione (2007) model can partially explain why Matsushima et al. (2008) were not able to successfully observe S-wave data in partially frozen brine.

To investigate the effects of freezing point T_0 on the predicted velocity and attenuation, the P- and S-wave velocities and attenuations predicted by the Leurer model at assumed freezing points of 0 °C (broken curve), –1 °C (dotted curve), and –2 °C (solid curve) are plotted as a function of temperature in Fig. 5.4. The modeling frequency for P-waves was 500 kHz and for S-waves was 150 kHz, and the average pore radius r_{av} was 15 μm. We can see that the P- (Fig. 5.4a) and S-wave (Fig. 5.4b) velocities predicted by the Leurer model did not begin to increase exactly at the freezing point. This is possibly because the amount of ice formed by the initial freezing was not enough to change the bulk and shear moduli of the ice-brine mixture. They increased after the freezing point, as shown in Figs 5.4a and 5.4b, and the higher freezing point (broken curve) corresponds to earlier increases in velocity than at a lower freezing point (solid curve). We can also see that the peak of P-wave attenuation (Fig. 5.4c) and S-wave attenuation (Fig. 5.4d) corresponded to the initial rapid increase in P-wave velocity (Fig. 5.4a) and S-wave velocity (Fig. 5.4b), respectively. By comparing P-wave attenuation (Fig. 5.4c) predicted by the Leurer model at a freezing point of –2 °C (solid curve) with

measured attenuation (solid curve with solid squares), I infer that the freezing point in partially frozen brine is possibly close to –2 °C.

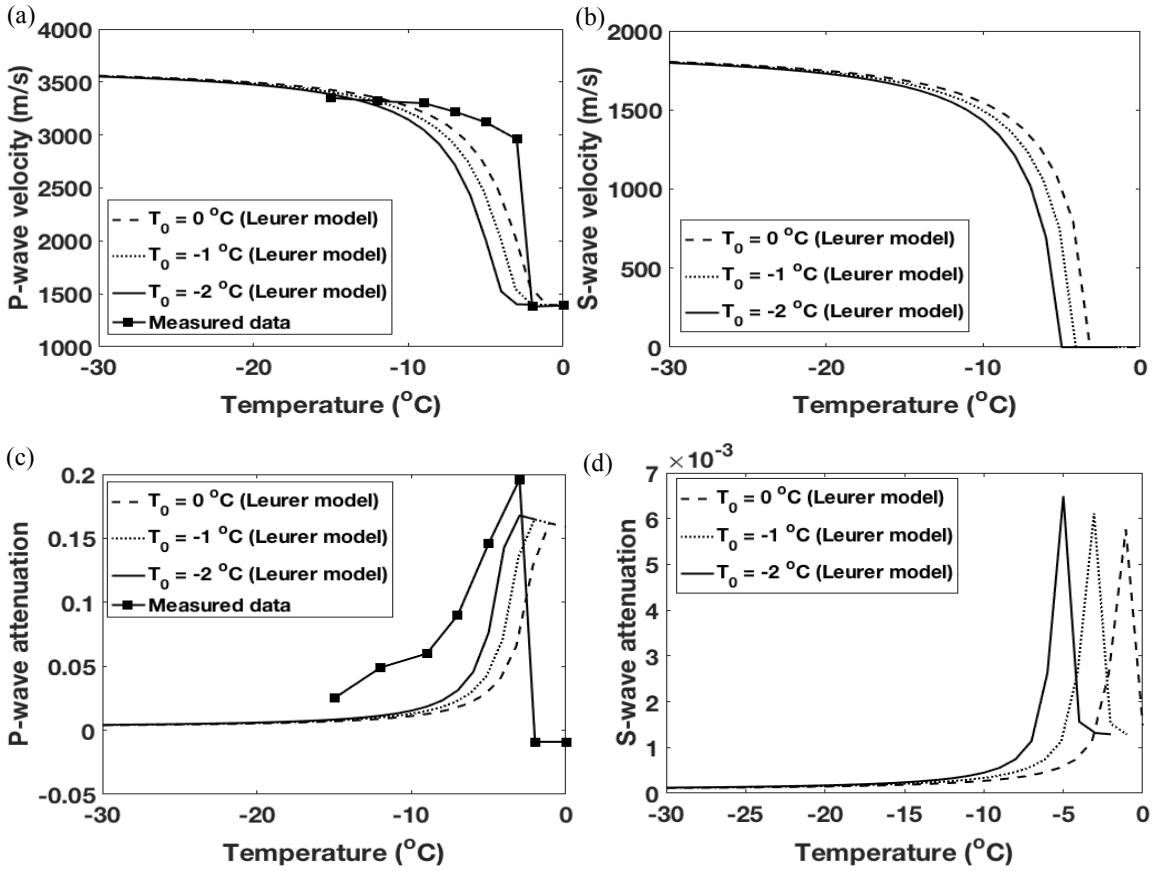

Figure 5. 4 Predicted and measured velocity and attenuation as a function of temperature in partially frozen brine at different freezing points T_0: (a) P-wave velocity, (b) S-wave velocity, (c) P-wave attenuation, and (d) S-wave attenuation. The P-wave velocity and attenuation were measured at 0 to –15 °C (solid curve with solid squares). The velocity and attenuation were predicted by the Leurer model at assumed T_0 of 0 °C (broken curve), –1 °C (dotted curve), and –2 °C (solid curve).

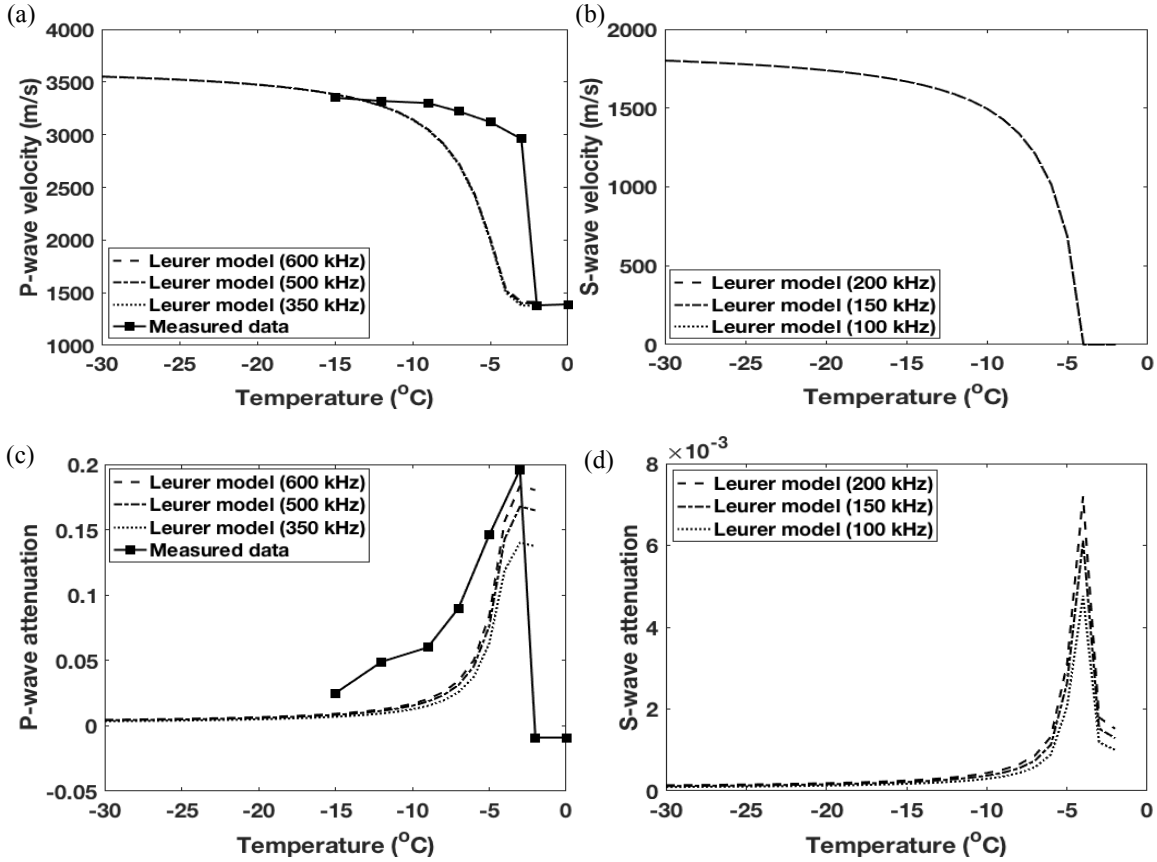

Figure 5. 5 Predicted and measured velocity and attenuation as a function of temperature in partially frozen brine at different frequencies: (a) P-wave velocity, (b) S-wave velocity, (c) P-wave attenuation, and (d) S-wave attenuation. The P-wave velocity and attenuation were measured at 0 to –15 °C (solid curve with solid squares). The velocity and attenuation were predicted by the Leurer model at assumed frequencies of 600 kHz (broken curve), 500 kHz (dotted-dashed curve), and 350 kHz (dotted curve) for P-waves (panels a and c) and 200 kHz (broken curve), 150 kHz (dotted-dashed curve), and 100 kHz (dotted curve) for S-waves (panels b and d).

The effects of wave frequency on the predicted velocity and attenuation are also investigated. Assuming freezing point T_0 of –2 °C and average pore radius r_{av} of 15 μm, the P-wave (Fig. 5.5a) and S-wave (Fig. 5.5b) velocities and P-wave (Fig. 5.5c) and S-wave (Fig. 5.5d) attenuations predicted by the Leurer model at different frequencies were plotted as a function of temperature. We can find that the frequency had a slight influence on P-wave velocity (Fig. 5.5a), but it had almost no influence on S-wave velocity (Fig. 5.5b). The P-wave attenuation (Fig. 5.5c) and S-wave attenuation (Fig. 5.5d) predicted by the Leurer model increased with increasing frequency in the domain of 350–600 kHz for P-waves and 100–200 kHz for S-waves. For P-wave attenuation (Fig. 5.5c), three different predicted attenuation curves at different frequencies of 350 kHz (lower limit of the processing frequency, dotted curve), 500 kHz (center of the processing frequency, dotted-dashed curve), and 600 kHz (upper limit

of the processing frequency, broken curve) were slightly different from each other (higher frequency results in higher attenuation) and were lower than the measured values (solid curve with solid squares). For S-wave attenuation (Fig. 5.5d), three different predicted attenuation curves at different frequencies of 100 kHz (lower limit of the processing frequency, dotted curve), 150 kHz (center of the processing frequency, dotted-dashed curve), and 200 kHz (upper limit of the processing frequency, broken curve) were slightly different from each other; that is, higher frequency resulted in higher attenuation.

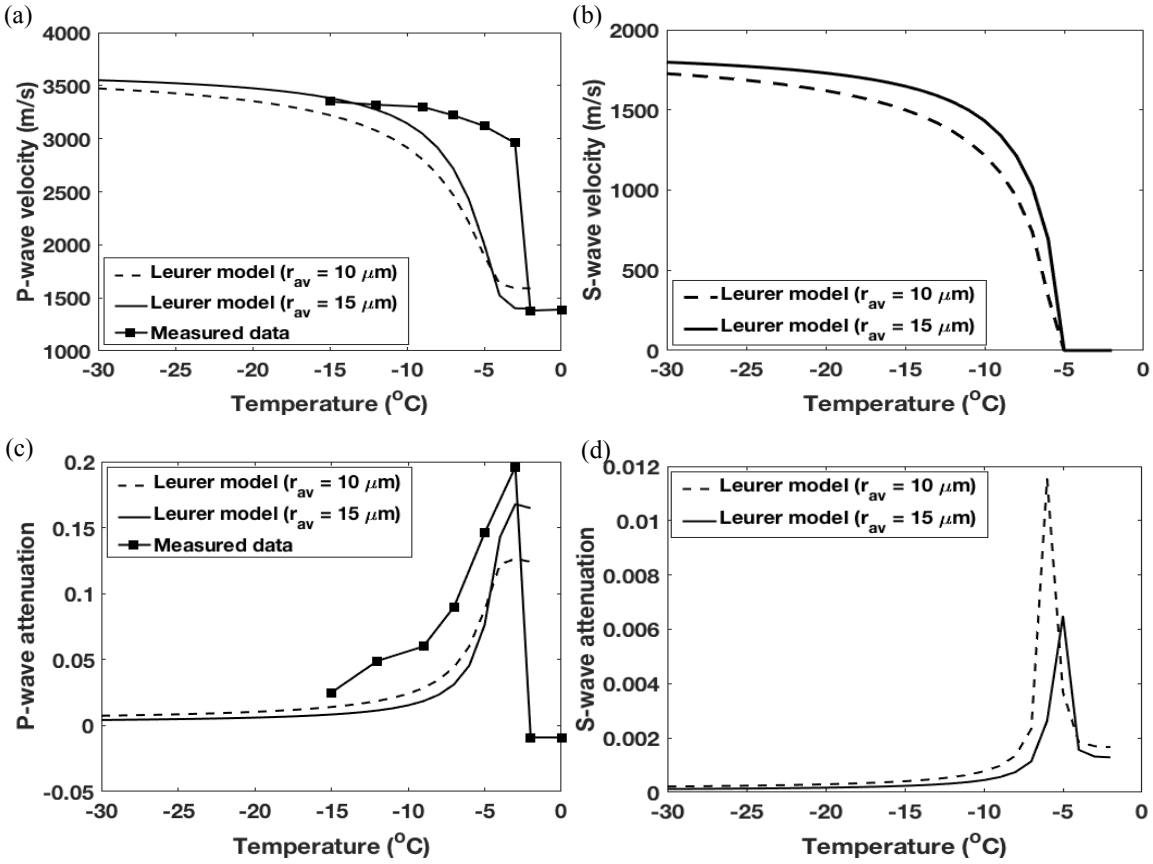

Figure 5. 6 Predicted and measured velocity and attenuation as a function of temperature in partially frozen brine for different average pore radii r_{av} : (a) P-wave velocity, (b) S-wave velocity, (c) P-wave attenuation, and (d) S-wave attenuation. The P-wave velocity and attenuation were measured at 0 to –15 °C (solid curve with solid squares). The velocity and attenuation were predicted by the Leurer model at assumed r_{av} of 10 μm (broken curve) and 15 μm (solid curve).

The effects of average pore radius r_{av} on the predicted velocity and attenuation are investigated. The r_{av} significantly affected the unfrozen brine saturation versus temperature curves. Assuming freezing point T_0 of –2 °C, the P-wave (Fig. 5.6a) and S-wave (Fig. 5.6b) velocities and P-wave (Fig. 5.6c) and S-wave (Fig. 5.6d) attenuations predicted by the Leurer model at r_{av} of 15 μm (solid curve)

and 10 μm (broken curve) were plotted as a function of temperature. The modeling frequency for P-waves was 500 kHz and for S-waves was 150 kHz. An r_{av} of 10 μm indicates larger unfrozen brine saturation compared with r_{av} of 15 μm, then results in lower P-wave (broken curve in Fig. 5.6a) and S-wave (broken curve in Fig. 5.6b) velocities at lower temperatures. By comparing the predicted and measured P-wave velocity (Fig. 5.6a) and attenuation (Fig. 5.6c) values, we can see that predicted velocity and attenuation at r_{av} of 15 μm (solid curve) is closer to measured values (solid curve with solid squares) than at r_{av} of 10 μm (broken curve). In Fig. 5.6d, the predicted S-wave attenuation at r_{av} of 15 μm (solid curve) is smaller than that at r_{av} of 10 μm (broken curve).

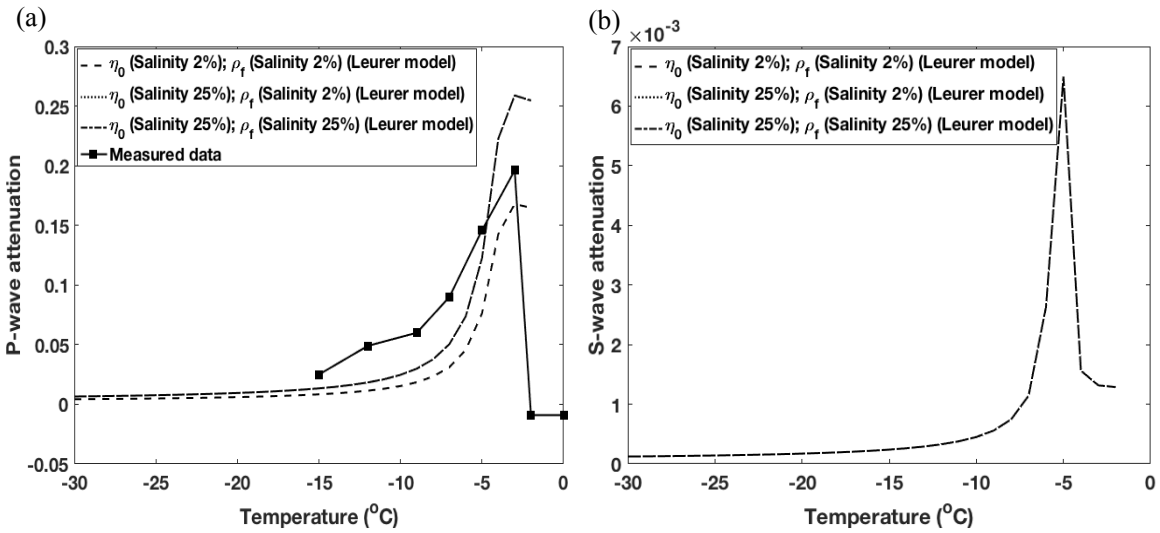

Figure 5. 7 Predicted and measured attenuation as a function of temperature in partially frozen brine: (a) P-wave attenuation and (b) S-wave attenuation. The P- and S-wave attenuations were measured at 0 to –15 °C (solid curve with solid squares), and the attenuations were predicted by the Leurer model at viscosity and density for salinity of 2% (broken curve), viscosity for salinity of 25% and density for salinity of 2% (dotted curve), and viscosity and density for salinity of 25% (dotted-dashed curve).

Finally, I investigated the effects of initial viscosity η_0 and density ρ_f of unfrozen brine on P- and S-wave attenuations. Assuming freezing point T_0 of –2 °C and average pore radius r_{av} of 15 μm, the P-wave (Fig. 5.7a) and S-wave (Fig. 5.7b) attenuations predicted by the Leurer model were plotted as a function of temperature. In Fig. 5.7a, we can see that the P-wave attenuation curve at η_0 for salinity of 25% and ρ_f for salinity of 2% (dotted curve) is the same as the attenuation at η_0 and ρ_f for salinity of 25% (dotted-dashed curve). Both of them were larger than the attenuation at η_0 and ρ_f for salinity of 2% (broken curve), which is more similar to the measured values (solid curve with solid

squares). In Fig. 5.7b, we can see that the three curves of S-wave attenuation under above three assumptions about η_0 and ρ_f of unfrozen brine are the same.

5.5.3 Application of Guerin model to partially frozen unconsolidated sand

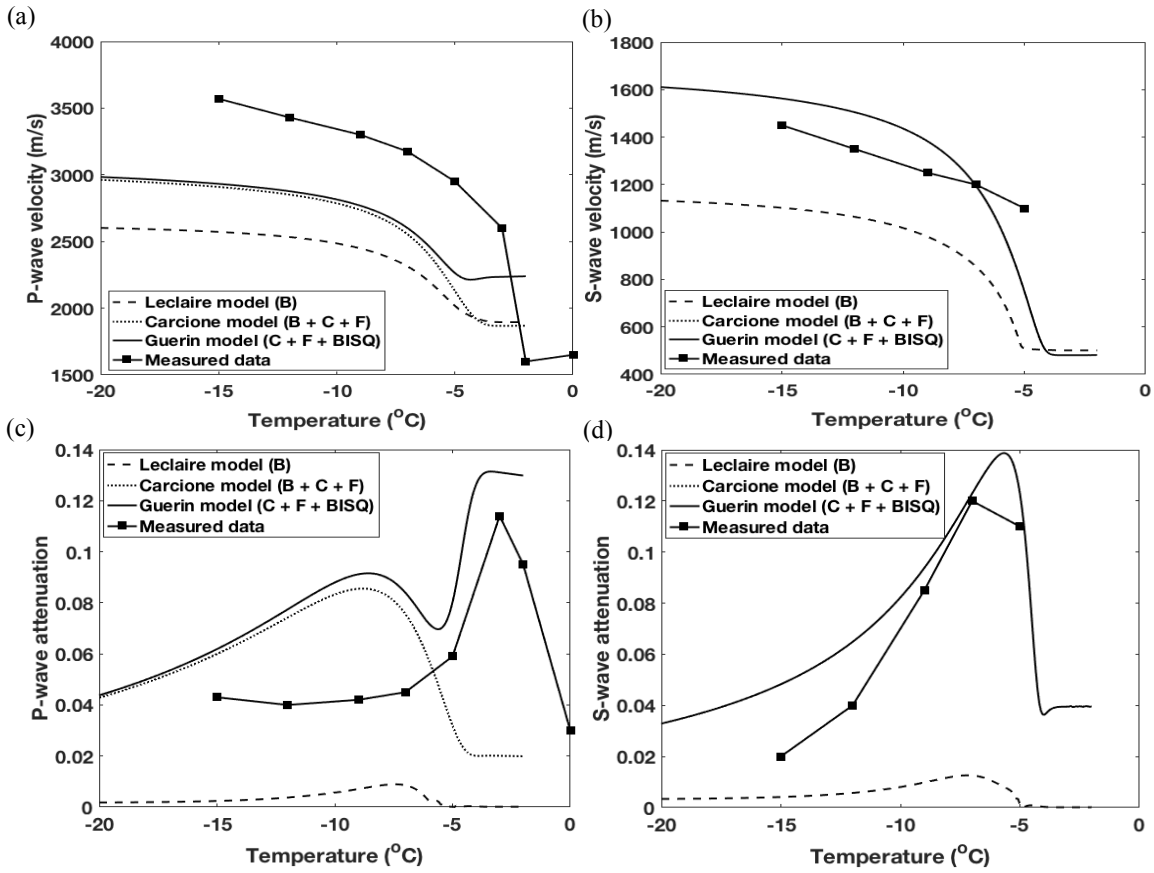

Figure 5. 8 Predicted and measured velocity and attenuation as a function of temperature for partially frozen unconsolidated sands using the Leclaire (broken curve), Carcione (dotted curve), and Guerin (solid curve) models: (a) P-wave velocity, (b) S-wave velocity, (c) P-wave attenuation, and (d) S-wave attenuation. "C" indicates cementation, "B" indicates Biot flow, and "F" indicates friction between the ice and sand grains, which was ignored in Carcione and Tinivella (2000) but was added in the implementation of the Carcione model. The S-wave velocity (b) and attenuation (d) predicted by the Carcione and Guerin models were the same. The P- and S-wave velocities and attenuations were measured at 0 to –15 °C (solid curve with solid squares).

The P-wave (Fig. 5.8a) and S-wave (Fig. 5.8b) velocities and P-wave (Fig. 5.8c) and S-wave (Fig. 5.8d) attenuations predicted by the Leclaire model (broken curve), Carcione model (dotted curve), and Guerin model (solid curve) were plotted as a function of temperature. The modeling frequency for P-waves was 500 kHz and for S-waves was 150 kHz, the average pore radius r_{av} was 15 μm, and the

freezing point T_0 was –2 °C. As shown in Fig. 5.8a, the predicted P-wave velocity values (broken, solid, and dotted curves) were lower than measured values (solid curve with solid squares). In Fig. 5.8b, we can see that the S-wave velocity predicted by the Guerin model (solid curve) was higher than the measured velocity (solid curve with solid squares) at less than –7 °C. This is possibly explained by cementation between ice and sand grains, which is considered in the Guerin model, significantly increasing S-wave velocity. For P-wave (Fig. 5.8c) and S-wave (Fig. 5.8d) attenuations, the attenuation curve predicted by the Leclaire model, which is based only on Biot flow (broken curve), was extremely lower than the measured attenuation (solid curve with solid squares). The P-wave attenuation curve (Fig. 5.8c) predicted by the Carcione model (dotted curve) has a shape similar to the measured attenuation curve (solid curve with solid squares), but the predicted attenuation peak shifted to a lower temperature compared with the measured peak. Meanwhile, the S-wave attenuation (Fig. 5.8d) was more coincident with the measured attenuation than it was for P-waves. Regarding P-wave attenuation in Fig. 5.8c, the values predicted by the Guerin model (solid curve) were higher than the measured values, but the predicted attenuation peak correlated well with the measured peak. In Fig. 5.8d, the S-wave attenuation predicted by the Carcione model (dotted curve) was identical to that predicted by the Guerin model (solid curve) because squirt flow has no effect on S-waves in the Guerin model.

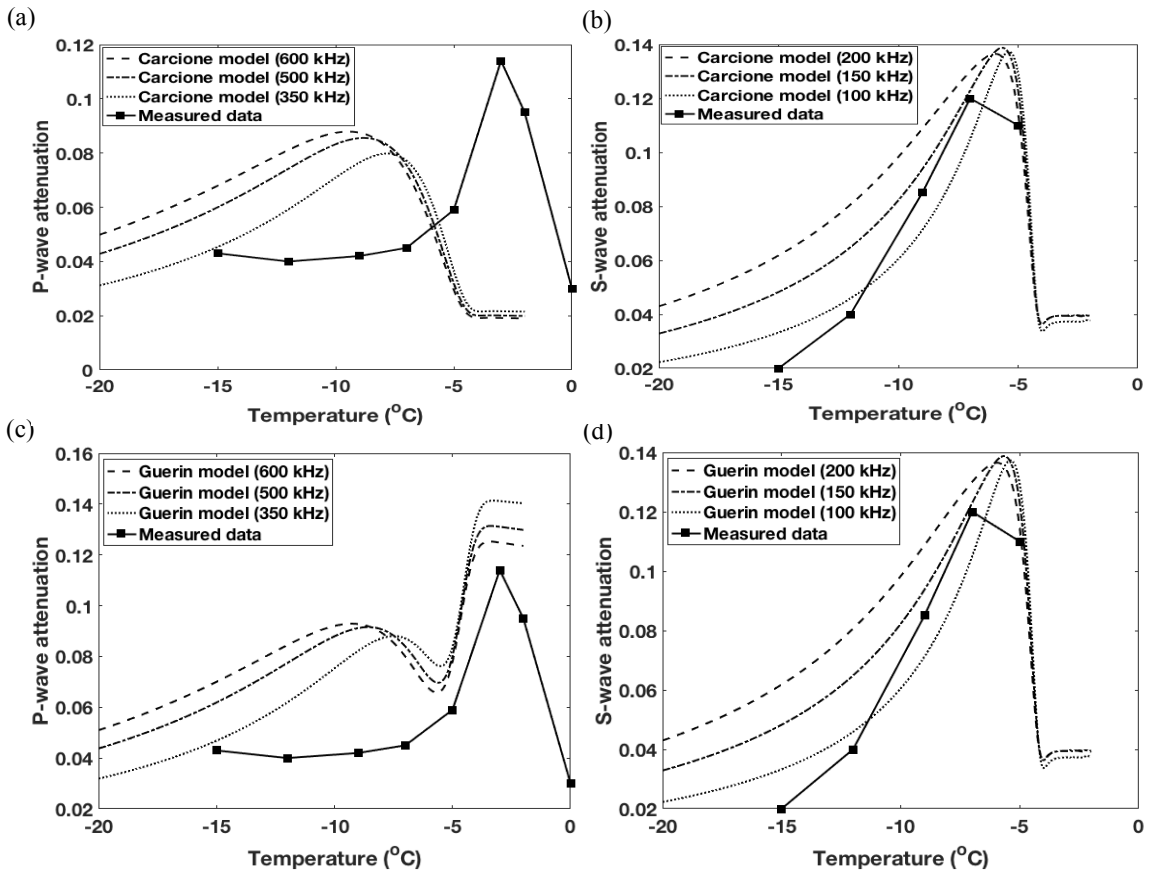

Figure 5. 9 Predicted and measured attenuation as a function of temperature in partially frozen unconsolidated sands at different frequencies: (a) P-wave attenuation (Carcione model), (b) S-wave attenuation (Carcione model), (c) P-wave attenuation (Guerin model), and (d) S-wave attenuation (Guerin model). The attenuations were predicted for assumed frequencies of 600 kHz (broken curve), 500 kHz (dotted-dashed curve), and 350 kHz (dotted curve) for P-waves, and 200 kHz (broken curve), 150 kHz (dotted-dashed curve), and 100 kHz (dotted curve) for S-waves. The P- and S-wave attenuations were measured at 0 to –15 °C (solid curve with solid squares).

In Fig. 5.9, the effect of the modeled wave frequency on the P- and S-wave attenuation curves predicted by the Carcione and Guerin models were showed. The average pore radius r_{av} was 15 μm, and the freezing point T_0 was –2 °C. The P-wave (Fig. 5.9a) and S-wave (Fig. 5.9b) attenuations predicted by the Carcione model, and P-wave (Fig. 5.9c) and S-wave (Fig. 5.9d) attenuations predicted by the Guerin model were plotted as a function of temperature on the assumption of frequencies of 600 kHz (upper limit of processing frequency, broken curve), 500 kHz (center of processing frequency, dotted-dashed curve), and 350 kHz (lower limit of processing frequency, dotted curve) for P-waves, and 200 kHz (upper limit of processing frequency, broken curve), 150 kHz (center of processing frequency, dotted-dashed curve), and 100 kHz (lower limit of processing frequency, dotted curve) for S-waves. We can see that the P-wave attenuation (Fig. 5.9a) and S-wave attenuation

(Fig. 5.9b) predicted by the Carcione model increased with increasing frequency at the domains of 350–600 kHz for P-waves and 100–200 kHz for S-waves. The S-wave attenuation predicted by the Guerin model (Fig. 5.9d) was almost the same as that predicted by the Carcione model (Fig. 5.9b). However, for P-wave attenuation predicted by the Guerin model (Fig. 5.9c), I found that the attenuation at temperatures lower than –7 °C increased with increasing frequency from 350 to 600 kHz, while the attenuation caused by squirt flow at temperatures higher than –5 °C (Fig. 5.9c) decreased with increasing frequency, and the predicted P-wave attenuation at three different frequencies was higher than the measured attenuation.

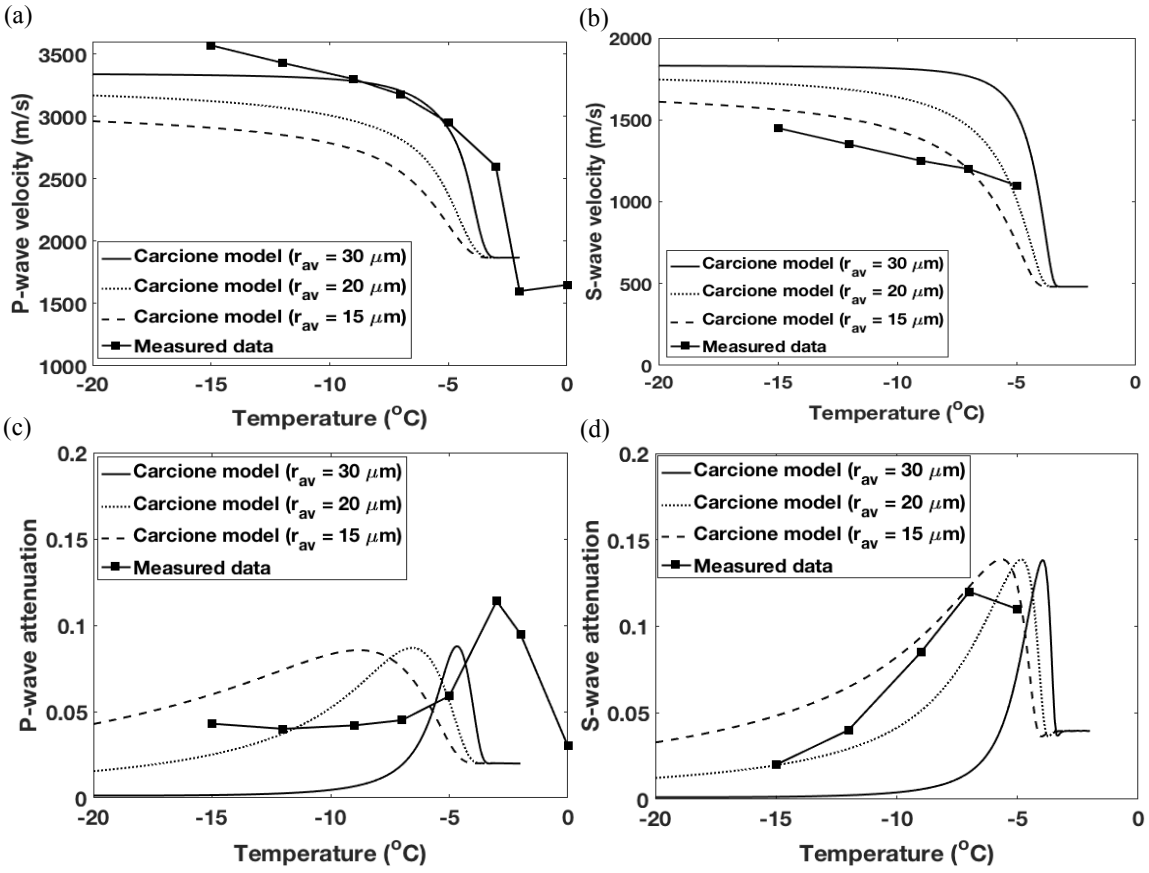

Figure 5. 10 Predicted and measured velocity and attenuation as a function of temperature in partially frozen unconsolidated sands using the Carcione model for different average pore radii r_{av} : (a) P-wave velocity, (b) S-wave velocity, (c) P-wave attenuation, and (d) S-wave attenuation. The velocity and attenuation were predicted by the Carcione model at assumed average pore radii r_{av} of 15 μm (broken curve), 20 μm (dotted curve), and 30 μm (solid curve). The P- and S-wave velocities and attenuations were measured at 0 to –15 °C (solid curve with solid squares).

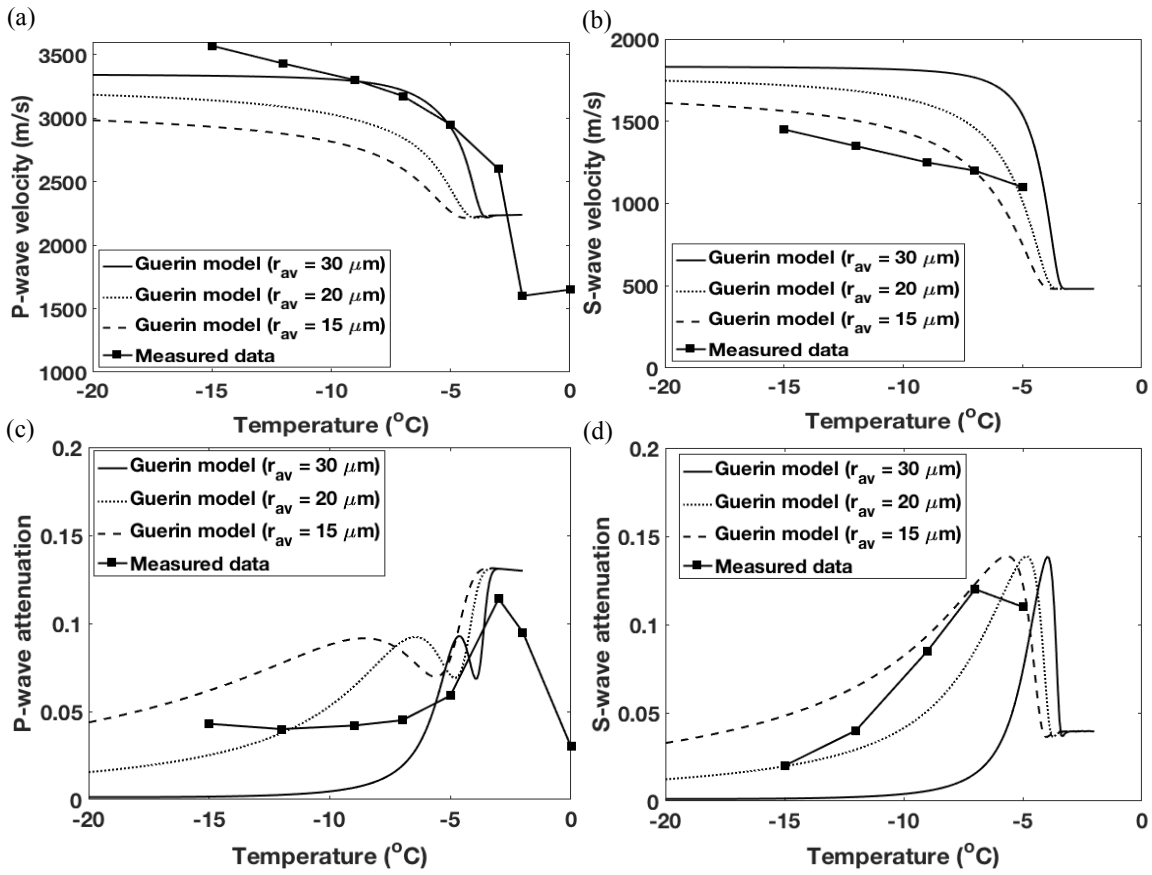

Figure 5. 11 Predicted and measured velocity and attenuation as a function of temperature in partially frozen unconsolidated sands using the Guerin model for different average pore radii r_{av} : (a) P-wave velocity, (b) S-wave velocity, (c) P-wave attenuation, and (d) S-wave attenuation. The velocity and attenuation were predicted by the Guerin model for assumed average pore radii r_{av} of 15 µm (broken curve), 20 µm (dotted curve), and 30 µm (solid curve). The P- and S-wave velocity and attenuation were measured at 0 to –15 °C (solid curve with solid squares).

The effect of the average pore radius r_{av} on velocity and attenuation curves predicted by the Carcione model was showed in Fig. 5.10 and Guerin model in Fig. 5.11. The modeling frequency for P-waves was 500 kHz and for S-waves was 150 kHz, and the freezing point T_0 was –2 °C. The P-wave (Fig. 5.10a) and S-wave (Fig. 5.10b) velocities and P-wave (Fig. 5.10c) and S-wave (Fig. 5.10d) attenuations predicted by the Carcione model were plotted as a function of temperature. The larger r_{av} of 30 µm indicated lower unfrozen brine saturation at temperatures lower than –7 °C, which produced higher predicted velocity for P- (solid curve in Fig. 5.10a) and S-waves (solid curve in Fig. 5.10b) and lower predicted attenuation for P- (solid curve in Fig. 5.10c) and S-waves (solid curve in Fig. 5.10d) at temperatures lower than –7 °C compared to the predicted values for a smaller r_{av} of 15 µm (broken curve). From Fig. 5.10b, the predicted S-wave velocity was larger than the measured velocity possibly

due to the effect of cementation between sand grains and ice in the Carcione model. In Figs 5.10c and 5.10d, we can see that the lower r_{av} (broken curve) leads to attenuation peaking at a lower temperature. By comparing the predicted P-wave (Fig. 5.10c) and S-wave (Fig. 5.10d) attenuations with the measured attenuations, we can see that the predicted values at r_{av} of 20 μm seem to fit the measured attenuations best. The P-wave (Fig. 5.11a) and S-wave (Fig. 5.11b) velocities and P-wave (Fig. 5.11c) and S-wave (Fig. 5.11d) attenuations predicted by the Guerin model were also plotted as a function of temperature. The S-wave velocity (Fig. 5.11b) and attenuation (Fig. 5.11d) predicted by the Guerin model were the same as those predicted by the Carcione model (Figs 5.10b and 5.10d). From Fig. 5.11a, the predicted P-wave velocity was slightly smaller than the measured value. From Fig. 5.11c, we can see that the predicted P-wave attenuation at temperatures ranging from –2 to –5°C was larger than the measured values, while the predicted P-wave attenuation at temperatures lower than –5°C was similar to that predicted by the Carcione model (Fig. 5.10c).

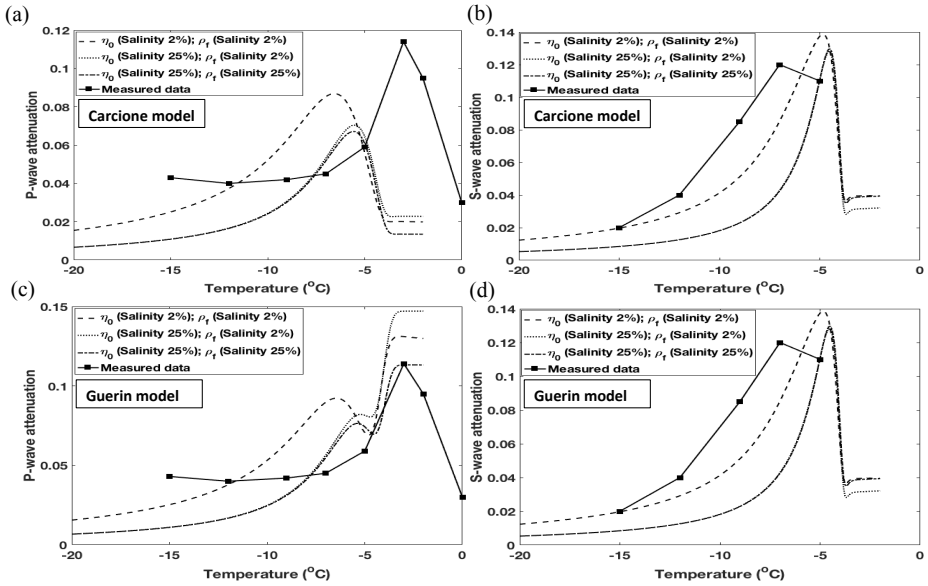

Figure 5. 12 Predicted and measured attenuation as a function of temperature in partially frozen unconsolidated sands: (a) P-wave attenuation (Carcione model), (b) S-wave attenuation (Carcione model), (c) P-wave attenuation (Guerin model), and (d) S-wave attenuation (Guerin model). The P- and S-wave attenuations were measured at 0 to –15 °C (solid curve with solid squares), and the attenuations were predicted at viscosity and density for salinity of 2% (broken curve), viscosity for salinity of 25% and density for salinity of 2% (dotted curve), and viscosity and density for salinity of 25% (dotted-dashed curve).

In Fig. 5.12, the effect of initial viscosity η_0 and density ρ_f of unfrozen brine on P- and S-wave attenuation curves predicted by the Carcione and Guerin models were showed. The modeling frequency for P-waves was 500 kHz and for S-waves was 150 kHz, the average pore radius r_{av} was 20

μm, and the freezing point T_0 was –2 °C. The P- (Fig. 5.12a) and S-wave attenuations (Fig. 5.12b) predicted by the Carcione model and P- (Fig. 5.12c) and S-wave attenuations (Fig. 5.12d) predicted by the Guerin model were plotted as a function of temperature. Based on the rock physics model, I simply divided the temperature range into three parts (–2 to –4 °C, –4 to –5 °C, and lower than –5 °C) and then described the different performances within each temperature range. From Figs 5.12a to 5.12d, we can see that at temperatures lower than –5 °C, the predicted attenuation at η_0 for salinity of 25% and ρ_f for salinity of 2% (dotted curve) is the same as the attenuation at η_0 and ρ_f for salinity of 25% (dotted-dashed curve). Both of them were smaller than the attenuation at η_0 and ρ_f for salinity of 2% (broken curve). At temperatures lower than –5 °C, P-wave attenuation (broken, dotted, and dotted-dashed curves in Fig. 5.12c) predicted by the Guerin model was similar to that predicted by the Carcione model (broken, dotted, and dotted-dashed curves in Fig. 5.12a). However, at –4 to –5 °C, in Figs 5.12a, 5.12b, and 5.12d, both predicted P- and S-wave attenuations sharply increased, and the difference among predicted curves under three assumptions about η_0 and ρ_f of unfrozen brine was very small. In Fig. 5.12c, the predicted P-wave attenuations sharply decreased, and the predicted attenuation at η_0 for salinity of 25% and ρ_f for salinity of 2% (dotted curve) was the same as the attenuation at η_0 and ρ_f for salinity of 2% (broken curve). Both of them were larger than the attenuation at η_0 and ρ_f for salinity of 25% (dotted-dashed curve). At –2 to –4 °C, we can see that the P-wave attenuation predicted by the Carcione (Fig. 5.12a) and Guerin (Fig. 5.12c) models at η_0 for salinity of 25% and ρ_f for salinity of 2% (dotted curve) is slightly larger than that at η_0 and ρ_f for salinity of 2% (broken curve). Both of them were further larger than the attenuation at η_0 and ρ_f for salinity of 25% (dotted-dashed curve). At –2 to –4 °C, the S-wave attenuation predicted by the Carcione (Fig. 5.12b) and Guerin (Fig. 5.12d) models at η_0 and ρ_f for salinity of 25% (dotted-dashed curve) was almost the same as that at η_0 and ρ_f for salinity of 2% (broken curve). Both of them were larger than the attenuation at η_0 for salinity of 25% and ρ_f for salinity of 2% (dotted curve). In Fig. 5.12c, the predicted P-wave attenuation (broken and dotted curves) obtained by the Guerin model at –2 to –4 °C was significantly larger than the measured attenuation (solid curve with solid squares). In Figs 5.12b and 5.12d, we also can see that the predicted S-wave attenuation at η_0 and ρ_f for salinity of 2% (broken curve) match the measured values best. In Fig. 5.12a, the predicted and measured curves were similar, although their peaks did not coincide.

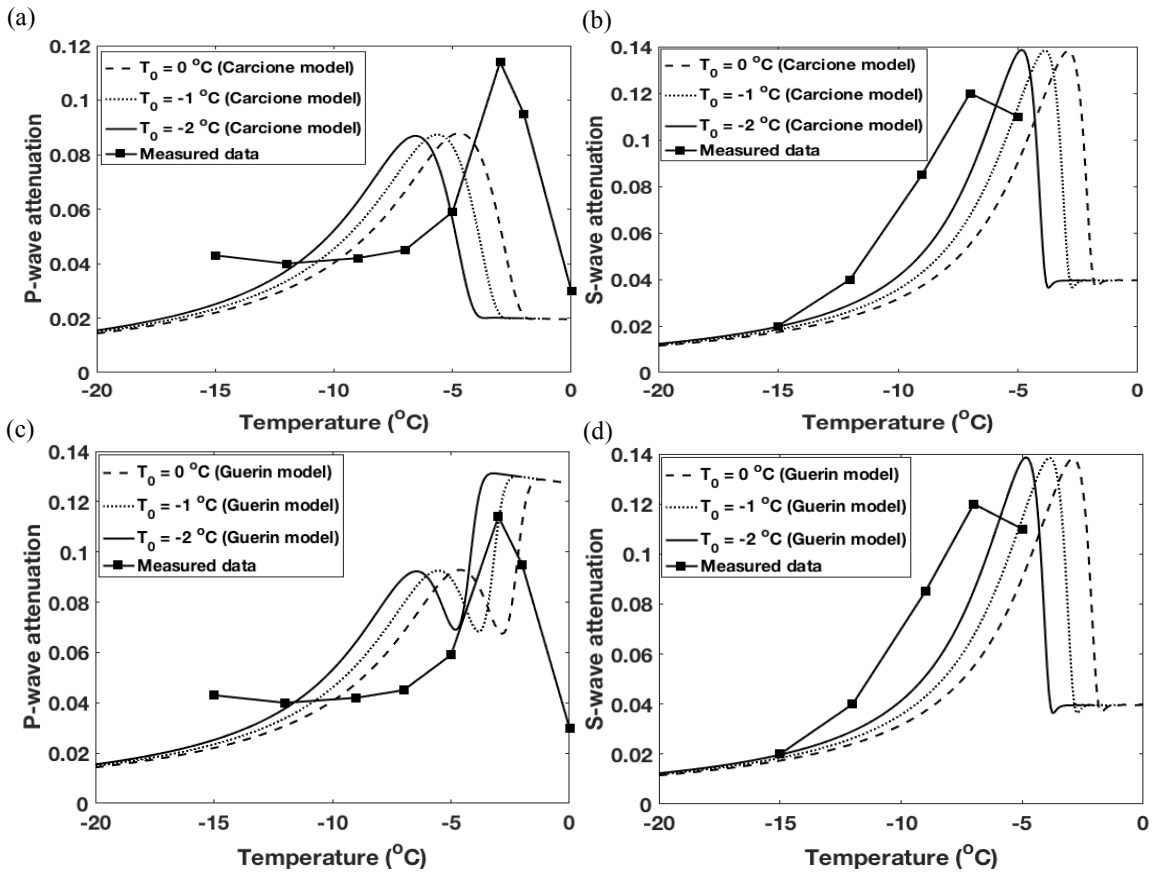

Figure 5. 13 Predicted and measured attenuation as a function of temperature in partially frozen unconsolidated sands at different freezing points T_0 : (a) P-wave attenuation (Carcione model), (b) S-wave attenuation (Carcione model), (c) P-wave attenuation (Guerin model), and (d) S-wave attenuation (Guerin model). The attenuation was measured at 0 to –15 °C (solid curve with solid squares). The attenuation was predicted for assumed freezing points T_0 of 0 °C (broken curve), –1 °C (dotted curve), and –2 °C (solid curve).

Finally, in Fig. 5.13, the effect of the freezing point on P- and S-wave attenuation curves predicted by the Carcione and Guerin models were showed. The modeling frequency for P-waves was 500 kHz and for S-waves was 150 kHz, and the average pore radius r_{av} was 20 μm. The P-wave attenuation (Fig. 5.13a) and S-wave attenuation (Fig. 5.13b) predicted by the Carcione model, and P-wave attenuation (Fig. 5.13c) and S-wave attenuation (Fig. 5.13d) predicted by the Guerin model at assumed freezing points T_0 of 0 °C (broken curve), –1 °C (dotted curve), and –2 °C (solid curve) were plotted as a function of temperature. I found that the freezing point affected the location of the predicted attenuation peak for both P- and S-waves. The lower freezing point (–2 °C) produced an attenuation peak at lower temperatures (solid curve) than that produced at a higher freezing point (0 °C) (broken curve). For P-wave attenuation predicted by the Carcione (Fig. 5.13a) and Guerin (Fig. 5.13c) models, the attenuation at a freezing point of 0 °C most closely matched the measured

attenuation (solid curve with solid squares). For S-wave attenuation predicted by the Carcione (Fig. 5.13b) and Guerin (Fig. 5.13d) models, the attenuation at a freezing point of –2 °C s most closely matched the measured attenuation (solid curve with solid squares).

5.6 Discussion

Based on the application of the Leurer model to partially frozen brine and application of the Guerin model to partially frozen unconsolidated sand, this section discusses possible attenuation mechanisms responsible for the measurements for these two systems.

5.6.1 Effects of freezing point, viscosity, and average pore radius on attenuation

5.6.1.1 Uncertainty of temperature measurement

When estimating the amount of unfrozen brine using equation 2, the freezing point T_0 affects the upper limit of the integral, which affects the final estimation of unfrozen brine saturation. Moreover, T_0 affects the initial freezing of brine, and few measurements at this point have indicated a close relationship between attenuation peak and initial freezing (Matsushima et al., 2016; Wu et al., 2017).

In ultrasonic measurements, the temperature setting is always different from the temperature where the source/receiver is located due to the inhomogeneous temperature field inside the measurement sample. Suzuki et al. (2010) indicated that the temperature in the measurement sample is different from the chamber temperature setting. The fact that the temperature in the upper part of the measurement sample is lower than that in its center and bottom parts can be explained by the endothermic effect of vaporization in the upper part. This effect leads to the lowest temperature being at the top of the measurement sample, so the freezing process begins near the top and then moves slowly downward (Suzuki et al., 2010). The ultrasonic source/receiver in their measurements was located at the center of the sample, but the measured temperature indicated the temperature setting, and they could not exactly measure the real temperature at the ultrasonic source/receiver location. Therefore, this temperature measurement uncertainty results in uncertainty in the curves for unfrozen brine saturation, velocity, and attenuation versus temperature.

Figs 5.4 and 5.13 show that the locations of the predicted P- and S-wave peak attenuations are significantly controlled by freezing point T_0. The P-wave attenuation predicted by the Leurer model at an assumed T_0 of –2 °C (solid curve in Fig. 5.4c) seems to best fit the attenuation measured for partially frozen brine. The S-wave attenuation predicted by the Guerin model at T_0 of –2 °C (solid curve in Fig. 5.13d) seems to best fit the attenuation measured for partially frozen unconsolidated sand.

However, the P-wave attenuation predicted by the Carcione model (broken curve in Fig. 5.13a) at T_0 of 0 °C best fitted the measured P-wave attenuation for partially frozen unconsolidated sand. This might be caused by uncertainties in the estimation of temperature and unfrozen brine saturation.

5.6.1.2 Effect of viscosity on attenuation

In freezing brine, salts are rejected from the ice crystals and remain in the unfrozen liquid. As a result, the salinity in the remaining brine increases continuously with decreasing temperature. This increased salinity further lowers the freezing point of unfrozen brine (Banin and Anderson, 1974), and increases its viscosity and density (Francke & Thorade, 2010; Simion et al., 2015). Although I have considered the effect of decreasing temperature on viscosity in the rock physics models, I did not consider the effect of increasing salinity caused by decreasing freezing point on viscosity and density. However, the comparison between predicted and measured viscosity at an initial salinity of 25% indicates a small difference in the temperature range of interest (dotted and broken curves in Fig. 5.1), which implies that increasing salinity has a small effect on viscosity within this temperature range (0 to –15 °C).

The effect of viscosity on P- and S-wave attenuations in partially frozen brine was shown in the attenuation curves predicted by the Leurer models (Fig. 5.7). In Figs 5.7a and 5.7b, the predicted attenuation at η_0 for salinity of 25% and ρ_f for salinity of 2% (dotted curve) was the same as the attenuation at η_0 and ρ_f for salinity of 25% (dotted-dashed curve). It implies that the ρ_f does not affect both the P- and S-wave attenuations in partially frozen brine. The predicted P-wave attenuation (Fig. 5.7a) at η_0 for salinity of 25% and ρ_f for salinity of 2% (dotted curve) was larger than the attenuation at η_0 and ρ_f for salinity of 2% (broken curve), while these two curves were the same for S-wave attenuation (Fig. 5.7b). It might imply different effect of viscosity on P- and S-wave attenuations. The η_0 for salinity of 25% is larger than that for salinity of 2%. The above results might be explained by that the squirt flow caused by the brine inclusions in porous ice increases with increasing viscosity, and then enhances P-wave attenuation (Fig 5.7a). The squirt flow, however, has no effect on S-wave attenuation (Fig 5.7b).

The effect of viscosity on P- and S-wave attenuations was shown in the attenuation curves predicted by the Carcione and Guerin models (Fig. 5.12). At temperatures lower than –5 °C, from Figs 5.12a to 5.12d, the attenuation at η_0 for salinity of 25% and ρ_f for salinity of 2% (dotted curve) was the same as the attenuation at η_0 and ρ_f for salinity of 25% (dotted-dashed curve). In fact, as shown in Fig. 5.2b, the amount of ice in pores exceeded 80% (dotted curve) at temperatures lower than –5 °C.

At this temperature range, the attenuation caused by fluid flow is very small, and then ρ_f might have little effect on both P- and S-wave attenuation. The attenuation at η_0 and ρ_f for salinity of 2% (broken curve) was larger than the attenuation at η_0 for salinity of 25% and ρ_f for salinity of 2% (dotted curve). These results imply that larger viscosity leads to smaller attenuation. A possible reason for this is that the larger viscosity enhances the coupling between ice (or sand) and unfrozen brine, and then weakens the relative motion between ice and sand grains, finally resulting in smaller attenuation.

In addition, at –2 to –4 °C, the most of pore is saturated with unfrozen brine. For P-waves, Carcione et al. (2007) inferred that Biot flow dominated P-wave attenuation at the initial freezing temperature for partially frozen juice, and Guerin and Goldberg (2005) indicated that squirt flow dominated the P-wave attenuation at lower hydrate saturation. The P-wave attenuation predicted by the Carcione model is caused by the Biot flow in pores between sand grains or ices, while for the Guerin model is caused by the Biot and squirt flow in pores between sand grains or ices. The increasing ρ_f would make the flow of unfrozen brine difficult, and then decreasing the attenuation caused by Biot flow or squirt flow. This might explain why the attenuation at η_0 for salinity of 25% and ρ_f for salinity of 2% (dotted curve) was larger than the attenuation at η_0 and ρ_f for salinity of 25% (dotted-dashed curve) in Figs 5.12a and 5.12c. The increasing η_0 would increase the attenuation caused by Biot flow or squirt flow. This might explain why the attenuation at η_0 for salinity of 25% and ρ_f for salinity of 2% (dotted curve) was larger than the attenuation at η_0 and ρ_f for salinity of 2% (broken curve) in Figs 5.12a and 5.12c. For S-wave attenuation predicted by the Carcione (Fig. 5.12b) and Guerin (Fig. 5.12d) models at η_0 and ρ_f for salinity of 2% (broken curve) was larger than the attenuation at η_0 for salinity of 25% and ρ_f for salinity of 2% (dotted curve). This can be explained by that the increasing η_0 would enhance the coupling between sand grains and brine, and then decrease the relative motion between sand grains and brine.

At temperatures ranging from –4 to –5 °C, we can find that the ice saturation sharply increased from less than 5% to more than 80% (dotted curve in Fig. 5.2b). For P- (Fig. 5.12a) and S-wave (Fig. 5.12b) attenuation predicted by the Carcione model and S-wave attenuation predicted (Fig. 5.12d) by the Guerin model, the friction between sand grains and ice is the dominant attenuation mechanism. Within this temperature range, the effect of increasing ice (decreasing unfrozen brine) overwhelms the effect of other parameters on attenuation, such as viscosity. This might explain the small difference among the three predicted attenuation curves in Figs 5.12a, 5.12b, and 5.12d. For predicted P-wave attenuation (Fig. 5.12c) by the Guerin model at temperatures ranging from –4 to –5 °C, the attenuation

mechanism is a mixture of increasing friction between sand grains and ice, and decreasing squirt flow caused by the ice formation. The decreasing P-wave attenuations under three assumptions about η_0 and ρ_f of unfrozen brine sharply decrease possibly because of the overwhelming decrease squirt flow caused by the decreasing permeability due to ice formation. In summary, I infer that the increasing salinity increased the viscosity of unfrozen brine, but it produced two opposite effects on the attenuation: (1) increasing attenuation caused by Biot and squirt flow, and (2) decreasing attenuation caused by inertial coupling between brine and sand grains (ice).

5.6.1.3 Effect of average pore radius on attenuation

A certain amount of unfrozen fluid still exists even at very low temperatures in a partially frozen system. NMR data showed that the unfrozen water saturation ϕ_w was approximately 15% at –20 °C and 5% at –50 °C in partially frozen orange juice (Carcione et al., 2007). For another example, water saturation of 10%–20% still existed in frozen limestone rock, even at a temperature as low as –40 °C (Bellanger et al., 1996). It is believed to exist either as solely adsorbed water on the capillary walls or as both adsorbed and free water that is unaffected by the water-ice phase change. In my case, the quantity of unfrozen brine at low temperature (–15 °C) was verified by the NMR data in partially frozen brine (34% at –15 °C) in Fig. 5.2a and partially frozen unconsolidated sand (20% at –15 °C) in Fig. 5.2b. In the rock physics models, we could change the freezing rate and final unfrozen brine saturation by changing the average pore radius r_{av} in equation 2. As Fig. 5.2b shows, comparison of the unfrozen brine saturation predicted by the Leclaire model with different r_{av} shows that a larger average radius (dotted-dashed curve) results in a faster reduction rate and lower final unfrozen brine saturation than that produced by a smaller average radius (solid curve). This can be explained by the liquid beginning to freeze in pore spaces with smaller surface-to-volume ratios (larger pores), and then ice forming in smaller pores as the temperature decreases further (Timur, 1968; Matsushima et al., 2016). As Figs 5.6, 5.10, and 5.11 show, the shape and peak position of predicted P- and S-wave attenuations are significantly controlled by r_{av}. For partially frozen brine, the P-wave attenuation (solid curve in Fig. 5.6c) at r_{av} of 15 μm seems to best fit the measured values. The P- and S-wave attenuations predicted by the Carcione model (dotted curve in Figs 5.10c and 5.10d) and Guerin model (dotted curves in Figs 5.11c and 5.11d) at r_{av} of 20 μm seem to fit the measured values best, especially for S-waves (dotted curves in Figs 5.10d and 5.11d).

However, note that in Fig 5.2b, the unfrozen brine saturation predicted by the Leclaire model for an average pore radius of 20 μm is less than 10% at –15 °C, which is much lower than the 20% measured by NMR at the same temperature for partially frozen unconsolidated sand. In addition, the

unfrozen brine saturation versus temperature curves show that for partially frozen brine, the unfrozen brine saturation at r_{av} of 10 μm fits the NMR data best (solid curve in Fig. 5.2a), and for partially frozen unconsolidated sand, this value is 15 μm (solid curve in Fig. 5.2b). This discrepancy implies a possible uncertainty in estimation of unfrozen brine saturation by the NMR technique (Matsushima et al., 2016). Matsushima et al. (2016) indicated that the increase of the viscosity of the remaining unfrozen brine with high salinity resulted in an overestimation of the number of smaller pores, which further affected the relaxation time exhibited in NMR measurements. This uncertainty of estimation of unfrozen brine saturation may cause the possibly poor fit between the predicted and measured values for unfrozen brine saturation versus temperature.

5.6.2 Attenuation mechanisms in partially frozen brine

Carcione et al. (2007) used a Biot poroelastic model to successfully predict velocity and attenuation in partially frozen orange juice. Matsushima et al. (2011) employed this Biot poroelastic model to predict P-wave attenuation in partially frozen brine at a frequency of 500 kHz. They compared the predicted attenuation with laboratory ultrasonic data and concluded that Biot flow cannot completely predict the measured attenuation and then inferred that the squirt flow mechanism or wave scattering effect should be taken into account. In the rock physics modeling, we could also see that the P-wave attenuation (broken curve in Fig. 5.3c) predicted by the Carcione (2007) model was much lower than the measured attenuation at around –5 to –3 °C. In contrast, although the P-wave attenuation predicted by the Leurer model (solid curve in Fig. 5.3c) was slightly lower than the measured attenuation, the curve shapes were similar at temperatures below –2 °C. This similarity implies that the P-wave attenuation predicted by the Leurer model to some extent describe the P-wave propagation in partially frozen brine. The application of the Leurer model to partially frozen brine describes decreasing squirt flow with decreasing temperature because the inclusion concentration c_i becomes smaller as ice is formed below the freezing point. In other words, weakened squirt flow may be responsible for reduced P-wave attenuation during the freezing process after the attenuation reaches its peak. The application of the Carcione (2007) model describes the attenuation due to Biot flow (broken curve in Fig. 5.3c), and it cannot adequately explain the peak attenuation, especially near the freezing point.

Although several experiments have produced data associated with P-wave attenuation for partially frozen two-phase systems (Prasad and Dvorkin, 2004; Carcione et al., 2007; Matsushima et al., 2008; Pohl et al., 2017), few experiments have produced data for S-waves. Spetzler and Anderson (1968) observed a sharply increasing S-wave attenuation associated with the onset of partial melting at the eutectic point for ice with a salinity of 1%, which is less than our salinity (2%). Rock physics

modeling in this study may provide an insight into the S-wave propagation in partially frozen brine. The S-wave attenuation predicted by the Leurer model (solid curve in Fig. 5.3d) is obviously lower than that predicted by the Carcione model (broken curve in Fig. 5.3d), and the S-wave attenuation predicted by the Carcione model is quite large at the freezing point. This is possibly explained by a significant amount of unfrozen brine near the freezing point being unable to propagate S-waves. Furthermore, the magnitude of predicted S-wave attenuation is significantly larger than that for P-waves. This may explain why S-waves are difficult to observe in the measurement of partially frozen brine.

The application of the Leurer model to partially frozen brine seems to provide good prediction performance and also validates the inclusion theory. So far, several measurements have confirmed the existence of fluid inclusions in a two-phase system. Arenson and Sego (2006) identified ice needles with channels containing unfrozen saline water between ice crystals by fluorescent tracer technology. The residual unfrozen water between ice needles might be similar to fluid inclusions in porous ice. Matsushima et al. (2011) identified brine inclusions (less than 1 mm) and their connectivity by a diffusion-weighted magnetic resonance imaging technique. Pohl et al. (2017) identified the presence of water between THF hydrate grains by NMR and concluded that aqueous squirt flow increased attenuation in THF hydrate above the freezing point of water. These experiments and speculations might support the validity of applying the Leurer model to the partially frozen brine system.

5.6.3 Attenuation mechanisms in partially frozen unconsolidated sand

5.6.3.1 Attenuation mechanisms for P-waves

A P-wave attenuation peak around the freezing point has been indicated by several laboratory experiments (Matsushima et al., 2016; Wu et al., 2017). Dou et al. (2016) explained their observation as follows: (1) a wave-induced phase transition could absorb energy from P-waves and then might yield some intrinsic attenuation, (2) wave-induced fluid flow caused by pressure gradients (wavelength-scale Biot flow, pore-scale squirt flow, and mesoscopic flow) might lead to intrinsic attenuation, and (3) elastic scattering due to the heterogeneity of the partially frozen medium might result in apparent attenuation. Dou et al. (2016) also indicated that the P-wave attenuation peak occurred at an unfrozen brine saturation of 30% in unconsolidated saline permafrost. In contrast, Matsushima et al. (2016) observed a P-wave attenuation peak at –3 °C. The results indicate that the unfrozen brine saturation at –3 °C is estimated as 60% for an average pore radius r_{av} of 15 μm (solid curve in Fig. 5.2b), 50% for r_{av} of 20 μm (dotted curve in Fig. 5.2b), and 50% by NMR measurement. The P-wave attenuation predicted by the Carcione model (dotted curve in Fig. 5.8c) indicates

increasing P-wave attenuation from –2 to –9 °C. The unfrozen brine saturation at –9 °C was estimated as 20% for r_{av} of 15 μm (solid curve in Fig. 5.2b), 15% for r_{av} of 20 μm (dotted curve in Fig. 5.2b), and 25% by NMR measurement. This unfrozen brine saturation is similar to that corresponding to the P-wave attenuation peak observed by Dou et al. (2016). But the P-wave attenuation predicted by the Carcione model (dotted curve in Fig. 5.8c) displayed an inconsistent peak temperature with measured attenuation (solid curve with solid squares in Fig. 5.8c), though their curves are similar. The friction between sand grains and ice has been included in the implementation of the Carcione and Guerin models, and the attenuation peak at about –9 °C (dotted and solid curves in Fig. 5.8c) is attributed to the friction between sand grains and ice during ice formation.

In addition, although the P-wave attenuation predicted by the Guerin model (solid curve in Fig. 5.8c) from –2 to –5 °C failed to predict the peak of measured P-wave attenuation (solid curve with solid squares in Fig. 5.8c), their magnitude was similar. Guerin and Goldberg (2005) indicated that squirt flow in pores between sand grains or between hydrates increased P-wave attenuation at lower hydrate saturation, while the effect of squirt flow became negligible at higher hydrate saturation due to the extreme decrease in effective permeability. The peak of measured P-wave attenuation (solid curve with solid squares in Fig. 5.8c) at –3 °C might be explained by squirt flow in pores between sand grains. The decreasing P-wave attenuation from –3 to –15 °C (solid curve with solid squares in Fig. 5.8c) may be explained as follows: (1) squirt flow becomes smaller from –3 to –5 °C due the formation of ice (ice saturation from 50% to 60% shown as solid curve in Fig. 5.2b) and decreases the effective permeability and (2) the friction between sand grains and ice becomes smaller as the temperature decreases from –9 to –15 °C because the elasticity of partially frozen ice increases with increasing ice content. This increasing elasticity of frozen ice decreases the elastic contrast between sand grains and ice and then decreases the friction between sand grains and ice.

5.6.3.2 Attenuation mechanisms for S-waves

There are very few analytical and theoretical studies of the attenuation mechanism of S-waves in partially frozen systems. Guerin and Goldberg (2005) indicated that squirt flow has no effect on S-wave attenuation because the pore fluid does not transmit shear waves; they attributed the S-wave attenuation to the friction between sand grains and hydrates. Therefore, the S-wave attenuation predicted by the Carcione model (dotted curve in Fig. 5.8d) and Guerin model (solid curve in Fig. 5.8d) are coincidental. The S-wave attenuation predicted by the Guerin model (Figs 5.10d, 5.11d, 5.12d, and 5.13d) seems to agree well with measured S-wave attenuation. Matsushima et al. (2016) concluded that friction due to the elastic contrast between the ice and sand grains increases the S-wave attenuation and that the contribution of friction becomes smaller at a constant rate with decreasing

temperature because the elasticity of partially frozen ice increases with increasing ice content. The S-wave attenuation peak predicted by the Guerin model (solid curve in Fig. 5.8d) occurred at –7 °C (ice saturation of 70%, shown as solid curve in Fig. 5.2b). In spite of the lack of S-wave attenuation at temperatures higher than −5 °C, the Guerin model seems to accurately predict the measured S-wave attenuation (Figs 5.11d, 5.12d, and 5.13d). I conclude that the increased S-wave attenuation measured at temperatures higher than −7 °C is caused by friction between ice and sand grains as ice forms during the freezing process. At ice saturation lower than 70%, the elastic contrast between ice and sand grains increases the attenuation caused by the friction between them. At temperatures lower than −7 °C, the further formation of ice increases the elasticity of frozen ice and decreases the elastic contrast between ice and sand grains, which then decrease the attenuation caused by the friction between them. The agreement between measured and predicted S-wave attenuation implies that the friction between ice and sand grains is likely responsible for S-wave attenuation in partially frozen unconsolidated sand in the ultrasonic frequency domain.

5.7 Conclusion of this chapter

To elucidate the velocity and attenuation observed in ultrasonic measurement of two partially frozen systems, partially frozen brine and partially frozen unconsolidated sand, at 0 to −15 °C, two different rock physics models are adopted: the Leurer model for partially frozen brine and the Guerin model for partially frozen unconsolidated sand. Then, the possible attenuation mechanisms responsible for both partially frozen systems are quantitatively evaluated. By matching predicted and measured values, I find that the average pore radius of porous ice significantly affects the predicted P- and S-wave attenuations, and then I assumed average pore radius was 15 μm for partially frozen brine and 20 μm for partially frozen unconsolidated sand. The rock physics modeling also implied that the freezing point is another influential parameter and that its optimum value is around −2 °C for our partially frozen systems. For partially frozen brine, the rock physics study suggested that the squirt flow caused by unfrozen brine inclusions in porous ice could be responsible for high P-wave attenuation around the freezing point (i.e., around −2 to −3 °C) and that the decreasing P-wave attenuation below the freezing point can be explained by the gradual decrease of squirt flow due to the gradual decrease of unfrozen brine. For partially frozen unconsolidated sand, the rock physics study suggests that squirt flow between ice grains is a dominant factor for increasing P-wave attenuation around the freezing point. With decreasing temperature below the freezing point, the friction between ice and sand grains becomes an increasingly dominant factor for P-wave attenuation because the decrease of unfrozen brine reduces squirt flow between ice grains, while the generation of ice enhances the friction. This study also indicates that increasing friction between ice and sand grains caused by the generation of ice is possibly responsible for increasing S-wave attenuation as the

temperature decreases (from −5 to −7 °C). Generation of more ice with further cooling (from −7 to −15 °C) reduces the elastic contrast between ice and grains, which hinders the relative motion between ice and sand grains and reduces the P- and S- wave attenuations.

CHAPTER 6. CONCLUSION AND OUTLOOK

This rock physics study investigates frequency dependent attenuation of MH-bearing sediments by the application of various rock physics models. The agreement between observed data from field data/laboratory measurement data and predicted data by rock physics modeling validates the applied rock physics models, and then provides an insight on attenuation mechanisms at different frequencies. This chapter summarizes the conclusions that can be drawn from this thesis, and then provides the limitation of this study. Finally, some outlook remarks are also added to provide the possible direction for the future research.

6.1 Conclusion

6.1.1 Implication of the hydrate morphology of MH-bearing sediments at Nankai Trough

Accurate assessment of the hydrate saturation and distribution of MH at Nankai Trough requires the understanding of how hydrate morphology affects the rock properties of MH-bearing sediments. Determination of hydrate saturation in MH-bearing sediments at Nankai Trough without information about the hydrate morphology would result in large uncertainty.

1. The application of the Marin-Moreno model to sonic logging data demonstrated that the previous assumption of sole hydrate morphology cannot fully explain the observed sonic velocity and attenuation. The rock physics modeling demonstrates that multiple hydrate morphologies (cementing and pore-filling hydrate) might be a better candidate to explain the observed sonic velocity and attenuation at Nankai Trough.

6.1.2 Attenuation mechanisms responsible for P- and S-wave attenuations at sonic frequency domain

Through the application of the Marin-Moreno model and the Guerin model to sonic logging data at Nankai Trough, two goals have been achieved: (1) through rock physical studies, the sensitivities of input parameters of these models were analyzed, and it will be beneficial to the transplantation of these rock physics models into other MH-bearing sediments, and (2) the possible attenuation mechanisms responsible for P- and S-wave attenuations at sonic frequencies in Nankai Trough are investigated.

2. Through the sensitivity analysis of input parameters, suitable parameter setting for the application of rock physics models to sonic data can be identified. To some extent this

parameter setting also reflects the real rock physical properties of MH-bearing sediments at Nankai Trough, such as permeability, viscosity, and parameters of microstructure.

3. In terms of P-wave attenuation in the sonic frequency range, two types of squirt flow may be dominant attenuation mechanisms: (1) squirt flow due to fluid inclusion in a microporous hydrate and (2) the Biot-squirt (BISQ) mechanism in pore spaces between hydrate grains and pore spaces between solid grains.
4. The rock physics modeling also confirms that the viscous friction between solid grain and hydrate might be the responsible attenuation mechanism for S-wave attenuation at sonic frequencies.

6.1.3 Attenuation mechanisms responsible for frequency dependent attenuations at VSP and sonic frequency domain

In the application of two different models (the Marin-Moreno and Guerin models), through rock physical studies, the theoretical possibility of the frequency dependence of attenuation obtained from sonic and VSP data in MH-bearing sediments at the Nankai Trough is demonstrated.

5. In terms of P-wave attenuation in the seismic frequency range, squirt flow was also a dominant attenuation mechanism, and two key parameters cause large variations in attenuation in the seismic frequency range: (1) the inclusion aspect ratio in hydrate grains and (2) the combined effect of the degree of hydrate saturation and two permeable systems in pore spaces between hydrate grains and pore spaces between sand grains.
6. The microporous hydrates with smaller inclusion aspect ratios resulted in significant P-wave attenuation at seismic frequencies, while the larger inclusion aspect ratios led to significant P-wave attenuation at sonic frequencies.
7. In the two permeable systems (between sand grains and within hydrate), the higher permeability component caused the significant P-wave attenuation at seismic frequencies, while smaller permeability component resulted in significant P-wave attenuation at sonic frequencies.
8. In contrast to significant S-wave attenuation at sonic frequencies, no significant S-wave attenuation can be observed at seismic frequencies, which implies frequency dependent S-wave attenuation between w-VSP and sonic frequencies in MH-bearing sediments. I have clarified this dependence by the application of the Guerin model. Friction between hydrate and sand grains dominates the S-wave attenuation at sonic frequencies, whereas the Biot flow and friction between hydrate and sand grains are possible attenuation mechanisms at seismic frequencies.

6.1.4 Attenuation mechanisms responsible for P- and S-wave attenuations at ultrasonic frequency domain

To elucidate the attenuation observed in ultrasonic measurement of two partially frozen systems: partially frozen brine and partially frozen unconsolidated sand, at 0 to −15 °C, two different rock physics models are adopted: the Leurer model for partially frozen brine and the Guerin model for partially frozen unconsolidated sand. Then, the possible attenuation mechanisms responsible for both partially frozen systems are quantitatively evaluated.

9. By matching predicted and measured values, the average pore radius was assumed as 15 μm for partially frozen brine and 20 μm for partially frozen unconsolidated sand. The optimum value of the freezing point is around −2 °C for our partially frozen systems.
10. For partially frozen brine, the rock physics study suggested that the squirt flow caused by unfrozen brine inclusions in porous ice could be responsible for high P-wave attenuation around the freezing point (i.e., around −2 to −3 °C) and that the decreasing P-wave attenuation below the freezing point can be explained by the gradual decrease of squirt flow due to the gradual decrease of unfrozen brine.
11. For partially frozen unconsolidated sands, the rock physics study suggests that squirt flow between ice grains is a dominant factor for increasing P-wave attenuation around the freezing point. With decreasing temperature below the freezing point, the friction between ice and sand grains becomes an increasingly dominant factor for P-wave attenuation because the decrease of unfrozen brine reduces squirt flow between ice grains, while the generation of ice enhances the friction. My study also indicates that increasing friction between ice and sand grains caused by the generation of ice is possibly responsible for increasing S-wave attenuation as the temperature decreases (from −5 to −7 °C). Generation of more ice with further cooling (from −7 to −15 °C) reduces the elastic contrast between ice and grains, which hinders the relative motion between ice and sand grains and reduces the P- and S- wave attenuations.

6.2 Limitations and outlook

There are some limitations in the current rock physics modeling that limit the further application of these rock physics models.

1. There is a fundamental problem that the larger inclusion concentration (c_i) will violate the non-interaction assumption for fluid inclusion when applying the effective medium model. If this happens, we will get a negative shear modulus of effective hydrate grain

that is obviously counterintuitive. This limits and challenges the application of effective medium model.

2. Although there are some similarities between the properties of ice and hydrate, their physical properties such as molecular size and interfacial tension, are different. Recent studies showed that THF (tetrahydrofuran) might be a perfect candidate to substitute hydrate in laboratory measurements. However, there are still some discrepancies between them (Lee et al., 2007; Yun et al., 2007).
3. The rock physical models that are considered in the present study assumed a sandy reservoir in which there is only effect of clay on permeability and mineral composition. Further development of our rock physical model is needed in order to consider the effect of the presence of clay on attenuation caused by clay squirt flow.

The final goal of this study on the application of rock physics modeling to MH-bearing sediments is to identify MH-bearing sediments and quantify the hydrate saturation within hosted sediments. There are still some problems that should be solved:

Can hydrate saturation be reliably predicted by seismic velocity and attenuation?

How will clay content affect the seismic attenuation?

Can we develop rock physics models to quantitatively explain the observed attenuation?

How to confirm or deny the speculations on the attenuation mechanisms at different frequencies domains?

Following on these questions, there are several directions for future research.

1. Necessity of direct measurements and observation on in situ MH-bearing sediments samples. Recent advance on the in situ sampling allow us to obtain the microstructure and rock properties of in situ MH-bearing sediments samples. To confirm which type of squirt flow is reasonable, further technology such as scanning electron microscopy technology or X-ray microtomography, is required to recognize the microstructure of in situ hydrate samples at Nankai Trough.
2. Necessity of new rock physics model. The Marin-Moreno model encounters the inevitable problem of negative shear modulus when violating the non-interaction assumption for fluid inclusion. Moreover, the Guerin model tends to pore-filling hydrate morphology due to the nature of percolation theory. Therefore, a new rock physics model that includes the above attenuation mechanisms as many as possible is needed.

3. Mapping the hydrate saturation based on the rock physics models. There are few inversion examples of hydrate saturation from velocities based on the assumption of hydrate morphology by using rock physics modeling. But there is no general consensus on the natural hydrate morphology in MH-bearing sediments. Moreover, a joint inversion of hydrate saturation based on the combination of velocity and attenuation should improve the reliability of this method.

ACKNOWLEDGEMENTS

Firstly, I would like to thank the Ministry of Economy, Trade and Industry (METI) and the Japan Oil, Gas and Metals National Corporation (JOGMEC) for allowing the use of their wireline logging data. I also would like to give great thanks to my supervisor Dr. Jun Matsushima, who gave me this special opportunity to study in the University of Tokyo with him. He helped me decide this interesting topic and roadmap of my research. During the past five years, he has always been there to encourage me patiently. Even a conference paper, he taught me how to organize it. Without his support and inspiration, I could not finish this thesis. I will never forget the weekends and nights when we discussed our papers by phone or e-mail. In addition to guidance for my research, he showed me that how to become a qualified researcher and supervisor. I am deeply appreciated of his support during the past five years, and deeply admire his charming personality. I also would like to express my sincere gratitude to Prof. Yoshihiro Masuda, Prof. Kimihiro Hashiba, Prof. Yoshihiro Konno, and Prof. Nozomu Takeuchi for all their advice and support. Their suggestions improve this thesis very much.

I owe my thanks to my friends, Dr. Deyu Tian, Dr. Li Wang, Dr. Xiaoguang Zhao, and Dr. Guangwen Jin, for giving me a warm, confortable and appropriate living environment in Japan. They are really perfect listeners. I also thank all the students in the Matsushima Lab for providing a friendly and stimulated environment to me. They helped me in many ways: solving mathematical problems, giving me positive energy, and so on.

I must to think my Mom and Dad, who give me endless love and have always believed me though they might not know what are methane hydrates. Finally I would like to give my special thanks to my wife Dr. Wu Man. I would like to thank all those who have helped me during my research.

APPENDIX A. THE LEURER MODEL

In ice-brine binary system, the effective bulk and shear modulus K_r and μ_r of the effective ice grain including brine inclusion can be given by (Kuster and Toksoz, 1974):

$$\frac{K_r - K_i}{3K_r + 4\mu_i} = \frac{1}{3}\frac{K_f - K_i}{3K_i + 4\mu_i}\sum_m c(\alpha_m)T_{iijj} \qquad \text{(A-1)}$$

$$\frac{\mu_r - \mu_i}{6\mu_r(K_i + 2\mu_i) + \mu_i(9K_i + 8\mu_i)} = \frac{\mu_f - \mu_i}{25\mu_i(3K_i + 4\mu_i)}\sum_m c(\alpha_m)(T_{iijj} - \frac{1}{3}T_{ijij}) \quad \text{(A-2)}$$

The required symbols are defined in Tables 2.1 and 2.4. In equations A-1 and A-2, $c(\alpha_m)$ represents the inclusion concentration for each aspect ratio (α_m). Here, I assume that the ice size distribution match a 2n-fold subdivision as follows (Leurer, 1997):

$$c(\alpha_m) = \frac{D(\alpha_m)c_i}{2^5} \qquad \text{(A-3)}$$

Similar to Leurer (1997), I assume the distribution of the aspect ratios of brine inclusions as $D(\alpha_m) = 0.45 + 0.046\ln(\alpha_m)$, with distribution of α_m ranging from 0.0005 to 0.05. In equation A-3, c_i represents total brine inclusion concentration in ice-brine coexisting system. By letting,

$$L(\alpha_m) = \frac{K_f - K_i}{3K_i(3K_i + 4\mu_i)}\sum_m c(\alpha_m)T_{iijj} \qquad \text{(A-4)}$$

$$L_1(\alpha_m) = \frac{\mu_f - \mu_i}{25\mu_i(3K_i + 4\mu_i)}\sum_m c(\alpha_m)(T_{iijj} - \frac{1}{3}T_{ijij}) \quad \text{(A-5)}$$

I rewrite equations A-4 and A-5 as:

$$K_r = K_i\frac{1 + 4\mu_i\sum_m c(\alpha_m)L(\alpha_m)}{1 - 6K_i\sum_m c(\alpha_m)L(\alpha_m)} \qquad \text{(A-6)}$$

$$\mu_r = \mu_i\frac{1 + (9K_i + 8\mu_i)\sum_m c(\alpha_m)L_1(\alpha_m)}{1 - 6(K_i + 2\mu_i)\sum_m c(\alpha_m)L_1(\alpha_m)} \quad \text{(A-7)}$$

Now we need to calculate the scalar qualities T_{iijj} and $T_{iijj} - \frac{1}{3}T_{ijij}$. When the aspect ratio of the inclusion is small but non-zero, their expressions are simplified as follows (Walsh, 1969; Leurer, 1997):

$$\frac{1}{3}T_{iijj} = \frac{3K_i + 4\mu_f}{3K_f + 4\mu_f + K_1} \qquad \text{(A-8)}$$

$$T_{iijj} - \frac{1}{3}T_{ijij} = 1 + \frac{8\mu_i}{4\mu_f + K_2} + \frac{2(3K_f + 4\mu_i)}{3K_f + 4\mu_f + K_1} \qquad \text{(A-9)}$$

where

$$K_1 = \frac{3\pi\alpha_m\mu_i(3K_i + \mu_i)}{3K_i + 4\mu_i} \qquad \text{(A-10)}$$

$$K_2 = \frac{3\pi\alpha_m\mu_i(3K_i + 2\mu_i)}{3K_i + 4\mu_i} \qquad \text{(A-11)}$$

Then, the correspondence principle is applied into bulk and shear moduli of fluid inclusion (Johnston et al., 1979) as following:

$$K_f^{'} = K_f + j2\pi f K_i\gamma\ ,\ \mu_f^{'} = j2\pi f\eta \qquad \text{(A-12)}$$

where γ is relaxation time for brine inclusion flow, η is viscosity of brine changing with reducing temperature (Carcione & Tinivella, 2000), j is an imaginary number, and f is the frequency. The other required symbols are defined in Table 2.4. Incorporating squirt flow due to brine inclusion in microporous ice, and then replacing K_f and μ_f in equations A-1, A-2, A-8 and A-9 with $K_f^{'}$ and $\mu_f^{'}$ in equation A-12, the complex effective bulk and shear moduli of ice with brine inclusion (Leurer, 1997) can be obtained: $K_r^{'}$ and $\mu_r^{'}$. The velocity and attenuation of P- and S-waves can be expressed as(Johnstonet al., 1979):

$$V_p = \sqrt{\frac{[Re(K_r^{'}) + 4Re(\mu_r^{'})/3]}{\rho_e}}\ ,\ Q_p^{-1} = \sqrt{\frac{[Im(K_r^{'}) + 4Im(\mu_r^{'})/3]}{[Re(K_r^{'}) + 4Re(\mu_r^{'})/3]}}$$

$$V_s = \sqrt{\frac{Re(\mu_r^{'})}{\rho_e}}\ ,\ Q_s^{-1} = \sqrt{\frac{Im(\mu_r^{'})}{Re(\mu_r^{'})}} \qquad \text{(A-13)}$$

where the *Re* and *Im* are real and imaginary parts of $K_r^{'}$ and $\mu_r^{'}$, and ρ_e is the effective density of the partially frozen system.

APPENDIX B. THE MARIN-MORENO MODEL

B.1 Effective medium model

The correspondence principle is applied to the bulk ($K_f^{'}$) and shear ($\mu_f^{'}$) moduli of fluid inclusion (Johnston et al. 1979), as follows:

$$K_f^{'} = K_f + j2\pi f K_h \gamma \,,\ \mu_f^{'} = j2\pi f \eta \tag{B-1}$$

The symbols are defined in Tables 2.2 and 2.5. By incorporating the squirt flow due to fluid inclusion in a microporous hydrate, the effective bulk ($K_h^{'}$) and shear ($\mu_h^{'}$) moduli of the hydrate with fluid inclusion are given as follows (Leurer 1997; Best et al. 2013; Marín-Moreno et al. 2017):

$$K_h^{'} = (K_h + 4c_i\mu_h L_{k\alpha}) / (1 - 3c_i L_{k\alpha}) \tag{B-2}$$

$$\mu_h^{'} = \mu_h[1 + c_i L_{\mu\alpha}(9K_h + 8\mu_h)] / [1 - c_i L_{\mu\alpha}(6K_h + 12\mu_h)] \tag{B-3}$$

where the intermediate variables $L_{k\alpha}$ and $L_{\mu\alpha}$ are given by (Kuster & Toksoz 1974; Leurer 1997):

$$L_{k\alpha} = [(K_f^{'} - K_h) / (3K_h + 4\mu_h)]\{K_h / [K_f^{'} + \pi\alpha\mu_h(3K_h + \mu_h) / (3K_h + 4\mu_h)]\} \tag{B-4}$$

$$L_{\mu\alpha} = \frac{\mu_f^{'} - \mu_h}{25\mu_h(3K_h + 4\mu_h)} \left\{ 1 + \frac{8\mu_h}{4\mu_f^{'} + \pi\alpha\mu_h[1 + 2(\frac{3K_h + \mu_h}{3K_h + 4\mu_h})]} + 2[\frac{3K_f + 2(\mu_f^{'} + \mu_h)}{3K_f + 4\mu_f^{'} + 3\pi\alpha\mu_h(\frac{3K_h + \mu_h}{3K_h + 4\mu_h})}] \right\} \tag{B-5}$$

B.2 Hydrate contact model

Then the real bulk and shear moduli of hydrate in hydrate contact model proposed by Ecker et al (1998, 2000) can be replaced with above complex bulk and shear moduli of the effective hydrate. The dry effective bulk and shear moduli of hydrate-bearing sediment with four modes of hydrate morphologies (contact cementing, envelope cementing, load-bearing, and pore-filling) can be obtained respectively. In my study, the multiple hydrate morphologies (contact cementing and pore-filling) are

assumed, and the effective bulk and shear moduli of the dry frame are represented as K'_{dryc}, K'_{drypf}, μ'_{dryc}, and μ'_{drypf} respectively. Note that hydrate is divided into contact cementing hydrate as solid frame and pore-filling hydrate as fluid. Therefore, the effective elastic moduli for solid phase (sand grain and contact cementing hydrate), fluid phase (water and pore-filling hydrate) are also become complex, and they are given by (Marín-Moreno et al. 2017):

$$K'_{dry} = [c_{pf} / K'_{drypf} + (1 - c_{pf}) / K'_{dryc}]^{-1} \quad \text{(B-6)}$$

$$\mu'_{dry} = [c_{pf} / \mu'_{drypf} + (1 - c_{pf}) / \mu'_{dryc}]^{-1} \quad \text{(B-7)}$$

$$K'_{solid} = \{F_s K_s + (1 - F_s) K'_h + [F_s / K_s + (1 - F_s) / K'_h]^{-1}\} \quad \text{(B-8)}$$

$$\mu'_{solid} = \{F_s \mu_s + (1 - F_s) \mu'_h + [F_s / \mu_s + (1 - F_s) / \mu'_h]^{-1}\} \quad \text{(B-9)}$$

$$K'_{fp} = [\phi_0 (1 - S_h) / K_f + S_h c_{pf} / K'_h]^{-1} \quad \text{(B-10)}$$

where c_{pf} is the fraction of pore-filling hydrate and F_s is fraction of sand grains.

B.3 Biot-Stoll model

The effective and complex moduli of solid phase (K'_{solid} and μ'_{solid}), fluid phase (K'_{fp}), and dry frame (K'_{dry} and μ'_{dry}) (see Table 2.2) are then introduced into Biot-Stoll model (Stoll & Bryan 1970), and *a*, *b*, *c*, and *q* are calculated from Biot coefficients (see Table 2.2). The intermediate variables *P* and *S* are given by:

$$P = -(b \pm \sqrt{b^2 - 4ac}) / 2, \; S = (q\rho_e - \rho_f^2) / (q\mu'_{dry}) \quad \text{(B-11)}$$

where μ'_{dry} indicates shear modulus of dry frame, and ρ_e indicates effective density of hydrate-bearing sediments..

The Marin-Moreno model assumes that the presence of hydrate decreases the effective permeability (k) of the medium (Marín-Moreno et al. 2017), which is expressed as:

$$k = \{c_{pf} / [k_0 (1 - S_h)^{n_{kp}}] + (1 - c_{pf}) / [k_0 (1 - S_h)^{n_{kc}}]\}^{-1} \quad \text{(B-12)}$$

The required parameters are listed in Tables 2.2 and 2.5. Therefore, using Eq. (B-11), the fast P-wave velocity (V_{p1}), the slow P-wave velocity (V_{p2}), the S-wave velocity (V_s), the fast P-wave attenuation (Q_{p1}^{-1}), the slow P-wave attenuation (Q_{p2}^{-1}), and the S-wave attenuation (Q_s^{-1}) are calculated as follows (Marín-Moreno et al. 2017):

$$V_{p1} = Re(\sqrt{P/c}),\ V_{p2} = Re(\sqrt{a/P}),\ V_s = Re(\sqrt{1/S}),\ Q_{p1}^{-1} = 2Im(\sqrt{P/c})/Re(\sqrt{P/c}),$$

$$Q_{p2}^{-1} = 2Im(\sqrt{a/P})/Re(\sqrt{a/P}), \text{ and } Q_s^{-1} = 2Im(\sqrt{1/S})/Re(\sqrt{1/S}) \qquad \text{(B-13)}$$

APPENDIX C. THE GUERIN MODEL

Guerin and Goldberg (2005) presented the propagation equations for P- and S-waves as follows:

$$R\nabla\varphi = \rho\ddot{\varphi} + A\dot{\varphi} \text{ (P-wave), and } \mu\nabla\psi = \rho\ddot{\psi} + A\dot{\psi} \text{ (S-wave)} \quad \text{(C-1)}$$

The overdots in the above equations indicate time derivatives, φ and ψ are compressional and shear displacement potentials, respectively. The complex roots of the above polynomials are calculated using the rigidity matrix *R*, the shear matrix μ, the density matrix ρ, and the friction matrix *A*, which are given by (Guerin and Goldberg, 2005):

$$R = \begin{pmatrix} R_{ss} & R_{sf} & R_{si} \\ R_{sf} & R_{ff} & R_{fi} \\ R_{si} & R_{fi} & R_{ii} \end{pmatrix},\ \mu = \begin{pmatrix} \mu_{ss} & 0 & \mu_{si} \\ 0 & 0 & 0 \\ \mu_{si} & 0 & \mu_{ii} \end{pmatrix},\ \rho = \begin{pmatrix} \rho_{ss} & \rho_{sf} & \rho_{si} \\ \rho_{sf} & \rho_{ff} & \rho_{fi} \\ \rho_{si} & \rho_{fi} & \rho_{ii} \end{pmatrix}$$

$$\text{and } A = \begin{pmatrix} b_{ss} + b_{si} & -b_{ss} & -b_{si} \\ -b_{ss} & b_{ss} + b_{ii} & -b_{ii} \\ -b_{si} & -b_{ii} & b_{si} + b_{ii} \end{pmatrix} \quad \text{(C-2)}$$

where subscripts *s*, *f*, and *i* indicate values for sand grains, fluid, and ice, respectively. The meanings and definitions of symbols in these coefficient matrices are shown in Table 2.3. There are three modes of P-waves and two modes of S-waves (the complex roots for equation C-1 are Λ and Ω), and the P- and S-waves with the highest velocity and the lowest attenuation correspond to the P- and S-waves in a geophysical survey (Berryman and Wang, 2000):

$$V_{pi} = \left[Re(\sqrt{\Lambda_i}) \right]^{-1},\ Q_{pi}^{-1} = \left| \frac{Im(\sqrt{\Lambda_i})}{Re(\sqrt{\Lambda_i})} \right|,\ i = 1,2,3 \text{ (P-wave)} \quad \text{(C-3)}$$

$$V_{si} = \left[Re(\sqrt{\Omega_i}) \right]^{-1},\ Q_{si}^{-1} = \left| \frac{Im(\sqrt{\Omega_i})}{Re(\sqrt{\Omega_i})} \right|, i = 1,2 \text{ (S-wave)} \quad \text{(C-4)}$$

where the *Re* and *Im* are the real and imaginary parts, respectively, of the complex roots of equation C-1.

C.1 Determination of the rigidity matrix

For rigidity matrix R, the coefficients R_{ss} and R_{ii} are given in Table 2.3. Leclaire et al. (1994) neglected the coefficient R_{si}, but Carcione and Tinivella (2000) took this coefficient into consideration. Table 2.3 shows the expressions of these coefficients. In addition, Guerin and Goldberg (2005) introduced squirt flow in sand grains and ice grains as follows:

$$R_{ff} = f_1\phi_1 + f_3\phi_3,\ R_{sf} = f_1(\alpha_1 - \phi_1),\ \text{and}\ R_{fi} = f_3(\alpha_3 - \phi_3) \qquad \text{(C-5)}$$

The fractions of ice, fluid, and sand grain is denoted as ϕ_i, ϕ_f ,and ϕ_s, respectively. The parameters in equation C-5 are given by:

$$\phi_1 = \frac{\phi_f}{1-\phi_i} \quad , \quad Q_1 = \frac{K_s}{1-\phi_1 - K_{sm}/K_s} \quad , \quad \phi_3 = \frac{\phi_f}{\phi} \quad , \quad f_1 = \frac{1}{[1/K_f + 1/(\phi_1 Q_1)]} \quad , \quad Q_3 = \frac{K_i}{1-\phi_3 - K_{im}/K_h} \quad ,$$

$$f_3 = \frac{1}{[1/K_f + 1/(\phi_3 Q_3)]},\ \alpha_1 = \frac{1 - K_{sm}/K_s + 2\phi_1}{3},\ \text{and}\ \alpha_3 = \frac{1 - K_{im}/K_s + 2\phi_3}{3} \qquad \text{(C-6)}$$

The symbols in the above equations are defined in Table 2.3.

C.2 Determination of the mass density matrix

For mass density matrix ρ, ρ_{ss}, ρ_{sf}, ρ_{ff}, ρ_{fi}, and ρ_{ii} are given in Table 2.3. Carcione and Tinivella (2000) added the apparent mass density between sand and ice grains, which was neglected in the Leclaire model, as follows:

$$\rho_{si} = -\phi_s\rho_s(a_{si} - 1) - \phi_i\rho_i(a_{is} - 1) \qquad \text{(C-7)}$$

with parameters:

$$a_{si} = 1 + \frac{r_{si}\phi_i(\phi_s\rho_s + \phi_i\rho_i)}{\phi_s\rho_s(\phi_s + \phi_i)},\ a_{is} = 1 + \frac{r_{is}\phi_s(\phi_s\rho_s + \phi_i\rho_i)}{\phi_i\rho_i(\phi_s + \phi_i)} \qquad \text{(C-8)}$$

C.3 Determination of the shear moduli and friction matrices

Finally, for the shear moduli matrix μ and the friction coefficient matrix A, μ_{ss}, μ_{ii}, b_{ss}, and b_{ii} are defined in Table 2.3. The cementation between ice and sand grains will sharply increase the velocity of the S-wave and proposed the following expression:

$$\mu_{si} = \mu_{si0}(\phi_i \phi_s)^2 \qquad \text{(C-9)}$$

Furthermore, the friction between sand grains and the ice is defined as:

$$b_{si} = b_{si0}(\phi_i \phi_s)^2 \qquad \text{(C-10)}$$

REFERENCES

[1] Adkins, J. F. (2002). The Salinity, Temperature, and delta 18O of the Glacial Deep Ocean. *Science*, *298*(5599), 1769–1773.

[2] Archie, G. E. (1942). The Electrical Resistivity Log as an Aid in Determining Some Reservoir Characteristics.

[3] Arenson, L. U., & Sego, D. C. (2006). The effect of salinity on the freezing of coarse-grained sands. *Canadian Geotechnical Journal*, *43*(3), 325–337.

[4] Ashi, J., Tokuyama, H., & Taira, A. (2002). Distribution of methane hydrate BSRs and its implication for the prism growth in the Nankai Trough. *Marine Geology*, *187*(1–2), 177–191.

[5] Ba, J., Nie, J. X., Cao, H., & Yang, H. Z. (2008). Mesoscopic fluid flow simulation in double-porosity rocks. *Geophysical Research Letters*, *35*(4), 1–5.

[6] Baba, K., & Yamada, Y. (2004). BSRs and associated reflections as an indicator of gas hydrate and free gas accumulation: An example of accretionary prism and forearc basin system along the Nankai Trough, off Central Japan. *Resource Geology*, *54*(1), 11–24.

[7] Banin, A., & Anderson, M. D. (1974). Effects of Salt Concentration Changes During Freezing on the Unfrozen Water Content of Porous Materials. *Water Resources Research*, *10*(1), 124–128.

[8] Barton, N. (2007). *Rock Quality, Seismic Velocity, Attenuation and Anisotropy*. London: CRC Press.

[9] Batzle, M. L., Han, D.-H., & Hofmann, R. (2006). Fluid mobility and frequency-dependent seismic velocity — Direct measurements. *Geophysics*, *71*(1), N1.

[10] Bauer, K., Pratt, R. G., Haberland, C., & Weber, M. (2008). Neural network analysis of crosshole tomographic images: The seismic signature of gas hydrate bearing sediments in the Mackenzie Delta (NW Canada). *Geophysical Research Letters*, *35*(19), 1–6.

[11] Bellanger, M., Rémy, J. M., & Homand, F. (1996). Ultrasonic wave attenuation as a tool for estimating frost action on limestone rocks. *Materials and Structures/Materiaux et Constructions*, *29*(193), 552–561.

[12] Bellefleur, G., Riedel, M., & Brent, T. (2006). Seismic characterization and continuity analysis of gas-hydrate horizons near Mallik research wells, Mackenzie Delta, Canada. *The Leading Edge*, *25*, 599.

[13] Bellefleur, G., Riedel, M., Brent, T., Wright, F., & Dallimore, S. R. (2007). Implication of seismic attenuation for gas hydrate resource characterization, Mallik, Mackenzie Delta, Canada. *Journal of Geophysical Research: Solid Earth*, *112*(10), 1–11.

[14] Berryman, J. G. (1995). *Mixture theory for rock properties*. *AGU Handbook of Physical Constants*.

[15] Berryman, J. G., & Wang, H. F. (2000). Elastic wave propagation and attenuation in a double-porosity dual-permeability medium. *International Journal of Rock Mechanics and Mining Sciences*, *37*(1–2), 63–78.

[16] Best, A. I., Huggett, Q. J., & Harris, A. J. K. (2001). Comparison of in situ and laboratory acoustic measurements on Lough Hyne marine sediments. *The Journal of the Acoustical Society of America*, *110*(2), 695.

[17] Best, A. I., Priest, J. A., Clayton, C. R. I., & Rees, E. V. L. (2013). The effect of methane hydrate morphology and water saturation on seismic wave attenuation in sand under shallow sub-seafloor conditions. *Earth and Planetary Science Letters*, *368*, 78–87.

[18] Biot, M. A. (1956a). Theory of Propagation of Elastic Waves in a Fluid‐Saturated Porous Solid. I. Low‐Frequency Range. *The Journal of the Acoustical Society of America*, *28*(2), 168–178.

[19] Biot, M. A. (1956b). Theory of Propagation of Elastic Waves in a Fluid‐Saturated Porous Solid. II. Higher Frequency Range. *The Journal of the Acoustical Society of America*, *28*(2), 179–191.

[20] Bornhold, B. D., & Prior, D. B. (1989). Sediment blocks on the sea floor in British Columbia fjords. *Geo-Marine Letters*, *9*(3), 135–144.

[21] Borowski, W. S. (2004). *A review of methane and gas hydrates in the dynamic, stratified system of the Blake Ridge region, offshore southeastern North America*. *Chemical Geology* (Vol. 205).

[22] Boswell, R., & Collett, T. S. (2011). Current perspectives on gas hydrate resources. *Energy Environ. Sci.*, *4*(4), 1206–1215.

[23] Bu, Q. T., Hu, G. W., Ye, Y. G., Liu, C. L., Li, C. F., Best, A. I., & Wang, J. S. (2017). The elastic wave velocity response of methane gas hydrate formation in vertical gas migration systems. *Journal of Geophysics and Engineering*, *14*(3).

[24] Buffett, B. A. (2000). Clathrate Hydrates. *Annual Review of Earth and Planetary Sciences*, *28*(1), 477–507. https://doi.org/10.1146/annurev.earth.28.1.477

[25] Bugge, T., Befring, S., Belderson, R. H., Eidvin, T., Jansen, E., Kenyon, N. H., et al. (1987). A giant three-stage submarine slide off Norway. *Geo-Marine Letters*, *7*(4), 191–198.

[26] Carcione, J. M., & Gei, D. (2004). Gas-hydrate concentration estimated from P- and S-wave velocities at the Mallik 2L-38 research well, Mackenzie Delta, Canada. *Journal of Applied Geophysics*, *56*(1), 73–78.

[27] Carcione, J. M., & Seriani, G. (1998). Seismic and ultrasonic velocities in permafrost. *Geophysical Prospecting*, *46*(4), 441–454.

[28] Carcione, J. M., & Seriani, G. (2001). Wave Simulation in Frozen Porous Media. *Journal of Computational Physics*, *170*(2), 676–695.

[29] Carcione, J. M., & Tinivella, U. (2000). Bottom-simulating reflectors: Seismic velocities and AVO effects. *Geophysics*, *65*(1), 54–67.

[30] Carcione, J. M., Campanella, O. H., & Santos, J. E. (2007). A poroelastic model for wave propagation in partially frozen orange juice. *Journal of Food Engineering*, *80*(1), 11–17.

[31] Carpenter, G. (1981). Coincident sediment slump / clathrate complexes on the U . S . Atlantic continental slope. *Geo-Marine Letters*, *1*(1), 29–32.

[32] Chand, S., & Minshull, T. A. (2003). Seismic constraints on the effects of gas hydrate on sediment physical properties and fluid flow: A review. *Geofluids*, *3*(4), 275–289.

[33] Chand, S., Minshull, T. A., Gei, D., & Carcione, J. M. (2004). Elastic velocity models for gas-hydrate-bearing sediments—a comparison. *Geophysical Journal International*, *159*(2), 573–590.

[34] Chand, S., Minshull, T. A., Priest, J. A., Best, A. I., Clayton, C. R. I., & Waite, W. F. (2006). An effective medium inversion algorithm for gas hydrate quantification and its application to laboratory and borehole measurements of gas hydrate-bearing sediments. *Geophysical Journal International*, *166*(2), 543–552.

[35] Charles K. Paull, W. P. D. (2001). *Natural gas hydrates: occurrence, distribution, and detection*. (W. P. Dillon & C. K. Paull, Eds.). Washington, DC: American Geophysical Union.

[36] Choi, J. H., Dai, S., Cha, J. H., & Seol, Y. (2014). Laboratory formation of noncementing hydrates in sandy sediments. *Geochemistry, Geophysics, Geosystems*, *15*(4), 1648–1656.

[37] Chong, Z. R., Yang, S. H. B., Babu, P., Linga, P., & Li, X. Sen. (2016). Review of natural gas hydrates as an energy resource: Prospects and challenges. *Applied Energy*, *162*, 1633–1652.

[38] Collett, T. S. (2002). Energy Resource Potential of Natural Gas Hydrates. *AAPG Bulletin*, *86*(11), 1971–1992.

[39] Collett, T. S., & Ladd, J. (2000). Detection of Gas Hydrate with Downhole Logs and Assessment of Gas Hydrate Concentrations (Saturations) and Gas Volumes on the Blake Ridge with Electrical Resistivity Data. *Proceedings of the Ocean Drilling Program, Scientific Results*, *164*, 179–191.

[40] Collett, T. S., Lewis, R. E., Winters, W. J., Lee, M. W., Rose, K. K., & Boswell, R. M. (2011). Downhole well log and core montages from the Mount Elbert Gas Hydrate Stratigraphic Test Well, Alaska North Slope. *Marine and Petroleum Geology*, *28*(2), 561–577.

[41] Collett, T. S., Boswell, R., Cochran, J. R., Kumar, P., Lall, M., Mazumdar, A., et al. (2014). Geologic implications of gas hydrates in the offshore of India: Results of the National Gas Hydrate Program Expedition 01. *Marine and Petroleum Geology*, *58*(PA), 3–28.

[42] Cook, A. E., & Goldberg, D. (2008). Extent of gas hydrate filled fracture planes: Implications for in situ methanogenesis and resource potential. *Geophysical Research Letters*, *35*(15), 1–5.

[43] Coren, F., Volpi, V., & Tinivella, U. (2001). Gas hydrate physical properties imaging by multi-attribute analysis - Blake Ridge BSR case history. *Marine Geology*, *178*(1–4), 197–210.

[44] Dai, S., Santamarina, J. C., Waite, W. F., & Kneafsey, T. J. (2012). Hydrate morphology: Physical properties of sands with patchy hydrate saturation. *Journal of Geophysical Research B: Solid Earth*, *117*(11).

[45] Dash, R., & Spence, G. (2011). P-wave and S-wave velocity structure of northern Cascadia margin gas hydrates. *Geophysical Journal International*, *187*(3), 1363–1377.

[46] Dawe, R. A., & Thomas, S. (2007). A large potential methane source - Natural gas hydrates. *Energy Sources, Part A: Recovery, Utilization and Environmental Effects*, *29*(3), 217–229.

[47] Demirbas, A. (2010). Methane hydrates as potential energy resource: Part 1 - Importance, resource and recovery facilities. *Energy Conversion and Management*, *51*(7), 1547–1561.

[48] Demirbas, A., Rehan, M., Al-Sasi, B. O., & Nizami, A. S. (2016). Evaluation of natural gas hydrates as a future methane source. *Petroleum Science and Technology*, *34*(13), 1204–1210.

[49] Diallo, M. S., & Appel, E. (2000). Acoustic wave propagation in saturated porous media: Reformulation of the Biot/Squirt flow theory. *Journal of Applied Geophysics*, *44*(4), 313–325.

[50] Dillon, W. P., Lee, M. W., Fehlhaber, K., & Coleman, D. F. (1993). Gas Hydrates on the Atlantic Continental Margin of the United States - Controls on Concentration. *The Future of Energy Gases*, *1570*(September 2015), 313–330.

[51] Dou, S., Nakagawa, S., Dreger, D., & Ajo-Franklin, J. (2016). A rock-physics investigation of unconsolidated saline permafrost: P-wave properties from laboratory ultrasonic measurements. *Geophysics*, *81*(1), WA233-WA245.

[52] Dou, S., Nakagawa, S., Dreger, D., & Ajo-Franklin, J. (2017). An effective-medium model for P-wave velocities of saturated, unconsolidated saline permafrost. *Geophysics*, *82*(3), EN33-EN50.

[53] Dvorkin, J. & Nur, A. (1993). Dynamic poroelasticity: A unified model with the squirt and the Biot mechanisms, *Geophysics*, 58, 524-533.

[54] Dvorkin, J., Mavko, G. & Nur, A. (1995). Squirt flow in fully saturated rocks, *Geophysics*, 60, 97-107.

[55] Dvorkin, J., & Nur, A. (1996). Elasticity of high-porosity sandstones; theory for two North Sea data sets. *Geophysics*, *61*(5), 1363–1370.

[56] Dvorkin, J., & Uden, R. (2004). Seismic wave attenuation in a methane hydrate reservoir. *The Leading Edge*, *23*(8), 730–732.

[57] Dvorkin, J., Prasad, M., Sakai, A., & Lavoie, D. (1999). Elasticity of marine sediments: Rock physics modeling. *Geophysical Research Letters*, *26*(12), 1781–1784.

[58] Ecker, C., Dvorkin, J., & Nur, A. (1998). Sediments with gas hydrates: Internal structure from seismic AVO. *Geophysics*, *63*(5), 1659.

[59] Ecker, C., Dvorkin, J., & Nur, A. M. (2000). Estimating the amount of gas hydrate and free gas from marine seismic data. *Geophysics*, *65*(2), 565–573.

[60] Foldvik, A., & Kvinge, T. (1974). Conditional instability of sea water at the freezing point. *Deep-Sea Research and Oceanographic Abstracts*, *21*(3), 229–243.

[61] Francke, H., & Thorade, M. (2010). Density and viscosity of brine: An overview from a process engineers perspective. *Chemie Der Erde*, *70*(SUPPL. 3), 23–32.

[62] Gei, D. & Carcione, J. M. (2003). Acoustic properties of sediments saturated with gas hydrate, free gas and water. *Geophysical Prospecting*, *51*(2), 141–158.

[63] Ghosh, R., Sain, K., & Ojha, M. (2010a). Effective medium modeling of gas hydrate-filled fractures using the sonic log in the Krishna-Godavari basin, offshore eastern India. *Journal of Geophysical Research: Solid Earth*, *115*(6), 1–15.

[64] Ghosh, R., Sain, K., & Ojha, M. (2010b). Estimating the amount of gas-hydrate using effective medium theory: A case study in the Blake Ridge. *Marine Geophysical Researches*, *31*(1), 29–37.

[65] Gilpin, R. R. (1980). Wire regelation at low temperatures. *Journal of Colloid and Interface Science*, *77*(2), 435–448.

[66] Guerin, G., & Goldberg, D. (2002). Sonic waveform attenuation in gas hydrate-bearing sediments from the Mallik 2L-38 research well, Mackenzie Delta, Canada. *Journal of Geophysical Research B: Solid Earth*, *107*(5), EPM 1-1-EPM 1-12.

[67] Guerin, G., & Goldberg, D. (2005). Modeling of acoustic wave dissipation in gas hydrate-bearing sediments. *Geochemistry, Geophysics, Geosystems*, *6*(7), 1–16.

[68] Guerin, G., Goldberg, D., & Meltser, A. (1999). Characterization of in situ elastic properties of gas hydrate-bearing sediments on the Blake Ridge. *Journal of Geophysical Research*, *104*(B8), 781–795.

[69] Haflidason, H., Sejrup, H. P., Nygård, A., Mienert, J., Bryn, P., Lien, R., et al. (2004). The Storegga Slide: Architecture, geometry and slide development. *Marine Geology*, *213*(1–4), 201–234.

[70] Haflidason, H., Lien, R., Sejrup, H. P., Forsberg, C. F., & Bryn, P. (2005). The dating and morphometry of the Storegga Slide. *Marine and Petroleum Geology*, *22*(1–2 SPEC. ISS.), 123–136.

[71] Haq, B. U. (1999). Methane in the deep blue sea. *Science*, *285*(5427), 543–544.

[72] Harvey, L. D. D., & Huang, Z. (1995). Evaluation of the potential impact destabilization on future global warming. *Journal of Geophysical Research*, *100*, 2905–2926.

[73] Helgerud, M. B., Dvorkin, J., Nur, A., Sakai, A., & Collett, T. (1999). Elastic-wave velocity in marine sediments with gas hydrates: Effective medium modeling. *Geophysical Research Letters*, *26*(13), 2021–2024.

[74] Hobro, J. W. D., Minshull, T. A., Singh, S. C., & Chand, S. (2005). A three-dimensional seismic tomographic study of the gas hydrate stability zone, offshore Vancouver Island. *Journal of Geophysical Research: Solid Earth*, *110*(9), 1–14.

[75] Holbrook, W. S., Hoskins, H., Wood, W. T., Stephen, R. A., & Lizarralde, D. (1996). Methane hydrate and free gas on the Blake Ridge from vertical seismic profiling. *Science*, *273*(5283), 1840–1843.

[76] Hornbach, M. J., Holbrook, W. S., Gorman, A. R., Hackwith, K. L., Lizarralde, D., & Pecher, I. (2003). Direct seismic detection of methane hydrate on the Blake Ridge. *Geophysics*, *68*(1), 92–100.

[77] Hornbach, M. J., Lavier, L. L., & Ruppel, C. D. (2007). Triggering mechanism and tsunamogenic potential of the Cape Fear Slide complex, U.S. Atlantic margin. *Geochemistry, Geophysics, Geosystems*, *8*(12).

[78] Huang, J. W., Bellefleur, G., & Milkereit, B. (2009). Seismic modeling of multidimensional heterogeneity scales of mallik gas hydrate reservoirs, Northwest territories of Canada. *Journal of Geophysical Research: Solid Earth*, *114*(7), 1–22.

[79] Jacoby, M., Dvorkin, J., & Liu, X. (1996). Elasticity of partially saturated frozen sand. *Geophysics*, *61*(1), 288–293.

[80] Jaiswal, P., Dewangan, P., Ramprasad, T., & Zelt, C. A. (2012). Seismic characterization of hydrates in faulted, fine-grained sediments of Krishna-Godavari Basin: Full waveform inversion. *Journal of Geophysical Research: Solid Earth*, *117*(10).

[81] Jakobsen, M., Hudson, J. A., Minshull, T. A., & Singh, S. C. (2000). Elastic properties of hydrate-bearing sediments using effective medium theory. *Journal of Geophysical Research*, *105*, 561–577.

[82] Jia, J., Tsuji, T., & Matsuoka, T. (2017). Gas hydrate saturation and distribution in the Kumano Forearc Basin of the Nankai Trough. *Exploration Geophysics*, *48*(2), 137–150.

[83] Jin, Y., Konno, Y., Yoneda, J., Kida, M., & Nagao, J. (2016). In Situ Methane Hydrate Morphology Investigation: Natural Gas Hydrate-Bearing Sediment Recovered from the Eastern Nankai Trough Area. *Energy and Fuels*, *30*(7), 5547–5554.

[84] Johnston, D. H., Toksoz, M. N., & Timur, A. (1979). Attenuation of seismic waves in dry and saturated rocks; II, Mechanisms. *Geophysics*, *44*(4), 691–711.

[85] Johnston, D. H., Toksöz, M. N., & Timur, A. (1979). Attenuation of seismic waves in dry and saturated rocks: II. Mechanisms. *Geophysics*, *44*(4), 691.

[86] Jones, T. D. (1986). Pore fluids and frequency-dependent wave propagation in rocks. *Geophysics*, *51*(10), 1939–1953.

[87] Kayen, R. E., & Lee, H. J. (1991). Pleistocene slope instability of gas hydrate‐laden sediment on the Beaufort sea margin. *Marine Geotechnology*, *10*(1–2), 125–141.

[88] Kelland, M. (1994). Natural gas hydrates: Energy for the future. *Marine Pollution Bulletin*, *29*(6–12), 307–311.

[89] Kim, G. Y., Yi, B. Y., Yoo, D. G., Ryu, B. J., & Riedel, M. (2011). Evidence of gas hydrate from downhole logging data in the Ulleung Basin, East Sea. *Marine and Petroleum Geology*, *28*(10), 1979–1985.

[90] King, M. S., & Marsden, J. R. (2002). Velocity dispersion between ultrasonic and seismic frequencies in brine-saturated reservoir sandstones. *Geophysics*, *67*(1), 254.

[91] Konno, Y., Oyama, H., Nagao, J., Masuda, Y., & Kurihara, M. (2010). Numerical analysis of the dissociation experiment of naturally occurring gas hydrate in sediment cores obtained at the eastern nankai trough, Japan. *Energy and Fuels*, *24*(12), 6353–6358.

[92] Konno, Y., Jin, Y., Yoneda, J., Kida, M., Egawa, K., Ito, T., et al. (2015). Effect of methane hydrate morphology on compressional wave velocity of sandy sediments : Analysis of pressure cores obtained in the Eastern Nankai Trough. *Marine and Petroleum Geology*, *66*, 425–433.

[93] Konno, Y., Fujii, T., Sato, A., Akamine, K., Naiki, M., Masuda, Y., et al. (2017). Key Findings of the World's First Offshore Methane Hydrate Production Test off the Coast of Japan: Toward Future Commercial Production. *Energy and Fuels*, *31*(3), 2607–2616.

[94] Kuhs, W. F., Genov, G., Goreshnik, E., Zeller, A., Techmer, K. S., & Bohrmann, G. (2004). The impact of porous microstructures of gas hydrates on their macroscopic properties. *International Journal of Offshore and Polar Engineering*, *14*(4), 305–309.

[95] Kumar, P., Collett, T. S., Boswell, R., Cochran, J. R., Lall, M., Mazumdar, A., et al. (2014). Geologic implications of gas hydrates in the offshore of India: Krishna-Godavari Basin, Mahanadi Basin, Andaman Sea, Kerala-Konkan Basin. *Marine and Petroleum Geology*, *58*(PA), 29–98.

[96] Kumar, P., Collett, T. S., Vishwanath, K., Shukla, K. M., Nagalingam, J., Lall, M. V, et al. (2016). Gas-hydrate-bearing sand reservoir systems in the offshore of India: Results of the India National Gas Hydrate Program Expedition 02. *Methane Hydrate Newsletter*, *16*(1), 1–20.

[97] Kuster, G. T., & Toksoz, M. N. (1974). Velocity and attenuation of seismic waves in two-phase media; Part I, Theoretical formulations. *Geophysics*, *39*(5), 587–606.

[98] Kvenvolden, K. A. (1988). Methane hydrates and global climate. *Global Biogeochemical Cycles*, *2*(3), 221–229.

[99] Kvenvolden, K. A. (1993). Gas hydrates—geological perspective and global change. *Reviews of Geophysics*, *31*(2), 173–187.

[100] Leclaire, P., Cohen‐Ténoudji, F., & Aguirre‐Puente, J. (1994). Extension of Biot's theory of wave propagation to frozen porous media. *The Journal of the Acoustical Society of America*, *96*(6), 3753–3768.

[101] Lee, J. Y., Yun, T. S., Santamarina, J. C., & Ruppel, C. (2007). Observations related to tetrahydrofuran and methane hydrates for laboratory studies of hydrate-bearing sediments. *Geochemistry, Geophysics, Geosystems*, *8*(6), 1–10.

[102] Lee, J. Y., Francisca, F. M., Santamarina, J. C., & Ruppel, C. (2010). Parametric study of the physical properties of hydrate-bearing sand, silt, and clay sediments: 2. Small-strain mechanical properties. *Journal of Geophysical Research: Solid Earth*, *115*(11), 1–11.

[103] Lee, M. W., & Collett, T. S. (2009). Gas hydrate saturations estimated from fractured reservoir at Site NGHP-01-10, Krishna-Godavari Basin, India. *Journal of Geophysical Research: Solid Earth*, *114*(7), 1–13.

[104] Lee, M. W., & Waite, W. F. (2007). Amplitude loss of sonic waveform due to source coupling to the medium. *Geophysical Research Letters*, *34*(5), 1–4.

[105] Lee, M. W., & Waite, W. F. (2008). Estimating pore-space gas hydrate saturations from well log acoustic data. *Geochemistry, Geophysics, Geosystems*, *9*(7), 1–8.

[106] Lee, M. W., Hutchinson, D. R., Collett, T. S., & Dillon, W. P. (1996). Seismic velocities for hydrate-bearing sediments using weighted equation. *Journal of Geophysical Research: Solid Earth*, *101*(B9), 20347–20358.

[107] Lee, M. W., Collett, T. S., & Inks, T. L. (2009). Seismic-attribute Analysis for Gas-hydrate and Free-gas Prospects on the North Slope of Alaska. *Natural Gas Hydrates— Energy Resource Potential and Associated Geologic Hazards*, 541–554.

[108] Lerche, I., & Menke, W. (1986). An inversion method for separating apparent and intrinsic attenuation in layered media. *Geophysical Journal of the Royal Astronomical Society*, *87*(2), 333–347.

[109] Leurer, K. C. (1997). Attenuation in fine-grained marine sediments; extension of the Biot-Stoll model by the "effective grain model" (EGM). *Geophysics*, *62*(5), 1465–1479.

[110] Leurer, K. C., & Brown, C. (2008). Acoustics of marine sediment under compaction: binary grain-size model and viscoelastic extension of Biot's theory. *The Journal of the Acoustical Society of America*, *123*(4), 1941–51.

[111] Madrussani, G., Rossi, G., & Camerlenghi, A. (2010). Gas hydrates, free gas distribution and fault pattern on the west Svalbard continental margin. *Geophysical Journal International*, *180*(2), 666–684.

[112] Marín-Moreno, H., Sahoo, S. K., & Best, A. I. (2017). Theoretical modeling insights into elastic wave attenuation mechanisms in marine sediments with pore-filling methane hydrate. *Journal of Geophysical Research: Solid Earth*, *122*(3), 1835–1847.

[113] Marketos, G., & Best, A. I. (2010). Application of the BISQ model to clay squirt flow in reservoir sandstones. *Journal of Geophysical Research: Solid Earth*, *115*(6), 1–12.

[114] Maslin, M., Owen, M., Betts, R., Day, S., Dunkley Jones, T., & Ridgwell, A. (2010). Gas hydrates: past and future geohazard? *Philosophical Transactions. Series A, Mathematical, Physical, and Engineering Sciences*, *368*(1919), 2369–2393.

[115] Matsushima, J. (2005). Attenuation measurements from sonic waveform logs in methane hydrate-bearing sediments at the Nankai Trough exploratory well off Tokai, central Japan. *Geophysical Research Letters*, *32*(3), 1–5.

[116] Matsushima, J. (2006). Seismic wave attenuation in methane hydrate-bearing sediments vertical seismic profiling data from the Nankai trough exploratory well, offshore Tokai, central Japan. *Journal of Geophysical Research: Solid Earth*, *111*(10), 1–20.

[117] Matsushima, J., Suzuki, M., Kato, Y., Nibe, T., & Rokugawa, S. (2008). Laboratory experiments on compressional ultrasonic wave attenuation in partially frozen brines. *Geophysics*, *73*(2), N9–N18.

[118] Matsushima, J., Nibe, T., Suzuki, M., Kato, Y., & Rokugawa, S. (2011). A poroelastic model for ultrasonic wave attenuation in partially frozen brines. *Exploration Geophysics*, *42*(1), 105–115.

[119] Matsushima, J., Suzuki, M., Kato, Y., & Rokugawa, S. (2011). Estimation of ultrasonic scattering attenuation in partially frozen brines using magnetic resonance images. *Geophysics*, *76*(1), T13–T25.

[120] Matsushima, J., Suzuki, M., Kato, Y., & Rokugawa, S. (2013). Effects of viscosity of unfrozen brine in partially frozen unconsolidated sediments on ultrasonic wave attenuation. *Proceedings of the 11th SEGJ International Symposium*, (1), 383–386.

[121] Matsushima, J., Suzuki, M., Kato, Y., & Rokugawa, S. (2015). Ultrasonic measurements of attenuation and velocity of compressional and shear waves in partially frozen unconsolidated sediment and synthetic porous rock. *Geophysics*, *81*(2), D141–D153.

[122] Matsushima, J., Ali, M. Y., & Bouchaala, F. (2016). Seismic attenuation estimation from zero-offset VSP data using seismic interferometry. *Geophysical Journal International*, *204*(2), 1288–1307.

[123] Matsushima, J. (2015). S-wave attenuation estimation from walkaway VSP data in methane hydrate-bearing sediments. The 133rd (2015 FALL) SEGJ Conference. Japanese with English abstract.

[124] Mavko, G., & Jizba, D. (1991). Estimating grain-scale fluid effects on velocity dispersion in rocks. *Geophysics*, *56*(12), 1940–1949.

[125] Mavko, G. M., & Nur, A. (1979). Wave attenuation in partially saturated rocks. *Geophysics*, *44*(2), 161–178.

[126] McIver, R. D. (1977). Hydrates of Natural Gas--Important Agent in Geologic Processes. *Geological Society of America-Abstracts with Programs*, *20*(9), 1089–1090.

[127] Menke, W., & Dubendorff, B. (1985). Discriminating intrinsic and apparent attenuation in layered rock. *Geophysical Research Letters*, *12*(10), 721–724.

[128] Merey, Ş. (2016). Drilling of gas hydrate reservoirs. *Journal of Natural Gas Science and Engineering*, *35*(Part A), 1167–1179.

[129] Mikhaltsevitch, V., Lebedev, M., & Gurevich, B. (2014). A laboratory study of low-frequency wave dispersion and attenuation in water-saturated sandstones. *The Leading Edge*, *33*(6), 616–622.

[130] Müller, T. M., & Gurevich, B. (2005). Wave-induced fluid flow in random porous media: Attenuation and dispersion of elastic waves. *The Journal of the Acoustical Society of America*, *117*(5), 2732–2741.

[131] Murphy, W. F., Winkler, K. W., & Kleinberg, R. L. (1986). Acoustic relaxation in sedimentary rocks: Dependence on grain contacts and fluid saturation. *Geophysics*, *51*(3), 757–766.

[132] Murphy, W. M. (1983). Effects of partial water saturation on attenuation in Massillon sandstone and Vycor porous glass. *J. Acoust. Soc. Am.*, *71*(1982), 1458–1486.

[133] Nakano, Y., & Arnold, R. (1973). Acoustic properties of frozen Ottawa sand. *Water Resources Research*, *9*(1), 178–184.

[134] Nakano, Y., Martin, R. J., & Smith, M. (1972). Ultrasonic velocities of the dilatational and shear waves in frozen soils. *Water Resources Research*, *8*(4), 1024–1030.

[135] Nittala, S., Sain, K., & Nara, D. (2017). Seismic vis-a-vis sonic attenuation in gas hydrate bearing sediments of Krishna-Godavari basin, Eastern Margin of India. *Geophysical Journal International*, *209*(2), 1195–1203.

[136] Nouzé, H., Henry, P., Noble, M., Martin, V., & Pascal, G. (2004). Large gas hydrate accumulations on the eastern Nankai Trough inferred from new high-resolution 2-D seismic data. *Geophysical Research Letters*, *31*(13), 2–5.

[137] Papadakis, E. P. (1965). Ultrasonic Attenuation Caused by Scattering in Polycrystalline Metals. *The Journal of the Acoustical Society of America*, *37*(4), 711–717.

[138] Paull, C. K., Brewer, P. G., Ussler, W., Peltzer, E. T., Rehder, G., & Clague, D. (2002). An experiment demonstrating that marine slumping is a mechanism to transfer methane from seafloor gas-hydrate deposits into the upper ocean and atmosphere. *Geo-Marine Letters*, *22*(4), 198–203.

[139] Paull, C. K., Ussler, W., Dallimore, S. R., Blasco, S. M., Lorenson, T. D., Melling, H., et al. (2007). Origin of pingo-like features on the Beaufort Sea shelf and their possible relationship to decomposing methane gas hydrates. *Geophysical Research Letters*, *34*(1), 1–5.

[140] Pecher, I. A. (2003). Seismic anisotropy in gas-hydrate- and gas-bearing sediments on the Blake Ridge, from a walkaway vertical seismic profile. *Geophysical Research Letters*, *30*(14), 1–4.

[141] Peters, L. E., Anandakrishnan, S., Alley, R. B., & Voigt, D. E. (2012). Seismic attenuation in glacial ice: A proxy for englacial temperature. *Journal of Geophysical Research: Earth Surface*, *117*(2), 1–10.

[142] Petersen, C. J., Papenberg, C., & Klaeschen, D. (2007). Local seismic quantification of gas hydrates and BSR characterization from multi-frequency OBS data at northern Hydrate Ridge. *Earth and Planetary Science Letters*, *255*(3–4), 414–431.

[143] Pohl, M., Prasad, M., & Batzle, M. L. (2017). Ultrasonic Attenuation of Pure THF-Hydrate. *Geophysical Prospecting*, being published.

[144] Prasad, M., & Dvorkin, J. (2004). Velocity and attenuation of compressional waves in brines. *SEG Technical Program Expanded Abstracts 2004*, (January 1999), 1666–1669.

[145] Pride, S. R., Berryman, J. G., & Harris, J. M. (2004). Seismic attenuation due to wave-induced flow. *Journal of Geophysical Research: Solid Earth*, *109*(B1), 1–19.

[146] Priest, J. A., Best, A. I., & Clayton, C. R. I. (2005). A laboratory investigation into the seismic velocities of methane gas hydrate-bearing sand. *Journal of Geophysical Research: Solid Earth*, *110*(4), 1–13.

[147] Priest, J. A., Best, A. I., & Clayton, C. R. I. (2006). Attenuation of seismic waves in methane gas hydrate-bearing sand. *Geophysical Journal International*, *164*(1), 149–159.

[148] Priest, J. A., Rees, E. V. L., & Clayton, C. R. I. (2009). Influence of gas hydrate morphology on the seismic velocities of sands. *Journal of Geophysical Research: Solid Earth*, *114*(11), 1–13.

[149] Priest, J. A., Clayton, C. R. I., & Rees, E. V. L. (2014). Potential impact of gas hydrate and its dissociation on the strength of host sediment in the Krishna-Godavari Basin. *Marine and Petroleum Geology*, *58*(PA), 187–198.

[150] Riedel, M., Willoughby, E. C., Chen, M. A., He, T., Novosel, I., Schwalenberg, K., et al. (2006). Gas hydrate on the northern Cascadia margin: regional geophysics and structural framework. *Proceedings of the IODP, 311*, *311*, 1–28.

[151] Riedel, M., Bellefleur, G., Mair, S., Brent, T. A., & Dallimore, S. R. (2009). Acoustic impedance inversion and seismic reflection continuity analysis for delineating gas hydrate resources near the Mallik research sites, Mackenzie Delta, Northwest Territories, Canada. *Geophysics*, *74*(5), B125–B137.

[152] Riedel, M., Willoughby, E., & Chopra, S. (2010). *Geophysical Characterization of Gas Hydrates*. *Geophysical Developments Series*. Society of Exploration Geophysicists.

[153] Rossi, G., Gei, D., Böhm, G., Madrussani, G., & Carcione, J. (2007). Attenuation tomography: an application to gas-hydrate and free gas detection. *Geophysical Prospecting*, *55*(5), 655–669.

[154] Ru Shan, W. (1982). Attenuation of short period seismic waves due to scattering. *Geophysical Research Letters*, *9*(1), 9–12.

[155] Ruppel, C. D. (2011). Methane Hydrate and Contemporary Climate Change. *Nature Education Knowledge*, *3*(10), 29.

[156] Ruppel, C. D., & Kessler, J. D. (2017). The interaction of climate change and methane hydrates. *Reviews of Geophysics*, *55*(1), 126–168.

[157] Ryu, B., & Riedel, M. (2017). Gas hydrates in the Ulleung Basin , East Sea of Korea. *Terrestrial Atmospheric and Oceanic Sciences*, *28*(6), 943–963.

[158] Sams, M. S., Neep, J. P., Worthington, M. H., & King, M. S. (1997). The measurement of velocity dispersion and frequency-dependent intrinsic attenuation in sedimentary rocks. *Geophysics*, *62*(5), 1456–1464.

[159] Santamarina, J. C., & Ruppel, C. (2010). 26. The Impact of Hydrate Saturation on the Mechanical, Electrical, and Thermal Properties of Hydrate-Bearing Sand, Silts, and Clay. *Geophysical Characterization of Gas Hydrates*, (Icgh), 373–384.

[160] Schindler, M., Batzle, M. L., & Prasad, M. (2016). Micro X-Ray computed tomography imaging and ultrasonic velocity measurements in tetrahydrofuran-hydrate-bearing sediments. *Geophysical Prospecting*, 1025–1036.

[161] Sell, K., Quintal, B., Kersten, M., & Saenger, E. H. (2017). Squirt flow due to interfacial water films in hydrate bearing sediments. *Solid Earth Discuss*, (September), 1–25.

[162] Shankar, U., & Riedel, M. (2011). Gas hydrate saturation in the Krishna-Godavari basin from P-wave velocity and electrical resistivity logs. *Marine and Petroleum Geology*, *28*(10), 1768–1778.

[163] Simion, A. I., Grigoraş, C.-G., Roşu, A.-M., & Lucian Gavrilă. (2015). Mathematical modelling of density and viscosity of nacl aqueous solutions. *Journal of Agrolimentaryprocesses and Tecnologies*, *21*(1), 41–52.

[164] Sloan, E. D., & Koh, C. (2006). *Clathrate Hydrates of Natural Gases*. *CRC Press* (Vol. 3rd ed.).

[165] Sondergeld, C. H., & Rai, C. S. (2007). Velocity and resistivity changes during freeze-thaw cycles in Berea sandstone. *Geophysics*, *72*(2), E99–E105.

[166] Spetzler, H., & Anderson, D. L. (1968). The effect of temperature and partial melting on velocity and attenuation in a Simple Binary System. *Journal of Geophysical Research*, *73*(18), 6051–6060.

[167] Stoll, R. D., & Bryan, G. M. (1970). Wave Attenuation in Saturated Sediments. *The Journal of the Acoustical Society of America*, *47*(5), 1440–1447.

[168] Summerhayes, C. P., Bornhold, B. D., & Embley, R. W. (1979). Surficial slides and slumps on the continental slope and rise of South West Africa: A reconnaissance study. *Marine Geology*, *31*(3–4), 265–277.

[169] Suzuki, H., & Matsushima, J. (2013). Quantifying uncertainties in attenuation estimation at methane-hydrate-bearing zones using sonic waveform logs. *Geophysics*, *78*(5), D339–D353.

[170] Suzuki, M., Matsushima, J., & Kato, Y. (2010). Ultrasonic wave-transmission measurement system on an ice-brine coexisting system. *Butsuri-Tansa(Geophysical Exploration)*, *63*(3), 239–249.

[171] Swaranjit Singh, A. A. (2015). Natural Gas Hydrate as an Upcoming Resource of Energy. *Journal of Petroleum & Environmental Biotechnology*, *06*(01), 1–6.

[172] Takayama, T., Nishi, M., Yamamoto, H., Sanada, Y., Matsuda, S., & Uchida, T. (2004). Occurrence of free-gas associated with methane-hydrate-bearing formations in the MITI Nankai Trough wells, offshore Tokai, Japan. *Resource Geology*, *54*(1), 89–98.

[173] Timur, A. (1968). Velocity of compressional waves in porous media at permafrost temperatures. *Geophysics*, *33*(4), 584–595.

[174] Tisato, N., & Quintal, B. (2013). Measurements of seismic attenuation and transient fluid pressure in partially saturated Berea sandstone: Evidence of fluid flow on the mesoscopic scale. *Geophysical Journal International*, *195*(1), 342–351.

[175] Tisato, N., Quintal, B., Chapman, S., Podladchikov, Y., & Burg, J. P. (2015). Bubbles attenuate elastic waves at seismic frequencies: First experimental evidence. *Geophysical Research Letters*, *42*(10), 3880–3887.

[176] Tsuji, Y., Ishida, H., Nakamizu, M., Matsumoto, R., & Shimizu, S. (2004). Overview of the MITI Nankai Trough wells: A milestone in the evaluation of methane hydrate resources. *Resource Geology*, *54*(1), 3–10.

[177] Uchida, T., Lu, H., Tomaru, H., Matsumoto, R., Senoh, O., Oda, H., et al. (2004). Subsurface occurrence of natural gas hydrate in the Nankai Trough area: Implication for gas hydrate concentration. *Resource Geology*, *54*(1), 35–44.

[178] Waite, W. F., Santamarina, J. C., Cortes, D. D., Dugan, B., Espinoza, D. N., Germaine, J., et al. (2009). Physical properties of hydrate-bearing sediments. *Reviews of Geophysics*, *47*(4), n/a-n/a.

[179] Walsh, J. B. (1966). Seismic Wave Attenuation in Rock Due to Frcition. *Journal of Geophysical Research*, *71*(10), 2591–2599.

[180] Walsh, J. B. (1969). New analysis of attenuation in partially melted rock. *Journal of Geophysical Research*, *74*(17), 4333–4337.

[181] Wang, X., Hutchinson, D. R., Wu, S., Yang, S., & Guo, Y. (2011). Elevated gas hydrate saturation within silt and silty clay sediments in the Shenhu area, South China Sea. *Journal of Geophysical Research: Solid Earth*, *116*(5), 1–18.

[182] Wang, X., Lee, M., Wu, S., & Yang, S. (2012). Identification of gas hydrate dissociation from wireline-log data in the Shenhu area, South China Sea. *Geophysics*, *77*(3), B125–B134.

[183] Westbrook, G. K., Chand, S., Rossi, G., Long, C., Bünz, S., Camerlenghi, A., et al. (2008). Estimation of gas hydrate concentration from multi-component seismic data at sites on the continental margins of NW Svalbard and the Storegga region of Norway. *Marine and Petroleum Geology*, *25*(8), 744–758.

[184] White, J. (1975). Computed seismic speeds and attenuation in rocks with partial gas saturation. *Geophysics*, *40*(2), 224–232.

[185] Winkler, K. W., & Nur, A. (1982a). Seismic attenuation: Effects of pore fluids and frictional-sliding. *Geophysics*, *47*(1), 1–15.

[186] Winkler, K. W., & Nur, A. (1982b). Seismic attenuation: Effects of pore fluids and frictional-sliding. *Geophysics*, *47*(1), 1–15.

[187] Winters, W., Walker, M., Hunter, R., Collett, T., Boswell, R., Rose, K., et al. (2010). Physical properties of sediment from the Mount Elbert Gas Hydrate Stratigraphic Test Well , Alaska North Slope. *Marine and Petroleum Geology*, *28*(2), 1–20.

[188] Winters, W. J., Waite, W. F., & Mason, D. H. (2009). Effects of methane hydrate on the physical properties of sediments. *In T. Collett, A. Johnson, C. Knapp, and R. Boswell, Eds., Natural Gas Hydrates—Energy Resource Potential and Associated Geologic Hazards: AAPG Memoir 89*, 714–722.

[189] Wood, W. T., Holbrook, W. S., & Hoskins, H. (2000). *In situ measurements of P-wave attenuation in the methane hydrate- and gas-bearing sediments of the Blake Ridge*. *Proceedings of the Ocean Drilling program, Scientific Results* (Vol. 164).

[190] Wu, T. Te. (1966). The effect of inclusion shape on the elastic moduli of a two-phase material. *International Journal of Solids and Structures*, *2*(1), 1–8.

[191] Wu, Y., Nakagawa, S., Kneafsey, T. J., Dafflon, B., & Hubbard, S. (2017). Electrical and seismic response of saline permafrost soil during freeze - Thaw transition. *Journal of Applied Geophysics*, *146*, 16–26.

[192] Yang, Y., Forsyth, D. W., & Weeraratne, D. S. (2007). Seismic attenuation near the East Pacific Rise and the origin of the low-velocity zone. *Earth and Planetary Science Letters*, *258*(1–2), 260–268.

[193] Yuan, T., G. D. Spence, R. D. Hyndman, T. A. Minshull, and S. C. S. (1999). Seismic velocity studies of a gas hydrate bottom‐simulating reflector on the northern Cascadia continental margin: Amplitude modeling and full waveform inversion. *Journal of Geophysical Research: Solid Earth*, *104*(B1), 1179–1191.

[194] Yuan, T., Hyndman, R. D., Spence, G. D., & Desmons, B. (1996). Seismic velocity increase and deep-sea gas hydrate concentration above a bottom-simulating reflector on the northern Cascadia continental slope. *Journal of Geophysical Research*, *101*(B6), 13655.

[195] Yun, T. S., Francisca, F. M., Santamarina, J. C., & Ruppel, C. (2005). Compressional and shear wave velocities in uncemented sediment containing gas hydrate. *Geophysical Research Letters*, *32*(10), 1–5.

[196] Yun, T. S., Santamarina, C. J., & Ruppel, C. (2007). Mechanical properties of sand, silt, and clay containing tetrahydrofuran hydrate. *Journal of Geophysical Research: Solid Earth*, *112*(4), 1–13.

[197] Zatsepina, O. Y., & Buffett, B. A. (1997). Phase equilibrium of gas hydrate: Implications for the formation of hydrate in the deep sea floor. *Geophysical Research Letters*, *24*(13), 1567–1570.

[198] Zimmerman, R. W., & Kingt, M. S. (1986). The effect of the extent of freezing on seismic velocities in unconsolidated permafrost. *Geophysics*, *51*(6), 1285–1290.